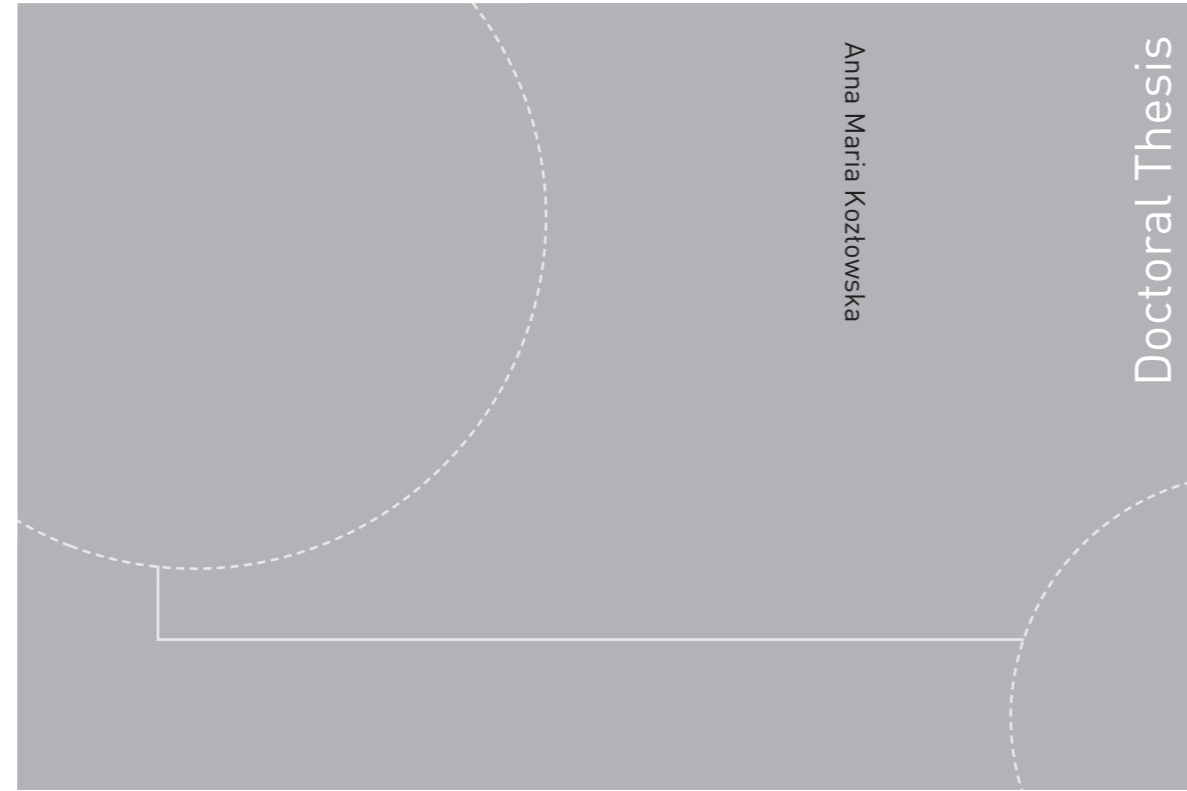


ISBN 978-82-326-3774-4 (printed version)  
ISBN 978-82-326-3775-1 (electronic version)  
ISSN 1503-8181



Doctoral theses at NTNU, 2019:86

**NTNU**  
Norwegian University of  
Science and Technology  
Faculty of Engineering  
Department of Marine Technology

Doctoral theses at NTNU, 2019:86

Anna Maria Kozłowska

**Hydrodynamic Loads on Marine  
Propellers Subject to  
Ventilation and Out of Water Condition**

 **NTNU**  
Norwegian University of  
Science and Technology

 NTNU

 **NTNU**  
Norwegian University of  
Science and Technology

Anna Maria Kozłowska

# Hydrodynamic Loads on Marine Propellers Subject to Ventilation and Out of Water Condition

Thesis for the degree of Philosophiae Doctor

Trondheim, March 2019

Norwegian University of Science and Technology  
Faculty of Engineering  
Department of Marine Technology



Norwegian University of  
Science and Technology

**NTNU**

Norwegian University of Science and Technology

Thesis for the degree of Philosophiae Doctor

Faculty of Engineering  
Department of Marine Technology

© Anna Maria Kozłowska

ISBN 978-82-326-3774-4 (printed version)

ISBN 978-82-326-3775-1 (electronic version)

ISSN 1503-8181

Doctoral theses at NTNU, 2019:86



Printed by Skipnes Kommunikasjon as

# PREFACE

The thesis was carried out at the University Technology Centre (UTC) of Rolls Royce at NTNU (Trondheim) as a part of the European Research project “PropSeas”, sponsored by the Rolls Royce Marine and Research Council of Norway. The research was carried out from November 2007 to September 2010. Then it was a break in the following project. I applied for the leave of absence and started work in oil and gas company. From 2016, I have decided to go back to the research and complete the thesis. The thesis is based on three conference publications, which were published in the year 2009, 2010 and 2011 as well as two latest journal publications, which were published in the year 2017.

I am grateful to have an opportunity working with my supervisor Professor Sverre Steen. I would like to thank you for a good discussion, guidance and suggestions. I really appreciated your support and interest for the past years.

I would like to thank my co-supervisor Professor Kourosh Koushan to inspire me in the beginning of the work, by introducing his previous work and findings about the propeller ventilation. I would also thank the employees in Rolls Royce Marine As especially Leif Vartdal and Leif Aarseth for their help and valuable discussions.

I also want to thank Dr. Andrea Califano, Dr. Luca Savio and Øyvind Dalheim for sharing their knowledge about the propeller hydrodynamics. Dr. Luca Savio always shows interests in discussing my findings and progress as well as help me with the experimental set up and processing scripts. I would like to thank Luca Savio for suggesting the model for predicting the vortex ventilation.

I would like to thank Torgeir Wahl, Morten Korsvold and Silas Spence for excellent guidance and help in the MCLab and towing tank experiments at Sintef Ocean.

Many thanks to my colleagues at Marine Technology Department, I could not listed them all but special thanks go to Dr. Thomas Sauder, Dr. Asle Natskår, Dr. Lucia Sileo, Dr. Ida Aglen, Dr. Mia Abrahamsen-Prsic, Dr. Erin Bachynski and Dr. Fatemeh Dadmarzi. You have been so important to these years and made my working days enjoyable and fun.

I am grateful to my family, in particular to my mother and father for providing me a solid background of mathematics and show on their example than the research work can be interesting and exciting.

Finally, I would like to thank my husband, Grzegorz. His everyday support and believe in me, gives me a strong power to improve my self-confidence, and has been the most important foundation for this accomplishment. Nobody is born with limitless self-confidence, but “low self-esteem is like driving through the life with your hands brake on” – Maxwell Maltz. I am also grateful to my children Natalia and Tomasz for giving me an important perspective of life.

# TABLE OF CONTENTS

<b>NOMENCLATURE .....</b>	<b>VII</b>
<b>1 INTRODUCTION.....</b>	<b>1</b>
1.1 Background and motivation.....	1
1.2 Propeller ventilation.....	4
1.3 Slamming on propeller blade.....	6
1.4 Objective and scope.....	7
1.5 Present work and outline of thesis.....	8
1.6 List of publications .....	10
<b>2 OUTLINE OF THEORY FOR HYDRODYNAMIC LOADS ON PROPELLERS IN WAVES AND PARTIAL SUBMERCENCES. ....</b>	<b>13</b>
2.1 Theory for propeller ventilation.....	13
2.2 Vortex theory.....	28
2.3 Propeller analysis.....	34
2.4 Steady state vortex models .....	37
2.5 Inception of cavitating / ventilating vortex.....	40
2.6 Slamming forces .....	43
<b>3 MODEL TESTS .....</b>	<b>45</b>
3.1 Overview of complete model tests .....	45
3.2 Geometry of propeller models .....	49
3.3 Main dimension of thruster bodies .....	49
3.4 <i>Koz17</i> .....	51
3.5 <i>Koz10</i> .....	62
3.6 <i>Kou10</i> .....	70
3.7 <i>Koz09</i> .....	72
3.8 <i>Koz08</i> .....	74
3.9 <i>Kou2006_I and Kou2006_II</i> .....	76
<b>4 EXPERIMENTAL RESULTS .....</b>	<b>81</b>
4.1 Ventilation regimes and critical advance numbers ( <i>Koz17</i> ) .....	81
4.2 Relation between thrust and torque loss factor ( <i>Kou2006_I</i> ) .....	86

4.3	The time influence of ventilation inception ( <i>Kou2006_I</i> ).....	87
4.4	Thrust hysteresis effect ( <i>Kou2006_I and Kou2006_II</i> ).....	88
4.5	Comparison between static and dynamic thrust loss ( <i>Kou2006_I, Kou2006_II</i> )..	90
4.6	Importance of heave motion period for thrust loss ( <i>Kou2006_I and Kou2006_II</i> )	92
4.7	Propeller Ventilation by Vortex Formation ( <i>Koz09, Koz10, Kou10, Koz17</i> ).....	95
4.8	Comparison between PHVC, and PFSVV ( <i>Koz09, Koz17</i> ).....	97
4.9	Inception of ventilating vortex ( <i>Kou2006_I, Koz09, Koz10, Kou10 and Koz17</i> )	100
4.10	Comparison between CFD calculations and model experiments ( <i>Koz10</i> ).....	104
<b>5</b>	<b>CALCULATION MODEL FOR THRUST LOSS DUE TO VENTILATION AND OUT OF THE WATER EFFECT.....</b>	<b>121</b>
5.1	Deeply submerged.....	121
5.2	Submerged, vortex ventilation .....	122
5.3	Ventilation by piercing the free surface .....	129
5.4	Overview of complete calculation model.....	133
5.5	Comparison between calculation model and experimental results ( <i>Koz17</i> ).....	134
<b>6</b>	<b>SIMULATION MODEL FOR THRUST LOSS DUE TO VENTILATION AND OUT OF THE WATER EFFECT .....</b>	<b>141</b>
6.1	Time domain simulation model: PropSim 2018 and PropSim 2016.....	141
6.2	Simulation model validation .....	143
<b>7</b>	<b>THE PROPELLER BLADE SLAMMING HYPOTHESIS .....</b>	<b>161</b>
7.1	Introduction .....	161
7.2	Msc Thesis by Mork (2007).....	161
7.1	Model Tests, ( <i>Koz08</i> ).....	167
<b>8</b>	<b>DISCUSSION, CONCLUSIONS AND RECOMMENDATIONS FOR FUTURE WORK.....</b>	<b>171</b>
8.1	Discussion .....	171
8.2	Conclusions .....	186
8.3	Recommendations for future work.....	188
<b>APPENDIX A</b>	<b>PROPELLERS GEOMETRY: P1374 AND P1440</b>	
<b>APPENDIX B</b>	<b>EXPERIMENTAL SET UP AND TESTING CONDITIONS</b>	
	<b>EXPERIMENTS: KOU2006_I</b>	

<b>APPENDIX C</b>	<b>EXPERIMENTAL SET UP AND TESTING CONDITIONS EXPERIMENTS: <i>KOU2006 II</i></b>
<b>APPENDIX D</b>	<b>EXPERIMENTAL SET UP AND TESTING CONDITIONS EXPERIMENTS: <i>KOZ09</i></b>
<b>APPENDIX E</b>	<b>EXPERIMENTAL SET UP, TESTING CONDITIONS AND EXPERIMENTAL RESULTS EXPERIMENTS: <i>KOZ10</i>,</b>
<b>APPENDIX F</b>	<b>EXPERIMENTAL SET UP, TESTING CONDITIONS AND EXPERIMENTAL RESULTS EXPERIMENTS: <i>KOZ17</i></b>
<b>APPENDIX G</b>	<b>EXPERIMENTAL SET UP, TESTING CONDITIONS AND EXPERIMENTAL RESULTS SLAMMING EXPERIMENTS: <i>KOZ08</i></b>
<b>APPENDIX H</b>	<b>CALCULATION MODEL, VENTILATION</b>





## NOMENCLATURE

### Acronyms

2D	Two dimensional
ABS	American Bureau of Shipping
BEMT	Blade Element Momentum Theory
CFD	Computational Fluid Dynamics
DES	Detached Eddy Simulation
DNV GL	Det Norske Veritas (Norway) and Germanischer Lloyd (Germany)
DP	Dynamic Positioning
<i>Kou2006_I</i>	Ventilation tests performed by Koushan in 2006
<i>Kou2006_II</i>	Ventilation tests performed by Koushan in 2006
<i>Koz08</i>	Slamming tests performed by Kozłowska in 2008
<i>Koz09</i>	Ventilation tests performed by Kozłowska in 2009
<i>Koz10</i>	Ventilation tests performed by Kozłowska in 2010
<i>Kou10</i>	Ventilation tests performed by Koushan in 2010
<i>Koz17</i>	Ventilation tests performed by Kozłowska in 2017
<i>LES</i>	Large Eddy Simulation
<i>LRS</i>	Lloyd Register of Shipping
<i>P1362</i>	Propeller model used by Mork (2007)
<i>P1374</i>	Propeller model used in experiments
<i>P1440</i>	Propeller model used in experiments
<i>PFSVV</i>	Propeller Free Surface Vortex Ventilation
<i>PHVC</i>	Propeller Hull Vortex Cavitation
<i>RANS</i>	Reynolds-Averaged Navier Stokes Equations
<i>RPM</i>	Revolution per minute
<i>S.D.</i>	Standard Deviation
<i>Slam 2D</i>	Computer program based on Wagner theory (slamming)
<i>TIFF</i>	Tooth Interior Fatigue Fracture
<i>TUHH</i>	Hamburg University of Technology

## Latin Letters

$A_0$	$[m^2]$	propeller disc area
$A/R$	$[-]$	Amplitude of heave motion divide by propeller radius
$A/T$	$[m/s]$	Amplitude of heave motion divide by heave motion period
$A$	$[m^2]$	propeller emerged area
$AA_0$	$[-]$	emerged area to suction area ratio
$A_{NV}$	$[m^2]$	non-ventilated propeller disc area
$A_V$	$[m^2]$	ventilated propeller disc area
$A_{V0} = A_V/A_0$	$[-]$	ventilated propeller disk area ratio
$A_{NV0} = A_V/A_0$	$[-]$	non - ventilated propeller disk area ratio
$A_E/A_0, EAR$	$[-]$	Blade area ratio
$a$	$[1/s]$	flow suction gradient
$a_v$	$[mm]$	Radius of ventilating vortex
$c_t$	$[mm]$	Tip clearance, distance from propeller tip to free surface
$c/D_{0.7R}$	$[-]$	Chord diameter ratio
$c_{Pmax}$	$[-]$	Pressure coefficient at maximum pressure (slamming)
$c$	$[mm]$	Chord length
$c_L$	$[-]$	lift coefficient
$c_{L0.7}$	$[-]$	lift coefficient at 70% radius
$c_{0.7}$	$[m]$	chord length at 70% radius
$c_{LV}$	$[-]$	lift coefficient for ventilated propeller
$c_T$	$[-]$	propeller load coefficient
$c_Q$	$[-]$	Torque load coefficient
$c_{TH}$	$[-]$	Thrust loading coefficient
$c_{Tn}$	$[m]$	propeller load coefficient for non-ventilated deeply submerged propeller
$d/D$	$[-]$	Hub diameter ratio
$D, R$	$[m]$	propeller diameter, propeller radius
$F_{nD}$	$[-]$	Froude number based on diameter
$F_{nh}$	$[-]$	Froude number based on submergence
$g$	$[m/s^2]$	acceleration of gravity
$h$	$[m]$	propeller submergence
$H$	$[m]$	distance from the mirror plane to the sink

$h_{RA}$	[-]	propeller submergence to suction radius $R_A$
$h/R$	[-]	propeller submergence from the shaft center to the free surface
$J$	[-]	advance number
$K_T, K_Q$	[-]	time-averaged mean value of the thrust/torque coefficient
$K_{Tn}, K_{Qn}$	[-]	Thrust/torque coefficient for non-ventilated deeply submerged propeller
$k_{0.7}$	[-]	Ratio equal to 1.5, for typical propeller acc. to Gutsche (1962)
$n$	[Hz]	propeller revolutions
$n_s$	[-]	Minimum number of propeller revolution needed to establish a ventilation
$n_v$	[-]	Minimum number of propeller revolution needed for ventilation to disappear
$p_{at}$	[Pa]	Atmospheric pressure
$p_{cav}$	[Pa]	Vapor pressure
$P/D$	[-]	propeller pitch ratio
$q_3$	[m <sup>3</sup> /s]	loss of propeller flow rate
$Q_p$	[m <sup>3</sup> /s]	volumetric propeller flow rate
$Q_t$	[Nm]	Actual propeller torque
$Q_n$	[Nm]	Torque obtained for deeply submerged condition
$Q$	[kNm]	propeller torque
$Re$	[-]	Reynolds number
$Re_{0.7}$	[-]	Local Reynolds number for $r/R=0.7$
$r^*$	[m]	viscous core diameter
$s$	[m]	propeller span
$S$	[Nm]	Surface tension
$t$	[mm]	Blade thickness
$t/c_{0.7R}$	[-]	Thickness /Chord ratio
$T_H$	[s]	Period of propeller heave motion
$T$	[N]	propeller thrust
$T_t$	[N]	Propeller actual thrust
$T_n$	[N]	Propeller thrust for non ventilating condition
$U_r$	[m/s]	r components of vortex velocity
$We$	[N/m]	Surface tension of the water
$V_i$	[m/s]	Inlet velocity

$V_0$	[m/s]	Propeller advance velocity
$V_\theta$	[m/s]	$\theta$ components of vortex velocity
$V_A, V$	[m/s]	speed of advance
$V_\infty$	[m/s]	local relative velocity
$z_{max}$	[m]	Z coordinate of maximum pressure

### Greek Letters

$\alpha$	[deg]	angle of attack of 70% radius of propeller blade section
$\beta_1$	[-]	thrust loss due to steady weave motion
$\beta_0$	[-]	thrust loss due to loss of propeller disk area
$\beta_T$	[-]	total thrust loss factor
$\beta_{VC}$	[-]	thrust loss due to ventilation
$\beta_w$	[-]	Thrust loss due to Wagner effect
$\sigma_V$	[-]	ventilation number
$\sigma_{cav}$	[-]	Cavitation number
$\Gamma$	[m <sup>2</sup> /s]	circulation strength of the vortex
$\theta/2$	[rad]	submergence angle
$\rho$	[kg/m <sup>3</sup> ]	density of water
$\Delta S_s$	[Pa]	spatial extent of slamming pressure exceeding 50% of maximum pressure
$\nu$	[m <sup>2</sup> /s]	kinematic viscosity
$\eta$	[-]	Propeller efficiency
$\eta_\Gamma$	[-]	tuning constant added to the calculation model
$\eta_I$	[-]	Ideal efficiency
$\lambda$	[-]	Scale ratio

# 1 INTRODUCTION

## 1.1 BACKGROUND AND MOTIVATION

In the last years, ship operations offshore have increased as a consequence of increasing offshore oil & gas activity. The activity is particularly high in open ocean areas like the North Sea, where the typical significant wave height is around  $2m$  and calm water is a very rare event. According to Faltinsen (1990) the significant wave height can be larger than  $2m$  for 60% of the time in areas like the North Sea and wave heights higher than  $30m$  can occur. The mean wave period can be from  $15s$  to  $20s$  in extreme weather situations and it is seldom below  $4s$ . Therefore, the propellers might be required by the DP system to operate at very high loadings in order to keep the vessel in position and heading in heavy seas. Due to motions of the vessel (heaving, rolling and pitching), the position of the propulsion system oscillates vertically, see *Figure 1-1* and the propeller blades might come close to the free surface, leading to propeller ventilation and out-of-water events, causing oscillation of blade forces with large amplitudes, resulting in large torque variations as well as large side-forces and bending moments, see for instance Califano and Steen (2011\_a and 2011\_b) and Savio and Steen (2012).



*Figure 1-1 Ships operating in extreme wave conditions.*

Propulsive power is transmitted from the motor to the propeller through a transmission system, which consist of bearings, gears and shafts. The use of azimuth propulsors as main propulsion device has grown considerably over the last years. According to the statistic of survey records of major classification societies (e.g. ABS, DNV and LRS), the failure of gears and bearings are among the first three major kind of damages, see *Table 1-1*. Typical damages found in mechanical thruster are broken tooth of the bevel gear and burnt bearings of the pinion shaft. TIFF (Tooth Interior Fatigue Failure), see *Figure 1-3* starts as a small crack below the surface of the active flank of a tooth, most often within the transition zone between the case and core material. The failure is characterized by a fracture at approximately mid-height on the tooth of the gear. The crack for a TIFF is initiated in the interior of the tooth. This distinguishes TIFF from other fatigue failures of gears. MackAldener and Olsson (2000) describe the crack producing stress of TIFF as a twofold process: constant residual stress in the interior of the tooth due to case hardening and alternating stress due to idler usage of the gear wheel. Although marine propellers are not much subject to idler usage, alternating stresses can arise from excessive torsional vibrations, causing gear hammering. In severe cases, the upper part of the tooth will be lost. According to the damage statistics made by the major classification societies (e.g. ABS, DNV GL) the failure of gears and bearings are among the first three major types of failures, see *Table 1-1*.

Components	Percentage of damages
Propellers	24%
Gears	12%
Bearings	11%
Ducts	3%
Steering gears	0%

*Table 1-1 Classification statistic of mechanical damage at azimuth thruster, Dang et.al. (2013).*

The shaft torque stiffness of an azimuth thruster is typically 15 times higher than a typical conventional propeller shaft (*Figure 1-2*). Therefore, an impact loading from the propeller is expected to be more severe in a thruster transmission than the same load magnitude in the reduction gearbox of a conventional propeller. While the industry has reported numerous cases of gear failures of azimuthing thrusters, Dang et.al. (2013) and a very few cases of similar failures of reduction gearboxes of conventionally shafted propellers have been reported.

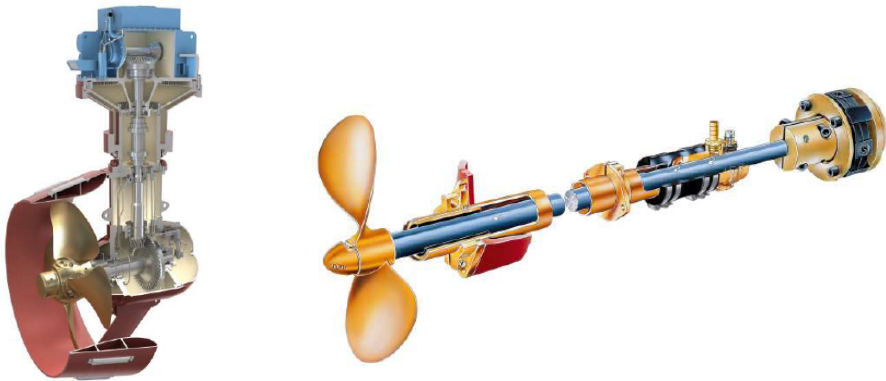


Figure 1-2 Example of azimuthing thruster- Rolls Royce Marine (left) and conventional shaft propeller drive trains (right).

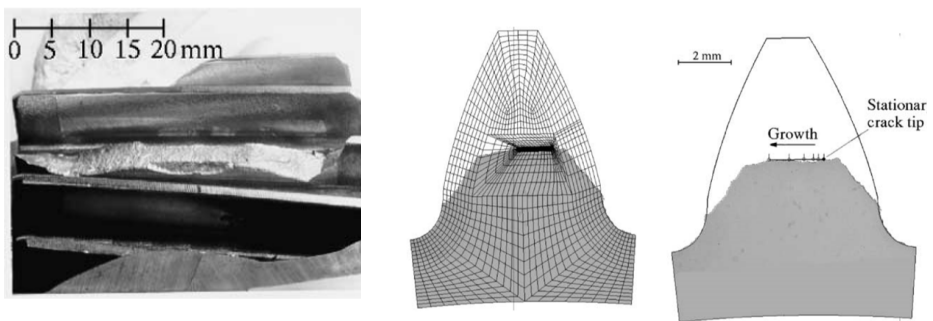


Figure 1-3 Typical fracture surface of a TUFF failure (left), Comparison of an observed fracture surface and FE-mesh with crack (middle), observed fracture surface and analysed crack lengths (right), see MackAldener and Olsson (2002).

One of the hypotheses that lead to the study of propeller ventilation, was that the TUFF damage can be initiated by a single event of very high overload around 2-4 times nominal torque. Nominal torque is the torque giving full power at the design RPM. It was believed that large torques and sudden variations of the load condition can be caused by intermittent ventilation. The other hypothesis for the mechanism of the critical load, which initiates the crack, was that a propeller blade, during a partial out-of-water event would slam into a patch of free surface with a low relative angle between the free surface and the propeller blade surface, leading to what was called propeller slamming Mork (2007).

Traditionally ships and propulsion units have been optimised for operations in calm water. Consideration of hydrodynamic loads in calm water condition might not be enough since



the propeller always operate in heavy seas, subject to intermittent ventilation and strongly oblique flows. Operations in heavy seas have only been accounted for using crude safety factors. The average thrust/torque losses can be estimated using semi – empirical methods but there is a need for more knowledge in order to provide understanding and if possible computational methods to estimate dynamic forces (especially propeller thrust and torque). In addition, a better knowledge of the mechanism leading to ventilation inception can help to develop a control system that shall reduce the mechanical loads and increase the efficiency of propellers operating in extreme sea conditions.

## 1.2 PROPELLER VENTILATION

Ventilation is the phenomenon of air drawing on structures operating below the free surface, such as hydrofoils, rudders and propellers. Propeller ventilation is related to the propeller coming close to the free surface and “sucking” air into the propeller, or when the blades are piercing the free surface and the air is sucked down to the below-water parts of the propeller. In these cases, propeller ventilation leads to a sudden and large loss of propeller thrust and torque, which might lead to propeller racing and possibly damaging dynamic loads, as well as noise and vibration. Ventilation typically occurs when the propeller loading is high and the propeller submergence is limited, and when the relative motions at the propeller are large due to heavy seas. Propeller ventilation inception depends on different parameters i.e. propeller loading, forward speed and the distance from the propeller to the free surface, see for instance Califano (2010), Smogeli (2006), Koushan (2006a), Kozłowska et.al. (2009) and Kozłowska and Steen (2010).

A difficulty when creating a calculation model to study ventilation is covering all the ventilation regimes and submergences. Kozłowska et.al. (2017) showed two different ventilation inception mechanisms presented in *Figure 1-5* and based on the level of submergence of the propeller. Either ventilation can start by forming an air-filled vortex from free surface or the free surface can be sucked down to the propeller, or it becomes surface piercing, so air can enter the suction side of the blade directly from the atmosphere. For partially submerged propellers the one blade cycle can be divided in four phases, see *Figure 1-4*: 1<sup>st</sup> the blade entry phase, 2<sup>nd</sup> the in - water phase, 3<sup>rd</sup> the blade exit phase and 4<sup>th</sup> the in - air phase. The blade entry phase starts when the blade touches the free surface and finishes when the whole blade is submerged. The continuation of the blade entry phase is the in - water phase. The blade water phase is followed by blade exit phase, which starts when the leading edge of the blade touches the free surface and terminates when the whole blade is in the air – the in-air phase.

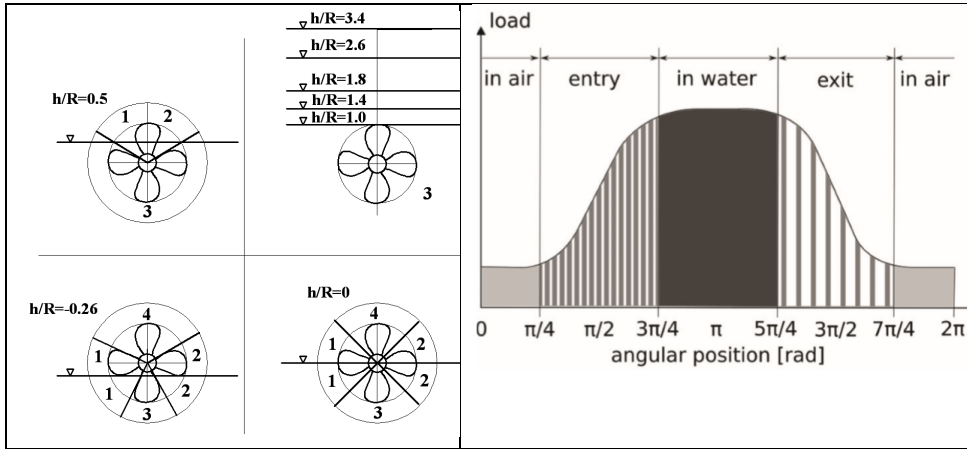


Figure 1-4 Blade cycle phase, 1-the blade entry phase, 2-the blade exit phase, 3-the in water phase, 4-the in air phase (left) see Kozłowska et al. (2009) and corresponding load (right), Olofsson (1996).

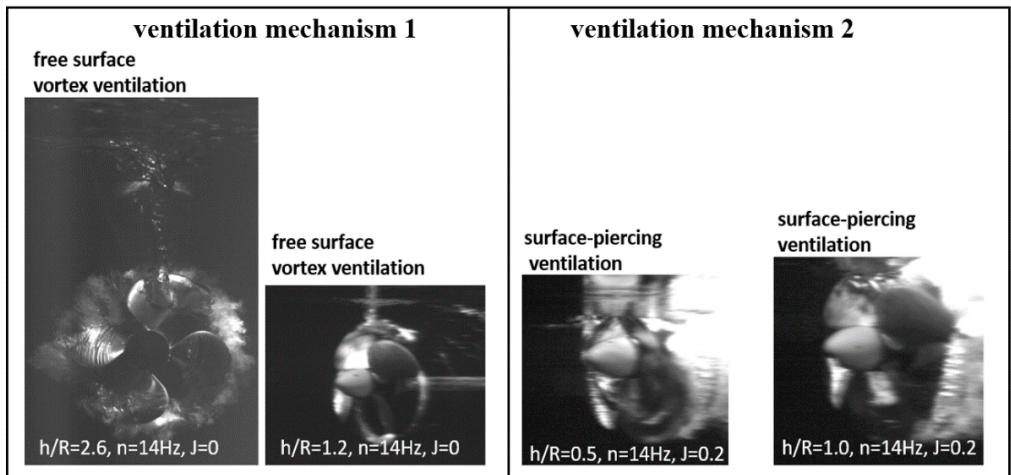


Figure 1-5 Impact of the free surface vortex ventilation (ventilation mechanism 1) and surface-piercing ventilation (ventilation mechanism 2), Kozłowska et al. (2017).

Free surface vortex ventilation is characterized by severe thrust losses occurring when a vortex appear on the blade surface, funneling air from the free surface down to the suction side of the blade. Surface piercing ventilation is characterized by uniform thrust losses during the complete revolution of the propeller. The propeller might be non-ventilated, partially or fully-ventilated depending on several factors, where submergence and advance number are clearly important. The typical thrust losses are not only a function of ventilation. Even bigger thrust loss is caused by the propeller coming partly out of the water, so that the effective propeller disk area is significantly reduced. When the propeller is partly out of the water, thrust loss can be computed from the fraction of the propeller disc area that is above the water. This is typically complemented by adding the loss caused by the so-called Wagner effect, which accounts for the dynamic lift effect of the recently immersed propeller blades. Thrust losses due to out-of-water effect has been studied by Gutsche (1967), Faltinsen et.al. (1981) and Minsaas et.al. (1983).

### 1.3 SLAMMING ON PROPELLER BLADE

When the angle between the water surface and the body is small, large loads may occur. The slamming load depends on the impact velocity and the highest natural period of the local structure, Faltinsen (2000). Mork (2007) was the first to study of slamming on a propeller blade. She performed model experiments of a slamming propeller, using only one blade see

*Figure 1-6.* Both impact velocity, stiffness of mechanical system and impact angle between blade and water were varied during the experiment. The results show that the critical magnitude 250-300% of nominal loads was exceed for impact angles as large as 28 deg at  $r/R=0.7$  for every rotational speed tested. It should be mentioned that the blade pitch angle was unrealistically large. This was done to obtain a sufficiently low relative angle between the blade surface and the flat, undisturbed water surface. The idea was that, on very rare occasions, the blade on the real propeller might hit a portion of the wavy free surface, which had, by chance, an angle leading to a similarly low relative angle between blade and water.

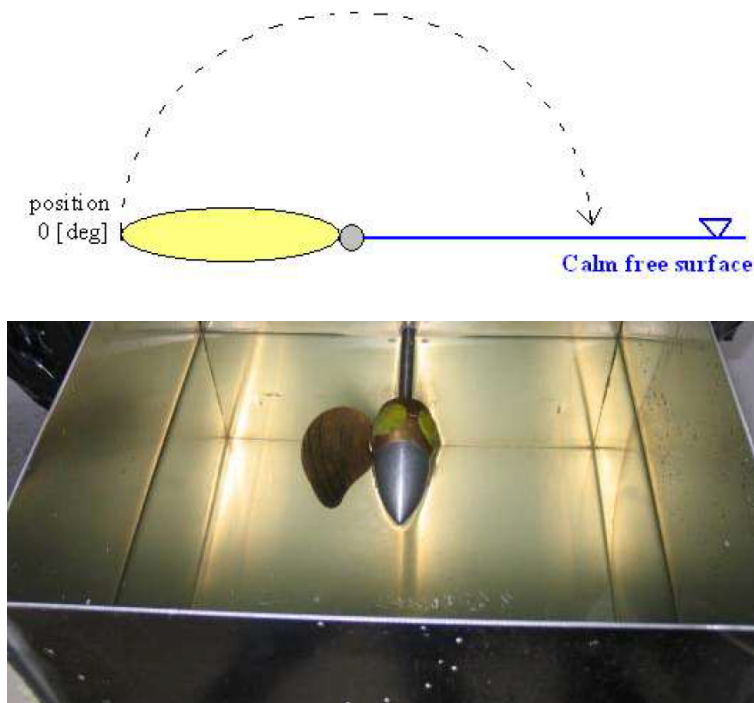


*Figure 1-6 Illustration of the blade start position (top) and photograph of propeller blade in basin (bottom), Mork (2007).*

#### **1.4 OBJECTIVE AND SCOPE**

The main objectives of the thesis are to provide understanding and computational methods to estimate dynamic forces (especially propeller thrust and torque) on propeller operating in heavy seas, subject to intermittent ventilation and out of water effects.

The following sub-objectives of the study have been defined as follows:

- Establish an understanding of the relation between forces and ventilation using high-speed video recording synchronized with experiments.
- Investigate the dynamic and average forces on the propeller subject to intermittent ventilation and to identify critical loads and operational conditions. Both model tests results and full-scale trial results shall be studied.
- Investigate the occurrence of the slamming on the propeller blade, and the forces and moments it might produce.

- Perform a classification of different types of propeller ventilation mechanisms and typical thrust losses and torque variations related to each of them.
- Perform a comparison between model test and CFD calculations. The comparisons aim at formulate a discussion of possible calculation methods.
- Create a simplified calculation model to study ventilation and out-of-water effect, which covers the thrust loss prediction for the range of different propeller submergence  $h/R$ , propeller revolutions  $n$  and propeller advance number  $J$ .
- Give recommendation for how the more harmful types of propeller ventilation might be avoided, either by design requirements or by operational conditions.

## 1.5 PRESENT WORK AND OUTLINE OF THESIS

The outline of the present work is given below, organized by the chapters where the main contributions are summarized and described below:

Chapter 2     *Outline of theory for hydrodynamic loads on propellers in waves and partial submergences*

It contains review of the available literature, which was used to describe the theory behind propeller ventilation and out of water effects and has been used as a starting point for this research. The review study contains also the description of other phenomena such as the inlet vortex in pump sumps, the ground vortex at the inlet of the aircraft engines and the propeller hull vortex cavitation (PHVC) which has analogies to propeller free surface vortex ventilation (PFSVV). The experience gained through many years of research in this area could be applied to the present work of propeller free surface vortex ventilation study.

Chapter 3     *Model Tests*

Seven different experimental campaigns are presented and analysed in this thesis. Model tests were performed with both open pulling and ducted pushing propeller. Propeller immersion ratios, carriage speed, propeller rate of revolutions, azimuth angle, period of heave oscillations and oscillation amplitude were varied during the experiments. The analysis of the results shows the relation between ventilation and thrust losses. The use of a 6-component force dynamometer on one of the four blades gives detailed insight into the forces on the propeller, while the use of high-speed underwater video gives a visual understanding of the ventilation phenomena.

Chapter 4     *Experimental Results*

Analysis of the propeller ventilation can be divided into the following parts:

- mean thrust and torque losses due to ventilation
- thrust loss as function of the blade position,
- the time influence on ventilation inception
- comparison between static and dynamic thrust loss (hysteresis effect)
- comparison between CFD calculations and model experiments
- comparison between PHVC (propeller hull vortex cavitation) and PFSVV (propeller free surface vortex ventilation)
- occurrence and flow field, ventilation regimes and critical advance number
- inception of cavitation, ventilating vortex.

#### Chapter 5 *Calculation model of thrust loss due to out of water effects and ventilation*

A calculation model, which is able to predict the thrust loss due to ventilation, is presented in this chapter. The model can be applied to estimate the thrust loss for a wide range of propeller submergence ratios and at different advance numbers. The calculation model predicts the total thrust loss factor  $\beta_T = K_T/K_{Tn}$ , where  $K_T$  is the actual thrust coefficient and  $K_{Tn}$  is the time-averaged mean value of the thrust coefficient at the relevant advance number  $J$  obtained from the calm water, deeply submerged non-ventilated propeller. The calculation also predicts the ventilated blade area ratio  $A_V/A_0$  since it is required for the calculation of thrust loss in partial ventilation.

#### Chapter 6 *Simulation model for thrust loss due to ventilation and out of water effect*

This chapter presents the time-domain simulation model PropSim (2018) for propeller forces due to vortex ventilation. The propeller simulation model is a further development of Dalheim's model, see Steen et al. (2016), which was updated by including a physical model for estimating ventilated blade area based on propeller loading. The ventilated blade area ratio is computed using the steady-state vortex ventilation model based on the vortex model by Rott (1958) and the propeller momentum theory as it was described in section *Section 2.4.2* and *Chapter 2*. The simulation model PropSim (2018) is static in the sense that it is assuming that the response is quasi steady and based on the calculation model presented in *Chapter 2*.

It is also discussed in this chapter how the dynamic effects i.e. hysteresis effect and blade frequency dynamics can be included in the existing model PropSim (2018).

## Chapter 7 *The propeller blade slamming hypothesis*

This chapter discusses the propeller blade slamming hypothesis, and present the description of the set up and the results for four bladed propeller (P1374) obtained by *Koz08*, together with a review of the results of the experiments made by Mork (2007) of a one bladed propeller (P1362).

## Chapter 8 *Discussion, conclusions and recommendation for further work*

This section discuss the expected generality of the presented results, when different conditions and propellers are considered. The amount of the approximation used in the calculation and simulation model are commented and justified. Then, conclusions are summarized and recommendations for further research given.

## 1.6 LIST OF PUBLICATIONS

The thesis is organized as a monograph. It is based on five published papers (three conference and two journal papers), which are explained below.

**I. Anna Kozłowska, Sverre Steen, Kourosh Koushan (2009) Classification of Different Type of Propeller Ventilation and Ventilation Inception Mechanisms, In: Proceedings of the First International Symposium on Marine Propulsors Trondheim, Norway.**

This paper is largely based on analysis of a series of experiments *Kou2006\_I* (see chapter 3 for an overview of the test campaigns and an explanation of the naming of the test campaigns) and *Kou2006\_II* where both open and ducted propellers are tested in conditions with intermittent ventilation. Analysis of propeller ventilation can be divided in two parts: aiming at classification of different types of propeller ventilation and typical thrust losses and torque variations related to each of them, and the discussion of the ventilation inception mechanism based on the requirements for propeller to ventilate: i.e. propeller loading, forward speed and submergence.

**II. Anna Kozłowska, Sverre Steen (2010) Ducted and Open Propeller Subjected to Intermittent Ventilation, In: Proceedings of Eighteen International Conference on Hydrodynamics in Ship Design, Safety and Operation, Gdansk, Poland.**

The analyses in this paper are based on experiments *Kou2006\_I* and *Kou2006\_II*. Analysis of the propeller ventilation can be divided in two parts: comparison between ventilation in static and dynamic conditions (heave motion) both for open and ducted propeller and the discussion how to estimate thrust loss. As a conclusion, a new formulation of the relations between ventilation and thrust losses was developed.

**III. Anna Kozłowska, Katja Wockner, Thomas Rung, Sverre Steen (2011) Numerical and Experimental Study of Propeller Ventilation, In: Proceedings of Second International Symposium on Marine Propulsors, Hamburg, Germany.**

The paper shows a comparison between model test *Koz10* and CFD calculations. The comparison contains two main parts: comparison between blade forces and moments during non-ventilating and ventilating phase as well as comparison between flow visualization using high-speed video (experiments) and CFD simulations. The comparison aims at identifying the degree of correlation and discuss reason for deviations. As a conclusion in order to have better comparison between CFD and experiments, the simulation time and the time duration of experiments should be more similar. The excessive amount of CPU time required makes it very difficult to perform computations for the same total number of revolutions as in the experiment. For the lowest advance numbers ( $J=0$ ,  $J=0.15$ ,  $J=0.3$ ) there is a marked difference between the experiments and calculations with respect how blade thrust varies with blade position. This difference might be explained by the fact that in the calculation the blade soon loses contact with the air-supplying vortex, while in the experiment the blade is continuously supplied with air from the surface.

**IV. Anna Kozłowska, Luca Savio, Sverre Steen (2017), Predicting Thrust loss of ship propellers due to ventilation and out of water effect. Journal of Ship research. Vol. 61 (4).**

This paper presents a vortex ventilation model, as well as results of a new set of propeller open water tests in limited submergence. The main purpose of the experiments was to obtain more data of thrust loss due to ventilation and out-of-water effect at higher advance numbers than the previous test campaigns, for validation purposes and to make a prediction model for thrust and torque loss due to free surface proximity. Tests were performed at different draughts. For each draught the propeller were tested at different advance numbers for the range from  $J = 0$  until  $J = 1.0$ . The different advance numbers were obtained at range of propeller speeds ( $n =$



9, 12, 16 and 16 Hz) so that for the same advance number different propeller thrusts were tested, so that the effects of thrust loading and advance number could be separated. The focus in this paper is to validate the prediction model for ventilation starting by vortex formation. By using a prediction model based on Rott vortex theory, it is possible to estimate the blade area ratio, which is ventilated due to the vortex formation. The thrust loss is calculated by means of the expression for the reduced thrust due to ventilation as described by Kozłowska and Steen (2010).

**V. Anna Kozłowska, Sverre Steen (2017), Experimental analysis on the risk of vortex ventilation and the free surface ventilation of marine propellers. Applied Ocean Research. Vol 67.**

The paper presents a discussion of the ventilation inception and air drawing prediction of ship propellers, aiming to predict under what conditions ventilation will happen, and the actual physical mechanism of the ventilation.

Ventilation by vortex formation has analogies with other phenomena, such as the inlet vortex in pump sumps, ground vortex at the inlet of the aircraft engines and the Propeller Hull Vortex Cavitation (PHVC). The paper includes comparison between Propeller Hull Vortex Cavitation (PHVC) and Propeller Free Surface Vortex Ventilation (PFSVV) as well as comparison between PFSVV and vortex formations of aero engines during high power operation near a solid surface. Experimental data based on several different model tests shows the boundary between the vortex forming, non-vortex forming and free surface ventilation flow regimes. For comparison the following parameters, which determined the intensity of the hydrodynamic interaction between the propeller and free surface have been used: propeller load coefficient  $c_T$ , tip clearance ratio  $c/D$ , propeller submergence ratio  $h/R$ , ambient velocity  $V_i$  and flow cavitation/ventilation number  $\sigma_{cav}/\sigma_{vent}$ .

## **2 OUTLINE OF THEORY FOR HYDRODYNAMIC LOADS ON PROPELLERS IN WAVES AND PARTIAL SUBMERCENCES.**

This chapter outlines important theory applied in this thesis.

Loss of thrust and torque of propellers operating close to the free water surface is caused by ventilation, meaning that the suction side of the propeller blades is (partly) covered by air, and/or by part of the propeller coming completely out of the water. Both of these effects are covered in the section on propeller ventilation below, even if they are different phenomena. Ventilation of a completely submerged propeller can happen by means of a vortex acting as a funnel for air from the free surface. Therefore, a section on vortex theory is included in this chapter.

Large, short-duration overloads are believed to be a reason for the in-service issues with marine thruster that is an important part of the background and motivation for this work. As mentioned in the introduction to the thesis, propeller blades slamming into the free surface might be a reason for large overloads. Therefore, a section on slamming is included.

A section reviewing numerical methods for propeller force prediction is also included.

### **2.1 THEORY FOR PROPELLER VENTILATION**

#### **2.1.1 Ventilation historical background**

Ventilation leads to a sudden large loss of propeller thrust and torque, which might lead to propeller racing and possibly damaging dynamic loads, as well as noise and vibrations. The effect of ventilation on average thrust and torque of propellers operating in waves was discussed by several researchers since 1934 see e.g. Kempf (1934), Shiba (1953), Faltinsen et.al. (1981), Minsaas et.al. (1975, 1983, 1987), Huse (1971), Olofsson (1996), Koushan (2006a, b and c), Kozłowska et.al. (2009, 2011, 2017) and Kozłowska and Steen (2010, 2017).

Kempf (1934) was one of the first researchers who studied the ventilation effect on propellers. He studied the torque and thrust losses due to ventilation using different propellers (three and four bladed) as well as different immersion ratios and propeller rate of revolutions. The ventilation effect on thrust and torque was also study by Shiba (1953),

who discussed the influence of different propeller design parameters e.g. expanded area ratio, contour of blade, radial variation of pitch, skewback, effect of rudder, turbulence of original flow as well as scale effects on ventilation.

Ventilation effects with respect to vessel operation in addition to added resistance in waves and reduction of propulsive efficiency can be found in Faltinsen et.al. (1981, 1983) and Minsaas et.al. (1975, 1981, and 1983). Minsaas et.al. (1983) discussed a method for estimation of thrust loss due to reduced propeller shaft immersion in open water. They developed an empirical expression for the combined effect of loss of disk area, wave making and Wagner effect; see equations (2-25) and (2-26). They also concluded that corrections due to wave effect are of particular importance when  $1 < \frac{h}{R} < 1.3$ , but when  $\frac{h}{R} < 1$ , the thrust must be corrected due to ventilation and the emergence of propeller. Minsaas et.al. (1983) presented a quasi-steady approximation of the effect on waves on propeller characteristics when ventilation does not occur. The thrust loss is then a consequence of loss of propeller disk area, steady wave generation and unsteady lift.

Olofsson (1996) studied the force and flow characteristics of surface piercing propellers – propellers designed to operate with the propeller disk only half submerged. Olofsson (1996) included dynamic effects, side forces, and bending moments in his study, which was primarily based on model experiments. Koushan (2006) performed extensive model tests on an azimuth thruster with 6 DoF measurements of forces on one of the four blades, as reported in three papers Koushan (2006a, b and c). Koushan (2006a) described the dynamics of ventilated propeller blade axial force on a pulling thruster at bollard condition running at several constant immersion ratios and constant propeller rate of revolution. Koushan (2006b) presented the dynamics of ventilated propeller blade axial force on pulling thruster at bollard condition and constant propeller rate of revolution moving with force sinusoidal heave motion. Koushan (2006c) presented the dynamics of ventilated propeller blade and duct loadings on a pushing ducted thruster running at bollard condition and constant propeller rate of revolution. He presented average duct and total thrust as well as average propeller torque under various submergence conditions.

Kozłowska (2009) focused on ventilation inception mechanisms, classification of types of ventilation, thrust loss related to each type of ventilation, and a simple calculation method for predicting thrust loss.

Kozłowska and Steen (2010) focused on comparison between ventilation in static and dynamic conditions (heave motion) both for open and ducted propeller, and discussed how to estimate thrust loss. As a conclusion, a new formulation of the relations between ventilation and thrust loss was developed.

Kozłowska et.al. (2011) presented comparison between model tests and numerical calculations of thrust loss due to ventilation. The comparison contains two main aspects: comparison between blade forces and moments during non-ventilating and ventilating phase and comparison of results of flow visualization using high speed video (experiments) with CFD simulation results. The comparisons aim at identifying the degree of correlation and discuss reasons for deviations.

Califano (2010) investigated the dynamic an average forces on propeller subject to intermittent ventilation and established a CFD model capable of predicting the extent of ventilation and the dynamic forces due to ventilation.

The occurrence of ventilation during DP operations has been studied by several researchers in order to develop new control systems, which can detect ventilation inception and control the motor to reduce the associated thrust losses, see for instance Smogeli (2006) and Ruth (2008).

### **2.1.2 Dimensionless parameters related to propeller ventilation**

In order to extrapolate the results from model test to full scale, the following conditions have to be satisfied:

- Boundary conditions must be geometrically similar
- Working conditions must be similar

The non-dimensional parameters, which are of importance of the propeller flow are as follows: advance number, Froude's number, Reynold's number, Weber's number and cavitation/ventilation number. The influence of these parameters for the propeller flow is described and discussed below. For a propeller working near the free surface, it is necessary for full-scale propeller and its model to be not only geometrically similar but also their position in the relation to the free surface must be similar. It is represented by the submergence ratio

$$I = \frac{h}{R} \tag{2-1}$$

Where  $h$  is propeller shaft submergence and  $R$  is propeller radius

The similarity in working condition will be satisfied if the moving path of blades is similar, and the submergence ratio is the same. The same advance number will ensure similar moving path of the blade.

- **Advance number**

$$J = \frac{V_F}{n_F D_F} = \frac{V_M}{n_M D_M} \quad (2-2)$$

When the propeller is working close to the free surface, so that surface waves might be created and influence the propeller performance, equality of Froude number should be ensured, as for ship hull model testing. When the equality in  $J$  value is satisfied the ratio between the velocity of advance ( $V$ ) and tangential velocity ( $nD$ ) is fixed and the results should be the same whether we take ( $nD$ ) or ( $V$ ) for the velocity in the definition of the Froude number. The velocity of advance ( $V$ ) is much smaller than the blade tangential velocity ( $nD$ ), especially at high propeller loadings. Therefore, the non-dimensional parameters, presented in this section, were defined using a velocity proportional to tangential velocity ( $nD$ )

- **Froude number based on diameter and submergence**

$$F_{nD} = \frac{nD}{\sqrt{gD}}, F_{nh} = \frac{nD}{\sqrt{gh}} \quad (2-3)$$

Shiba (1953) has linked the occurrence of ventilation with the pressure in the wake flow behind the submerged body. He has shown experimentally that the influence of the characteristics of the wake region for fully ventilated propeller disappears when  $F_{nD}$  value reaches approximately 3. According to Shiba (1953) typical full-scale propellers operate normally within a  $F_{nD}$  regime from 1.0 to 1.4. Therefore, in order to correctly model the flow, the Froude number  $F_{nD}$  must be identical in model and full scale. Similarity of depth Froude number ( $F_{nh}$ ) is automatically achieved if similarity of Froude number ( $F_{nD}$ ) and submergence ratio similarity is satisfied. Similarity of  $F_{nD}$  is automatically achieved when the advance number is the same and the forward speed (speed of advance) is “Froude scaled”, meaning  $V_F = V_M \cdot \sqrt{\lambda}$ .

The Reynolds number can be defined using propeller diameter and propeller speed instead of velocity, as discussed for the Froude number above.

**Reynolds number**

$$Re = \frac{nD^2}{\nu} \quad (2-4)$$

For presented experiments a local Reynolds number  $R_{e0.7}$  have been used

$$R_{e0.7} = \frac{\sqrt{V^2 + (0.7\pi nD)^2} \cdot c_{0.7}}{\nu} \quad (2-5)$$

Where  $c_{0.7}$  is the chord length at 0.7 radius.

In model scale, the flow can be laminar and turbulent, where it is always turbulent in full scale. The ITTC 1978 extrapolation method (to scale the measurement open water data to full scale propeller performance) recommends testing the propeller model at Reynolds number “not lower than  $2 \cdot 10^5$  at the open water test”. Minsas (1983) suggest  $R_e = 3 \cdot 10^5$  as a lower limit for the Reynold’s number, otherwise laminar and transition effects can become important. He also found that the minimum Reynolds number is valid both for deeply and partially submerged propellers. Helma (2015) published a paper about an extrapolation method suitable for scaling propellers of any design. She showed that the ITTC 1978 recommendation for a minimum Reynolds number of  $2 \cdot 10^5$  might be too low and it should be considered to be raised up to  $4.6 \cdot 10^5$ , see *Figure 2-1*.

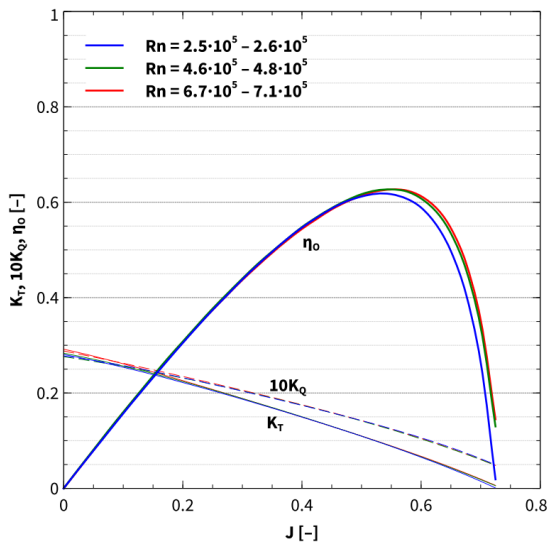


*Figure 2-1 Open-water characteristic of the conventional propeller, scaled according to the ITTC 1978 method, Helma (2015)*

For the tests presented in the thesis two different four-bladed propeller model denoted P1374 and P1440 were used. The geometries of the propellers are described in *Appendix A*. According to the calculation the Reynolds number based on the chord length at  $r/R=0.7$

for the model propeller (P1374,  $n=10\text{Hz}$ ) refers to  $R_{e0.7} = 4.7 \cdot 10^5$  and for the model propeller (P1440,  $n=18\text{Hz}$ ) refers to  $R_{e0.7} = 5 \cdot 10^5$ , which is above the minimum value  $R_{e0.7} = 4.6 \cdot 10^5$  recommended by Helma (2015) and also above the recommendations of Minsaas (1983) and ITTC 1978.

- **Weber number**

$$We = nD \sqrt{\frac{\rho D}{S}} \quad (2-6)$$

The Weber's number  $We$  describes the relationship between surface tension forces and inertial forces. Shiba (1953) concluded that the Weber number is important when determining the critical advance number. Critical advance number is the advance number at which ventilation occurs for a given submergence and shaft speed. In other words, surface tension has the effect to prevent the air from being sucked down, Califano (2010). It was shown experimentally by Shiba (1953) that surface tension would no longer influence the critical advance number when it is above 180. Full scale propellers usually operate far above a Weber's number of 180 but for model scale tests Weber's number could be lower than 180, and the requirement that  $We > 180$  will in many cases be decisive for the size of the model propeller.

In our cases only for propeller shaft speeds (propeller P1374) over  $n=13\text{Hz}$ ,  $We > 180$  so the influence of Weber's number can be neglected. Propeller model P1440 was tested for one constant propeller revolution equal to  $n=18\text{Hz}$ , so it operates for Weber number higher than the minimum of 180.

- **Cavitation and ventilation number**

$$\sigma_{cav} = \frac{p_{at} + \rho gh - p_{cav}}{\frac{1}{2} \rho V_{\infty}^2} \quad (2-7)$$

$$\sigma_{vent} = \frac{p_{at} + \rho gh - p_{at}}{\frac{1}{2} \rho V_{\infty}^2} = \frac{2gh}{V_{\infty}^2} \quad (2-8)$$

When the propeller is fully ventilated, the pressure on the suction side of the propeller is almost atmospheric. Cavitation and ventilation number similarity is actually obtained through kinematic similarity, submergence ratio similarity and Froude number similarity.

Since  $p_{cav} = p_{at}$  in case of ventilation, where  $p_{at}$  is the atmospheric pressure, the cavitation number, see equation (2-7) can be converted to the ventilation number, see equation (2-8).

For the partially ventilated regime, although the pressure in the ventilated cavity is nearly atmospheric, there may exist other non-ventilated air cavities (bubbles), Kruppa (1972). The non-ventilated cavities require cavitation number similarity in order to be properly represented in model scale. In order to fulfill this, model test should be performed in a cavitation tunnel with free surface. When tests are performed at scaled atmospheric pressure, the air in the closed cavities (bubbles) will have the right flexibility – the compressibility of the air will be scaled. If model tests are performed at full atmospheric pressure, the air will be practically incompressible, see for instance Califano (2010)

### 2.1.3 Dimensionless parameters to present propeller performance characteristic

Propeller performance characteristic are very often present in non-dimensional form of thrust  $K_T$ , torque  $K_Q$  and efficiency  $\eta$

$$K_T = \frac{T}{\rho \cdot n^2 \cdot D^4} \quad (2-9)$$

$$K_Q = \frac{Q}{\rho \cdot n^2 \cdot D^5} \quad (2-10)$$

$$\eta = \frac{J}{2\pi} \cdot \frac{K_T}{K_Q} \quad (2-11)$$

We can also express the non-dimensional thrust and torque in an alternative way, similar to a normal force coefficient formulation, where the rotational speed is excluded and the forward speed and propeller disk area are used instead

$$c_T = \frac{T}{0.5 \cdot \rho \cdot V^2 \cdot \pi R^2} = \frac{8 \cdot T}{\rho \cdot V^2 \cdot \pi D^2} \quad (2-12)$$

$$c_Q = \frac{Q}{0.5 \cdot \rho \cdot V^2 \cdot \pi R^3} = \frac{16 \cdot Q}{\rho \cdot V^2 \cdot \pi D^3} \quad (2-13)$$

Loss of thrust and torque due to ventilation and/or out-of-water are often present using the non-dimensional coefficients  $\beta_T$  and  $\beta_Q$ .



$$\beta_T = \frac{T_t}{T_n} \quad (2-14)$$

$$\beta_Q = \frac{Q_t}{Q_n} \quad (2-15)$$

Where:  $T_t$  is the actual, reduced thrust and  $T_n$  is the thrust obtained at the same rotational and forward speed in deeply submerged condition. Similarly,  $Q_t$  is the actual, reduced torque and  $Q_n$  is the torque obtained at the same rotational and forward speed in deeply submerged condition

$\beta_T, \beta_Q = 1$  means no thrust or torque losses and  $\beta_T, \beta_Q = 0$  means complete loss of thrust or torque losses due to ventilation and out of water effects.

### 2.1.4 Ventilation regimes and critical advance number

The propeller might be non-ventilated, partially or fully ventilated, depending on several factors, where submergence and advance number are clearly important. Olofsson (1996) divided these ventilation states into regimes, as illustrated in *Figure 2-2*. The partially ventilating regime is characterized by having varying part of the propeller blade covered by air. In this regime, the propeller thrust fluctuates rapidly. The regime is quite stable in time and lead to considerably reduced thrust. The propeller might also experience transition between fully and partially ventilated flow regimes. The range of advance numbers where this happens is called the unstable regime or transition regime. The sketch in *Figure 2-2* originally published in Olofsson (1996) is based on experiments with surface-piercing propellers (meaning propellers designed to operate submerged to the propeller center), but we observe similar regimes for normal propellers operating very close to the free water surface.

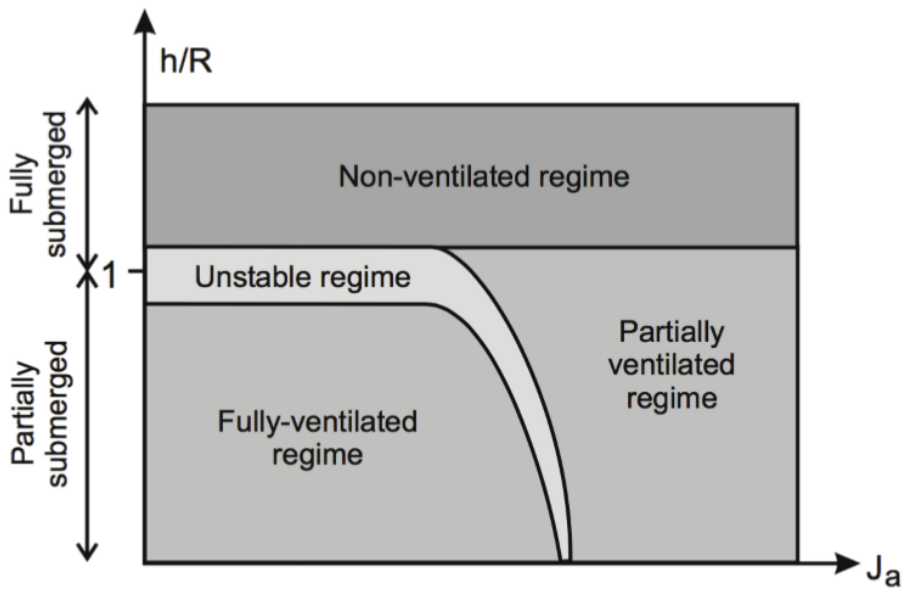


Figure 2-2 Ventilation flow regimes Olofsson (1996), surface piercing propellers.

### 2.1.5 Ventilation inception mechanisms

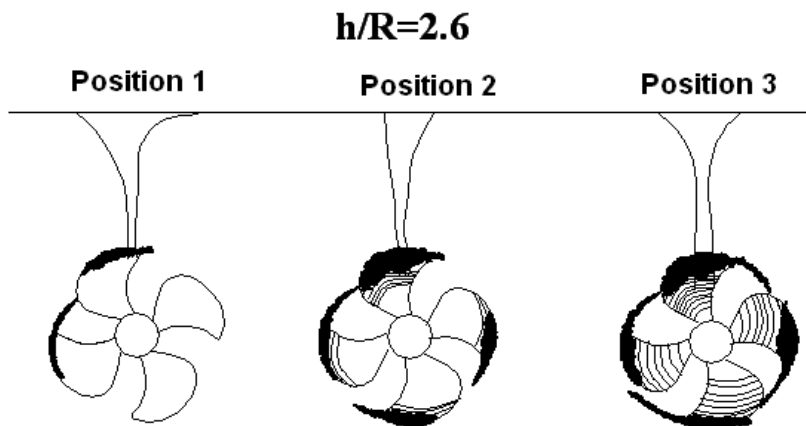


Figure 2-3 Different ventilation regimes, 1 – Ventilation inception, 2- Partially ventilated regime, 3 - Fully ventilated regime.

Ventilation inception mechanisms can be divided into different types:

- By vortex formation, when ventilation starts by forming an air filled vortex from the free surface
- The free surface is sucked down to the propeller or it becomes surface piercing, so air can enter the suction side of the blades directly from the atmosphere.
- Transition region, when both phenomena can lead to propeller ventilation but it is difficult to distinguish which has the dominant effect to ventilation inception. It either can start ventilating by forming an air-filled vortex from free surface or sucked down the free surface to propeller. Once the propeller has started ventilating, the sucking down free surface phenomena becomes dominating.

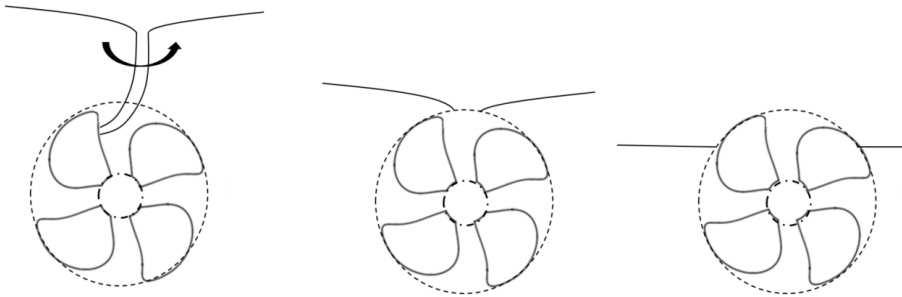


Figure 2-4 Impact of the free surface vortex ventilation (left side), free surface is sucked down to the propeller (middle) & surface-piercing ventilation (right side).

### 2.1.6 Ventilation losses

An expression of the reduced thrust only due to ventilation can be found in Minsaas et.al. (1983) assuming that suction side of the propeller blade is fully ventilated and the pressure on the pressure side of the propeller blade section is equal to static pressure.

$$\beta_{VC} = \frac{1.5 \cdot EAR}{K_{Tn}} [c_{L(\sigma_V=0)} + \sigma_V]_{(r/R=0.7)} \quad (2-16)$$

The above formula is derived using an approximate relation between propeller blade lift coefficient at 70% radius, thrust coefficient for non-ventilated deeply submerged propeller

$K_{Tn}$  and blade area ratio  $A_E/A_0$ , which according to Gutsche (1962) is valid for conventional propellers.

$$c_{L0.7} = \frac{K_{Tn}}{1.5EAR} \quad (2-17)$$

The equation (2-17) has been derived as a results of many analytical calculations of 2, 3, 4 and 5 bladed propellers covering a large range of blade area ratios  $0.2 < EAR < 1.1$ . The calculation results were in good agreement with test results. On the basis of the calculation results it was possible to derive a good approximation of the relation between the thrust coefficient of the propeller  $K_T$  and the lift coefficient of the characteristic blade section  $c_{L(0.7)}$  at  $r = 0.7R$ , Gutsche (1962). Still, it should be kept in mind that this is a rather rough approximation of the lift coefficient of the characteristic section of the propeller.

Equation (2-16) shows a direct connection between the reduced thrust and the lift coefficient. The lift coefficient is given by the contribution of the pressure side ( $p = p_{static}$ ) and ( $\sigma_V = 0$ ) and the suction side ( $p = p_{at}$ ) and ( $c_L = \sigma_V$ )

Tulin and Burkart (1956) have established an expression for the lift coefficient ( $c_L$ ) of a supercavitating hydrofoil.

$$c_{L(\sigma_V=0)} = \frac{\pi}{2} \cdot \alpha \quad (2-18)$$

In analogy with a cavitating case, Kozłowska et. al. (2009) have used equation (2-18) to calculate the lift coefficient obtained on the pressure side of the ventilated foil.

Thrust loss for ventilating fully submerged propellers might be calculated using the idea presented by Kozłowska and Steen (2010), where the change in propeller blade lift coefficient due to ventilation is used to calculate the change of  $K_T$ . The resulting formula for the thrust loss due to ventilation can be presented as follows

$$\beta_{VC} = \left( \frac{1.5EAR}{K_{Tn}} \cdot c_{LV} \cdot \frac{A_V}{A_0} \right) + \left( 1 - \frac{A_V}{A_0} \right) \quad (2-19)$$

where:  $A_V$  is ventilated propeller disc area,  $A_V=A_0$  means that the propeller is fully ventilated

$EAR$  is propeller blade area ratio,  $c_{LV}$  is the lift coefficient of the ventilated propeller, which can be calculated as:

$$c_{LV} = c_L(\sigma_V = 0) + \frac{2gh}{V_\infty^2} = \frac{\pi}{2}\alpha + \frac{2gh}{V_\infty^2} \quad (2-20)$$

Where:  $g$  is acceleration of gravity,  $V_\infty$  is the relative velocity at the 70% radius propeller blade section,  $h$  is shaft submergence and  $\alpha$  is the angle of attack of the 70% radius propeller blade section.

The main problem with using equation (2-19) is to estimate the blade area that is covered by air  $A_V/A_0$ . For bollard condition, a polynomial relation between the ventilated blade area ratio and submergence ratio was developed by Dalheim (2015) and presented by Steen et.al. (2016).

$$\frac{A_V}{A_0} = \begin{cases} -1.2276 \cdot \left(\frac{h}{R}\right)^2 + 2.2201 \cdot \left(\frac{h}{R}\right) - 0.1969 & \text{if } \frac{dh}{dt} < 0, \frac{h}{R} \in [1,1.7] \\ -0.1593 \cdot \left(\frac{h}{R}\right)^3 + 1.3420 \cdot \left(\frac{h}{R}\right)^2 - 3.7357 \cdot \left(\frac{h}{R}\right) + 3.4483 & \text{if } \frac{dh}{dt} > 0, \frac{h}{R} \in [1,3.4] \end{cases} \quad (2-21)$$

### 2.1.7 Thrust loss due to ventilation and out of water effect

Free surface ventilation occurs for propeller submergences  $-1 < h/R < 1.2$ . The dominating thrust losses are, at least in most cases with significant forward speed, not due to ventilation but due to loss of submerged propeller disk area. We can separate the thrust losses as follows: thrust loss due to loss of propeller disc area, thrust loss due to wave making, thrust loss due to ventilation and due to Wagner effect. For propeller submergence less than  $h/R < 1$  the thrust has to be corrected for loss of propeller disc area.

The total thrust losses can be divided in loss of propeller disc area ( $\beta_0$ ), Wagner effect ( $\beta_W$ ), steady wave motion ( $\beta_1$ ) and ventilation ( $\beta_{VC}$ ) as follows:

$$\beta_T = \beta_{VC} \cdot \beta_W \cdot \beta_0 \cdot \beta_1 \quad (2-22)$$

Loss of propeller disc area: for  $h/R < 1$  can be estimated using purely geometrical considerations as in Gutsche (1962) as follows:

$$\beta_0 = 1 - \frac{\arccos\left(\frac{h}{R}\right)}{\pi} + \frac{h}{\pi R} \sqrt{1 - \left(\frac{h}{R}\right)^2} \quad (2-23)$$

Dalheim (2015), reproduced in Steen et.al. (2016), gave a more elaborate formula, where the influence of the hub is included, but the difference is not very significant, and use of the above, much simpler formula is acceptable in most cases. The Wagner effect (Wagner, 1932) accounts for dynamic lift effect. If the lift of a foil is changed suddenly by sudden change in geometric angle of attack, then first the corresponding change in lift is only half of the final steady value due to induced angle of attack from the shed vortex formed by the time rate of change of circulation. This effect diminishes gradually, and a curve-fit formula is used in equation (2-24) below. It shows that the foil must travel about 20 chord lengths to recover almost full lift. The idea is that a similar effect occurs when a propeller blade is suddenly passing through the surface and into the water. The thrust loss factor  $\beta_W$  is calculated from the average value during the submerged part of the blade rotation. Thus, it will in general depend on the propeller radius as well as propeller submergence. For the simplified formula, the propeller model the characteristic section  $r/R=0.7$  is used. Therefore, the thrust loss factor due to dynamic lift effect, which is relevant only for  $h/R < 1$  is calculated as:

$$\beta_W = 0.5 + 0.5 \sqrt{1 - \left(\frac{155 - V_\infty \cdot t/c}{155}\right)^{27.59}} \quad (2-24)$$

Where  $V_\infty$  is the local relative velocity at the blade section, which, when ignoring induced velocities can be calculated as  $V_\infty = \sqrt{V_A^2 + (0.7\pi nD)^2}$ ,  $t$  is propeller blade thickness and  $c$  is the chord length.

Minsaas et al. (1983) proposed an empirical expression for the combined effect of loss of disk area, wave making and Wagner effect:

$$\beta = \beta_0 \cdot \beta_1 \cdot \beta_W \quad (2-25)$$

$$\beta = \begin{cases} 1 - 0.675 \left(1 - 0.769 \cdot \frac{h}{R}\right)^{1.258} & \text{for } h/R < 1.3 \\ 1 & \text{for } h/R \geq 1.3 \end{cases} \quad (2-26)$$

### 2.1.8 Hysteresis effect

A significant dynamic effect of the propeller ventilation is connected with thrust and torque hysteresis effect, appearing mostly in connection with intermittent ventilation. The hysteresis effect is caused by the fact that it takes a while for ventilation of a submerged propeller to be established, so in a situation with decreasing submergence or increasing propeller loading, there is less thrust loss than for the same condition in static operation, while when ventilation disappears, it takes time for thrust to build up, due to the Wagner effect, so then thrust loss is larger than the corresponding static operation.

According to Koushan (2004), a typical propeller with pitch ratio  $P/D=1.0$  must travel about 4 revolutions at full submergence to recover its full thrust. The Wagner effect is believed to be an important reason for this. It gives the previously observed hysteresis in thrust and torque production, see for instance Minsaas et.al. (1987); a sketch of the hysteresis of the measured thrust and torque denoted  $T_a$  and  $Q_a$  as a function of changing the relative submergence  $h/R$  during the ventilation event showing the hysteresis effect, see *Figure 2-5* from experimental results described by Smogeli (2006).

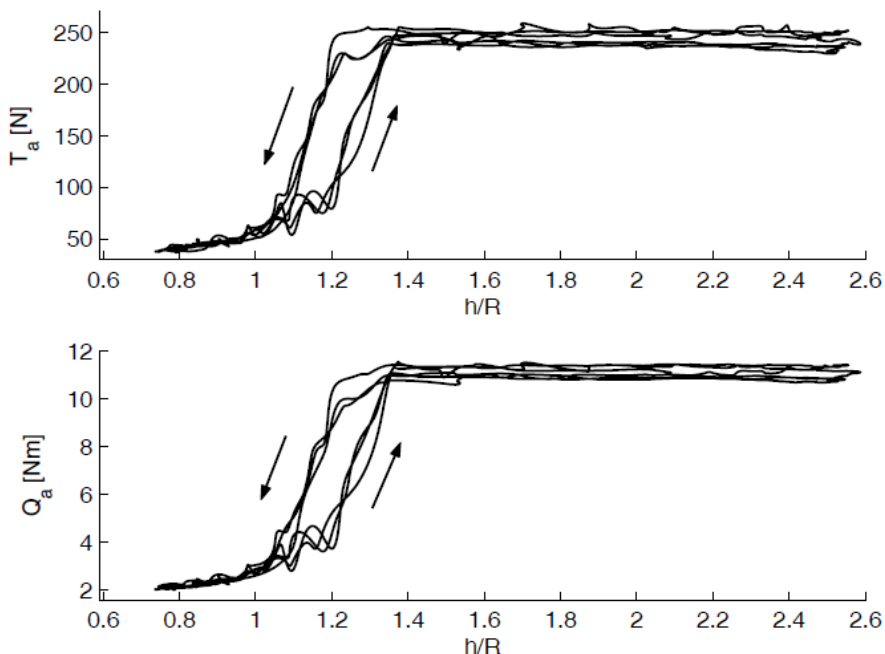


*Figure 2-5 Hysteresis effect as a function of the propeller submergence, Smogeli (2006).*

### 2.1.9 Dynamic loads

During ventilation, the loads on each propeller blade fluctuate in time as the blade goes through the four phases: in air, blade entry, in water and blade exit phase, as described in *Section 1.2*. These fluctuating forces introduce fluctuating structural loads on the propeller blades. It was observed by Huse (1971) that the force oscillations is also connected with the event of ventilation through the free surface vortex. Olofsson (1996) concludes that the high frequency dynamic loads occurring during ventilation are clearly important and can cause mechanical damage through wear and tear (especially in the transition region from partially to fully ventilated regime). It means that fatigue and resonant vibration issues must be considered during the design process. Resonant load variations can occur due to the cyclic loading and unloading of the blade due to a cyclic blade entry and exit phase from the free surface; if the blade pass frequency happens to be equal to an important structural natural frequency, or multiple of this. During resonance, the vibrations are amplified, and the resulting dynamic structural loads could be a combination of hydrodynamic and inertial loads. These loads can cause serious problems for the mechanical system including the propeller. Large stress may develop, and result in high peak stresses, which might even exceed the yield strength of the material, or cause fatigue fracture, Califano (2010).

Dynamic loads due to ventilation can be divide into three main categories:

1. Low frequency fluctuations, which are caused by waves or vertical motions of the vessel (These fluctuations occur when vessel operate in heavy seas),
2. High frequency fluctuations in the range of blade frequency. These fluctuations are caused by inhomogeneous inflow and are not usually very high compare to low frequency fluctuations,
3. Combinations of low and high frequency fluctuations. These fluctuations are caused when the propeller is ventilating especially in the unstable ventilation regime or become surface piercing. These combinations of low and high frequency fluctuations are believed to cause failure of power and transmission parts (gears) of many thrusters. For instance when ventilation occurs the propeller torque will decrease significantly. If the motor control system will increase the RPM to keep power constant, then it increases the potential dynamic overloads for the operating propeller, Hutchinson and Steen (2013).



## 2.2 VORTEX THEORY

### 2.2.1 Propeller hull vortex cavitation (PHVC)

When a ship propeller operates under highly loaded condition, unsteady line vortex cavitation may occur between the propeller tip and the hull. This type of cavitation is known as propeller - hull vortex cavitation (PHVC) and, if it occurs, it causes strong vibrations and noise in the stern of the ship, see Huse (1971). When a propeller is operating close to the free water surface, a vortex might form between the propeller and the free surface through which air can be drawn down to the propeller, so that it ventilates – a phenomenon we call Propeller Free Surface Vortex Ventilation (PFSVV). Such ventilation is described by several authors, see for instance Califano (2010), Hutchinson and Steen (2013), Kozłowska and Steen (2010, 2017) and Kozłowska et.al. (2009, 2011, 2017). It is likely that the physical phenomena causing vortex forming of PHVC and vortex ventilation are closely related, or even the same. It is well known from Helmholtz second theorem in fluid mechanics that a vortex cannot just end in the fluid; it must terminate against a surface, like a ship hull or the free surface. If the vortex created by the propeller terminates at the ship hull, it will not ventilate, but it might cavitate, if the vorticity is strong enough. On the other hand, if it terminates at the free surface, which might happen if there is no hull above the propeller, it is likely that the vortex will ventilate, so that it can act as a funnel for air to be sucked down to the low-pressure side of the propeller blades.

Huse (1971) first reported the PHVC phenomenon. Systematic observations had been carried out to investigate the effect of the afterbody form, tip clearance  $c_t$ , propeller loading  $c_T$  and cavitation number. Experimental observation with a flat, horizontal plate above the propeller in a cavitation tunnel showed that PHVC is more likely to occur for small tip clearances (up to 20% of propeller diameter,  $c_t = 0.2D$ ) for low values of the advance number  $J$ . Based on experimental investigations four hypotheses have been suggested for criteria leading to PHVC: a so called “starting vortex”, “vortices created by the shear flow in the wake field”, “vortices created in other regions of the flow field” as well as “the pirouette effect”, see

*Figure 2-6.* The “Starting vortex” hypothesis is based on Helmholtz’s second theorem, which states that a vortex must be either closed or terminate on the boundary of the fluid. *Figure 2-6* below shows the corresponding vortex line representation of a propeller blade. Circulation will also be closed on the shortest possible way. This means that the tip clearance must be less than the blade length and axial flow velocity in the region between hull and blade tip should be close to zero.

Hypothesis based on “vortices created by shear flow in the wake field” means that a high wake peak in the upper part of the propeller disk gives rise to intense shear flow in the region of highest velocity gradient. This represents a vorticity in the flow field that may “curl up” to form the concentrated vortices necessary to create PHVC.

The basic idea for the hypothesis based on “vortices created in other regions of the flow field” is that the cores of vortices will cavitate when entering the low pressure region between propeller and hull.

Huse (1971) concluded that the hypothesis based of the “pirouette effect” is probably the most correct. By this hypothesis the effect of tip clearance, randomness, effect of blade angular position and effect of vertical fins can be satisfactory explained. The basic phenomena related to “pirouette effect” were further explain later by Martio et.al. (2011). As the gap between the propeller blade tip and the wall is decreased, the blade suction side does not obtain enough water from the inlet side, so water is also sucked from downstream, causing a rotation of the flow, which is concentrated into a vortex by the so-called pirouette effect (rotational velocity has to increase considerably in order to keep the angular momentum constant, when the radius is reduced, thus forming a marked vortex) and finally causing the PHVC inception.

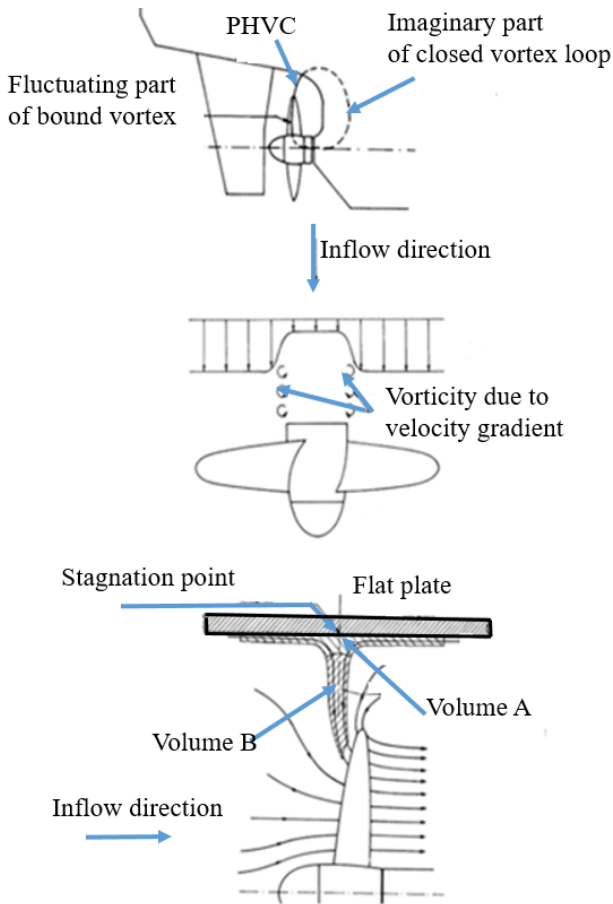
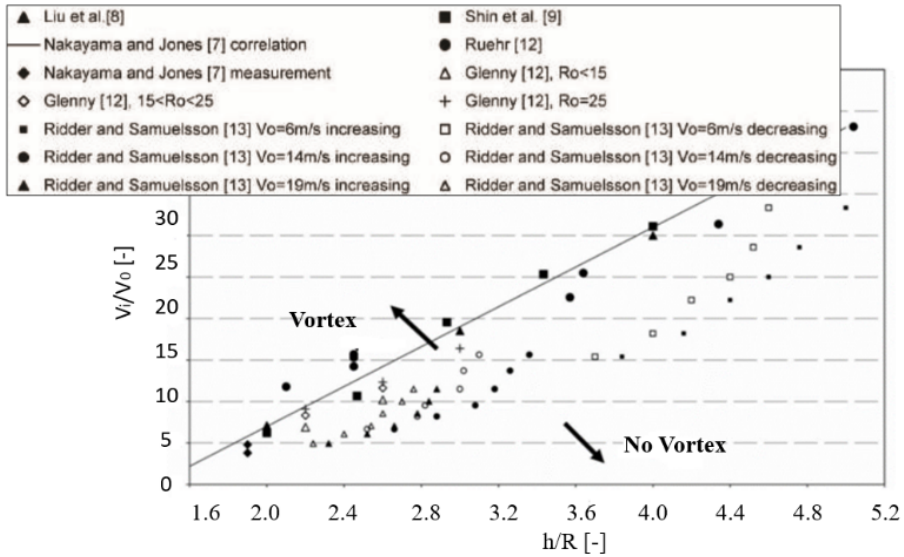


Figure 2-6 “starting vortex” (top), “vortices created by the shear flow in the wake field (middle) and “pirouette effect (bottom) hypothesis illustration, Huse (1971).

A more systematic investigation of the PHVC phenomena has been carried out by Sato et.al. (1986) and Nishiyama (1986). Sato et.al. (1986) presented observation of flow on horizontal flat plate above a working propeller to understand propeller hull vortex cavitation. Air bubbles were injected into the flow field in order to visualize streamlines of the plate. As a continuation of his work, the flow patterns were simulated by a RANS methods by Martio et.al. (2011). The agreement between the observations and computational results was considered to be satisfactory.

## 2.2.2 Inlet vortex

The threshold of formation of so-called ground vortices for aero engines during high power operation near a solid surface has been investigated since 1956 i.e., see for instance Nakayama and Jones (1996) and Jermy and Ho (2008). The factors determining the formation of vortex include engine thrust, distance from the ground and the ambient velocity are presented in *Figure 2-7*. The threshold of vortex formation numerically predicted agrees with previous wind tunnel studies



*Figure 2-7 Experimental data showing the boundary between the vortex forming and non-vortex forming flow regimes, Jermy and Ho (2008) as the function of the distance from the inlet center to the ground divided by inlet radius ( $h/R$ ) and the inlet velocity divided by ambient velocity ( $V_i/V_0$ ).*

### 2.2.3 Ground vortex

The formation of the ground vortex on airplane engines depends on the engine power, wind velocity and engine inlet height and size, Denny (1956). Previous published work, see for instance Bissinger and Brown (1974) about ground vortex shows that the phenomenon can only occur with the presence of a stagnation streamline between the ground and the inlet, which is dependent on the velocity ratio  $V_i/V_0$  and the non-dimensional height  $h/R$ , see *Figure 2-8* below. Typically, the formation of the ground vortices is characterized by low  $h/R$  and high  $V_i/V_0$ , which correspond to the engine close to the ground operating at high inlet velocity.

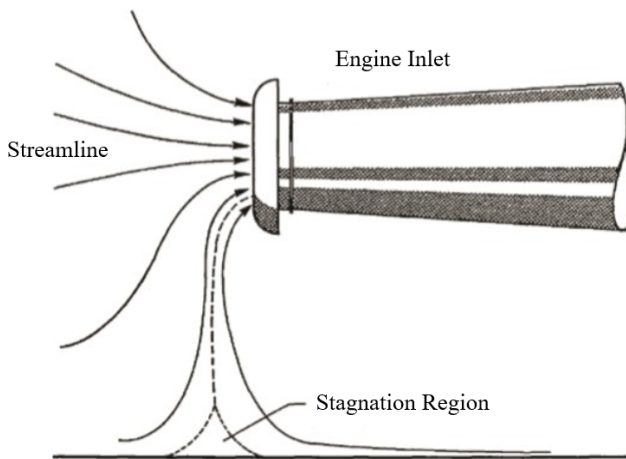


*Figure 2-8 Stagnation region under inlet Rodert and Garret (1955)*

The velocity ratios  $V_i/V_0$  and  $h/R$  combinations that correspond to the appearance or non-appearance of the ground vortex are shown in *Figure 2-8* above. The experimental data which allows to define the threshold for the vortex formation of the inlet vortex has been collected and plotted by several authors, see for instance Nakayama and Jones (1996). The boundary between the vortex forming and non-vortex forming for ground vortex flow regimes follow the straight line as shown in *Figure 2-7*, thus the empirical relation for critical velocity ratio at which a vortex first appears was derived by Nakayama and Jones (1996), as

$$(V_i/V_0)_{CRIT} = 24 \cdot (h/(2 \cdot R)) - 17 \quad (2-27)$$

Figure 2-7 indicates that a good correlation exists for the occurrence of an intake ground vortex in terms of relative flow rate and the position on the inlet.

### 2.2.4 Propeller ventilation

Ventilation by vortex formation has analogies to the inlet vortex. Using the same parameters for propeller and suction inlet, see Figure 2-9, the borderline between the vortex forming, non-vortex forming and free surface ventilation flow regimes for marine propellers can be drawn.

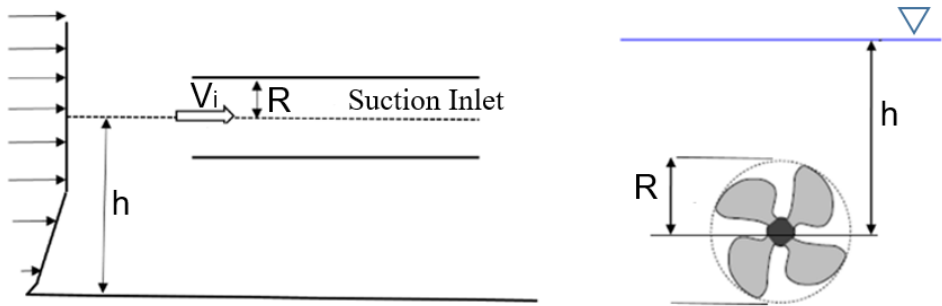


Figure 2-9 A sketch showing principal parameters,  $(V_i/V_0)$  and  $(h/R)$ .

Following the work for inlet vortices, the experimental results for model propellers are compared in order to calculate the boundaries between vortex forming, non-vortex forming and free surface ventilation flow regimes of marine propellers.

The two factors that were investigated as variables for the formation of the vortex were propeller radius divided by the distance from the propeller center to the free surface  $h/R$  and the velocity through the propeller disk  $V_i$  divided by the free stream velocity  $V_0$

$$V_i = V_0 + 0.5(-V_0 + \sqrt{V_0^2 + \frac{2T}{\rho \frac{\pi}{4} D^2}}), \text{ see Figure 2-9.} \quad (2-28)$$

Derivation of equation (2-28) is based on simple momentum theory, which is described in section 2.3 below.

## 2.3 PROPELLER ANALYSIS

### 2.3.1 Numerical approaches

Several numerical methods can be applied to calculate hydrodynamic forces and moments generated by the propeller. Numerical methods include both potential and viscous flow methods. A brief comparison of different computational methods can be found in Philips et.al. (2009) and Breslin and Andersen (1994). We can categorize different computational methods for modelling propellers as follows:

- Simple Momentum Theory (axial velocity only)
- Complete Momentum Theory (actuator disk theory)
- Blade Element Momentum Theory (BEMT)
- Lifting Line Methods
- Lifting Surface Methods
- Panel Methods
- CFD

The Simple Momentum Theory was first developed by Rankine (1865) for marine propellers. The main assumptions of the simple momentum theory is that the flow is steady, incompressible, inviscid and irrotational. The propeller is modeled as an actuator disc, which adds axial momentum and energy to the flow. Simple momentum theory connects thrust to the axial velocity increase through the disk, assuming uniform acceleration. The thrust is calculated from the flux through the propeller disk ( $A_0$ ) and the difference of the velocities in front and behind the propeller disk.

$$T = \rho v_p A_0 (v_B - v_A) = 2\rho v_p (v_p - v_A), \text{ with } v_0 = 0.5(v_B + v_A) \quad (2-29)$$

Where:  $v_B$  is the velocity in the slipstream far behind the propeller,  $v_A$  is the velocity in front of propeller. As it is shown in the *Figure 2-10* index “A” indicates a plane in front of propeller, index “p” is used for variables on the propeller plane and index “B” indicates a plane behind the propeller.

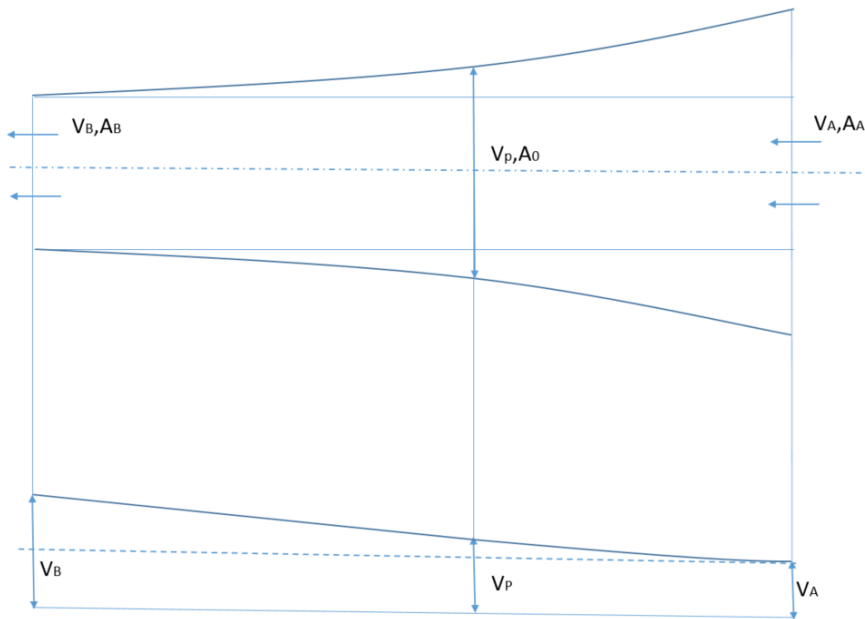


Figure 2-10 Characteristic of propeller stream according to momentum theory.

One of the parameters that can be obtained from simple momentum theory is ideal efficiency.

$$\eta_I = \frac{2}{1 + \sqrt{1 + c_{TH}}} \quad (2-30)$$

Where:

$$c_{TH} = \frac{T}{0.5\rho v_p^2 \cdot A_0} \quad (2-31)$$

$c_{TH}$  is the thrust loading coefficient, see Section 2.1.1.

It is not possible to obtain torque from the simple momentum theory, except by assuming the efficiency to be equal to the ideal efficiency and assume a propeller speed.

**Complete momentum theory** can be considered as an extension of simple momentum theory. For complete momentum theory the assumptions of inviscid, incompressible flow are still used, but the circumferential velocity change  $\Delta V_\theta = \omega \cdot r$  is added into the



momentum disc model, Betz (1920), where  $\Delta V_\theta$  is the circumferential velocity change,  $\omega$  is the propeller's rotation and  $r$  is the local radius. Furthermore, radial variation of the velocities are included, but no tangential variations.

The **Blade Element Momentum Theory** is a combination of Blade Element Theory (BET) and Complete Momentum Theory. BET calculates the forces and moments acting on the blade from a finite number of independent blade sections represented as 2D aerofoils at an angle of attack to the fluid flow. The advantage of BEMT theory over more advanced methods is that it allows the lift and drag properties of the 2D sections representing the blade to include viscous effects such as stall and the effects of laminar separation at low Reynolds numbers by using empirically based lift and drag curves for the blade sections. This method has been used to predict the propeller performance in terms of thrust and torque in axis symmetric flow for marine propellers, Carlton (2007), wind turbines Hansen (2008) and airplane propellers Glauert (1935).

A step towards a more complete modelling of the flow around propellers is to use methods based on the **lifting line theory**. In these methods, the propeller blades are represented by individual lifting lines, which have a varying circulation as a function of radius. The lifting line approach is only valid for light or moderately loaded high aspect ratio propeller blades, and is unable to capture the behaviour of stall, Lerbs (1952).

To increase the accuracy of the computational method, **lifting surface methods** can be used instead of the lifting line method. Here, the propeller blade is represented by an infinitely thin surface fitted to the blade camber line, so here the blade circulation is distributed not only spanwise but also chordwise, Pien (1961). The main advantage of this method compared to lifting line and BEMT method is that the propeller model is no longer two-dimensional. The most common numerical approaches based on lifting surfaces are called vortex lattice method (VLM), where the blade is modelled by a grid of vortices. Vortex-lattice methods are able to handle arbitrary blade geometries, but they do not consider the blade thickness in the solution of the lifting problem, Kerwin et.al. (1978). They cannot handle stall and other viscous effects on the blade lift. More details of the computational approach inside the vortex-lattice method are described in Bertram (2000).

**The panel method** is quite similar to Lifting Surface Methods. The main difference is that instead of using mean camber surface, the blade surface itself is discretised with a distribution of source or dipole panels, so that effects of lift and thickness are treated together, thereby relaxing the linear theory assumption of the lifting surface method. The panel method applied to propellers was studied and described by Kerwin et. al. (1987) and Kinnas and Hsin (1992), and many other authors as well. There are several variations of the panel method, and as for the lifting surface method, how the effect of the vertical wake is taken into account is a major issue, where several different approaches exist. The use of panel methods for a single propeller in open water conditions is known to predict the propeller torque and thrust with good accuracy close to the designed operating condition.

Numerical methods developed for investigation of the propeller flows usually consider only deep submerged propellers in calm water. In a **CFD** method, The Navier – Stokes equation are solved with the viscosity term and allowing the velocities and pressure to vary with time and position. CFD methods can be divided to Reynolds Averaged Navier Stokes equation (RANS) method, Large Eddy Simulation (LES) techniques and Detached Eddy Simulation (DES). Among these approaches, the RANS codes are the most used because of the lower computational time than the other methods.

The viscous-flow method used for studies covered in this thesis is the FreSco<sup>+</sup>, which uses a finite volume approach to solve the RANS equations. FreSco<sup>+</sup> is a joint development of Hamburg University of Technology and the Hamburg Ship Model Basin. More details about the FreSco<sup>+</sup> can be found in Rung (2009), while the numerical procedure is described in Ferziger and Peric (1996). The CFD work has been done by Wockner-Kluwe (2013) in cooperation with the author. Two existing in-house codes, the potential flow method *ISThydro* and the RANS method FreSCO<sup>+</sup> were improved in order to obtain more accurate modeling of the flow around the propeller.

## 2.4 STEADY STATE VORTEX MODELS

This section presents two different vortex models, which are the steady state solutions of the Navier-Stokes equation:  $(\partial/\partial t) = 0, t \rightarrow \infty$ , Rankine vortex and the vortex model from Rott (1958).

### 2.4.1 Rankine vortex

A simple model for a vortex is given by the combination of a rigid body rotation within the core and a decay of angular velocity outside the core. This can be describe mathematically as:

$$V_{\theta}(r) = \begin{cases} \omega r, & (r < R) \\ \frac{\omega R^2}{r} & (r > R) \end{cases} \quad V_r = V_z = 0 \quad (2-32)$$

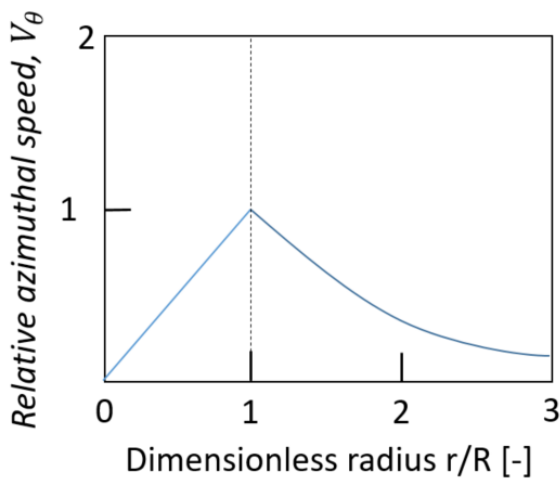


Figure 2-11 *Form of azimuthal velocity in a combined Rankine vortex.*

In a Rankine vortex, the interior flow field (core) include only the azimuthal velocity, which increase linearly from zero to maximum values at radius  $R$ . As a result, the entire region rotates, as a solid body even though it is a fluid. The outer flow (tail) also include only the azimuthal velocity, which decay outside the vortex core as  $1/r$ .

### 2.4.2 Rott vortex

The vortex model proposed by Rott (1958) is based on an analytical solution of the Navier-Stokes equation for a particular flow condition. The particular flow condition assumes that there are two sinks that are the distance  $2H$  from each other and that the vortex passes right through them. The two sinks generate the flow so that there exist a plane where the velocities through the plane are zero; this plane represent the water surface, see *Figure 2-13* below. The exact solution to the Navier-Stokes equation obtained by Rott (1958) assumes the mathematical form

$$\begin{aligned} V_r &= -ar \\ V_\theta &= \frac{\Gamma}{2\pi r} \left(1 - e^{-\frac{ar^2}{2\nu}}\right) \\ V_z &= 2az \end{aligned} \quad (2-33)$$

In the system of cylindrical polar coordinates  $r, \theta, z$  where the velocity components are  $V_r$  (radial),  $V_\theta$  (circumferential),  $V_z$  (vertical).  $\Gamma$  is the circulation strength of the vortex and  $a$  being the flow suction gradient, which is also related to the vortex strength, as explained below. The vortex has a central axis like a Rankine vortex around which there is azimuthal flow. However, unlike the Rankine vortex it has radial and vertical flows as well due to the sink. In this way, it closely resembles a “bathtub vortex”, which is what the ventilated propeller vortex looks like. The viscous core radius is defined as:

$$r^* = \sqrt{\frac{2\nu}{a}}, \nu - \text{kinematic viscosity} \quad (2-34)$$

The azimuthal velocity component reaches the a maximum value where

$$\frac{1}{2\pi} \left( \frac{a}{\nu} e^{-\frac{ar^2}{2\nu}} - \frac{1 - e^{-\frac{ar^2}{2\nu}}}{r^2} \right) = 0, r(a/2\nu)^{\frac{1}{2}} = 1.12. \quad (2-35)$$

The *Figure 2-12* below show the form of the azimuthal component. We can see that it is very similar to the Rankine vortex. The peak azimuthal velocity defines the boundary of the core, and the tail region contains momentum but very little vorticity.

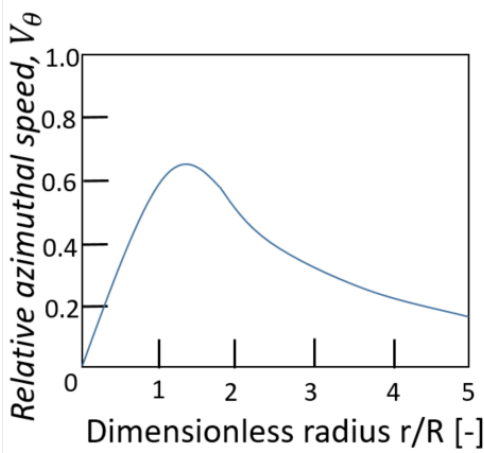


Figure 2-12 Form of azimuthal velocity in a Rott (1958) vortex.

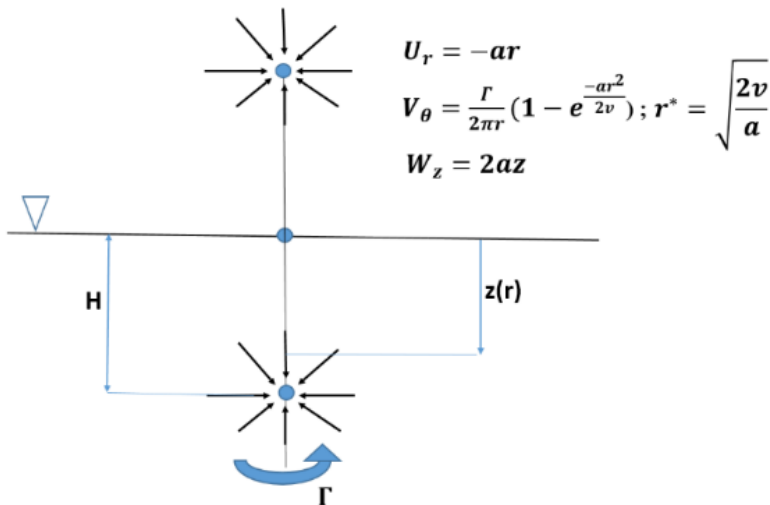


Figure 2-13 Vortex model from Rott (1958).

## 2.5 INCEPTION OF CAVITATING / VENTILATING VORTEX

Kozłowska and Steen (2017) investigate the relation between the pressure in the vortex core in order to define the vortex ventilation inception. As the result the formula for a radius of ventilating vortex, which depends on the propeller circulation and ventilation number was obtained. The theory belonging to this study is described below.

Inception of vortex cavitation is a complicated issue because it involves a vortex with a low pressure region in the core, but also nuclei to expand in that vortex core. When a

cavitation nuclei reach a critically low pressure it will rapidly expand so that the cavitation is formed.

Cavitation inception depends on the minimum pressure in the vortex core. The velocity distribution of a 2D vortex flow as given by two different vortex models is shown in the *Figure 2-14* below.

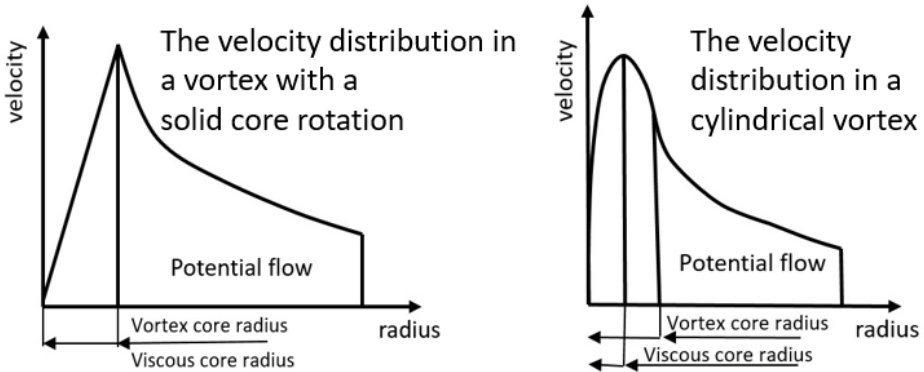


*Figure 2-14* The velocity distribution on the vortex flow.

The pressure distribution in the center of a vortex is lower than in the surrounding fluid because of the centrifugal effects of the rotating fluid. In a cylindrical vortex this can be easily derived from the force equilibrium on a fluid particle in rotating flow. A rotating particle which follows a cylindrical path around the vortex core is subjected to a centrifugal force, which has to be compensated by a pressure force in the radial direction

$$\frac{\partial p}{\partial r} = \rho \frac{v(r)^2}{r} \quad (2-36)$$

In the case of a Rankine vortex, the pressure integration over radius  $r$  from  $a$  to  $\infty$  results in

$$p_{\infty} - p(a) = \frac{\rho \Gamma^2}{4\pi^2 a_v^2} \quad (2-37)$$

Where  $a_v$  is the radius of the cavitating/ventilating vortex and  $\Gamma$  is the circulation strength.

For a ventilating vortex, the pressure in the center of the vortex is typically assumed to be equal to the atmospheric pressure,  $p_{at}$  while the pressure far away from the vortex,  $p_{\infty} = p_{at} + \rho gh$  so the equation (2-38) can be expressed as follows:

$$p_{at} + \rho gh - p_{at} = \frac{\rho \Gamma^2}{4\pi^2 a_v^2} \quad (2-38)$$

In order to estimate the radius of the viscous core at which ventilation inception starts, it is first needed to find the strength of the circulation  $\Gamma$ . This is difficult, and a simplified approach is taken, see Kozłowska and Steen (2017). The circulation should increase with the propeller loading, and it seems reasonable to link it to the circulation of a propeller blade. Therefore, the known approximate relation between propeller blade lift coefficient at 70% radius  $c_{L0.7}$  was used, thrust coefficient for non-ventilated, deeply submerged propeller  $K_{Tn}$  and blade area ratio  $EAR$  was used, which is valid as an approximation for typical conventional propellers Gutsche (1962):

$$c_{L0.7} = \frac{K_{Tn}}{1.5EAR} \quad (2-39)$$

Using the Kutta Joukowski theorem, the lift coefficient can be linked to the circulation at the same blade section:

$$c_{L0.7} = \frac{\rho \cdot \Gamma \cdot V_c}{0.5 \cdot \rho \cdot V_c^2 \cdot c_{0.7}} \quad (2-40)$$

Where  $V_c$  is the local relative velocity at the blade section, which, when ignoring induced velocities can be calculated as  $V_c = \sqrt{V_A^2 + (0.7\pi nD)^2}$  where  $n$  is the propeller speed. By combining the two expressions for the lift coefficient, the expression for the circulation strength is obtained:

$$\Gamma = \frac{V_c \cdot c_{0.7} \cdot K_{Tn}}{3 \cdot EAR} \quad (2-41)$$

By using the equation (2-41) to express the circulation a formula for the radius of ventilating vortex is obtained:

$$a_v = \frac{(V_c \cdot c_{0.7} \cdot K_{Tn}) / (3 \cdot EAR)}{2\pi\sqrt{gh}} \quad (2-42)$$

A question that remains is how large the radius  $a_v$  needs to be for ventilation to occur. For very small radii, the air flow velocity increases, leading to decreasing air pressure, so that the assumptions about atmospheric pressure used for deriving equation (2-38) is no longer valid. Decreasing air pressure means reduced radius, so assuming atmospheric pressure means that the vortex core radius is over-predicted especially for small radii. To correct for this effect, we need to know the air flow rate, something which is really quite hard to calculate, since it involves how the air is swept from the propeller into the free stream. A further discussion about how  $a_v$  is found is included in Section 4.9.

## 2.6 SLAMMING FORCES

Traditionally, the term slamming is used to describe the forward bottom impact, when the vessel rises up above the free surface and re-enter the water again. The probability of slamming is higher on the fore than on the aft part of the ship, since the relative velocity between the ship hull and the water is higher in the fore than the aft part, see Faltinsen (1990). Wave impacts can also cause bow damage above the waterline. On offshore oil and gas platforms, slamming is observed on the deck structures caused by green water on deck or by sloshing in the tanks.

In short, one can say that slamming is an impact between water and a structure, which is very concentrated in time and space, with large energy released. Slamming has been extensively studied by Von Karman (1929), Wagner (1932), Garabedian (1953), Dobrovol'skaya (1969), Faltinsen (1990), Zhao and Faltinsen (1993), Zhao et.al. (1996) and Howison et.al. (1991). Howison et. al. (1991) have further developed and extended Wagner's theory by using asymptotic expansion for impacting bodies with small deadrise angles. Dobrovol'skaya (1969) presented similarity solution for wedges that are forced with a constant velocity through the free surface. Zhao and Faltinsen (1993) and Zhao et.al. (1996) developed two different theoretical methods for predicting slamming loads. One of the methods was fully non linear numerical simulation. The other method was a simple asymptotic solution for small deadrise angles based on Wagner (1932) theory. Both methods have been verified by comparison with experimental results from drop test of ships cross section.

*Figure 2-15* illustrates the parameters characterising the slamming pressure during water entry of a blunt rigid body. Slamming pressure has a very short rise time followed by the



peak pressure ( $c_{Pmax}$ ). The decay time of the pressure ( $c_P < 0.5 \cdot c_{Pmax}$ ) is much larger than the rise time. Another important parameter is the spatial duration of the slamming pressure, denoted  $\Delta S_s$  in the figure below.

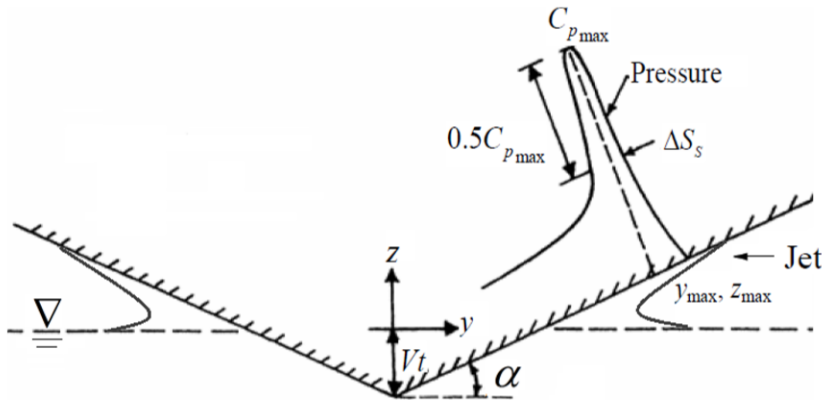


Figure 2-15 Definition of parameters characterizing slamming pressure during water entry of a blunt 2D bodies :  $\alpha$  (deadrise angle);  $c_{Pmax}$  (pressure coefficient at maximum pressure),  $z_{max}$  ( $z$ -coordinate of maximum pressure),  $\Delta S_s$  (spatial extent of slamming pressure exceeding 50% of maximum pressure),  $t$  (time),  $V$  (water entry velocity), Zhao and Faltinsen (1993).

Mork (2007) was one of the first researchers to study the propeller blade slamming hypothesis for surface piercing propellers (see section 1.1 for an introduction to this hypothesis). She performed slamming calculations using the program Slam2D and did model experiments for an idealized case, where a one bladed propeller set to very high pitch hits the undisturbed free surface. The results from the slamming propeller experiment were compared with the Slam 2D calculation results. Slam 2D is a computer program based on generalized Wagner theory – for wedges using potential theory and predicts forces, moments and pressure distribution on ship section, due to slamming, see Zhao et.al. (1996). A further description of slamming hypothesis and results from model experiments can be found in Section 7.

### 3 MODEL TESTS

In this chapter, the test matrices, test set-ups and main results are outlined for seven different test campaigns that together constitute the experimental data analysed in this thesis.

#### 3.1 OVERVIEW OF COMPLETE MODEL TESTS

The seven experimental campaigns in this thesis are referred to with acronyms as given in *Table 3-1* and *Table 3-2*. The majority of the results presented were obtained during the test campaigns presented in *Table 3-1*. Detailed description of these tests can be found in the following section. Some cases, which are listed in *Table 3-2*, from the other test campaigns were used for comparison or to investigate missing cases relevant to this study. Thus, only a brief description of these experiments is given in the following section. For all cases, the test campaign they belong to will always be referred to by its corresponding acronym.

Author	Acronym	Propeller	Publication
Kozłowska	<i>Koz17</i>	P1374, open	Kozłowska et.al.(2017) Kozłowska and Steen (2017)
Kozłowska	<i>Koz10</i>	P1440, open	Kozłowska et.al.(2011)
Kozłowska	<i>Koz08</i>	P1374, open	No publication
Koushan	<i>Kou2006_II</i>	P1374, Ducted: 19A	Kozłowska and Steen (2010) Koushan (2006c)
Koushan	<i>Kou2006_I</i>	P1374, open	Kozłowska et.al.(2009), Kozłowska and Steen (2010) Koushan (2006 a and b)

*Table 3-1 Test campaigns, detailed description can be found in the following section*

Author	Acronym	Propeller	Publication
Kourosh & Spence	<i>Kou10</i>	P1440, open	Koushan et.al. (2011)
Kozłowska & Califano	<i>Koz09</i>	P1374, open	Califano (2010)

*Table 3-2 Test campaigns, only a brief description can be found in the following section*

Summary of test descriptions as well as main objective for the tests are presented in *Table 3-3*

	Type of Test	Heave motion	Dynamometer /Place	Description / objective for the test
<i>Koz17</i>	ventilation	No	conventional two component propeller open water dynamometer / Towing Tank at Marine Technology Centre	Different propeller revolutions and speeds were tested to get better data for higher advance numbers. <i>Main objective: <u>obtain more data for validation purpose (empirical model for thrust loss)</u></i>
<i>Koz10</i>	ventilation	No	Novel blade dynamometer (2 <sup>nd</sup> version) improved design of (1 <sup>st</sup> version) by Marintek/NTNU capable of measuring blade forces and moments in five degrees of freedom / Towing Tank at Marine Technology Centre	One constant propeller revolution ( $n=18\text{Hz}$ ) was tested for different constant immersion ratios ( $h/R=2.5, 1.5, 1.0$ ) for advance number from zero up to 1.2. <i>Main objective: <u>comparison with CFD calculations</u></i>
<i>Kou10</i>	ventilation	No	Novel blade dynamometer (2 <sup>nd</sup> version) improved design of (1 <sup>st</sup> version) by Marintek/NTNU capable of measuring blade	Tests were performed in calm water. All tests were carried out at propeller revolution speed of 18Hz, for advance numbers from zero up to 1.2.

			forces and moments in five degrees of freedom / Towing Tank at Marine Technology Centre	<u>Main objective: comparison for thrust loss in calm water and waves.</u>
<i>Koz09</i>	ventilation	No	Novel blade dynamometer (2 <sup>nd</sup> version) improved design of (1 <sup>st</sup> version) by Marintek/NTNU capable of measuring blade forces and moments in five degrees of freedom / Marine Cybernetics Laboratories	Different propeller revolution were tested in the range of low advance numbers around ( $J=0.1$ ) at constant immersion. <u>Main objective: comparison with CFD calculations.</u>
<i>Koz08</i>	slamming	No	conventional two component propeller open water dynamometer / Towing Tank at Marine Technology Centre	Test was performed for high propeller pitch, different propeller revolutions and constant surface piercing submergences. <u>Main objective: Verify if slamming loads can occur for surface piercing propellers.</u>
<i>Kou2006_II</i>	ventilation	Yes	Novel blade dynamometer (1 <sup>st</sup> version) built by Marintek /NTNU) capable of measuring forces and moments in all	Tests were performed at different revolution rates and carriage speeds both at constant submersions and with periodically varying submersions, at constant azimuth angles and

			six degrees of freedom / Marine Cybernetics Laboratories	periodically varying azimuth angles. <i><u>Main objective: check the ventilation effect for thrust loss for constant immersion and under sinusoidal heave motion for ducted propeller.</u></i>
<i>Kou2006_I</i>	ventilation	Yes	Blade dynamometer provided by Rolls Royce Hydrodynamic Research Centre of Sweden / Marine Cybernetics Laboratories	Test was performed in at different revolution rates and carriage speed both at constant immersion and with periodically varying submersions for open propeller on a pulling thruster for low advance numbers <i><u>Main objective: check the ventilation effect for thrust loss for constant immersion and under sinusoidal heave motion for open propeller.</u></i>

*Table 3-3 Summary of performed test campaigns performed in the years 2006-2017 used in the thesis.*

### 3.2 GEOMETRY OF PROPELLER MODELS

Two different propeller models have been used for experiments presented in this thesis. The geometry of each propeller model is presented in *Table 3-4* and *Table 3-5* below. The propellers will later be referred to by their propeller number.

P1374	Symbol	Unit	MODEL
Propeller diameter	D	[mm]	250.00
Pitch ratio at $r/R=0.7$	$P/D_{0.7}$	[-]	1.100
Blade area ratio	$A_E/A_0$	[-]	0.600
Number of blades	Z	[-]	4
Chord / Diameter ratio	$c/D_{0.7R}$	[-]	0.3876
Thickness /Chord ratio	$t/c_{0.7R}$	[-]	0.0410
Hub diameter ratio	d/D	[-]	0.240

*Table 3-4 Geometry for propeller model P1374, experiments Koz17, Koz09, Koz08, Kou2006\_I and Kou2006\_II.*

P1440	Symbol	Unit	MODEL
Propeller diameter	D	[mm]	200.00
Pitch ratio at $r/R=0.7$	$P/D_{0.7}$	[-]	1.200
Blade area ratio	$A_E/A_0$	[-]	0.447
Number of blades	Z	[-]	4
Hub diameter ratio	d/D	[-]	0.06

*Table 3-5 Geometry for propeller model P1440, experiments Koz10 and Kou10.*

### 3.3 MAIN DIMENSION OF THRUSTER BODIES

In several of the tests, the propeller was mounted on an azimuthing thruster body. The thruster body used in experiments *Kou2006\_I* and *Koz09*, where an open propeller was tested is shown in *Figure 3-1* below. It was 281 mm long and has a maximum diameter of 109 mm. The thruster body was made relatively large to accommodate the model thruster drive.

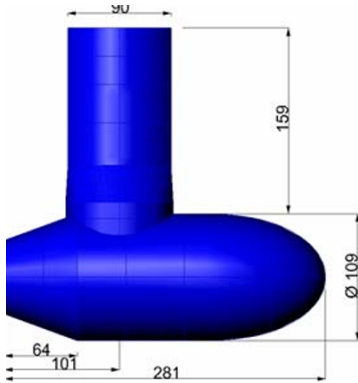


*Figure 3-1 Thruster body for open propeller used in experiments Kou2006\_I, Kou2006\_II and Koz09)*

The ducted propeller used in the experiments *Kou2006\_II* was mounted on a thruster body that was 181mm long and has a diameter of 92mm, see *Figure 3-2*.



*Figure 3-2 Thruster body for ducted propeller used in experiments Kou2006\_II.*

The thruster housing for model experiments *Kou10* was a model of an Azipull pulling thruster, which was slightly modified, see *Figure 3-3* in order to accommodate the required instrumentation, and the uppermost part of the thruster housing was extended upwards to allow varying the submergence, , since the full scale geometry is designed to be mounted beneath the submerged part of the aft body of a ship.



*Figure 3-3 Azipull-type thruster body for pulling open propeller used in experiments Kou10. Note the extension of the strut part of the thruster, made to allow variation of the submergence and to ensure that the instrumentation (visible in the top of the picture) came well above the water.*

### **3.4 KOZ17**

#### **3.4.1 Test Description (set up, test matrix, filter)**

The *Koz17* test was performed in the large towing tank at the Marine Technology Centre. Propeller model (P1374) was used. A conventional Kempf and Remmers two-components propeller open water dynamometer was used to measure propeller thrust and torque. The dynamometer with propeller mounted is shown in its above-water position in *Figure 3-4*. Due to the torque (15Nm) and force (400N) limits of the dynamometer the range of  $J$  values for the higher revolutions speeds had to be limited, the limits are given in *Table 3-6* below. During measurements, images are acquired with two high speed cameras (top and suction side view of the propeller) at a sampling frequency of 200 Hz. The cameras were controlled by a dedicated computer providing trigger pulses in order to extract time stamps for the acquired images. *Figure 3-4* shows a picture of the test set-up and a sample of the pictures from above-and underwater videos.



Propeller speed: $n[rps]$	9 rps	12 rps	14 rps	16 rps
Max Thrust: $T[N]$	194N	345 N	368N	335N
Max Torque: $Q[Nm]$	7.1Nm	12.7Nm	14.2Nm	14.3Nm
Min advance number: $J[-]$	0	0	0.3	0.6

*Table 3-6 Lower limits of advance number  $J$  due to the torque and thrust limits of the dynamometer. The max thrust and torque values are the maximum values measured during the experiments.*

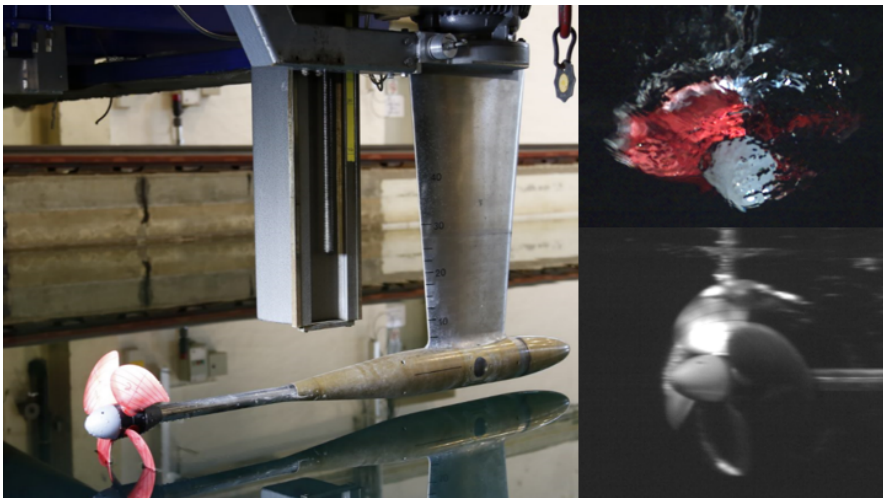


*Figure 3-4 Test set-up (left) and propeller view from underwater (bottom right) and above water camera (top right).*

The necessary light for the camera acquisition system is provided by two lamps: one above the water surface and one underwater. The signals were acquired at a sampling frequency of 200 Hz using a 20 Hz low-pass Butterworth filter. Tests were performed at different draughts and propeller speeds. For each draught and propeller speed, the propeller was tested at different advance numbers, ranging from the lower limit specified in Table 3-6 to  $J = 1.0$ . The different advance numbers were obtained at various propeller speeds so that for the same advance numbers different propeller thrusts were obtained, thus varying the Weber number and thrust loading. According to Shiba (1953) the influence of Weber's number disappears above the so-called minimum Weber's number, which is about 180. In our case only for propeller revolution speeds over  $n=13Hz$ , the influence of Weber's

number can be neglected, when following the advice by Shiba (1953). The complete test matrix is given in *Table 3-7* below.

$n$ [rps]	9 rps	12 rps	14 rps	16 rps
$J$ [-]	0 – 1.0	0 – 1.0	0.3 – 1.0 for $h/R > 1.4$ 0 – 1.0 for $h/R \leq 1.4$	0.6 – 1.0 for $h/R > 1.2$ 0 – 1.0 for $h/R \leq 1.2$
$V_A$ [-]	0 – 2.25	0 – 3.0	1.05 – 3.5 for $h/R > 1.4$ 0 – 3.5 for $h/R \leq 1.4$	2.4 – 4.0 for $h/R > 1.2$ 0 – 4.0 for $h/R \leq 1.2$
$h/R$ [-]	–0.5, 0, 0.5, 1.0, 1.2, 1.4, 1.5, 1.6, 1.8	–0.5, 0, 0.5, 1.0, 1.2, 1.4, 1.5, 1.6, 2.0	–0.5, 0, 0.5, 1.0, 1.2, 1.4, 1.5, 1.6, 2.0	–0.5, 0, 0.5, 1.0, 1.2, 1.4, 1.5, 1.6, 2.0

*Table 3-7 Test Matrix.*

### 3.4.2 Main Results – *Koz17*

The obtained results are presented in the form of total thrust (or torque) loss factor  $\beta_T = K_T/K_{Tn}$  where  $K_{Tn}$  is the time-averaged mean value of the thrust coefficient at the relevant advance number  $J$  obtained from the calm water, deeply submerged non-ventilated propeller.

The propeller torque  $K_Q$  has a similar behavior as propeller thrust and the relation between thrust loss and torque loss shows good agreement with the previous experimental finding in Kozłowska et.al. (2009), where  $K_T = \beta \cdot K_{Tn}$  and  $K_Q = \beta_T^m \cdot K_{Qn}$ ,  $m$  is constant between 0.8 and 0.85 (Minsaas et.al. (1983)), where  $K_{Qn}$  is the time-averaged mean value of the torque coefficient, at the relevant advance number  $J$ , obtained from the calm water, deeply submerged non-ventilated propeller.

The open water curve for the deeply submerged ( $K_{Tn}, K_{Qn}, \eta_n$ ) and ventilated ( $K_T, K_Q, \eta$ ) propeller is presented in *Figure 3-5*.

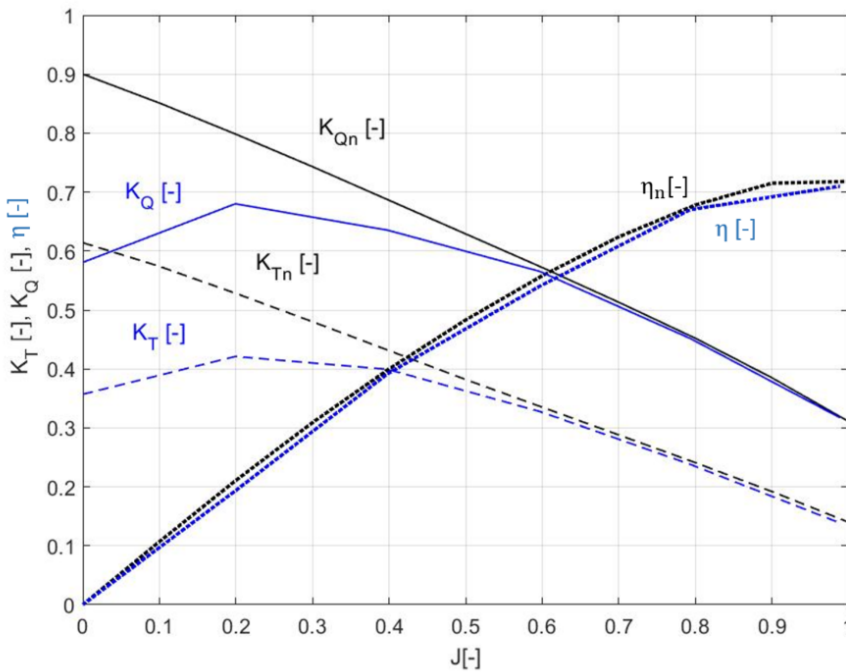
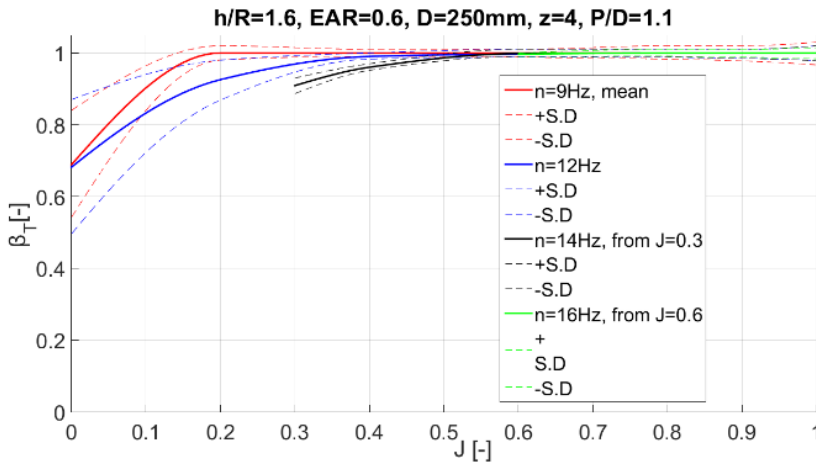


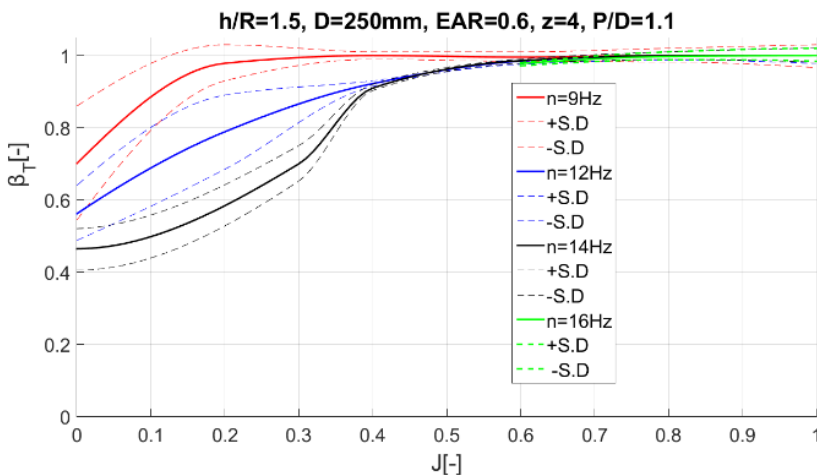
Figure 3-5 Open water curve for deeply submerged ( $K_{Tn}, K_{Qn}, \eta_n$ ) and ventilated ( $K_T, K_Q, \eta$ ) propeller,  $n=12\text{ rps}$ .

Figure 3-6 shows total thrust loss factor vs. advance number for tests performed in calm water at immersion ratio  $h/R = 1.6$  for different propeller revolutions  $n = 9, 12, 14$  and  $16\text{ rps}$ . Mean values as well as standard deviations (S.D.) about mean values are shown. Due to the significant submergence ratio, ventilation occurs only for low advance numbers  $J \leq 0.2$ . Standard deviations are the highest for  $0 \leq J \leq 0.2$ , where it is observed sudden thrust drop due to ventilation, since the propeller here operates in an unstable regime. It is observed only two different flow regimes in this submergence: unstable regime, where the propeller is partially ventilated and sub-critical regime, where the propeller is non-ventilated or experienced very little ventilation. For ventilation prediction, it is important to determine the critical advance number  $J_c$ , which separates ventilating and non-ventilating flow regimes. The similar phenomenon, that the propeller operate only in partially and non-ventilating regimes is observed for submergence  $h/R = 1.5$  and  $h/R = 1.4$ , see Figure 3-7 and Figure 3-8 below.

As it is observed from experiments for deeply submerged propeller in *Figure 3-6*, *Figure 3-7* and *Figure 3-8* the propeller rotational speed has significant impact on ventilation and thrust loss. The propeller ventilates more and the thrust loss is bigger for  $n=14\text{Hz}$  than  $n=12\text{Hz}$  or  $n=9\text{Hz}$ . Unfortunately, the highest propeller rotational speed  $n=16\text{Hz}$  has been tested only for high advance numbers ( $J \geq 0.6$ ) for deeply submerged propeller due to the torque and thrust limit of the dynamometer, so the ventilation has not been observed for the highest propeller revolutions.



*Figure 3-6* Total thrust loss factor vs.  $J$  value for propeller submergence  $h/R=1.6$  based on experimental values.



*Figure 3-7* Total loss factor vs.  $J$  value for propeller submergence  $h/R=1.5$  based on experimental values.

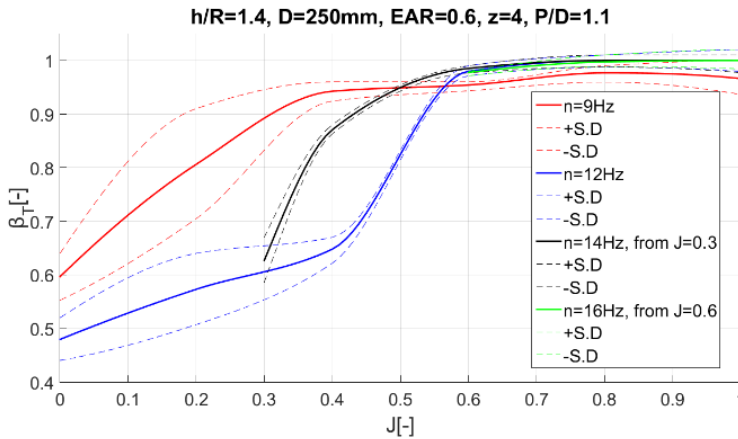


Figure 3-8 Total thrust loss factor vs.  $J$  value for propeller submergence  $h/R=1.4$ , based on experimental values.

Figure 3-9 shows total thrust loss factor vs. advance number for tests performed in calm water at immersion ratio  $h/R = 1.2$  for different propeller revolutions  $n = 9, 12, 14$  and  $16$  rps. Mean values as well as standard deviations about mean values are shown. Here it is observed all three flow regimes: super critical regime (fully ventilated propeller), unstable regime (partially ventilated propeller) and subcritical regime (non-ventilated propeller). It is observed that the standard deviation is highest in the unstable regime. For ventilation prediction it is important to find the critical advance number  $J_c$  and supercritical advance number  $J_{SC}$  that separates this three ventilation regimes.

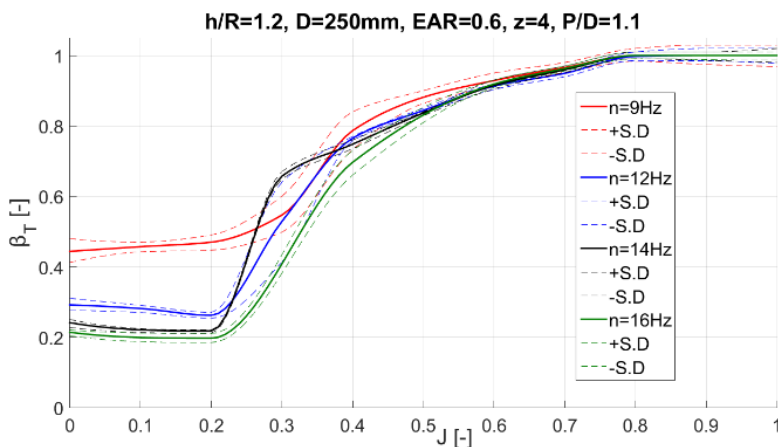


Figure 3-9 Total thrust loss factor vs.  $J$  value for propeller submergence  $h/R=1.2$  based on experimental values.

Figure 3-10 shows total thrust loss factor vs. advance number for tests performed in calm water at immersion ratio  $h/R = 1.0$  for different propeller revolutions  $n = 9, 12, 14$  and  $16$  rps. The biggest difference is observed between the lowest propeller revolution  $n=9$  and the higher propeller revolutions  $n=12, 14, 16$  Hz. The reason for this can be that the surface tension scale effects might influence the results. As it was mentioned before, according to Shiba (1953) the influence of Weber number disappears above the so-called minimum Weber number, which is approximately 180. For our experiments a Weber number larger than 180 corresponds to a propeller speed  $n \geq 13$  rps, meaning that for the 9 and 12 rps tests, surface tension related scale effects might influence the results.

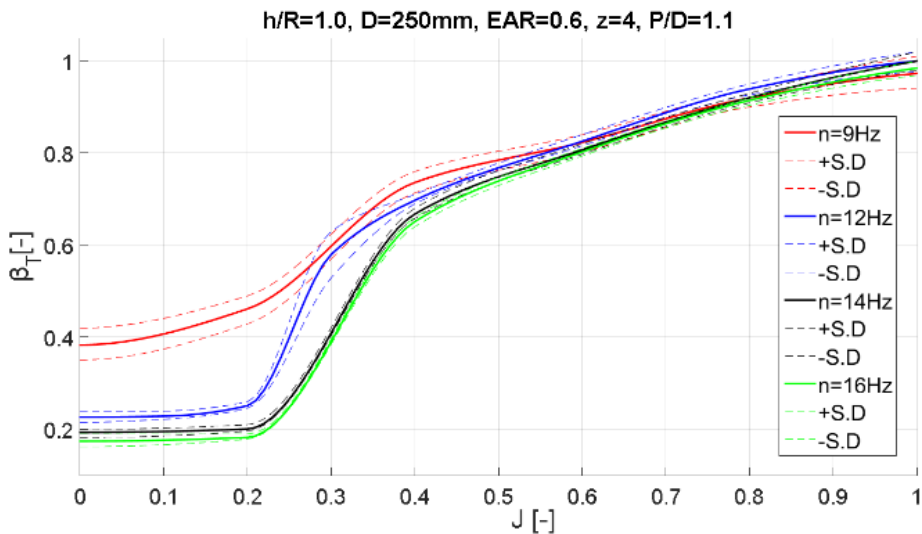


Figure 3-10 Total thrust loss factor vs.  $J$  value for propeller submergence ( $h/R=1.0$ ) based on experimental values.

Figure 3-11 shows total thrust loss factor vs. advance number for tests performed in calm water at immersion ratio  $h/R = 0.5$  for different propeller revolutions  $n = 9, 12, 14$  and  $16$  rps. It is observed the same phenomena here, that the biggest difference occurs for the lowest propeller revolution  $n=9\text{Hz}$  and  $n=12, 14, 16$  Hz.

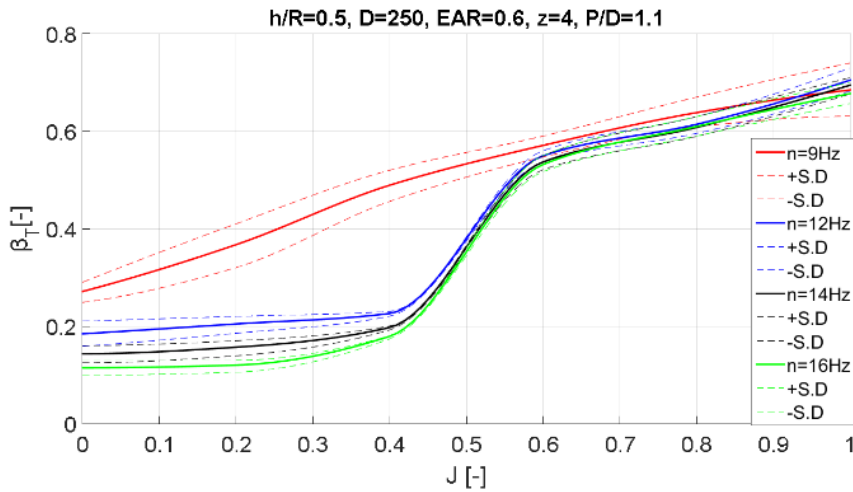


Figure 3-11 Total thrust loss factor vs.  $J$  value for propeller submergence  $h/R=0.5$  based on experimental values.

Figure 3-12 shows total thrust loss factor vs. advance number for tests performed in calm water at immersion ratio  $h/R = 0$ . For high advance numbers i.e.  $J=1.0$  it is observed no ventilation on the submerged part of propeller, thus  $\beta_{VC} = 1$ , and the total thrust loss factor is only due to out-of-water effect. The same phenomena it is observed for propeller submergence  $h/R=0.5, -0.5, 1.0$ .

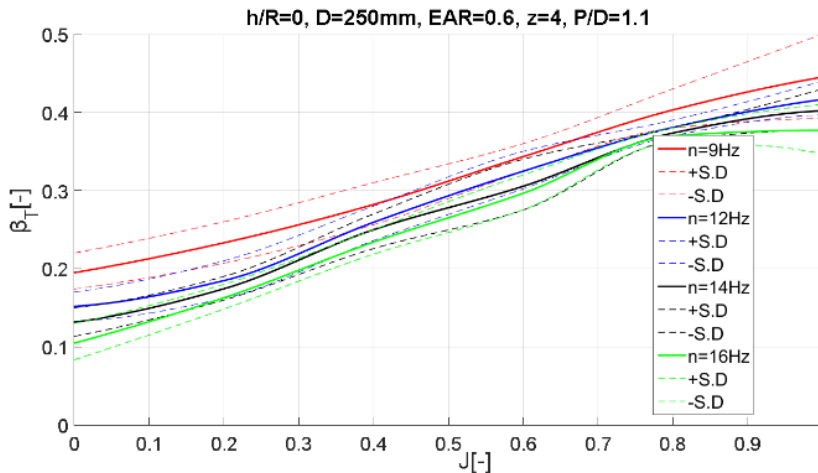


Figure 3-12 Total thrust loss factor vs.  $J$  value for propeller submergence  $h/R=0$  based on experimental values.

Figure 3-13 shows total thrust loss factor vs. advance number for tests performed in calm water at immersion ratio  $h/R = -0.5$ .

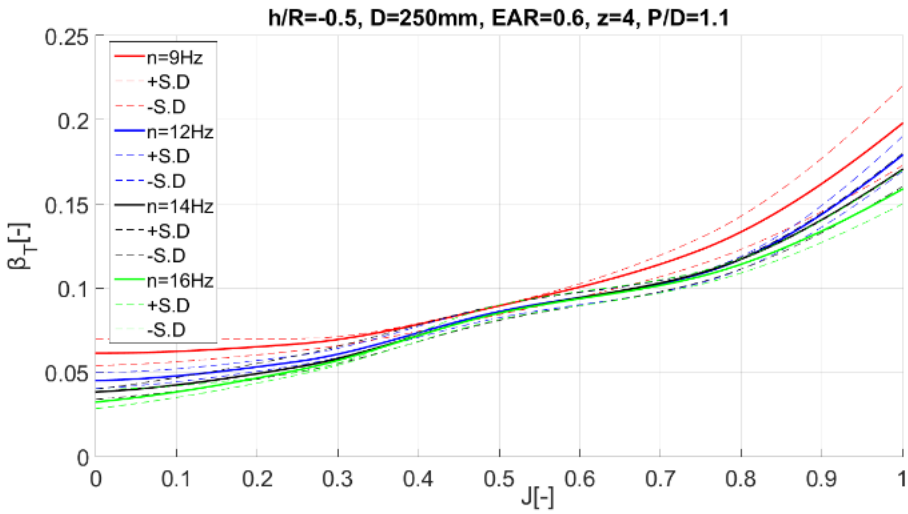


Figure 3-13 Total thrust loss factor vs.  $J$  value for propeller submergence  $h/R = -0.5$  based on experimental values.

Figure 3-14 combines the results shown in the previous plots to show total thrust loss factor as a function of advance number  $0 \leq J \leq 1.0$  and different submergences  $0 \leq h/R \leq 2.0$  for tests performed in calm water.

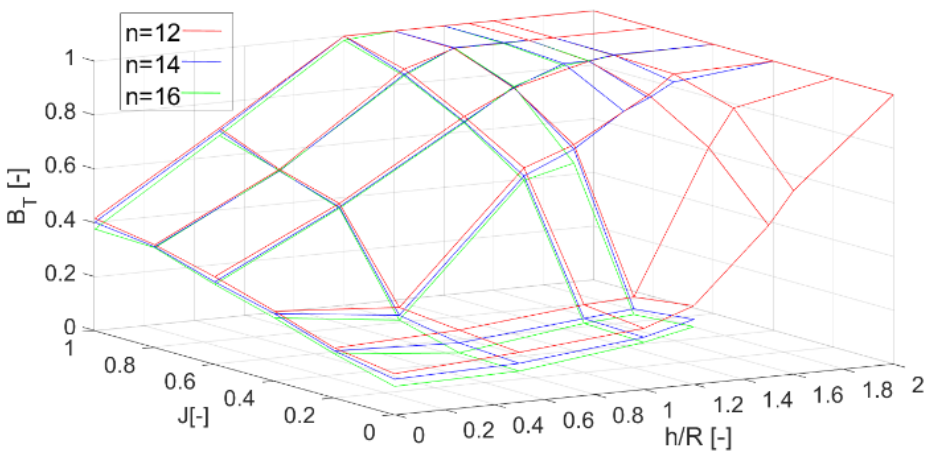
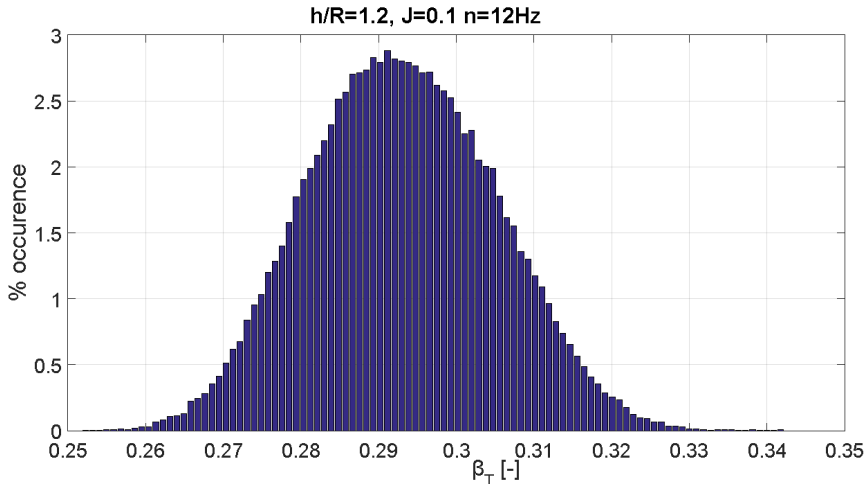


Figure 3-14 3D plot of total thrust loss factor vs.  $J$  value and propeller submergence  $h/R$  based on experimental values.



A histogram for super critical ventilation regime for  $h/R = 1.2$  is shown in *Figure 3-15*. Histograms summarize variations for the whole period of measurements. As mentioned before, the standard deviation about mean for the supercritical ventilation regime is relatively low.



*Figure 3-15* Histogram of total thrust loss factor for advance number  $J=0.1$ ,  $h/R=1.2$ , super-critical regime.

*Figure 3-16* and *Figure 3-17* shows histograms of total thrust loss factor for propeller operating in unstable ventilation regime. For  $h/R = 1.2$  two different thrust losses were observed for the same experimental conditions, indicating that the flows is “switching” between the two different states of ventilation.

It can see from the histogram that the thrust loss variations in time for the same experiments conditions are higher for unstable regime than for super-critical regime.

*Figure 3-18* shows histograms of total thrust loss factor for propeller operating in sub-critical ventilation regime, where the propeller experienced very small ventilation. It can be seen that the thrust loss is low and with little variation.

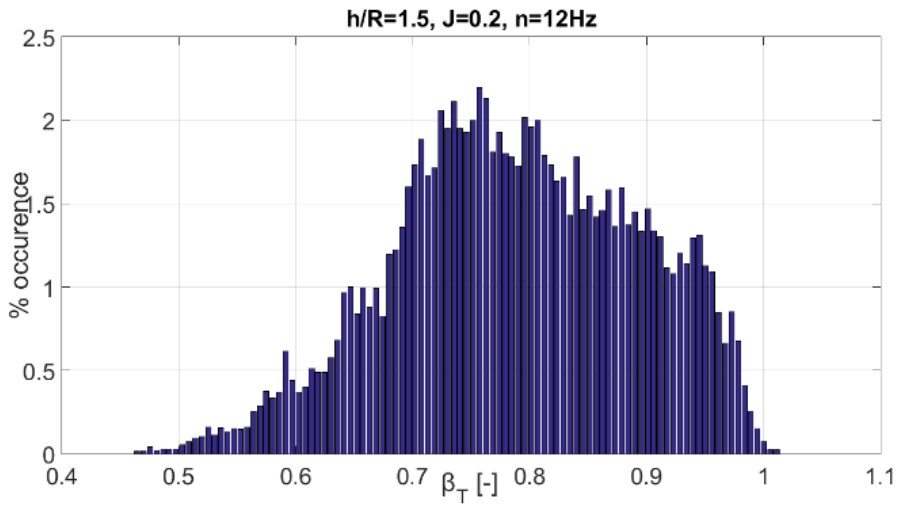


Figure 3-16 Histogram of total thrust loss factor for advance number  $J=0.2$ ,  $h/R=1.5$ , unstable regime.

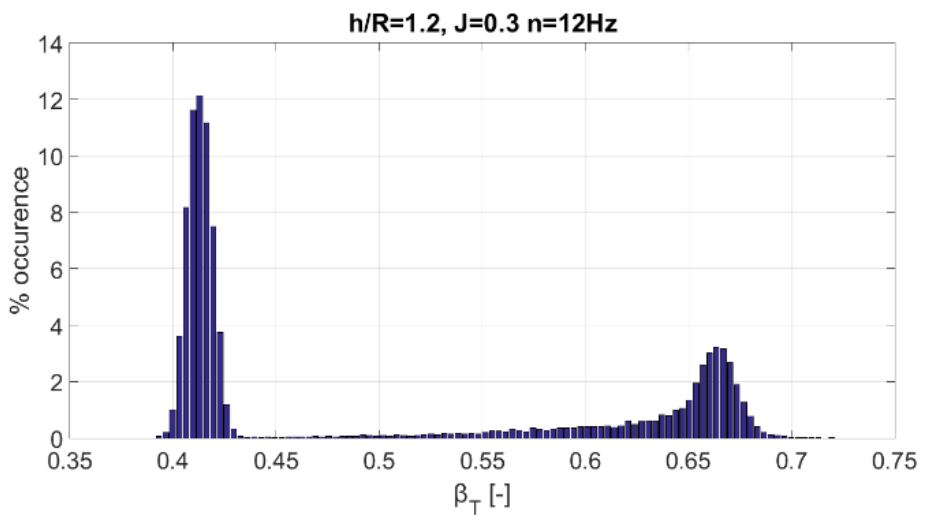


Figure 3-17 Histogram of total thrust loss factor for advance number  $J=0.3$ ,  $h/R=1.2$ , unstable regime.

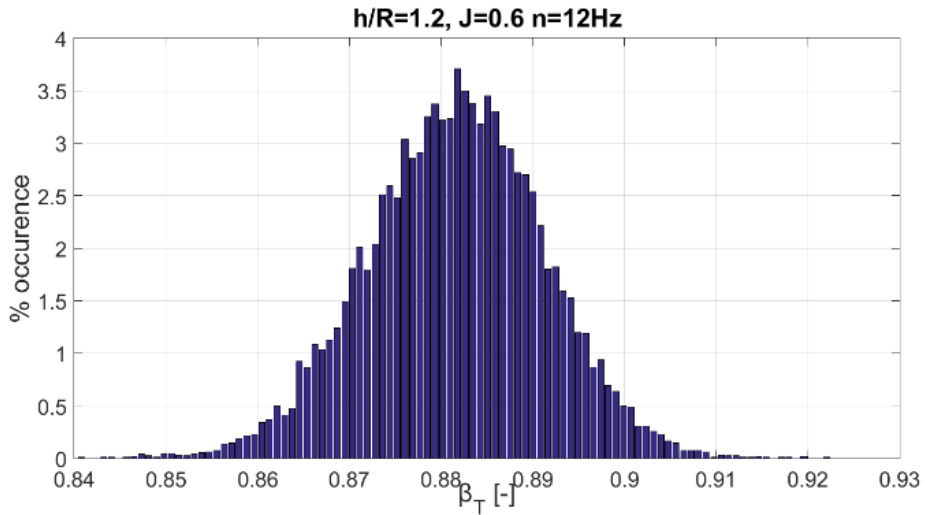


Figure 3-18 Histogram of total thrust loss factor for advance number  $J=0.6$ ,  $h/R=1.2$ , sub-critical regime.

As seen from the histograms the ventilation by vortex formation has a dynamic effect, which is connected with propeller loading. When the propeller starts ventilating, the thrust drops, propeller load factor  $c_T$  drops, and then the amount of ventilation changes. Thus, the ventilation can come and go during constant experimental conditions due to the dynamically changed propeller load factor.

### 3.5 KOZ10

#### 3.5.1 Test Description (set up, test matrix, filter)

The experiments were conducted in the large towing tank at The Marine Technology Centre. The four bladed right handed propeller P1440 was mounted on the open water test rig. A picture of the test set-up is shown in *Figure 3-19*. A novel blade dynamometer (2<sup>nd</sup> version) capable of measuring 5 degrees of freedom forces and moments (centrifugal force not measured) on a single propeller blade was used during these experiments. Use of high speed video cameras (one under and one above water) gave a visual understanding of ventilation phenomena.

Experiments were conducted for four submergence ratios  $h/R=2.5$ , 1.5, 1 and 0. For all four submergences the carriage speed was varied in order to obtain the following advance numbers ( $J=0$ , 0.15, 0.3, 0.45, 0.6, 0.75, 0.9, 1.05, 1.2). Propeller revolution speed was

constant and equal to 18 Hz. CFD calculations were performed for two propeller submergences  $h/R=2.5$ , 1.5 and nine propeller advance numbers ( $J=0.001$ , 0.15, 0.3, 0.45, 0.6, 0.75, 0.9, 1.05, 1.2). The main focus of this work was to improve numerical methods. Two existing in-house codes, the potential flow method *ISThydro* and the RANS method *FreSCO<sup>+</sup>* were improved in order to obtain more accurate modeling of the flow around the propeller. The CFD calculations presented in this thesis is based on *FreSCO<sup>+</sup>*.

*Figure 3-19* shows the co-ordinate system used for both experimental and numerical results.

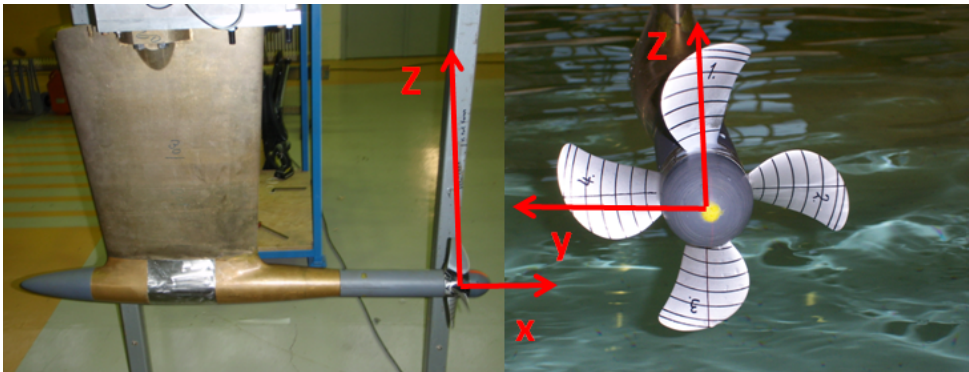


*Figure 3-19* Co-ordinate system - used for comparison between calculations and experiments

In order to capture the dynamics a high sampling frequency of 1200 Hz was used during these experiments. The power spectrum of blade thrust for raw data from experiments is plotted in *Figure 3-17* below, where the peaks due to propeller loads and due to noise can be noticed. A low-pass filter with a cut-off frequency of 160Hz was applied. *Figure 3-20* shows that the dominant frequency is the propeller shaft frequency. This is to be expected, since it is the blade thrust that is analyzed, not the propeller thrust.

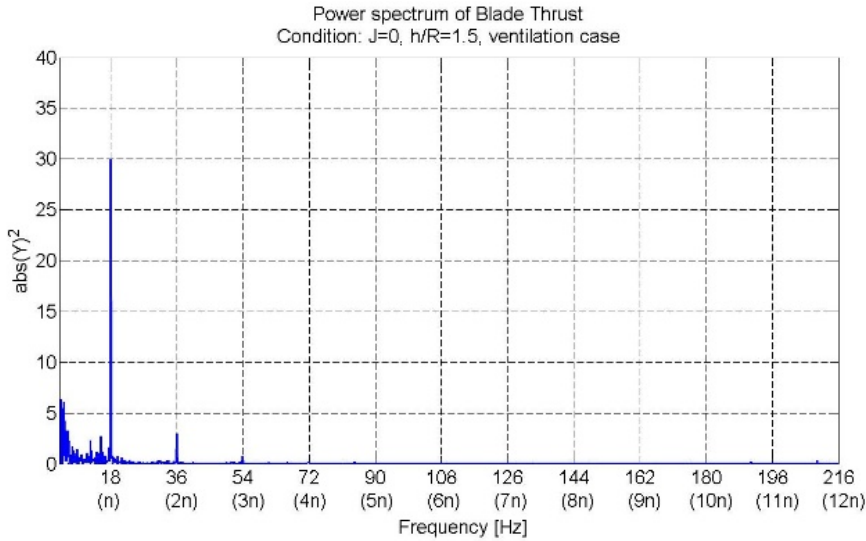


Figure 3-20 Power spectrum of unfiltered blade thrust during ventilation, *Koz10*

### 3.5.2 Main Results - *Koz10*

The obtained results are presented in the form of blade thrust and torque loss factors as a function of blade angular position. *Figure 3-21* shows the thrust and torque coefficients of the propeller blade in non ventilating, deep water conditions ( $h/R=2.5$ ). Experimental data from the towing tank tests with blade dynamometer are compared with tests using the normal propeller dynamometer, described in section 3.4.1. The comparison is satisfactory although experimental results denoted: *Koz10* and CFD calculations overpredicted the thrust and torque compared with the open water tests in the cavitation tunnel. The thrust and torque values from the conventional open water test has been divided by four to yield single blade values.

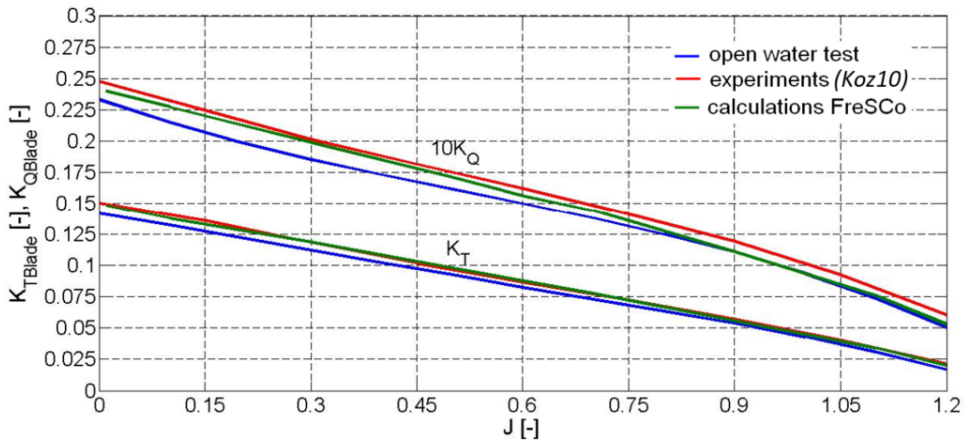


Figure 3-21 Deep water thrust and torque coefficients of a single blade.

Table 3-8 below show the occurrence for blade ventilation during the experiments. For  $h/R=1.5$  it is observed ventilation for high propeller loading up to  $J$  value equal to 0.45, for  $h/R=1.0$  the propeller ventilation stops for  $J$  value equal to 0.9. For  $h/R=2.5$  there is no ventilation observed. In Section 4.10 on the page 104 experiments were compared with CFD calculations for  $h/R=2.5$  and  $h/R=1.5$ .

	$h/R=2.5$	$h/R=1.5$	$h/R=1.0$
$J=0$	No ventilation	Ventilation	Ventilation
$J=0.15$	No ventilation	Ventilation	Ventilation
$J=0.3$	No ventilation	Ventilation	Ventilation
$J=0.45$	No ventilation	No ventilation	Ventilation
$J=0.6$	No ventilation	No ventilation	Ventilation
$J=0.75$	No ventilation	No ventilation	Ventilation
$J=0.9$	No ventilation	No ventilation	No ventilation
$J=1.05$	No ventilation	No ventilation	No ventilation
$J=1.2$	No ventilation	No ventilation	No ventilation

Table 3-8 Occurrence of ventilation during experiments, Koz10.

**Propeller ventilation ( $h/R=1.5$ ) and ( $h/R=1.0$ )**

*Figure 3-22* and *Figure 3-23* below show the thrust loss due to ventilation as a function of blade position for different advance numbers. The total thrust loss factor is denoted by the symbol  $K_T/K_{T0}$  in this section, for the other part of the thesis it is  $\beta_T$  index symbol used to describe the same total thrust loss factor. The propeller revolution was constant and equal to  $n=18\text{Hz}$ . The experiments were compared with CFD calculations, see *Section 4.10 on the page 104*. During measurements presented in *Figure 3-22* and *Figure 3-23* for  $h/R=1.5$  and  $h/R=1.0$  it is observed different thrust losses depending on the time in the experiments. The different thrust losses correspond to different ventilation extent. It is clear from the experiments that in this condition, the propeller can be both fully and partially ventilating, and that it changes between the different ventilating conditions without apparent reason.

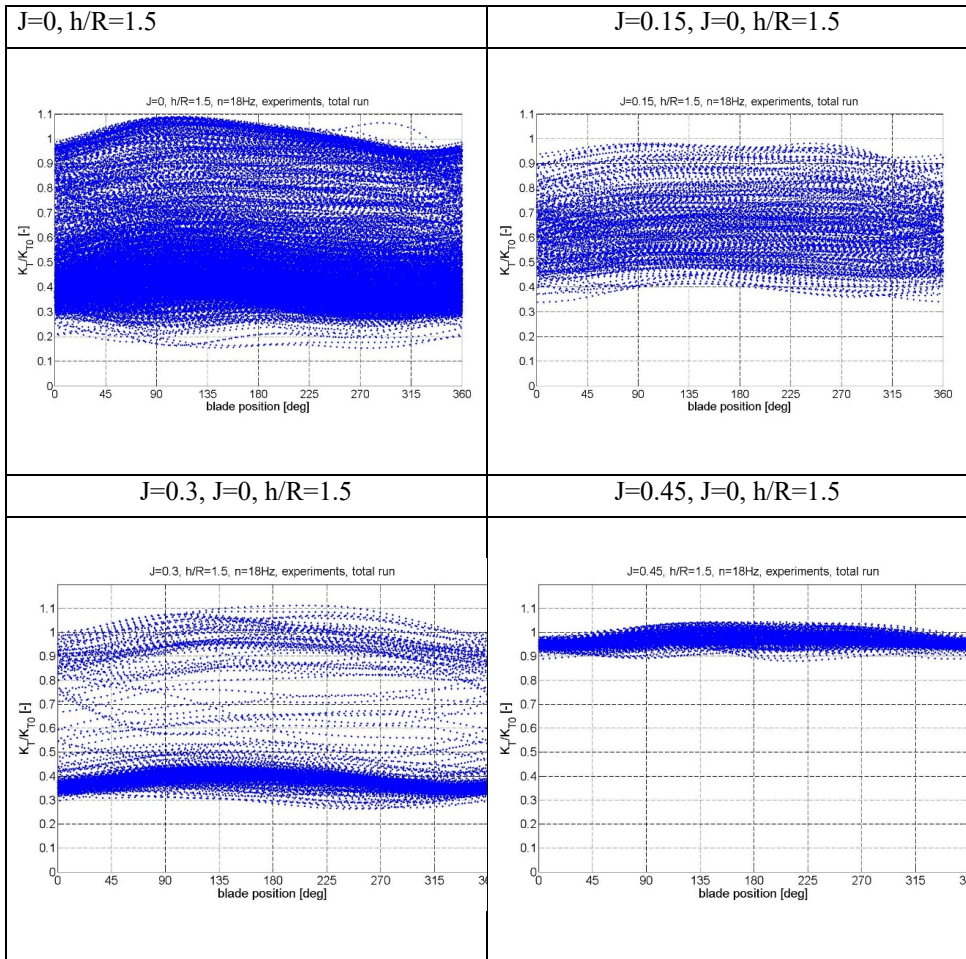


Figure 3-22 Total thrust loss factor as a function of blade position during each revolution for  $h/R=1.5$ .



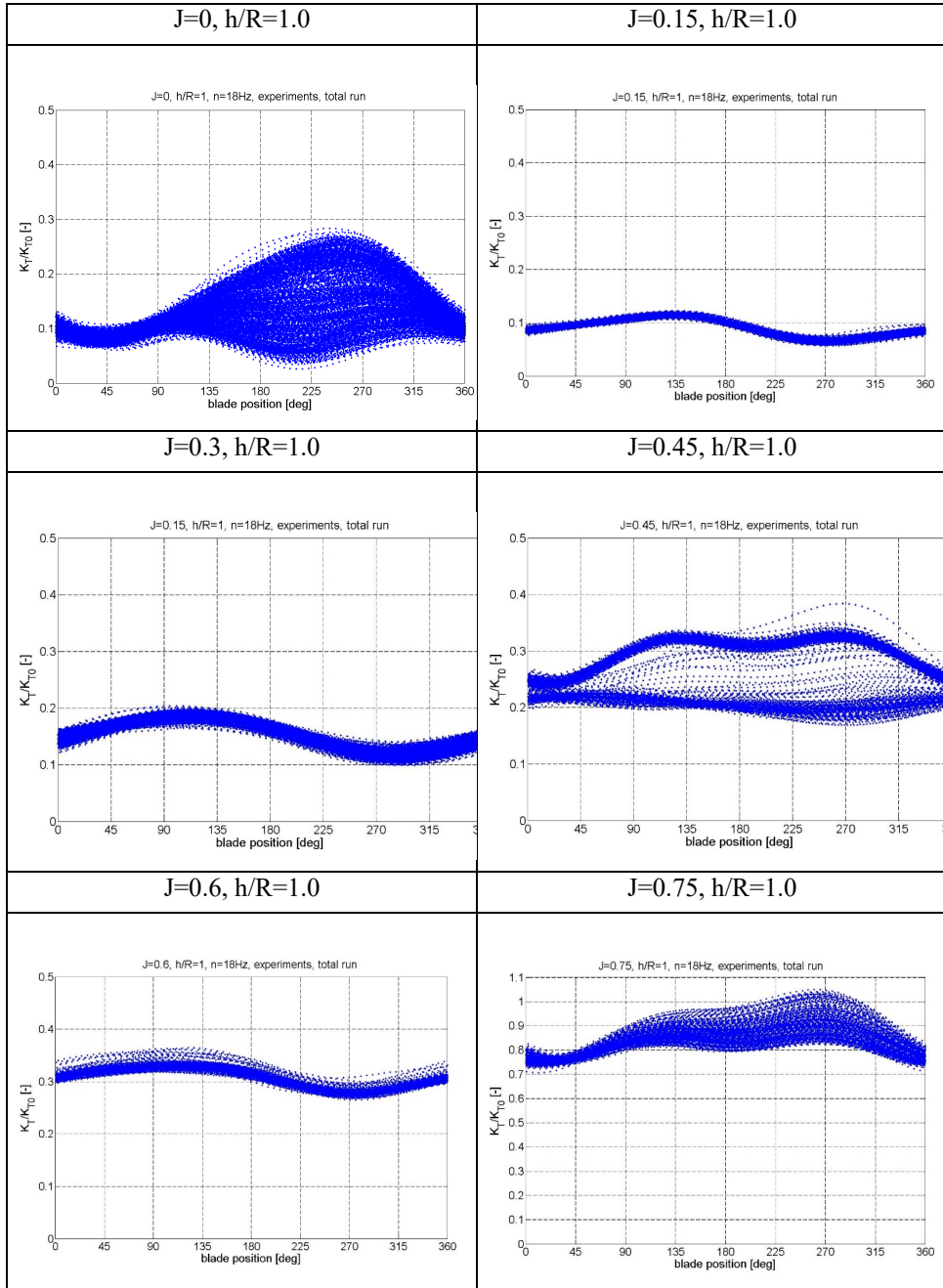
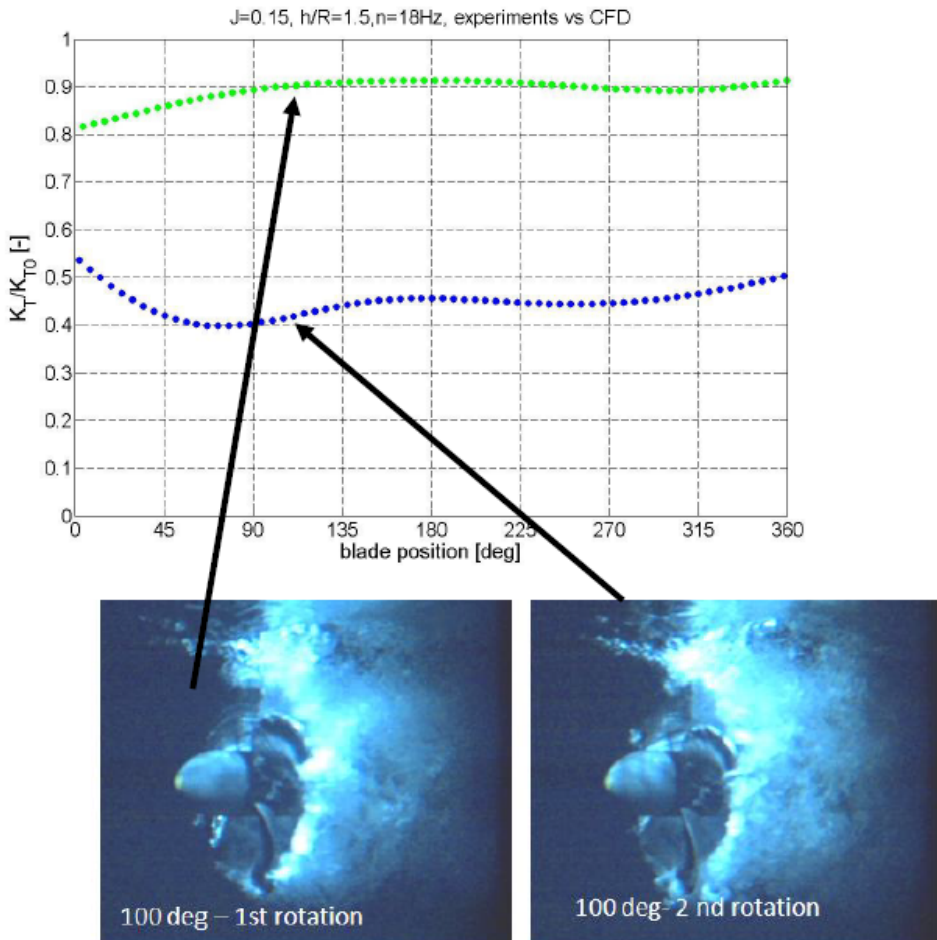


Figure 3-23 Total thrust loss factor as a function of blade position during each revolution for  $h/R=1.0$ .

It is also observed from the video that it is difficult to predict thrust loss based on the flow visualisation from the experiments. *Figure 3-24* shows a comparison between two different propeller rotations and the same blade position. The photos look very similar, a similar blade area is covered with air, but the blade thrust ratio is different for these two cases.



*Figure 3-24 Comparison between two different propeller rotations and the same blade position.*

## 3.6 *KOU10*

### 3.6.1 Test Description

The test campaign *Kou10* was published by Koushan et.al. (2011). The same propeller model (P1440) as for test campaign *Koz10* was used for the experiments. The tests were conducted using a model of a Rolls-Royce Azipull pulling thruster presented in *Figure 3-3*. Single propeller blade loading were measured used a novel developed blade dynamometer, the same as used for *Koz10* campaign. Test were conducted in the large towing tank at the Marine Technology Centre in calm water and two different propeller submergences  $h/R=2.5$  and  $h/R=1.0$ . Propeller revolution speed was constant and equal to  $18\text{ Hz}$ . For all four submergences, the carriage speed was varied in order to obtain the advance numbers in the range  $0 \leq J \leq 1.2$ .

### 3.6.2 Main Results

*Figure 3-25* shows thrust loss factor as a function of advance number in calm water for propeller immersion ratio  $h/R=1.0$ . Mean values as well as standard deviations about mean values are shown. It is observed from the *Figure 3-25* that above  $J=0.8$  ventilation stops and the measured thrust is close to values for deeply submerged case. A sudden drop in thrust is measured for the advance numbers  $0.4 \leq J \leq 0.8$ , where also the highest relative standard deviations are observed, see *Figure 3-26*.

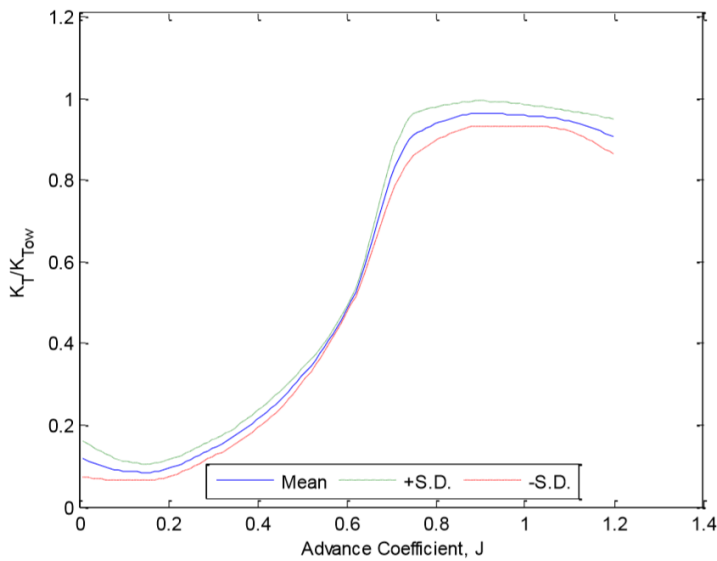


Figure 3-25 Thrust loss factor as a function of advance number in calm water for  $h/R=1.0$ ,  $n=18\text{Hz}$ , Mean and standard deviations are shown, Koushan et.al. (2011), ventilation loss factor is denoted by the symbol  $K_T/K_{Tow}$  for the other part of the thesis it is  $\beta_T$  index symbol used to describe the same total thrust loss factor.

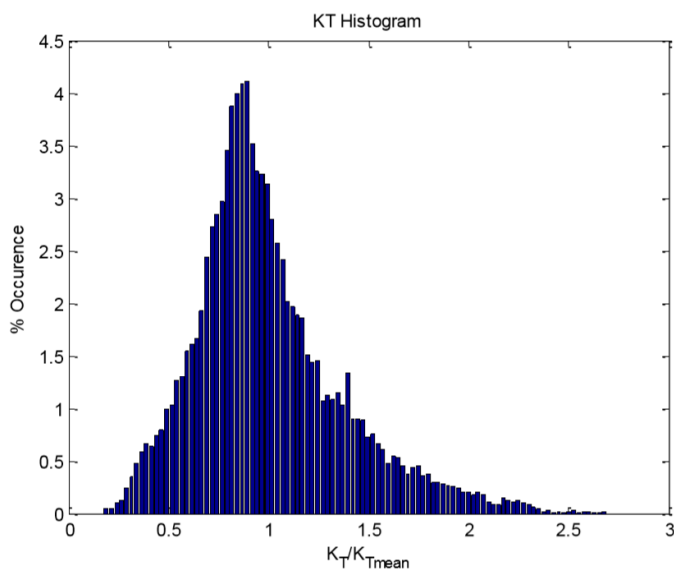


Figure 3-26 Histogram for total thrust loss factor for  $J=0.6$ ,  $h/R=1.0$ ,  $n=18\text{Hz}$ , Koushan et.al. (2011).

### 3.7 KOZ09

#### 3.7.1 Test Description (set up, test matrix, filter)

The experiments were performed by Kozłowska and Califano. The main motivation for these experiments was to monitor the time for ventilation to be established. These experiments were performed in the Marine Cybernetics Laboratory having dimensions (length  $\times$  breadth  $\times$  depth) of 40m $\times$ 6.45m  $\times$  1.5m. The propeller P1374 was used in open pulling condition, mounted on the azimuthing thruster model described in section 3.3 and shown in *Figure 3-1*. The blade dynamometer was the same as used for *Koz10* and *Kou10* experimental campaigns. The experiments were conducted at submergence ratios  $1.0 \leq h/R \leq 2.9$  in the Marine Cybernetics Laboratory. The carriage speed  $U$  and the propeller shaft frequency  $n$  has been combined in order to obtain advance numbers  $J$  around 0.1, see *Table 3-9*

$U$ [m/s]	$n = 12$ rps	$n = 14$ rps	$n = 16$ rps
0.3	$J=0.100$	$J=0.086$	$J=0.075$
0.35	$J=0.117$	$J=0.100$	$J=0.088$
0.4	$J=0.133$	$J=0.114$	$J=0.100$

*Table 3-9 Tested conditions for propeller submergences  $1.0 \leq h/R \leq 2.9$*

During measurements, images were acquired with a high speed camera at sampling frequency range between 160 and 480 Hz, depend on the test conditions. Power spectrum of unfiltered blade thrust during ventilation is presented in *Figure 3-27*.

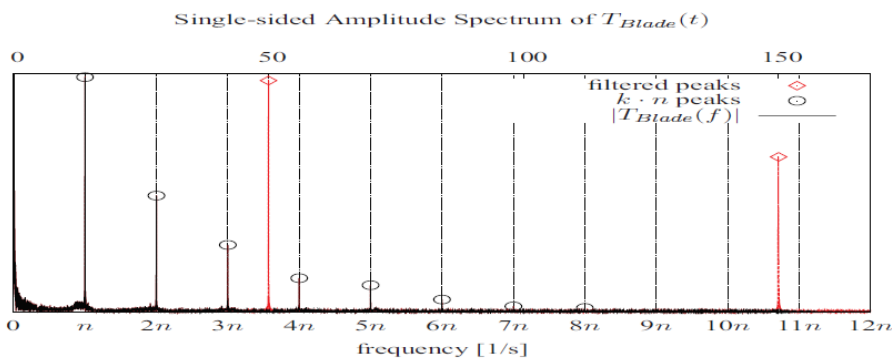


*Figure 3-27 Power spectrum of unfiltered blade thrust during ventilation, experiments Koz09 published by Califano (2010).*

### 3.7.2 Main Results

Koz09 tests focus on the thrust loss due to blade position for low advance number (around 0.1) at different propeller revolutions ( $n=12, 14$  and  $16\text{Hz}$ ). Figure 3-28 shows the thrust loss as a function of blade position for  $h/R=1.56$  and  $J=0.75$ . Figure 3-29 shows the thrust loss as a function of blade position for  $h/R=1.48$  and different propeller revolutions ( $n=12, 14$  and  $16\text{Hz}$ ). Total thrust loss factor is denoted by the symbol  $K_T/K_{T0}$  for the other part of the thesis it is  $\beta_T$  index symbol used to describe the same total thrust loss factor.

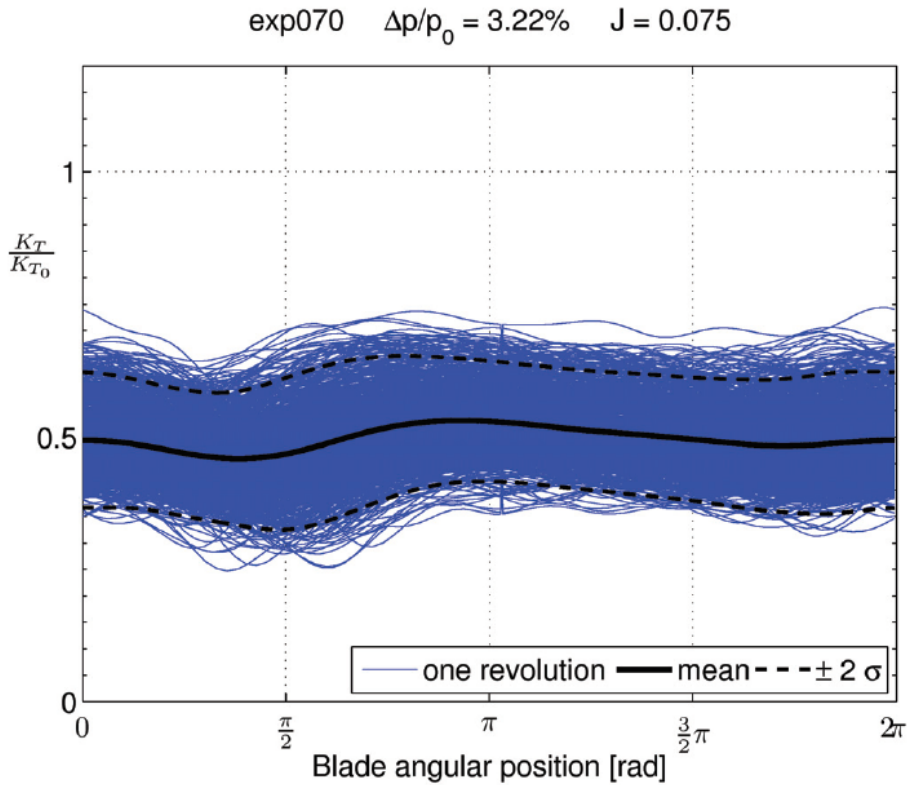


Figure 3-28 Total thrust loss factor  $K_T/K_{T0}$  as a function of blade position for  $h/R=1.48$  and  $n=16\text{Hz}$ , Califano (2010).

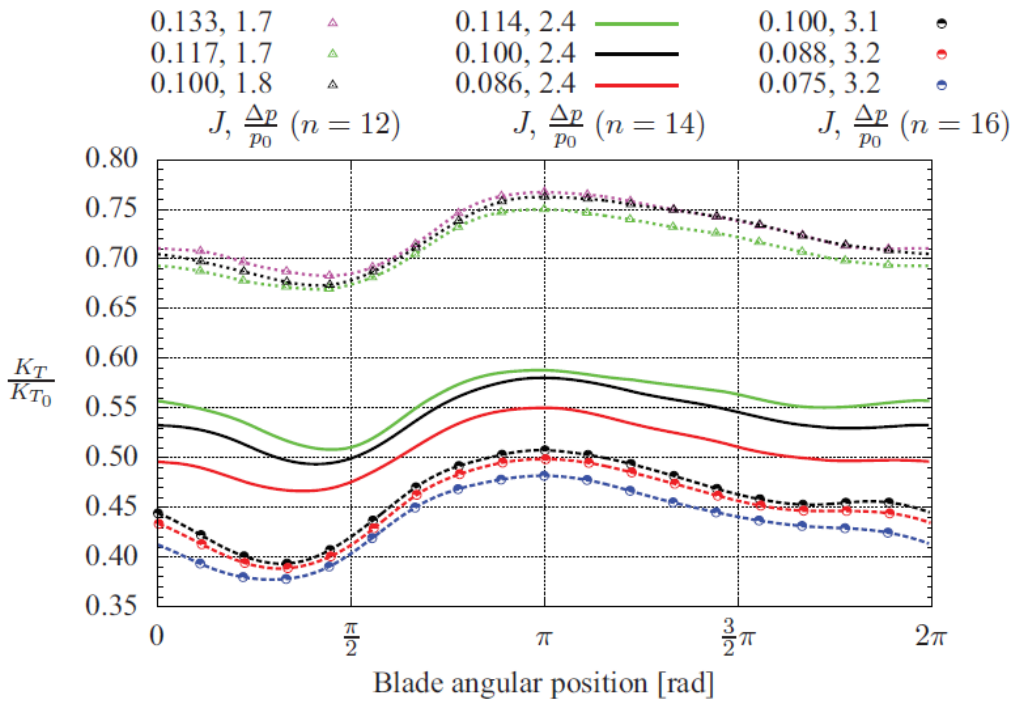


Figure 3-29 Total thrust loss factor  $K_T/K_{T0}$  for each blade angular position ( $h/R=1.48$ ), Califano (2010).

### 3.8 KOZ08

#### 3.8.1 Test Description (set up, test matrix, filter)

Model tests of the four bladed propeller P13174 were conducted in the large towing tank at the Marine Technology Centre. The main objective for the test was to check if slamming loads might occur for surface piercing propellers. Therefore, the tests were performed at extremely high propeller pitch,  $P/D=15$  and  $P/D=7$ , which corresponds to angles equal to  $8$  and  $18$  deg between the blade and free surface, see Figure 3-32. Three different propeller positions were investigated in the experiment: propeller was half immersed (The shaft was at the free surface position) and propeller hub was up/down  $30\text{mm}$  from the free surface, see Figure 3-30 and Figure 3-31. For all submergences, the propeller revolution speed ( $n=5, 8, 9, 10, 11$  &  $15$ ) and forward speed (up to  $8\text{m/s}$ ) were varied in order to obtain different loading conditions.

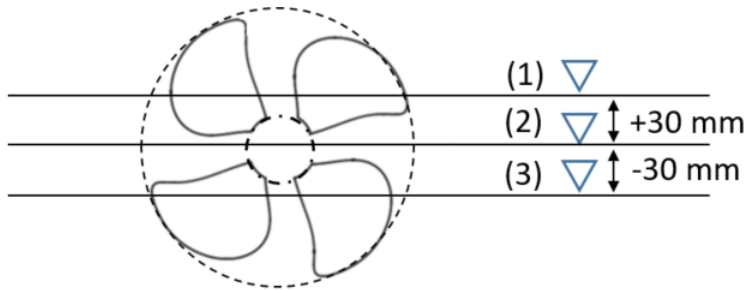


Figure 3-30 Illustration of three different propeller position acc. to free surface : propeller is half immersed, propeller hub is 30 mm down to FS, propeller hub is 30mm up to FS.



Figure 3-31 Three different propeller position acc. to free surface : propeller is half immersed (middle), propeller hub is 30 mm down to FS (right), propeller hub is 30mm up to FS (left).



Figure 3-32 Propeller pitch,  $P/D=15$  (left) and  $P/D=7$  (right), which correspond to angle equal to 8 and 18 deg between blade and free surface.



### 3.8.2 Main Results

Results obtained by *Koz08* were addressing the slamming hypothesis and is presented in Chapter 7, together with a review of the results of the experiments made by Mork (2007) of a one-bladed propeller.

## 3.9 KOU2006\_I AND KOU2006\_II

### 3.9.1 Test Description (set up, test matrix, filter)

The experiments were conducted in the Marine Cybernetics Laboratory. The same propeller model (*PI374*) was used for open pulling *Kou2006\_I* and ducted pushing *Kou2006\_II* configurations. In order to capture the dynamics a high sampling frequency was used during the experiments. Blade axial, radial, tangential forces and moments about all three axes were measured during the experiments. A pulse meter provided propeller rate of revolutions as well as indicating the angular position of the reference blade. For more detailed description see Koushan (2006 a, b, and c) or Kozłowska et.al. (2009).

Tested conditions are summarized in *Table 3-10* and *Table 3-11*. Submergence ratios for open propeller was summarized in *Figure 3-33*.

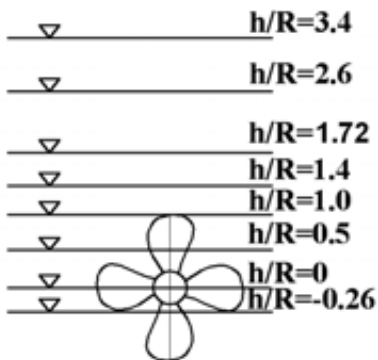


*Figure 3-33 Submergence ratios for open propeller, Kou2006\_I.*

Open propeller		Ducted propeller	
h/R [-], static condition			
<i>Kou 2006_I</i>		<i>Koz09</i>	<i>Kou 2006_II</i>
-0.26		1.6	0
0		1.68	1
0.5		1.76	2
1.0		1.84	2.4
1.72		1.92	
2.6		2	
3.4			

Table 3-10 Test conditions for open and ducted propeller and low advance numbers (around 0.1), static conditions.

Open propeller				Ducted propeller			
h/R [-], dynamic condition (heave motion)							
h/R		amplitude	period	h/R		amplitude	period
min	max	[-]	[s]	min	max	[-]	[s]
-0.25	2.15	2.15	2	-0.92	0.88	1.8	2
1.1	3.25	2.15	2	0.08	1.88	1.8	2
2.2	3.3	1.1	2	0.93	2.03	1.1	2
-0.25	2.15	2.15	4	-0.92	0.88	1.8	4
1.1	3.25	2.15	4	0.08	1.88	1.8	4

Table 3-11 Tested conditions for open and ducted propellers with dynamic heave motions.

The power spectrum of blade thrust for the raw data from experiments is plotted in Figure 3-34. It was observed during experiments (*Koz09*, *Kou\_2006\_I* and *Kou\_2006\_II*) that the dominant frequency is the propeller shaft frequency both for non-ventilating and fully ventilating cases, which is as expected since blade thrust is studied.

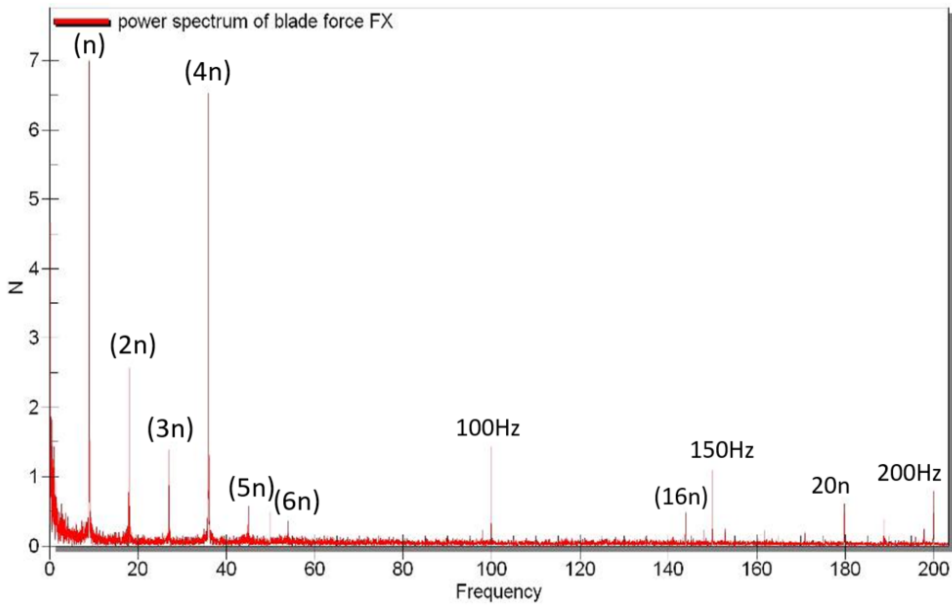


Figure 3-34 Power spectrum of blade thrust,  $n=9\text{Hz}$ , ventilation phase, Kou\_2006\_I.

### 3.9.2 Main Results

In this thesis the results from *Kou2006\_I* and *Kou2006\_II* has been used for comparison between ventilation in static and dynamic condition (heave motion) for both open and ducted propeller and for estimation of the mean thrust loss due to ventilation and out of water effect. As the result, a new formulation of the relations between ventilation and thrust losses was developed, see Kozłowska and Steen (2010). *Kou2006\_I* results were also used for comparison between time-domain simulation model for propeller forces due to vortex ventilation in static and dynamic condition, see Chapter 6 in this thesis. The time-domain simulation model was originally developed by Dalheim (2015) and updated by Kozłowska et.al. (2017) by including a physical model for estimating ventilated blade area based on propeller loading. In *Figure 3-35* the total thrust losses are plotted as a function the submergence ratio and the shaft speed for bollard condition. *Figure 3-36* and *Figure 3-37* present the photographs for different ventilation regimes with respect to time for bollard condition.

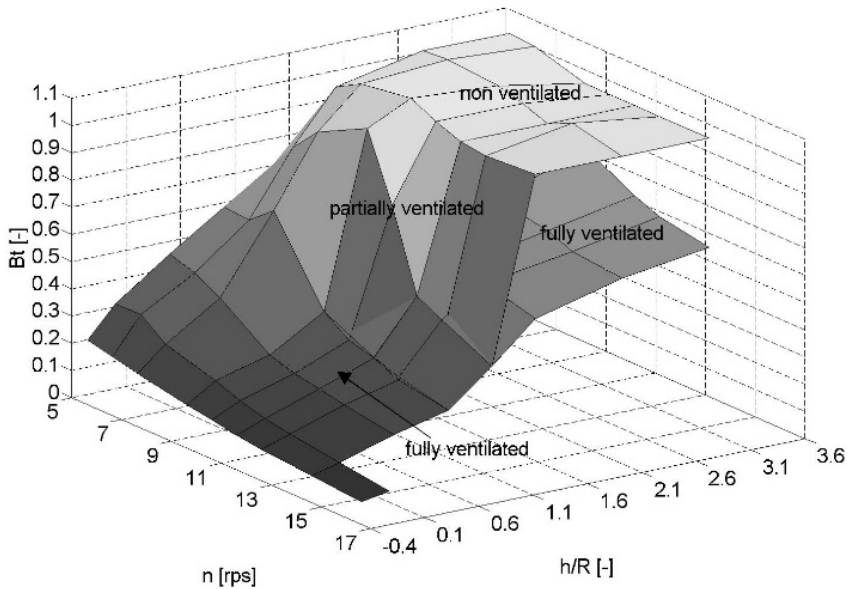


Figure 3-35 Mean total thrust loss factor as a function of submergence and shaft speed for bollard condition, open propeller. It includes both non ventilated and fully ventilated case, Kozłowska et.al. (2009).

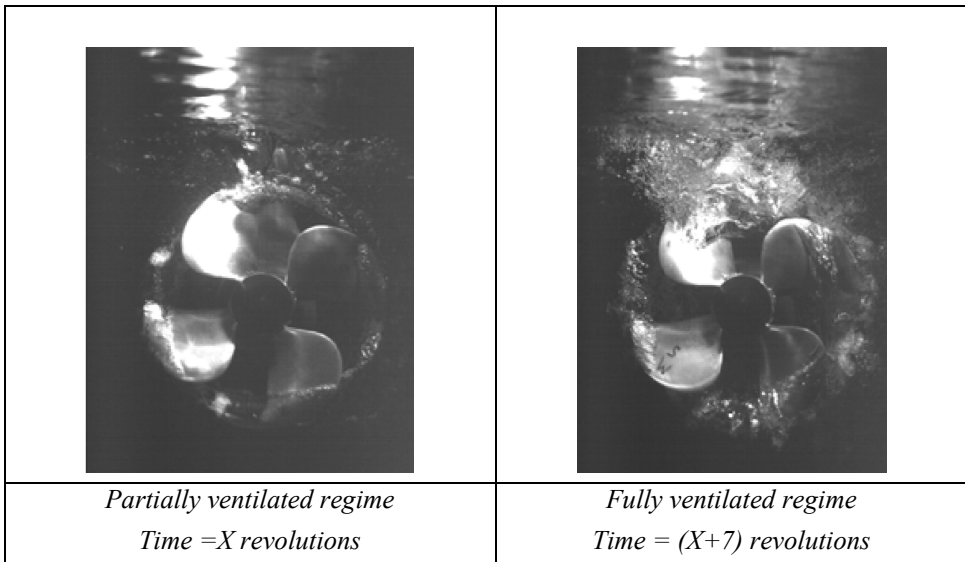


Figure 3-36 Different ventilation regimes for  $h/R=1.4$ ,  $n=9\text{Hz}$ , bollard condition, Kozłowska et.al.(2009).

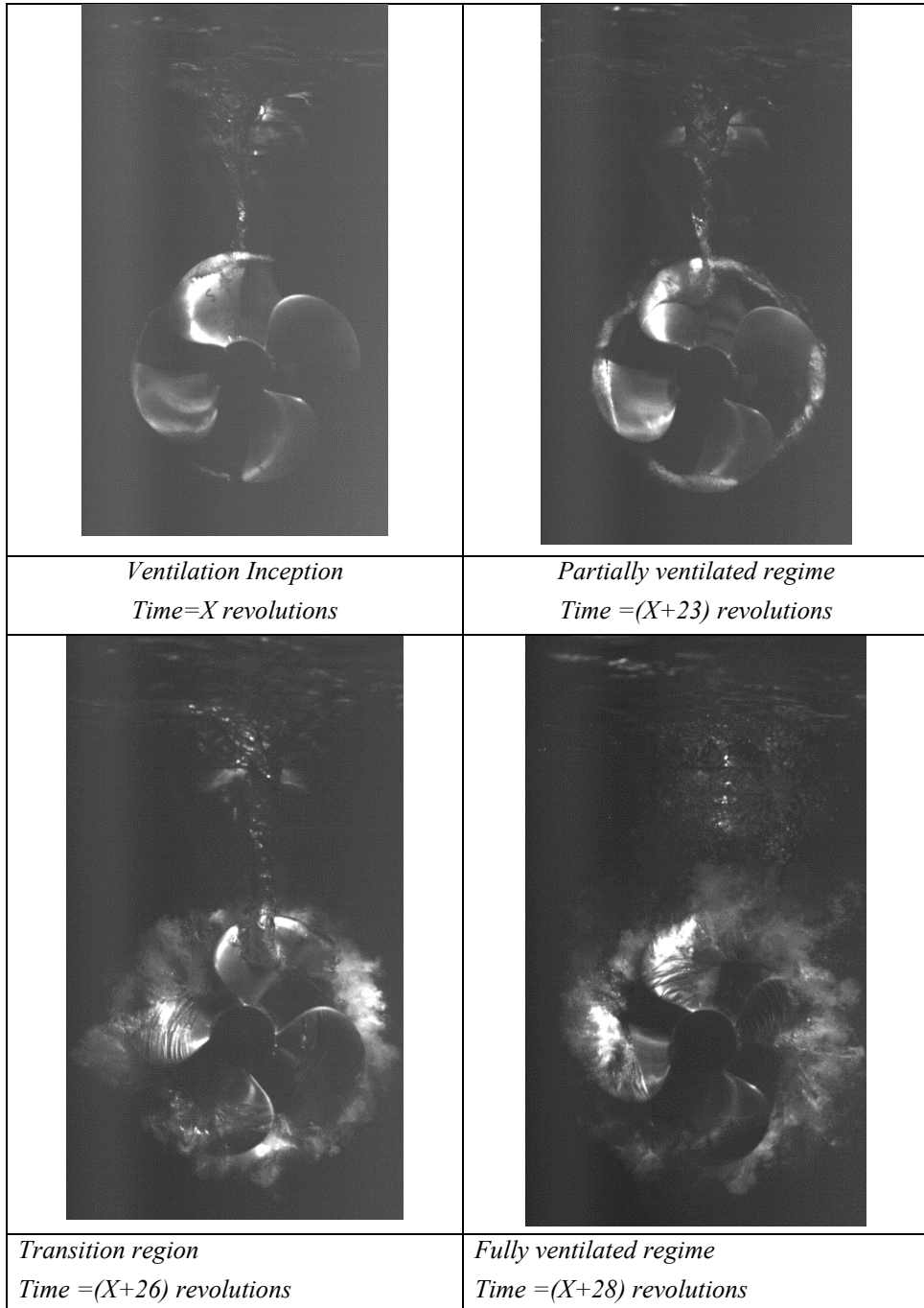


Figure 3-37 Different ventilation regimes for  $h/R=2.6$ ,  $n=14\text{Hz}$ , bollard condition, Kozłowska et.al.(2009).

## 4 EXPERIMENTAL RESULTS

This chapter presents the experimental results for ventilated propeller and the important findings from the analysis.

The influence of several factors i.e. type of propeller (open and ducted), advance numbers, propeller revolutions, submergences and time and their effect on ventilation inception and thrust loss is discussed.

The comparison between the ventilation for static condition (constant submergence) and dynamic condition (heave motion) as well as discussion of the influence of heave motion parameters i.e. heave motion period for the ventilation inception and thrust drop related to this are presented. The main objective was to check the ventilation effect for thrust loss for constant immersion and under sinusoidal heave motion.

Propeller Hull Vortex Cavitation (PHVC) and Propeller Free Surface Vortex Ventilation mechanisms are also compared in this chapter.

Experimental data are used to show the boundary between the vortex forming, non vortex forming and free surface ventilation flow regimes.

The relation between the cavitating/ventilating vortex and the pressure in the core of a given vortex was investigated in order to define the vortex ventilation inception.

The comparison between model tests and numerical calculations is also included in this chapter. The comparison contains two main parts: comparison between blade forces and moments during non-ventilating and ventilating phase as well as comparison between flow visualization using high speed video (experiments) and CFD simulation. The comparison aim at identifying the degree of correlation and discuss reasons for deviation.

### 4.1 VENTILATION REGIMES AND CRITICAL ADVANCE NUMBERS (*KOZ17*)

*This section based on Koz17, Koz10 and Koz09 experimental data*

Based on experiments performed in the years (2006-2017), and published by Koushan (2006 I and II), Kozłowska et.al. (2009), Kozłowska and Steen (2010), Califano (2011\_a), Califano (2011\_b), Koushan et.al. (2011) and Kozłowska et.al. (2011) the ventilation inception is divided in two different mechanisms:

1. Ventilation starts by forming an air filled vortex from the free surface.
2. The free surface is sucked down to the propeller or it becomes surface piercing, so air can enter the suction side of the blades directly from the atmosphere.

*Ventilation mechanism 1* by vortex formation is for completely submerged propellers, typically for submergence ratios  $h/R$  within the range of  $1.2 \leq h/R \leq 3.4$ , where  $h$  is the submergence of the propeller shaft and  $R$  is the propeller radius. *Ventilation mechanism 1* mainly occurs for highly loaded propellers at low advance number. The vortex funnel can reach the surface quite far from the propeller disc, especially for large submergence ratios. It might be difficult to observe the vortex for small submergences because the blade crosses the vortex and partially destroys it, producing a lot of air bubbles which makes observation more difficult. *Ventilation mechanism 2* by sucking down free surface or become surface piercing is observed for propeller submergences lower than  $h/R < 1.2$ , as shown in *Figure 4-1*. Although ventilation is always connected to relatively high propeller loadings, this mechanism typically occurs for higher advance numbers and/or lower loadings than mechanism 1.

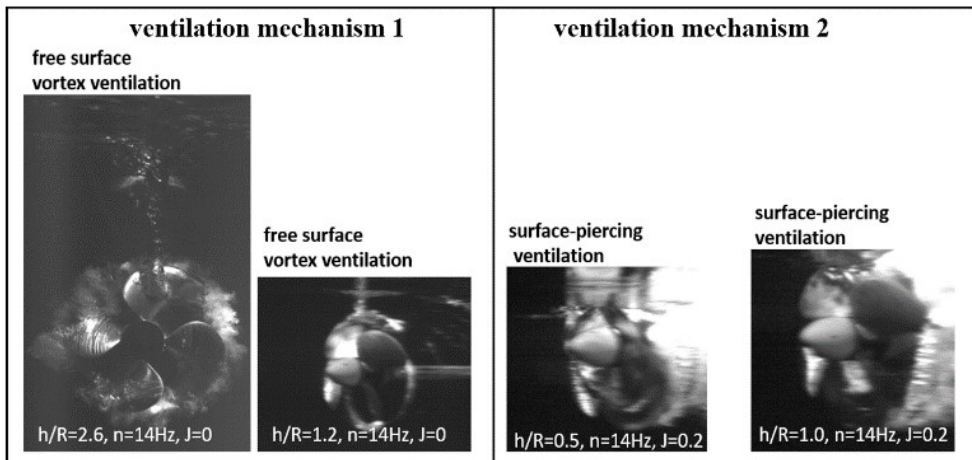


*Figure 4-1* Impact of the free surface vortex ventilation (*ventilation mechanism 1*) & surface-piercing ventilation (*ventilation mechanism 2*).

The propeller might be non-ventilated, partially or fully ventilated, depending on several factors, where submergence and advance number are clearly important. Olofsson (1996) divided these ventilation states into regimes illustrated in

*Figure 4-2*. Ventilation flow regimes were described in *Section 2.1.4*. The illustration presented as

Figure 4-2 was originally published in Olofsson (1996) and based on experiments with surface-piercing propellers. Thus, it was of interest to make a similar plot based on experiments with normal, non-ventilating propellers that are ventilating due to insufficient submergence. Such a plot has been made based on the three experimental campaigns listed *Koz17*, *Koz10* and *Koz09* and is shown in Figure 4-3. The main difference between these two plots is for non-ventilated and partially ventilated flow regimes. For submergences  $h/R \geq 1.4$  it is observed only two different flow regimes, Ventilation starts from the unstable regime (thus it is partially ventilated) and we do not observe the fully ventilated flow regime where the thrust loss is significant and stable.

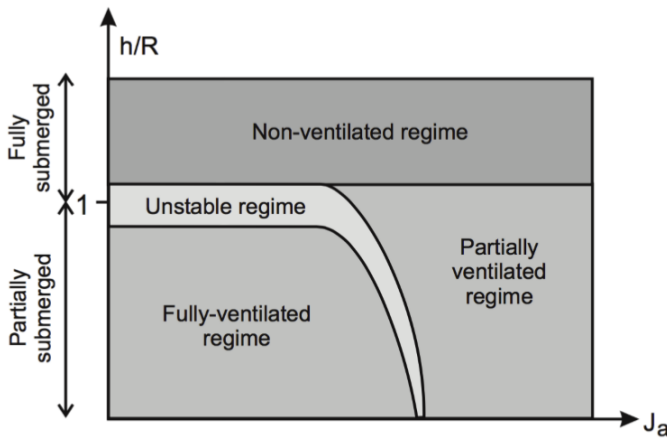


Figure 4-2 Ventilation flow regimes Olofsson (1996), surface piercing propellers.

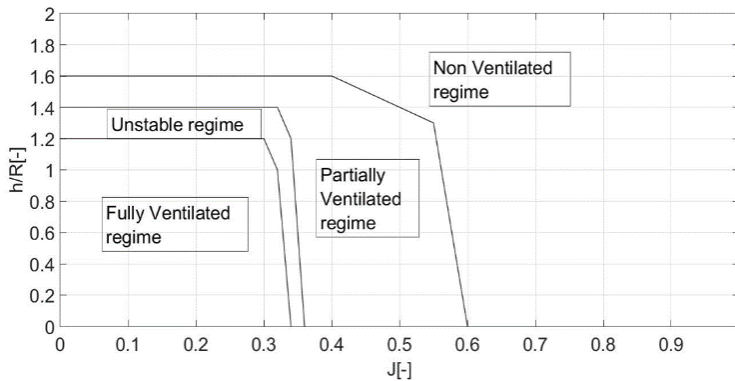
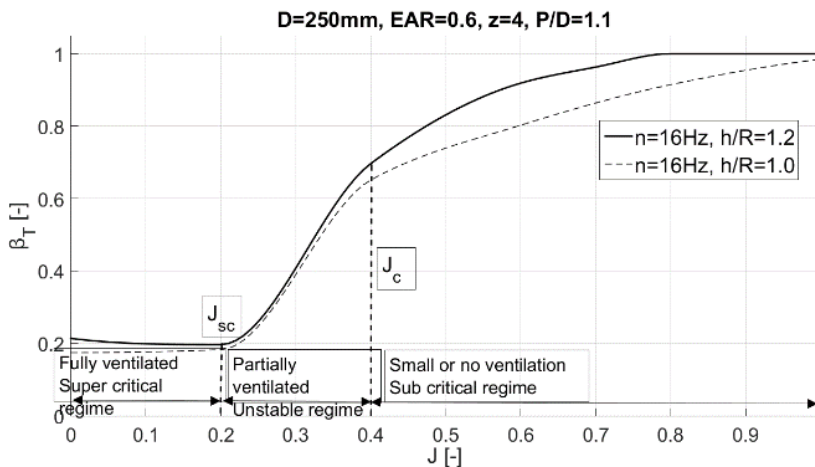


Figure 4-3 Ventilation flow regimes for a conventional propeller based on experiments *Koz17*, *Koz10* and *Koz09*.



Which of the three different flow regimes the propeller is operating in has a significant impact on the propeller thrust. In the fully ventilated regime when the propeller is highly loaded and fully ventilated, thrust loss is significant and quite stable, both in time and in the sense that a further reduction of the advance number does not change the propeller thrust coefficient  $K_T = T/\rho n^2 D^4$ . The advance number is below the super critical advance number  $J_{SC}$ . Above the super critical advance number  $J_{SC}$  and below the critical advance number  $J_C$  is the unstable regime, where the propeller is partially ventilated. This regime is characterized by large variation in time of the amount of ventilation and the amount of thrust loss. Above  $J_C$  is the sub critical regime, where the propeller is non ventilated or experiencing limited ventilation. For deeper submergences ( $h/R=1.5$ ,  $h/R=1.6$ ) it is observed only two different ventilation regimes, ventilation starts from the unstable regime at  $J=0$  and super critical ventilation regime is not observed, see *Figure 4-5*. Test results are presented in the form of total thrust loss factor  $\beta_T = K_T/K_{Tn}$  where  $K_{Tn}$  is the time-averaged mean value of the thrust coefficient at the relevant advance number  $J$  obtained from the calm water, deeply submerged non-ventilated propeller.



*Figure 4-4 Super critical, unstable and sub critical ventilation regime presented for  $h/R=1.0$  and  $1.2$ , Koz17.*

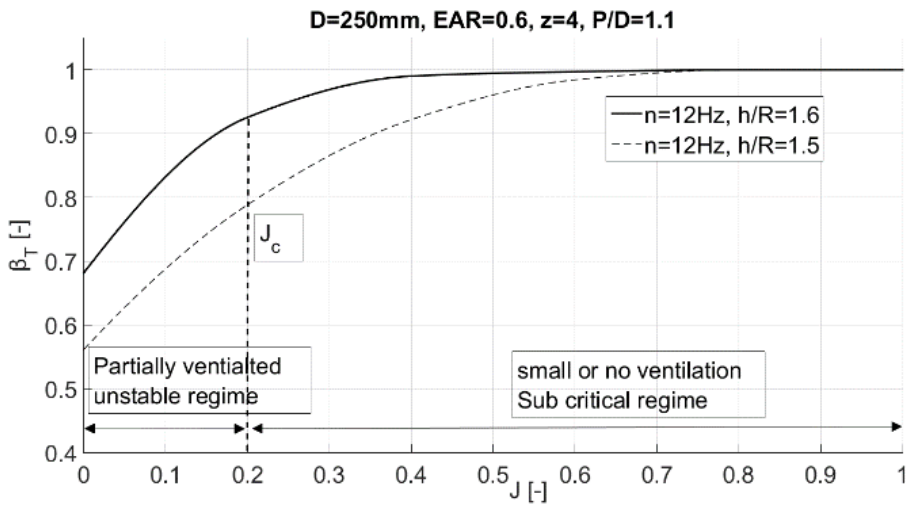


Figure 4-5 Unstable and sub critical ventilation regime presented for  $h/R=1.6$  and  $1.5$ , Koz17.

## 4.2 RELATION BETWEEN THRUST AND TORQUE LOSS FACTOR (*KOU2006\_I*)

*This section based on Kou2006\_I experimental data*

Figure 4-6 shows the relation between the torque losses factor and the thrust losses factor. As it is observed from the Figure 4-6 the propeller torque has the similar behavior as propeller thrust and shows good agreement with experimental results by Minsaas et.al. (1983), where

$$K_{Tt} = \beta \cdot K_{Tn} \quad (4-1)$$

$$K_{Qt} = \beta^m \cdot K_{Qn} \quad (4-2)$$

$m$  is constant between 0.8 and 0.85 Minsaas et.al. (1983).

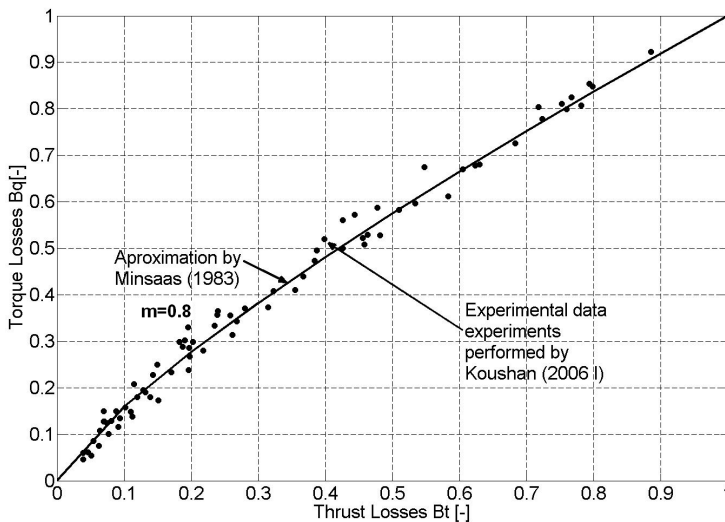


Figure 4-6 Relation between thrust and torque loss factors, based on experiments *Kou2006\_I*.

This means if the torque is measured, one can accurately know the thrust also in ventilation condition.

### 4.3 THE TIME INFLUENCE OF VENTILATION INCEPTION (KOU2006\_I)

This section is based on Kou2006\_I experimental data.

In Figure 4-7 and Figure 4-8 the ventilation inception time is plotted as a function of propeller revolutions, submergences and forward speed. Three propeller revolution speeds  $n=12\text{Hz}$ ,  $14\text{Hz}$ ,  $16\text{Hz}$  at three different carriage speeds  $v=0.3\text{m/s}$ ,  $0.35\text{m/s}$ ,  $0.45\text{m/s}$  were tested, which means that the loading parameter (advance number) is the same for different revolutions and carriage speeds – The test conditions are given in Table 4-1 below.

n=12 Hz	n=14 Hz	n=16 Hz	n=12 Hz	n=14 Hz	n=16 Hz
Carriage speed [m/s]			advance number $J[-]$		
0.3	0.3	0.3	0.100	0.086	0.075
0.35	0.35	0.35	0.117	0.100	0.088
0.4	0.4	0.4	0.133	0.114	0.100

Table 4-1 Ventilation inception, test conditions.

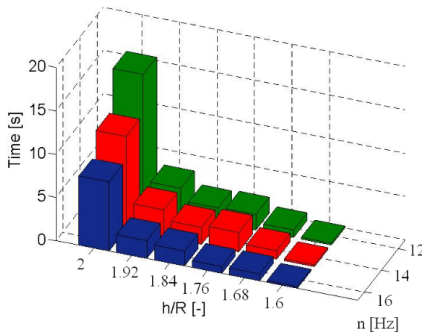


Figure 4-7 Ventilation inception time as a function of propeller submergence and propeller speed ( $J=0.1$  for  $n=12,14,16$  Hz), Kou2006\_I.

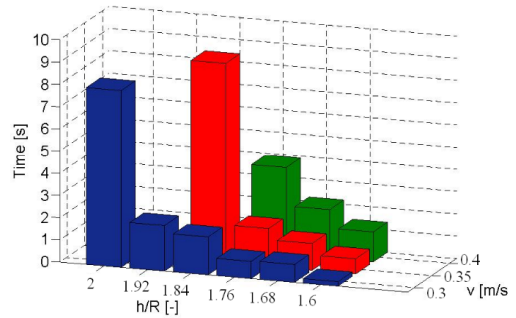


Figure 4-8 Ventilation inception time as a function of propeller submergence and forward speed ( $J=0.1$  for  $n=12$ (blue color),  $14$ (red color) and  $16\text{Hz}$  (green color)), Kou2006\_I.

From the results it is found that the ventilation inception time increases by decreasing the propeller speed or by increasing the carriage speed. Presented results are for propeller submergence from  $h/R=2$  to  $h/R=1.6$ , which means that the ventilation is vortex ventilation and the time is the time to establish vortex ventilation. It is observed from experiments that

for propeller submergence  $h/R \leq 1.4$  there is no marked difference for ventilation inception time for different loading conditions. Ventilations starts immediately after the propeller starts rotating. It is worth to mention that propeller advance number has more significant impact on ventilation inception than propeller speed. For example for propeller submergence  $h/R=1.92$  and propeller speed  $n=12\text{Hz}$  it is observed ventilation inception for  $v=0.3\text{ m/s}$  after c.a.  $2\text{s}$  and it is observed no ventilation for the same submergence condition but with increased forward speed to  $v=0.35\text{ m/s}$  and increasing propeller speed  $n=14\text{ Hz}$ . It seems that the vortex appearance is very sensitive to external flow condition. It was observed that for higher advance numbers the generated vortices does not reach the propeller blade, even for the same loading parameter ( $J = 0.1$ ).

#### **4.4 THRUST HYSTERESIS EFFECT (KOU2006\_I AND KOU2006\_II)**

*This section based on Kou2006\_I and Kou2006\_II experimental data.*

The hysteresis effect on thrust for an open propeller is presented in *Figure 4-9*. The figure shows the time series of thrust as a function of submergence ratio  $h/R$  during two different ventilation events. Ventilation is generated by sinusoidal vertical motion of the propeller with different amplitudes. For  $h/R > 3$  the propeller is deeply submerged and it is observed no thrust loss. When the submergence is reduced full thrust is maintained until  $h/R < 1.5$  where ventilation starts and then the thrust drops to 23% of nominal thrust at  $h/R=1$ .

For  $h/R < 1$  thrust loss is mainly due to loss of propeller disc area and no hysteresis effect is observed. When the submergence is increased the thrust is built up until we achieve 100% of nominal thrust for  $h/R=3$ . A similar phenomenon is also observed for the ducted propeller, see *Figure 4-10*. So it seems that the thrust loss depends on the direction of motion – when the propeller is going down the thrust loss is less compared to upward motions, which supports the conclusions that it is the time-dependence of the ventilation phenomenon that causes most of the hysteresis effect.

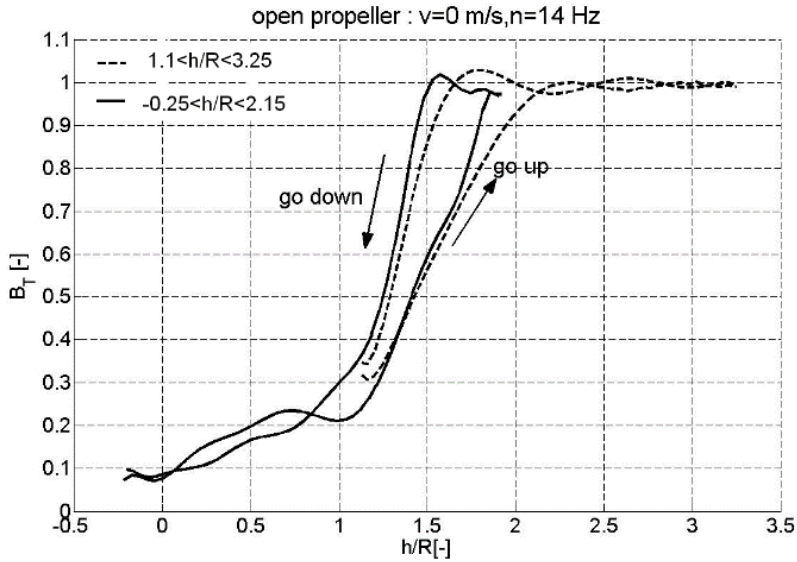


Figure 4-9 Hysteresis effect, open propeller, dynamic heave motion ( $T=4s$ ), based on experiments, Kou2006\_I.

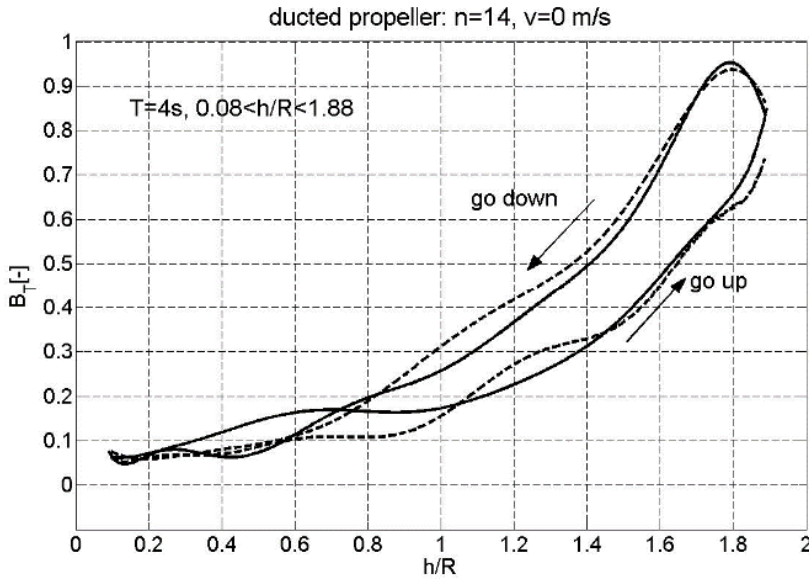


Figure 4-10 Hysteresis effect, ducted propeller, dynamic heave motion ( $T=4s$ ), based on experiments, Kou2006\_II.

Figure 4-11 shows the thrust loss coefficients for open and ducted propellers in static condition (no heave motion). It is observed from the figure that also in static condition

the thrust loss shows something similar to a hysteresis effect, since for the same value of submergence and propeller loading the propeller can both be ventilated and non-ventilated, resulting in significantly different thrust loss values. This is related to the fact that it takes time for ventilation to be established in well-submerged conditions, just as for the dynamic heave motion conditions.

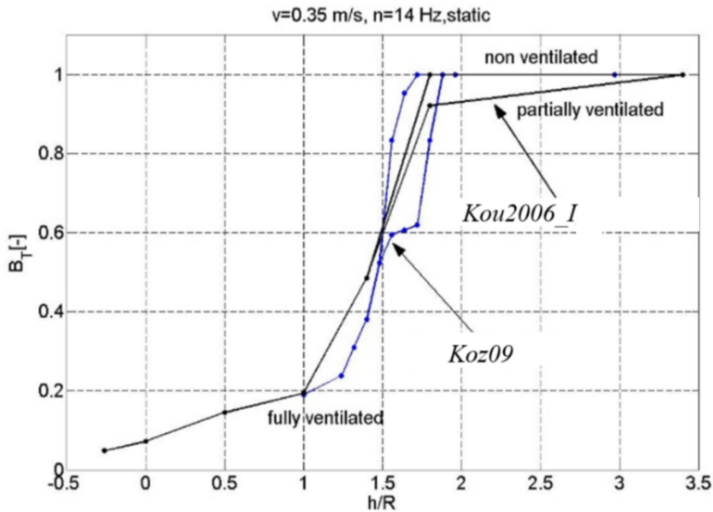


Figure 4-11 Thrust loss coefficients for open propeller in static condition (no heave motion), (Kou2006\_I, Koz09).

#### 4.5 COMPARISON BETWEEN STATIC AND DYNAMIC THRUST LOSS (KOU2006\_I, KOU2006\_II)

This section based Kou2006\_I and Kou2006\_II experimental data.

In order to check the importance of dynamic heave motion for thrust loss due to ventilation, the thrust loss as a function of submergence ratio is presented in dynamic and static conditions for both open and ducted propellers. It can be observed from the Figure 4-12 that for open propeller, the thrust is always larger in conditions with dynamic heave motion than in static condition.

From Figure 4-13 it is seen that for a ducted propeller there is less difference between thrust in static and dynamic conditions, although thrust in dynamic heave is still slightly larger than in static condition. The difference between dynamic and static thrust loss due to heave motion can be 20% for deeply submerged propellers in bollard conditions. The

effect of dynamic heave motion becomes less important for higher advance numbers. Again, the time delay in establishing vortex ventilation is believed to be the main cause of the observed effect, and that the delay in establishing ventilation is longer than for ventilation to disappear.

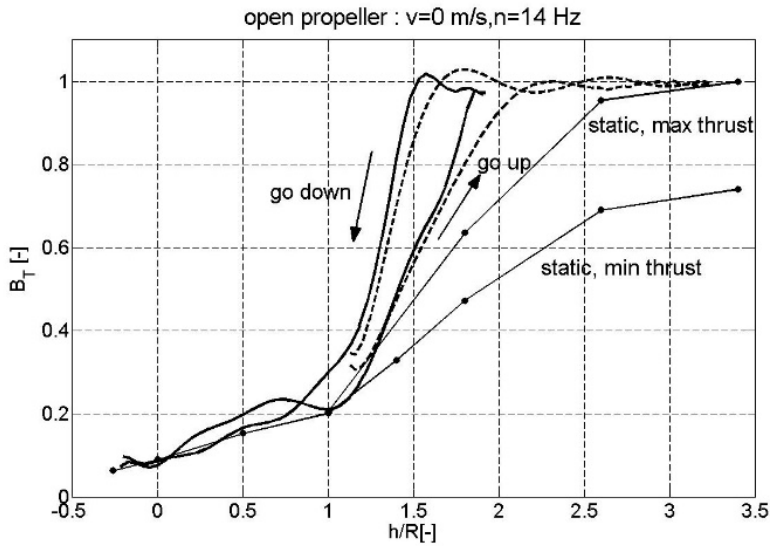


Figure 4-12 Open propeller, bollard condition. Propeller speed  $n=14$ Hz, Period of heave motion: 4s, Kou2006\_I.

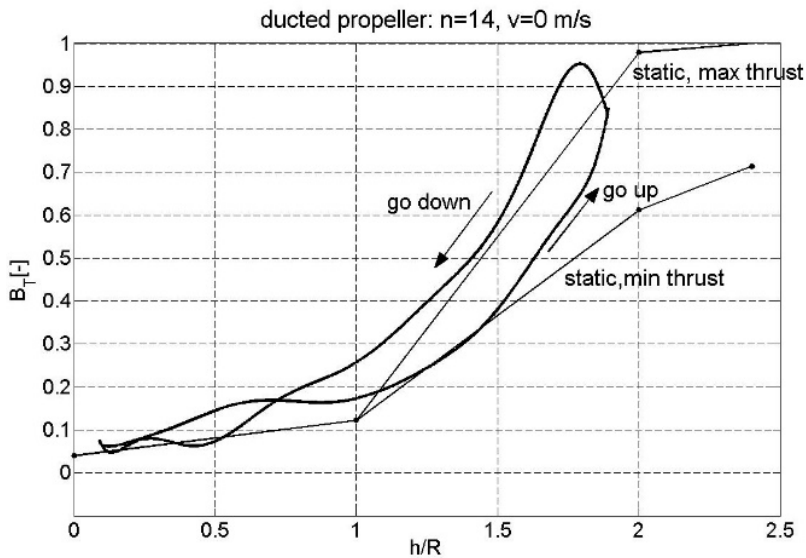


Figure 4-13 Ducted propeller, bollard condition. Propeller speed 14Hz, Period of heave motion: 4s, Kou2006\_II.



## 4.6 IMPORTANCE OF HEAVE MOTION PERIOD FOR THRUST LOSS (KOU2006\_I AND KOU2006\_II)

This section is based on experiments Kou2006\_I and Kou2006\_II experimental data.

### 4.6.1 Main Results

In order to check the importance of the heave oscillation period, two different periods: 2s and 4s were tested. Based on the measurement results it is found that one can get more ventilation for longer heave period. This can also be explained by the time-dependence of ventilation – since it takes a little while for ventilation to establish, as shown in section 4.3 above, it is as expected that longer heave oscillation period results in larger average thrust loss. For long heave amplitude the time is large enough for ventilation to be established. It is also observed the tendency that the heave motion period has not a significant influence for propeller submergence  $h/R < 1$ , it is much more important for deep submerged propellers but still the difference in thrust loss is not too large and probably can be neglected.

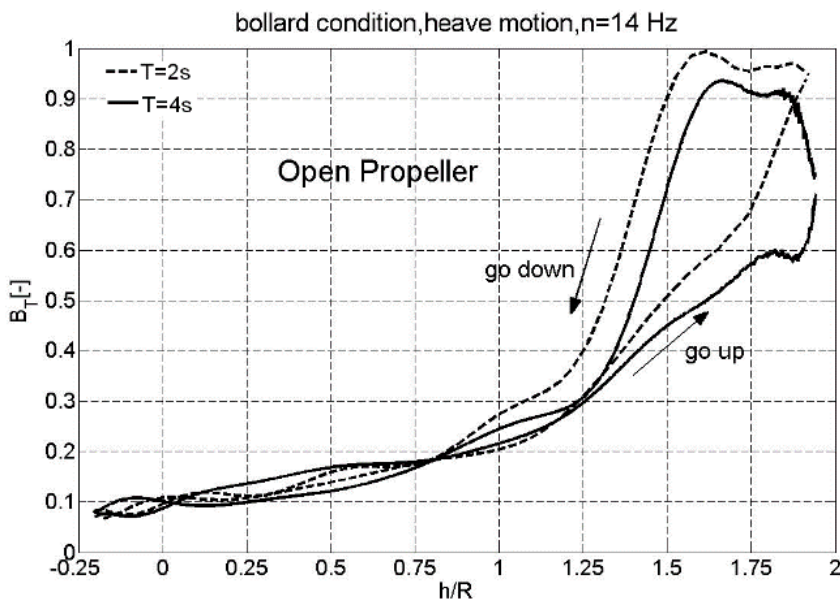


Figure 4-14 Comparison between different heave periods ( $T=4s$  and  $T=2s$ ), open propeller,  $v=0$  m/s,  $n=14\text{Hz}$ , Kou2006\_I.

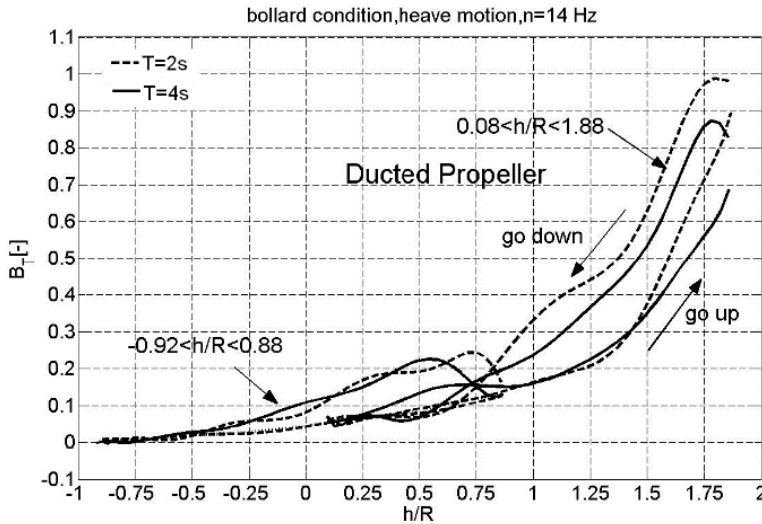


Figure 4-15 Comparison between different heave periods ( $T=4s$  and  $T=2s$ ), ducted propeller,  $v=0$  m/s,  $n=14Hz$ , Kou2006\_II.

#### 4.6.2 Comparison for thrust loss for open and ducted propeller (Kou2006\_I, Kou2006\_II).

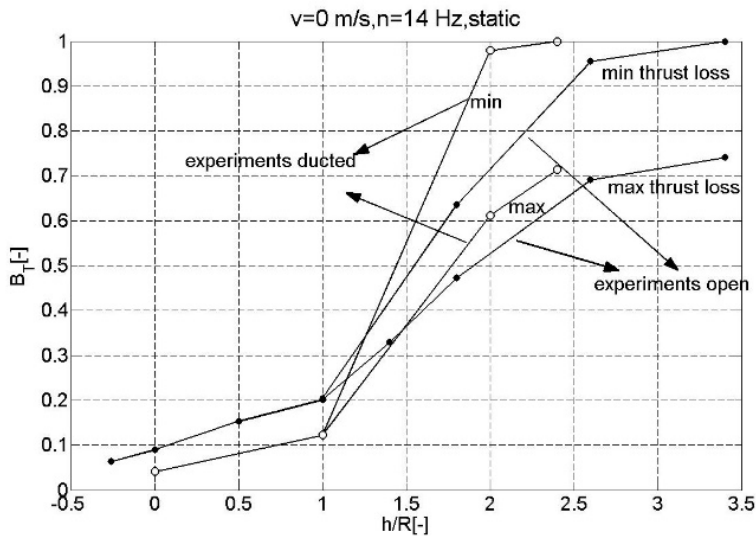


Figure 4-16 Comparison between thrust loss factor  $\beta$  for open and ducted propeller for bollard conditions,  $n=14$  Hz, static conditions- no heave motion, Kou2006\_I and Kou2006\_II.

Comparison between open pulling and ducting pushing propeller are shown in *Figure 4-16*, *Figure 4-17* and *Figure 4-18*

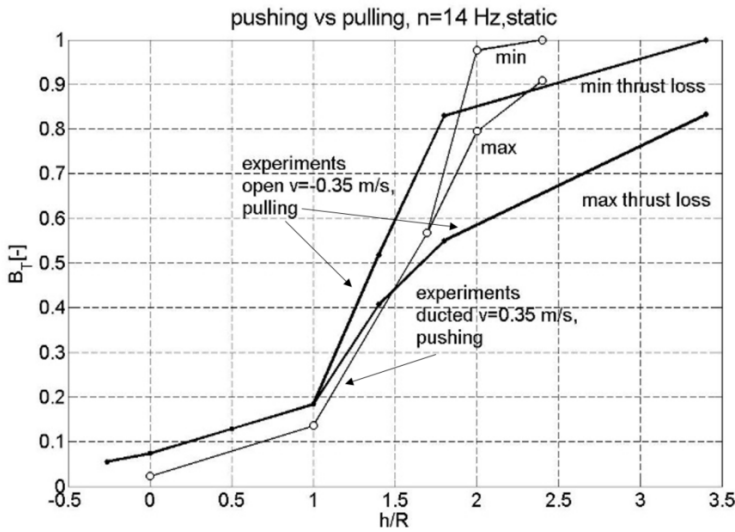


Figure 4-17 Comparison between thrust loss factor  $\beta$  for open pulling ( $v=-0.35$  m/s) and ducted pushing propeller ( $v=0.35$  m/s), static conditions – no heave motion, Kou2006\_I and Kou2006\_II.

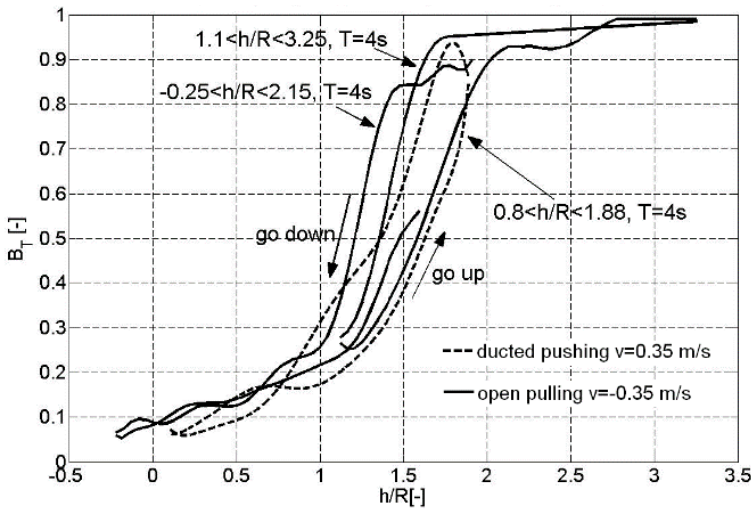


Figure 4-18 Comparison of thrust loss factor  $\beta$  between open pulling and ducted pushing propeller, dynamic conditions heave motion ( $T=4$ s), Kou2006\_I and Kou2006\_II.

As a conclusion one can say that the ducted propeller ventilates later than the open propeller but if it does ventilate the thrust loss is larger for the ducted propeller. Less difference between open and ducted propeller is observed for dynamic heave motion than for static condition.

#### 4.7 PROPELLER VENTILATION BY VORTEX FORMATION (KOZ09, KOZ10, KOU10, KOZ17)

*This section is based on experiments Koz09, Koz10, Kou10 and Koz17 experimental data.*

Two factors, which determined the formation of the vortex, were investigated as for the inlet vortex, propeller radius divided by the distance from the propeller centre to the free surface  $h/R$  and the velocity through the propeller disk  $V_i$  divided by the free stream velocity, see equation (2-28) at page 33 and Section 2.2.4 for more detailed description of the phenomena.

Experimental data based on the different model tests listed in Table 3-1 and Table 3-2 show the boundary between the vortex forming, non-vortex forming and free surface ventilation flow regimes. The type of ventilation is identified visually, either directly or from the video recordings. The effect of the vortex formation for marine propellers during transient operation near the free surface is presented in Figure 4-19 and Figure 4-20 below. The color of the data points specifies if ventilation is observed and what type it is – green means no ventilation, red means vortex ventilation and blue means free surface ventilation. Figure 4-19 include the whole range of tested propeller revolutions i.e.  $n \geq 9rps$ . According to Shiba (1953) the influence of the Weber's number disappears above the so-called minimum Weber number, which is approximately 180. For our experiments a Weber number larger than 180 corresponds to a propeller speed  $n \geq 13rps$ , meaning that for the 9 and 12rps tests, surface tension related scale effects might influence the results. Figure 4-20 presents the results only for tests with propeller revolutions  $n \geq 13rps$ , hence the influence of Weber's number can be neglected. In both figures, lines to divide the domain into different ventilation categories are tentatively included. These lines might be used (with care) to predict what type of ventilation that might appear in a given operational condition. Both plots are based on tests with two different model propellers; P1374:  $D=250mm$ ,  $P/D=1.1$ ,  $A_E/A_0=0.6$ ,  $z=4$ , and P1440:  $D=200mm$ ,  $P/D=1.2$ ,  $A_E/A_0=0.447$ ,  $z=4$ . The main difference between Figure 4-19 and Figure 4-20 is that Figure 4-19 contains data for propeller speed lower than 13rps, thus surface tension related scale effects

might influence the results. Figure 4-20 presents the results only for tests with propeller revolutions  $n \geq 13\text{rps}$ .

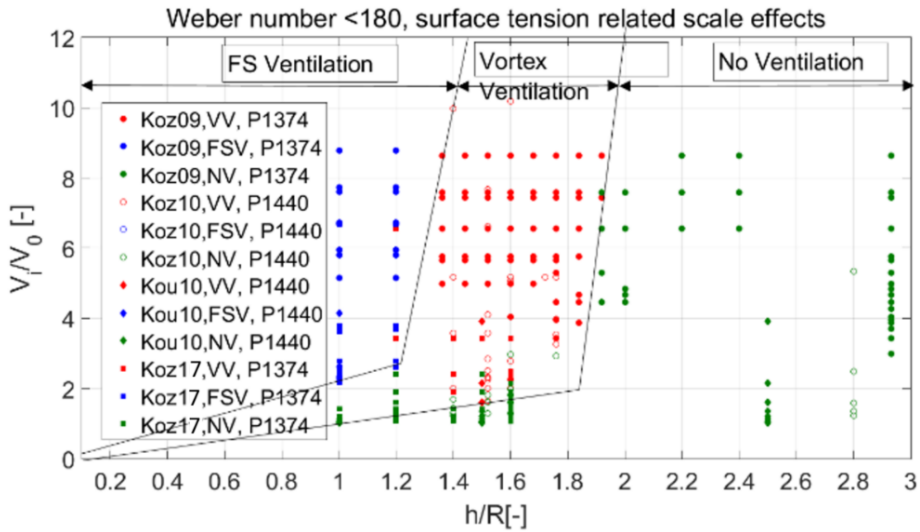


Figure 4-19 Experimental data showing the boundary between the vortex forming and no vortex forming flow regimes for marine propellers operating in transient condition (from low to high advance numbers), propeller revolutions: ( $n \geq 9\text{Hz}$ ,  $We \geq 132$ ). Acronyms included in the legend: VV means ventilation by vortex formation, FSV means free surface ventilation, NV means no ventilation, P1374: propeller model ( $D=250\text{mm}$ ,  $P/D=1.1$ ,  $A_E/A_0=0.6$ ,  $z=4$ ), P1440: propeller model ( $D=200\text{mm}$ ,  $P/D=1.2$ ,  $A_E/A_0=0.447$ ,  $z=4$ ).

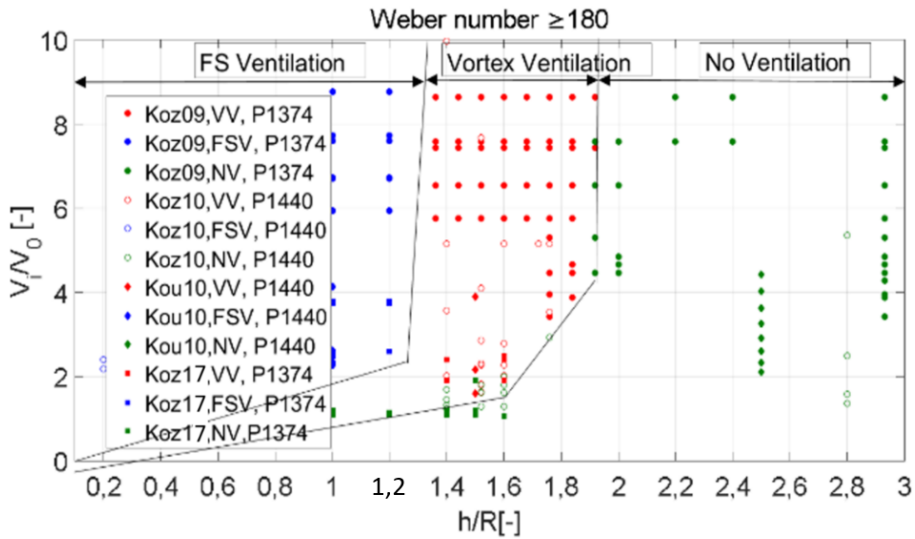


Figure 4-20 Experimental data showing the boundary between the vortex forming and no vortex forming flow regimes for marine propellers operating in transient condition (from low to high advance numbers), propeller revolutions ( $n \geq 13\text{Hz}$ ,  $We \geq 180$ ) Acronyms included in the legend: VV means ventilation by vortex formation, FSV means free surface ventilation, NV means no ventilation. P1374: propeller model ( $D=250\text{mm}$ ,  $P/D=1.1$ ,  $A_E/A_0=0.6$ ,  $z=4$ ), P1440: propeller model ( $D=200\text{mm}$ ,  $P/D=1.2$ ,  $A_E/A_0=0.447$ ,  $z=4$ ).

#### 4.8 COMPARISON BETWEEN PHVC, AND PFSVV (KOZ09, KOZ17)

This section is based on Koz09 and Koz17 experimental data

As it was described in *Chapter 2*, ventilation by vortex formation has a certain random character, and it is very sensitive to submergence and variations of external flow. Based on the images recorded during the experiments, three types of ventilating vortex impact on propeller blades was detected

- Impact on the port side of the propeller blade, see *Figure 4-22a*
- Impact of the starboards side of the propeller blade, see *Figure 4-22b*
- Impact of both vortices, see *Figure 4-22c*

As the general rule the occurrence of starboard side vortex is observed for deep submergences ( $\frac{h}{R} \geq 1.8$ ) and it happened very rare compare to the port side vortex. Port side vortex has a dominating effect for propeller ventilation, occasionally it is observed double vortex flow both for deep ( $\frac{h}{R} \geq 1.8$ ) and intermediate submergences ( $\frac{h}{R} \geq 1.2$ ), see *Figure 4-23*.

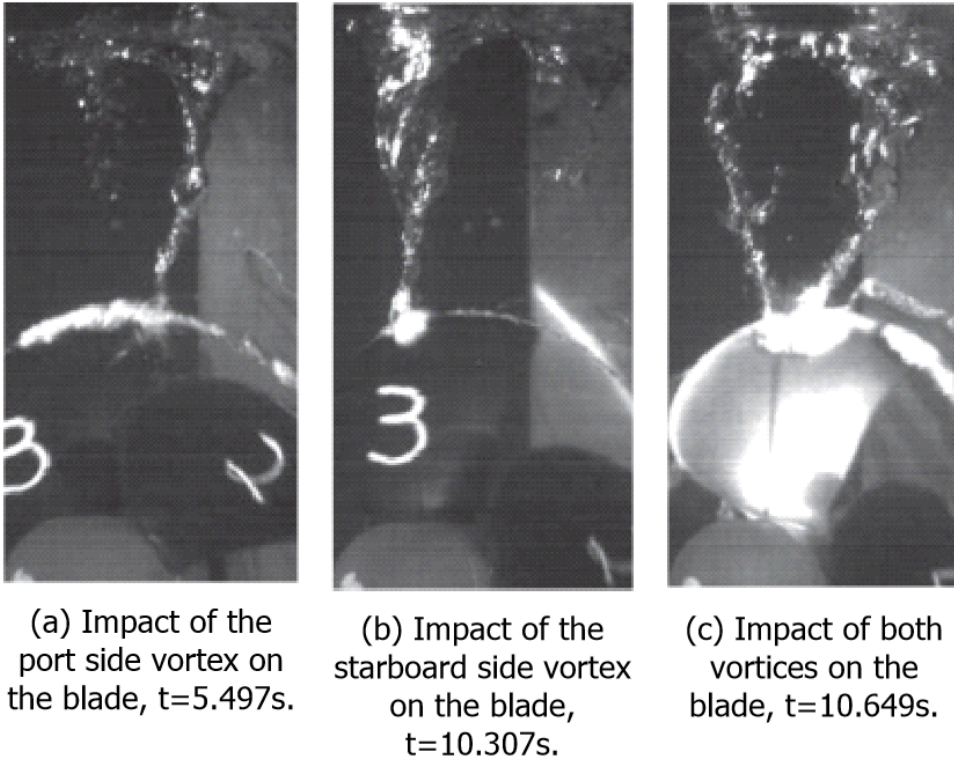


*Figure 4-21 PFSVV,  $h/R=2.04$ ,  $J=0.075$  ( $c_T=253$ ,  $c/D=0.52$ ), Califano (2010), experiments Koz09.*

Comparison between numerical RANS simulations (PHVC) performed by Martio et.al. (2011) and experiments (PFSVV) shows that ventilation vortex formation is very similar to propeller hull vortex cavitation phenomenon. The traced streamlines at  $J=0.326$  and  $J=0.433$  in *Figure 4-22* illustrate that for these cases the generated vortices on the surface do not interact with a blade at any position. It is observed the similar correlation for ventilation vortex phenomena see *Figure 4-23*. Above the so-called critical advance number  $J_c$  the thrust loss due to ventilation is much smaller than for advance numbers below the critical advance number. This is probably because that for higher advance

numbers the generated vortices on the free surface do not interact with the propeller, so the ventilation does not reach the propeller blades. The other reason for this is that the suction (described as propeller load factor  $c_T$ ) which is generated by the propeller is smaller for higher advance numbers.

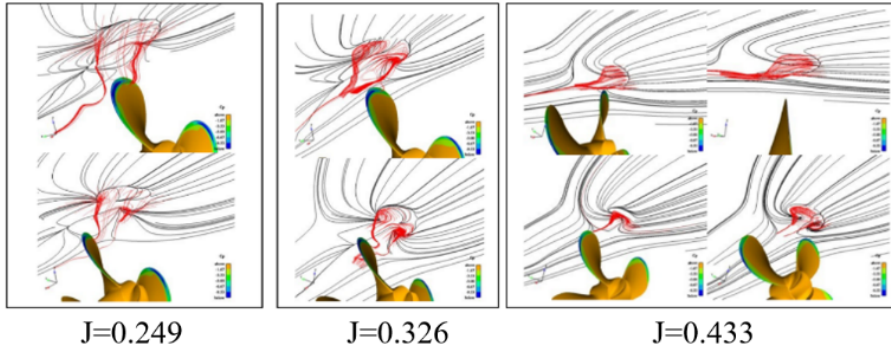


Figure 4-22 The streamlines and the distribution of  $c_p$  on the suction side (PHVC),  $c/D=0.157$ ,  $n=11.8$  rps,  $D=227$ ,  $z=4$ ,  $P/D=1.1$ , Martio et. al. (2011).

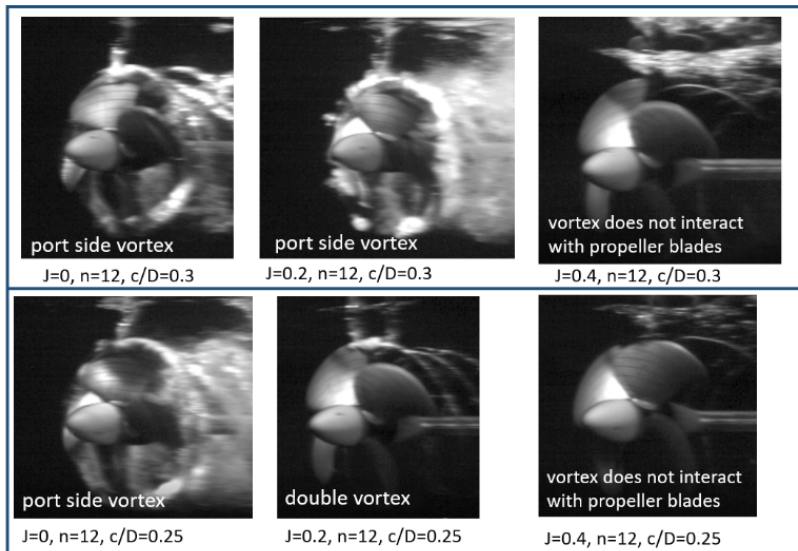


Figure 4-23 Appearance of ventilation for different advance numbers,  $c/D=0.25$  and  $c/D=0.3$ ,  $n=12$  rps, Kozłowska and Steen (2017), experiments Koz17.



#### **4.9 INCEPTION OF VENTILATING VORTEX (KOU2006\_I, KOZ09, KOZ10, KOU10 AND KOZ17)**

*This section based on Kou2006\_I, Koz09, Koz10, Kou10 and Koz17 experimental data.*

From the experiments, presented in *Table 3-1* and *Table 3-2* it is found that ventilation does not occur for bollard condition  $J=0$  for propeller submergences  $h/R$  over 3.4, see Kozłowska et.al. (2009). Based on this observation it is calculated, according to equation (2-42) that the minimum vortex core for ventilation to occur is equal to 3.3 mm for  $n=16\text{Hz}$ . *Figure 4-24* presents the results of the calculation of the radius of ventilating vortex for different submergences ( $h/R=3.4, 2.0, 1.8, 1.6, 1.4, 1.2$ ) and advance number from 0 to 0.7, based on equation (2-42). If it will be assumed that the minimum vortex radius for the propeller to ventilate is 3.3 mm then it is possible to calculate the maximum advance number for different submergences for a propeller to ventilate, see *Table 4-2*. For the known advance number and the propeller characteristics, it is straight forward to calculate also other parameters like the velocity through the propeller  $V_i$ , and the two formulations for propeller thrust coefficient  $c_{Tn}$  and  $K_{Tn}$ . If one wants to use the data in *Table 4-2* to estimate when vortex ventilation might occur for other propellers than the ones studied here, it is recommended to use a pitch-independent parameter like  $V_i$ . The minimum vortex radius will probably depend on the amount of air sucked through it, since a stronger air flow will reduce the pressure below atmospheric (which is the current approximation). Thus, the stronger the ventilation air flow, the larger the calculated minimum radius needs to be. An implication of this is that the calculated minimum radius will need to be bigger for full scale. How much is hard to say without quantifying the amount of air sucked through the vortex.

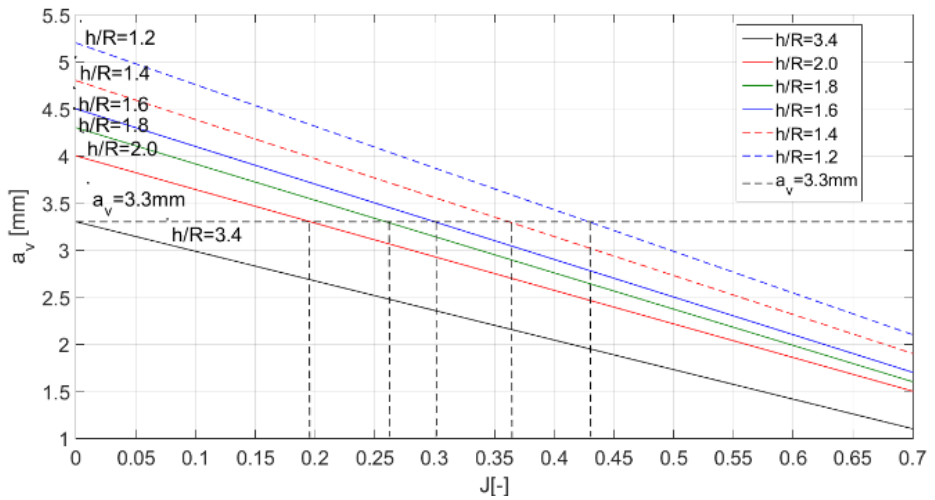


Figure 4-24 Minimum vortex radius for ventilation to occur for  $n=16\text{Hz}$ ,  $Koz17$  and corresponding maximum advance number.

$a_v$	$h/R$	$J_{max}$	$V_i$	$V_i/V_0$	$c_{Tn}$	$K_{Tn}$
[mm]	[-]	[-]	[m/s]	[-]	[-]	[-]
3.3	3.4	0.000	2.51	-	-	0.62
3.3	2.0	0.195	2.74	3.52	35.39	0.53
3.3	1.8	0.260	2.83	2.72	18.77	0.50
3.3	1.6	0.300	2.89	2.41	13.57	0.48
3.3	1.4	0.360	2.98	2.07	8.87	0.45
3.3	1.2	0.440	3.11	1.77	5.44	0.41

Table 4-2 Maximum advance number ( $J_{max}$ ) for ventilation to occur based on minimum radius of the vortex core  $a_v$ .

Comparison between the calculation of the maximum advance number for ventilation to occur for different submergence ratios presented in Table 4-2 based on the minimum radius of the vortex core correspond quite well with experiments, see Figure 4-26 and Figure 4-27. For deeply submerged propeller  $h/R=2.04$  it is observed ventilation for  $J=0.1$  and  $J=0.133$ , which correspond with the maximum advance number  $J_{max} = 0.195$ . For  $h/R=1.6$  ventilation stops above the  $J=0.2$ , which correspond with the maximum advance number  $J_{max} = 0.3$ . For propeller submergence  $h/R=1.2$  it is observed very little amount of ventilation for  $J>0.4$ .

It is of interest to compare the outcome of equation (2-42), given in Table 4-2, with the boundary lines in Figure 4-24. Such a comparison is given in Figure 4-25. It can be seen that the agreement between the two methods is good, given the inherent uncertainties in the observations that these methods are based on. The agreement is particularly good for  $h/R < 1.8$ . For deeply submerged propellers the presented method seems to over-predict the maximum advance number for ventilation, which might be caused by neglecting the effect of the air flow on the vortex core radius, as previously mentioned.

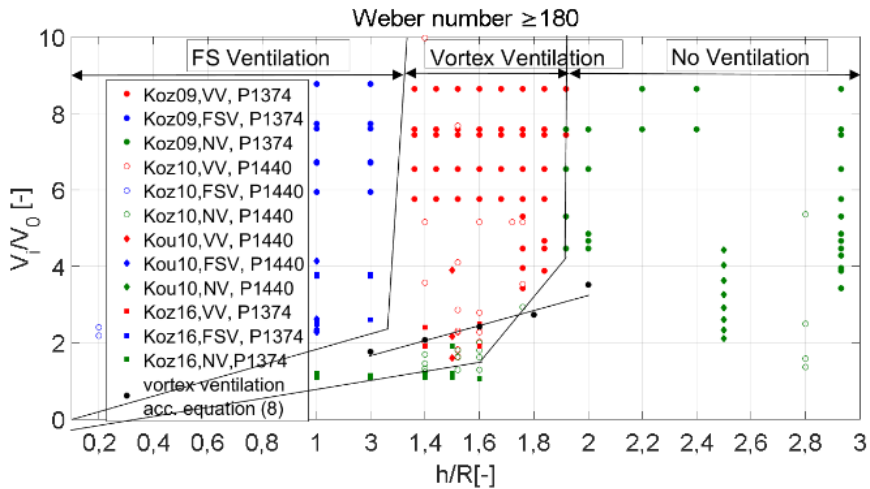


Figure 4-25 Comparison between two different methods of calculating if vortex ventilation will happened according to equation (2-42) and the boundary between vortex forming and non-vortex forming flow regimes, presented in Figure 4-20.

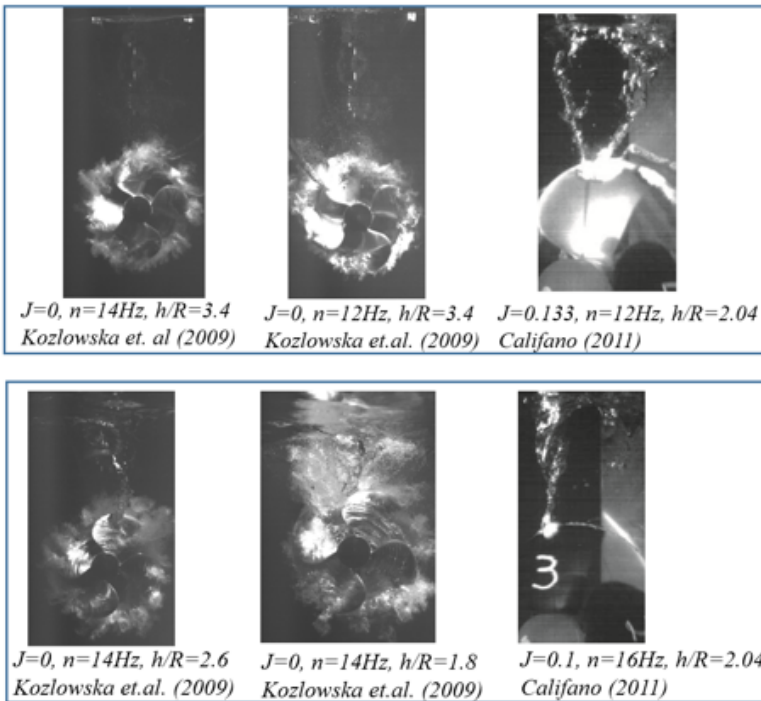


Figure 4-26 Ventilation inception by vortex formation based on experiments Kou2006\_I and Koz09.

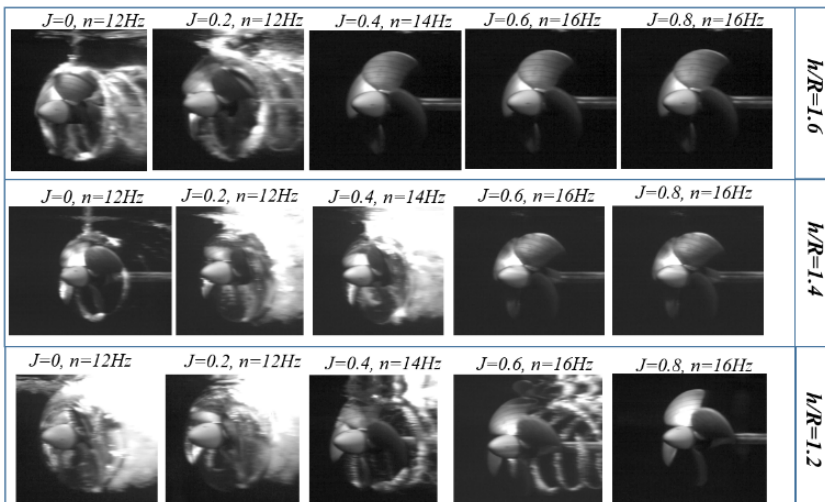


Figure 4-27 Ventilation inception by vortex formation based on experiments, Koz17.

## 4.10 COMPARISON BETWEEN CFD CALCULATIONS AND MODEL EXPERIMENTS (*KOZ10*)

This section is based on *Koz10* experimental data. The experiments were conducted in the large towing tank at The Marine Technology Centre. The four bladed right handed propeller P1440 was mounted on the open water test rig. A picture of the test set-up is shown in *Figure 3-19*. A novel blade dynamometer (2<sup>nd</sup> version) capable of measuring 5 degrees of freedom forces and moments (centrifugal force not measured) on a single propeller blade was used during these experiments. Use of high speed video cameras (one under and one above water) gave a visual understanding of ventilation phenomena.

The CFD work has been done by Wockner-Kluwe (2013) in cooperation with the author. Two existing in-house codes, the potential flow method *ISThydro* and the RANS method *FreSCO*<sup>+</sup> were improved in order to obtain more accurate modeling of the flow around the propeller. The CFD calculations presented in this article is based on the in-house code *FreSCO*<sup>+</sup>.

### 4.10.1 J=0

*Figure 4-28* shows the total thrust and torque loss factors  $\beta_T = \frac{K_T}{K_{T0}}$  and  $\beta_Q = \frac{K_Q}{K_{Q0}}$  as a function of blade position for a sequence of propeller revolutions. *Figure 4-28* shows that the variation in thrust and torque between revolutions is less for calculations than for the experimental results. However, the number of rotations simulated (18) equal to 1s of simulation time is much less than in the experiments (1620) equal to 90 s of measurement time. Thus, it might be that the current CFD calculations only capture one of several possible “flow modes”. During measurements the thrust loss is quite constant during each revolution and depends on the duration of the experiments. In the CFD, blade thrust has a strong variation with position, with large thrust loss around top position and small thrust loss around bottom position. This difference might be explained by the fact that in the calculation the blade loses contact with the air supplying vortex.

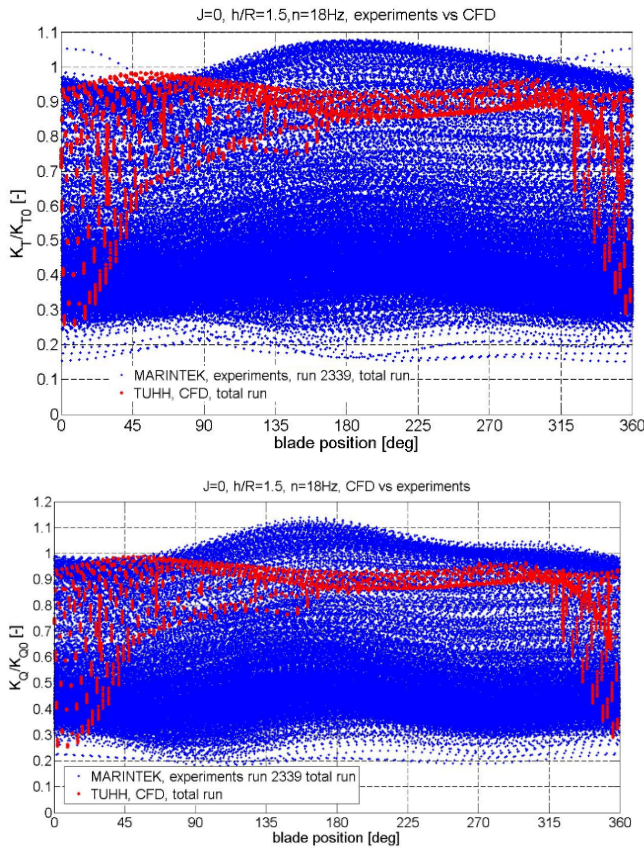
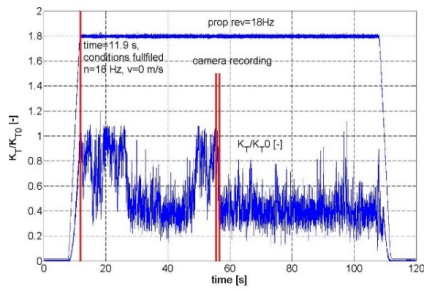


Figure 4-28 Comparison between calculated (red color) and measured (blue color) thrust (top side) and torque loss (bottom side) based on experiments (Koz10) for  $J=0$ ,  $h/R=1.5$  and  $n=18\text{Hz}$ .

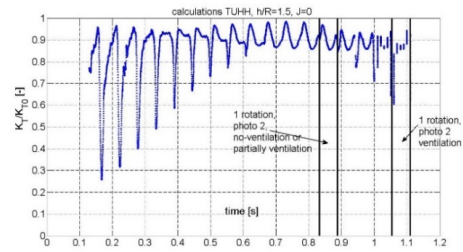
Figure 4-29b shows that the total time of CFD simulation was about 1.1 s, which correspond to 18 propeller rotations. Figure 4-29c shows that during the experiments, the first thrust drop occurred after 5.5 rotations from the starting point and another bigger drop occurs after 11.5 rotations. Thus, it can be compared with the CFD simulation since 18 propeller rotations were computed in the CFD simulation. Figure 4-29d presents the comparison between one of the first thrust drops during the experiments and the CFD calculations.

Figure 4-29e and Figure 4-29f shows comparison between thrust coefficient for CFD simulations and experiments during non-ventilating and partially ventilating phase. The green dots in Figure 4-29f correspond with a sequence of photos from experiments

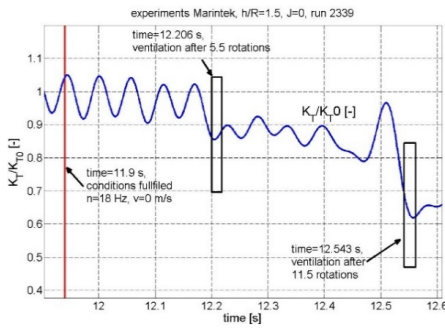
presented in *Figure 4-30* and correspond with screenshots of simulation (taking after 5.5 propeller rotation). Comparison between calculation and experiments in respect to simulation time and time duration of experiments has been summerized in *Table 4-3*.



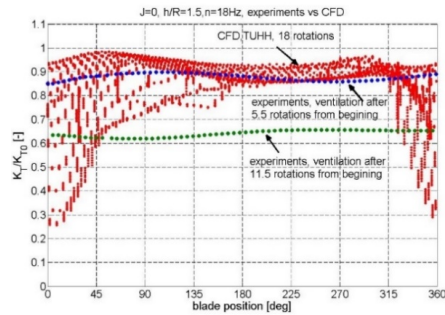
(a) Experiments, total run



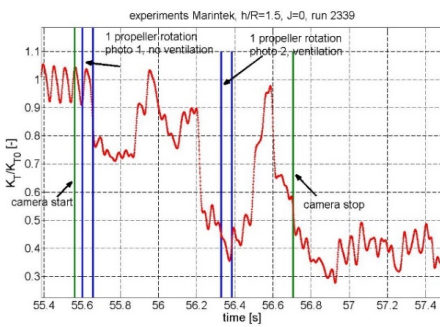
(b) CFD calculations, total run



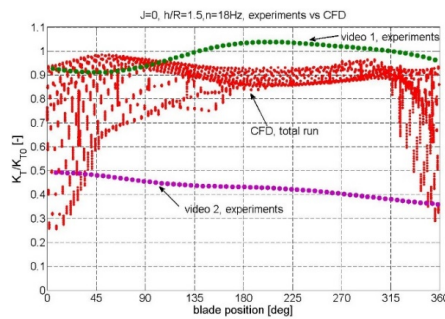
(c) One of the first thrust drops



(d) Comparison between one of the first thrust drops and CFD calculations



(e) Photo 1 & 2 cases chosen for comparison with CFD calculations



(f) Thrust ratio for photo cases chosen for comparison with CFD calculations

Figure 4-29 Comparison between calculated (CFD) and measured ( $K_{oz10}$ ) thrust loss for  $J=0$ ,  $h/R=1.5$  and  $n=18\text{Hz}$ .



Thrust (experiments)	Thrust (CFD)	Camera (experiments)	CFD (simulation)
Time (s)			
First thrust drop after 5.5 rotations = 0.306 s, see <i>Figure 4-30</i>	It was simulated 18 rotations	Camera started after 43.7 s from the beginning (when the propeller achieves 18 Hz).	No or partially ventilating case (0.833s-0.888s), see <i>Figure 4-30</i>
More significant thrust drop after 11.5 rotations=0.643 s, see <i>Figure 4-31</i>			Ventilating case (1.0545s:1.11s), see

*Table 4-3 Comparison of time of simulation (CFD) with time duration of experiments (Koz10) for  $J=0$ ,  $h/R=1.5$  and  $n=18\text{Hz}$ .*

*Table 4-3 above shows the details, which cases are compared in the *Figure 4-29*, *Figure 4-30* and *Figure 4-31*. For example in *Figure 4-30* first thrust drop occurs after 0.306s and it was compared with CFD simulation case from 0.833s to 0.888s. *Figure 4-31* presents the comparison between second thrust drop during experiments, which occurs after 0.643s and CFD simulation from 1.0545 to 1.11s.*

*Figure 4-30* shows that the mechanism for ventilation inception is similar for the calculation and for the experiments. Due to propeller rotation, ventilation starts by forming an air-filled vortex from FS. The vortex mainly appears in the blade position between 315-45 deg.

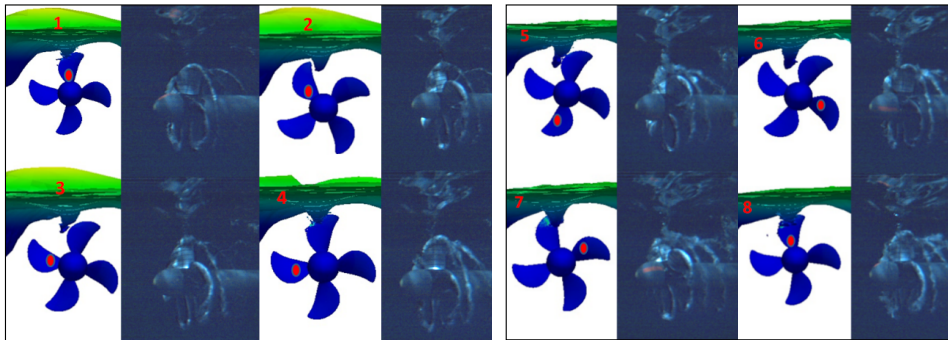


*Figure 4-30 Comparison of flow around the propeller for experiments (Koz10) and simulations (CFD) presenting one rotation of propeller blade after 5.5 rotations, no or partially ventilating regime is observed for  $J=0$ ,  $h/R=1.5$  and  $n=18\text{Hz}$ .*

Figure 4-31 show that the propeller ventilated more during the experiments. The tip vortex sucked down the air from FS and transported it in the direction of the propeller rotation; most of the air was transported downstream. In the experiments, it is observed an air cloud covering the entire blade, which indicates a fully ventilating propeller. This is believed to be caused by a stronger connection between blade and vortex in the experiment than in the corresponding CFD calculation. During CFD simulation, the blade loses the connection with a vortex after passing 90 deg and fully ventilating case was not observed. This might be due to problems with resolving a thin ventilating vortex in CFD. Also, problems representing air bubbles in the CFD might be a reason for the large difference in visual appearance.

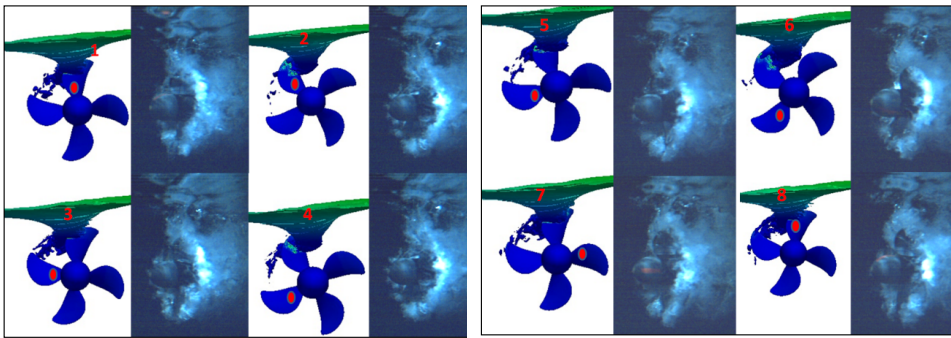


Figure 4-31 Comparison of flow around the propeller for experiments (Koz10) and simulations (CFD), presenting one rotation of propeller blade after 11.5 rotations, no or partially ventilating regime is observed for  $J=0$ ,  $h/R=1.5$  and  $n=18\text{Hz}$ .

#### 4.10.2 $J=0.15$

Figure 4-32 shows that prediction of thrust loss is more repeatable between revolutions for calculations than for experiments. On the other hand, the variations during a revolution is larger for the CFD results than for the experiments. From the simulation results similar thrust loss was observed for every propeller revolution. The biggest thrust loss is when the blade is close to the FS (between 315 and 90 deg), for the propeller blade position between 90 and 315 the thrust is built up again and achieve values close to nominal thrust. During measurements different thrust losses depending on the time in the experiments were observed. The different thrust losses correspond to different ventilation extent. It is clear from the experiments that in this condition, the propeller can be both fully and partly ventilating, and that it changes between the different ventilating conditions without an apparent reason. When the propeller starts ventilating the thrust loss is bigger than for the

simulation. Also, in ventilating condition, the experiments typically show much less variation in thrust during a single revolution.

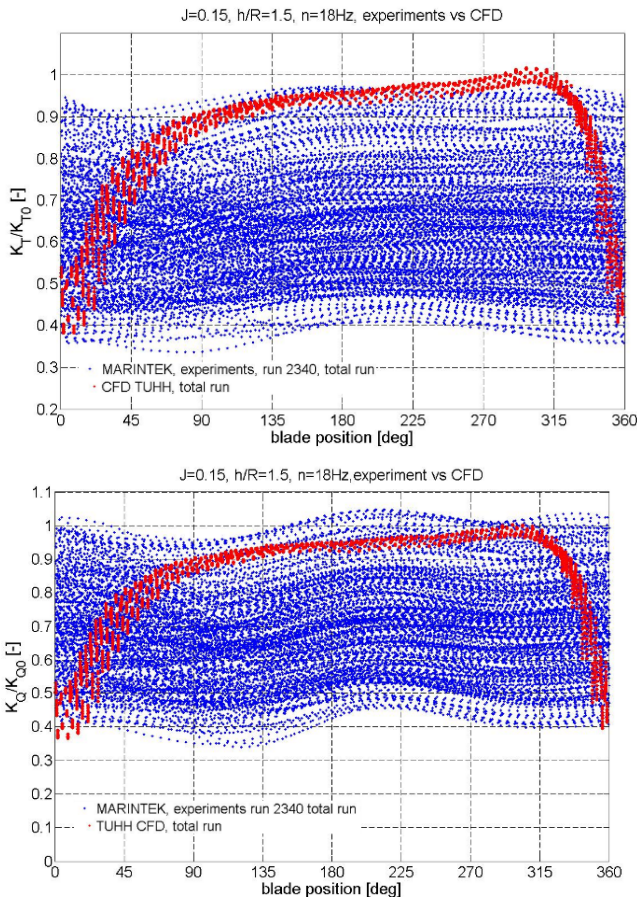
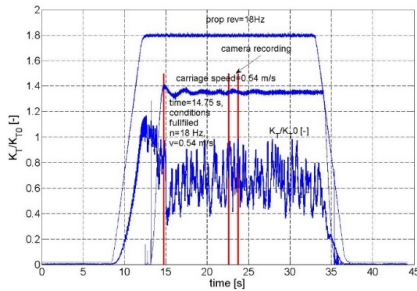


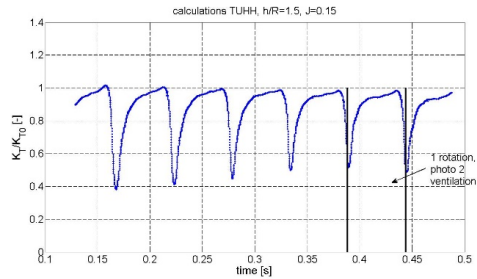
Figure 4-32 Comparison between calculated (CFD) and measured (Koz10) thrust (top side) and torque loss (bottom side) for  $J=0.15$ ,  $h/R=1.5$  and  $n=18\text{Hz}$ .

Figure 4-33 below shows the relation between the time of experiments and CFD simulations. It can be seen from the Figure 4-33a that the time for the propeller to reach the required speed of 18Hz is 14.75 s. This point can be treated as a starting point for the discussion. The whole run of experiment takes about 20 s (from starting point) which correspond to 360 propeller rotations. The first thrust drop occurred after 4.3 rotations. It means that this case can be comparable with the CFD computations, since in the CFD about 6 propeller rotations were simulated. The comparison between CFD computations and first thrust drop is shown in Figure 4-33d. The comparison between CFD and experiments shows one main difference: in the simulation results it is observed similar

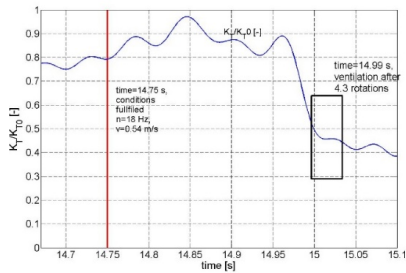
thrust and torque loss for every propeller revolution, while during measurements it is observed different thrust and torque losses depending on the duration of the experiments.



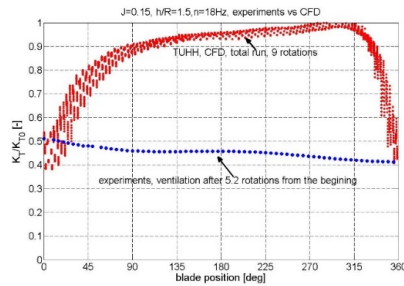
(a) Experiments, total run



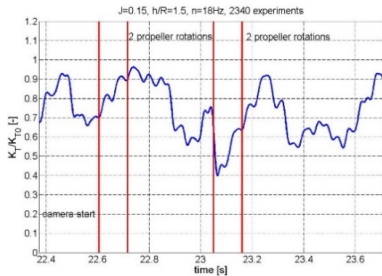
(b) CFD calculations, total run



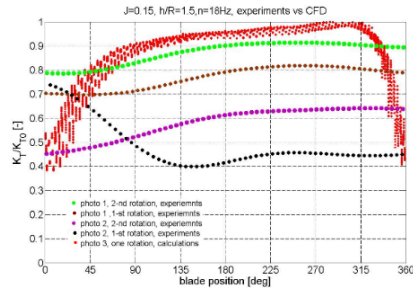
(c) One of the first thrust drops



(d) Comparison between one of the first thrust drops and CFD calculations



(e) Photo 1 & 2 cases chosen for comparison with CFD calculations



(f) Thrust ratio for photo cases chosen for comparison with CFD calculations

Figure 4-33 Comparison between calculated (CFD) and measured (Koz10) thrust loss for  $J=0.15$ ,  $h/R=1.5$  and  $n=18\text{Hz}$ .

Figure 4-34 shows that the propeller ventilates more during experiments. The tip vortex sucked down the air from FS and transported it in the direction of propeller rotation; most of the air was transported downstream. For experiments the connection between blade and

vortex are more significant. Thus, it is observed a fully ventilated case when the air cloud is covering the whole blade area. During CFD simulation the blade loses the connection with a vortex after passing 45 deg and fully ventilating case is not observed. This might be due to problems with resolving a thin ventilating vortex in CFD.

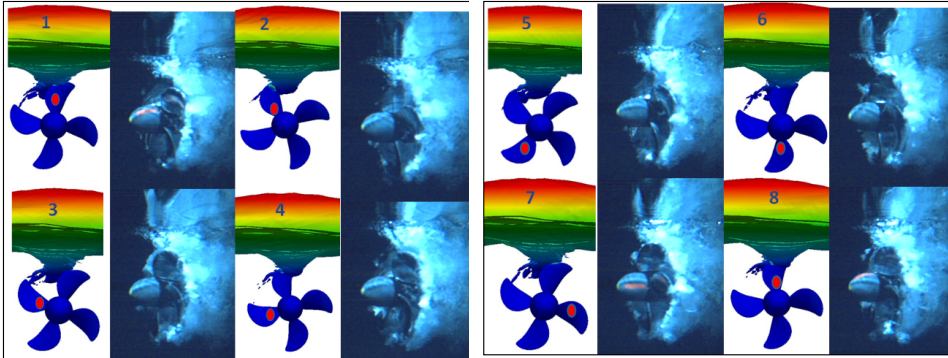


Figure 4-34 Comparison of flow around the propeller for experiments (Koz10) and simulations (CFD), fully ventilating regime is observed for one rotation,  $J=0.15$ ,  $h/R=1.5$   $n=18\text{Hz}$ .

It is worth mentioning that it is difficult to predict thrust losses based on the flow visualization from experiments. Figure 4-35 shows comparison between two different propeller rotations and the same blade position. The photos look very similar, the similar blade area is covered by air, but the blade thrust ratio is different for these two cases.

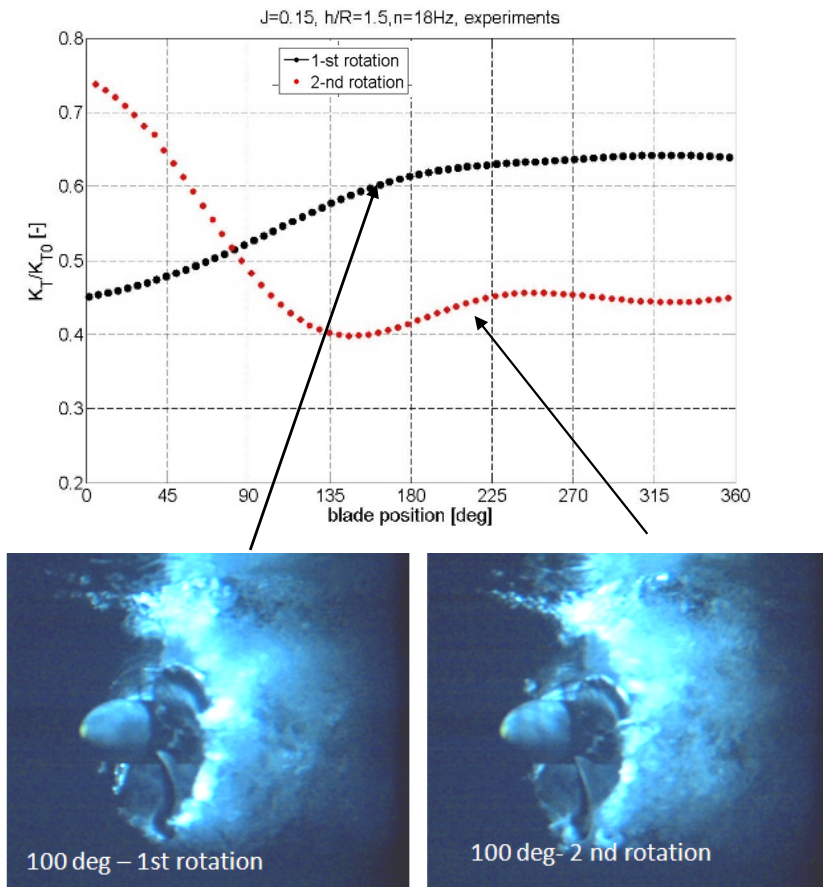


Figure 4-35 Comparison between two different propeller rotations and the same blade position (Koz10),  $J=0.15$ ,  $h/R=1.5$ ,  $n=18\text{Hz}$ .

### 4.10.3 $J=0.3$

Figure 4-36 shows that the thrust loss is bigger in the experiment. The main reason for this phenomenon is believed to be the time difference between the simulations and the experiments. During the experiments ( $J=0.15$ ,  $n=18\text{Hz}$ ,  $h/R=1.5$ ) 20s of measurements were recorded, which correspond to 360 propeller rotations. In order to compare these results with the calculations, the one should have the same number of propeller revolutions. For the calculations, only 6 propeller rotations were computed. The same phenomenon is observed for torque.

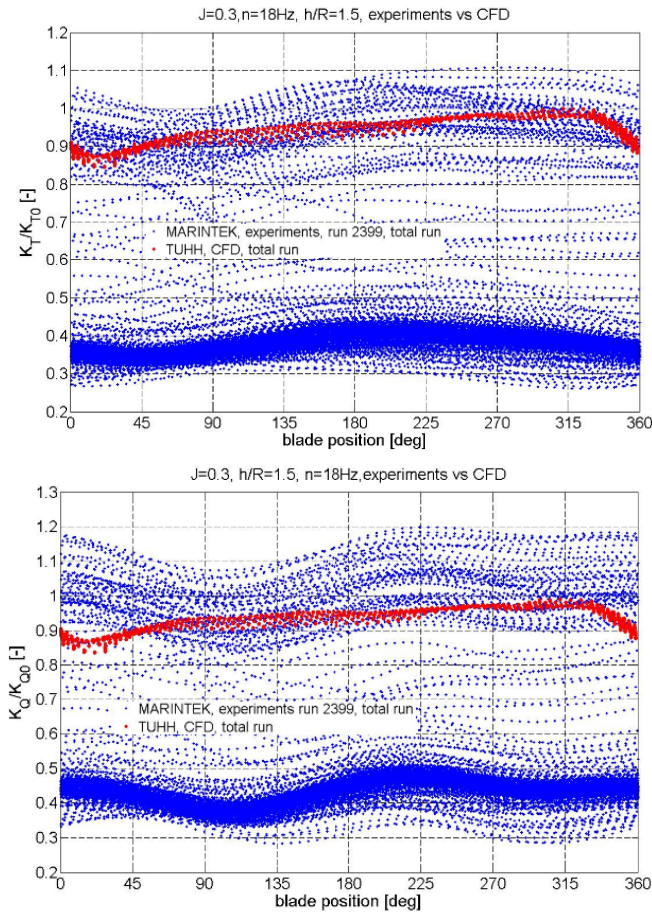
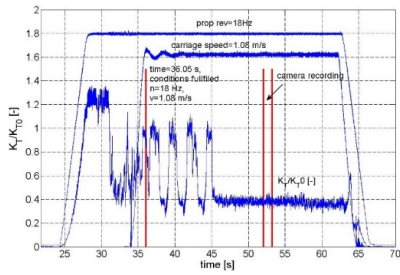
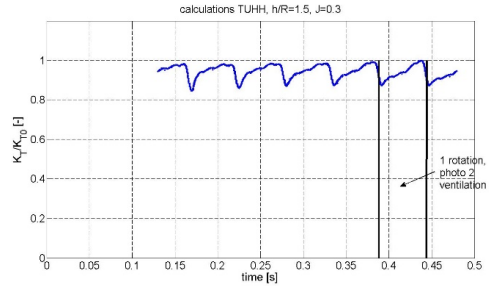


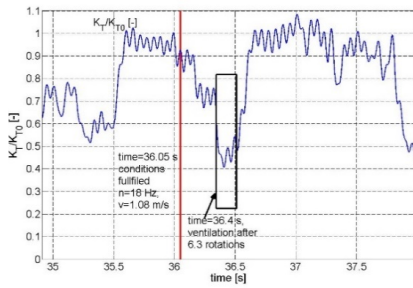
Figure 4-36 Comparison between calculated (blue color) and measured (red color) thrust (top side) and torque loss (bottom side) for  $J=0.3$ ,  $h/R=1.5$  and  $n=18\text{Hz}$ .



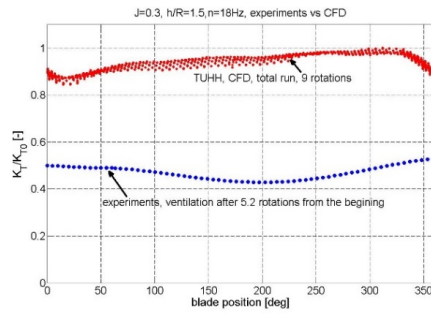
(a) Experiments, total run, two different flow regimes



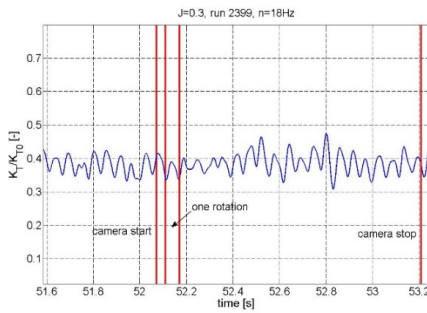
(b) CFD calculations, total run



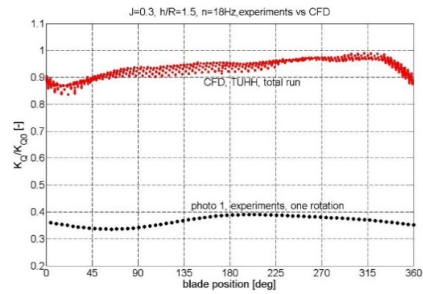
(c) One of the first thrust drops



(d) Comparison between one of the first thrust drops and CFD calculations



(e) Photo 1 & 2 cases chosen for comparison with CFD calculations



(f) Thrust ratio for photo cases chosen for comparison with CFD calculations

Figure 4-37 Comparison between calculated (CFD) and measured (Koz10) thrust loss,  $J=0.3$ ,  $h/R=1.5$  and  $n=18\text{Hz}$ .



*Figure 4-37* above shows the relation between the time of experiments and CFD simulations. It can be seen from the plots *Figure 4-37a* that the time for propeller to reach required speed equal to 18Hz takes 36.05 s. This point is called the starting point of the experimental results in the following discussion. The whole run of experiment takes about 30 s (from starting point). The first thrust drop occurred after 6.3 rotations from starting point. It means that CFD simulation can be compared with experimental results, since during CFD simulation about 6 propeller rotations were computed. The comparison between CFD computations and first thrust drop has been shown in *Figure 4-37d*. Comparison between calculation and experiments with respect to simulation time and time duration of experiments is summarized in *Table 4-4*.

Thrust (experiments)	Thrust (CFD)	Camera (experiments)	CFD (simulation)
Time (s)			
First thrust drop after 6.3 rotations	It was simulated 6 rotations	Camera started after 16.05 s from the beginning (starting point), which corresponds to 288 rotations.	Ventilating case (0.388s:0.444s) One rotation

*Table 4-4 Comparison of time of simulation with time duration of experiments Koz10,  $J=0.3$ ,  $h/R=1.5$ ,  $n=18\text{Hz}$ .*

*Figure 4-38* compares pictures of ventilation extent from experiments and CFD calculations. It shows that the propeller ventilates more during experiments than predicted by CFD. The tip vortex sucked down the air from FS and transported it in the direction of propeller rotation; most of the air was transported downstream. In the experiments, the connection between blade and vortex is more significant. Thus, it is observed fully ventilated case when the air cloud is covering the whole blade area. During CFD simulation blade loses the connection with a vortex after passing 20 deg and it is observed almost no thrust loss.

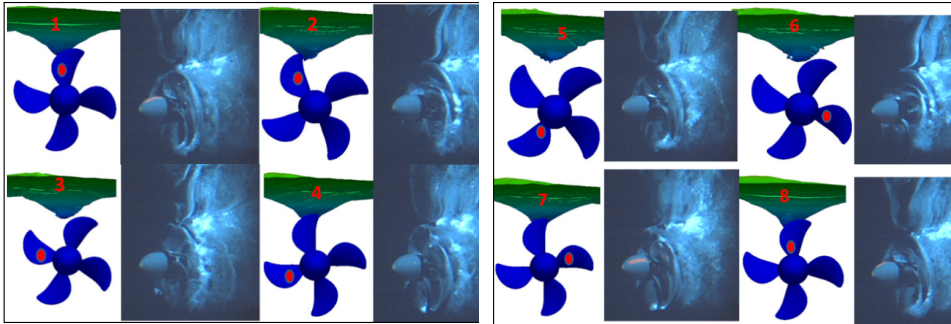


Figure 4-38 Comparison of flow around the propeller for experiments (Koz10) and simulations (CFD), fully or partially ventilating regime is observed for one rotation,  $J=0.3$ ,  $h/R=1.5$  and  $n=18\text{Hz}$ .

#### 4.10.4 J=0.6

Figure 4-39 and Figure 4-40 show good agreement between the calculations and the experiments. It is observed no thrust and torque loss during this case. This is because for high advance numbers ( $J=0.6$ ) the flow suppress the vortex and ventilation does not start in this case.

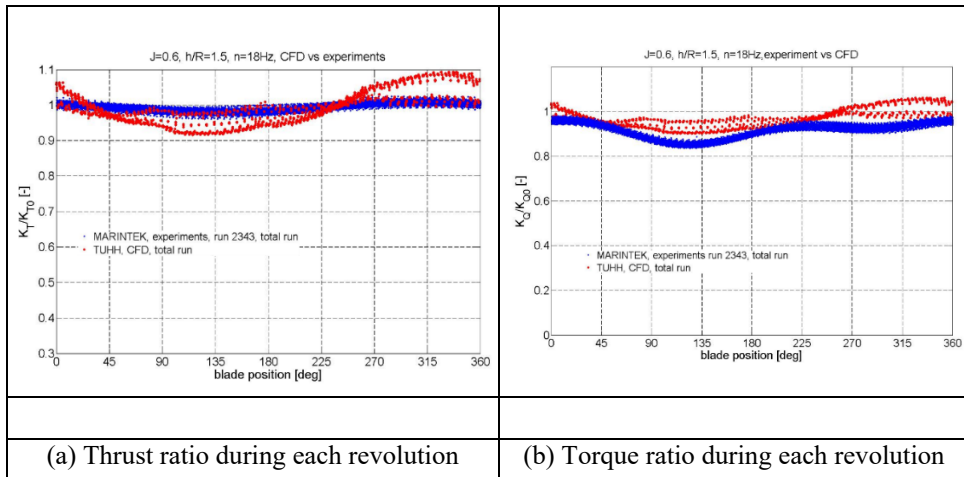


Figure 4-39 Comparison between calculated (CFD) and measured (Koz10) thrust and torque loss for  $J=0.6$ ,  $h/R=1.5$  and  $n=18\text{Hz}$ .

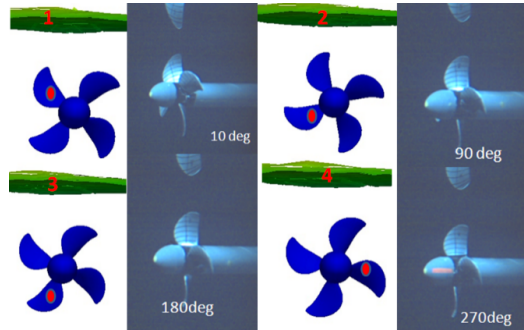


Figure 4-40.  $J=0.6$ , Comparison of flow conditions for experiments (Koz10) and simulations (CFD), non ventilating regime is observed for one rotation,  $J=0.6$ ,  $h/R=1.5$ ,  $n=18\text{Hz}$ .

Table 4-5 shows the minimum requirement in respect to time for ventilation inception based on experimental data and CFD calculation for advance numbers  $J = 0 - 1.2$ , propeller submergences  $h/R=1.5$ , and rotational speed  $n=18\text{Hz}$ .

Based on the Table 4-5 below the minimum time for ventilation to occur for bollard condition is equal to 5.5 propeller rotations for experiments and the total time for CFD simulation was 1.1s which correspond to 20 propeller rotations. For higher advance ratios i.e.  $J=0.3$  the first thrust drop due to ventilation occurs after 6.2 propeller rotation for experiments and CFD simulation time was equal to 0.44 s which correspond with 8 propeller rotations. In order to have good comparison between measurements and CFD calculation especially for low advance number, the CFD simulation time should be large enough to capture the first thrust drop measured during experiments.

	ventilation occurrence: <i>Koz10</i> Number of revolutions until ventilation starts	CFD calculations Number of revolutions during whole simulations
$J=0$	1 <sup>st</sup> – after 5.5 propeller rotations 2 <sup>nd</sup> – after 11.84 propeller rotations	20
$J=0.15$	1 <sup>st</sup> – after 4.2 propeller rotations	8
$J=0.3$	1 <sup>st</sup> – after 6.2 propeller rotations	8
$J=0.6, 0.9, 1.05, 1.2$	No ventilation	8

Table 4-5 Minimum requiremet in respect to time for ventilation based on experimental data and CFD calculation,  $J=0 - 1.2$ ,  $n=18\text{Hz}$ ,  $h/R=1.5$ .

### 4.10.5 Conclusions

Based on the comparisons presented in this *Chapter 4.10* the following conclusions are made:

- Thrust ratio for non-ventilating regime shows good correlation between the experiments and the calculations. The same good agreement is observed for the torque ratio.
- Flow visualization recorded by high-speed camera and simulation shows that the propeller ventilates more during the experiments than predicted by CFD. Ventilation starts by forming tip vortex, which sucks down the air from the free surface and transports it in the direction of the propeller rotation. During the experiments, the vortex is connected much longer to the blade than for the calculations. This might be due to problems with resolving a thin ventilating vortex in CFD. Also, problems representing air bubbles in the CFD might be a reason for the large difference in visual appearance.
- For the lowest advance numbers ( $J=0, 0.15, 0.3$ ), there is a marked difference between the experiments and the calculations with respect to how blade thrust varies with blade position. In the CFD, blade thrust has a strong variation with position, with large thrust loss around top position and small thrust loss around bottom position; while in the experiments the thrust loss is quite constant during a revolution. This difference might be explained by the fact that in the calculation the blade soon loses contact with the air-supplying vortex, while in the experiments it looks like the blade is continuously supplied with air from the surface.
- In order to have a better comparison between CFD and experiments, the simulation time and time duration of experiments should be more similar. The excessive amount of CPU time required makes it very difficult to perform computations for the same total number of revolutions as in the experiment. *Table 4-5* compares the time until the first ventilation event for experiments, and compares it to the number of revolutions simulated in CFD. Although the minimum requirement, first ventilation event, was fulfilled for all presented cases, we see that the simulated time is very short compared to the time-scale of the ventilation, and as a result, important phenomena might be missing from the simulation results due to the short simulated time



## 5 CALCULATION MODEL FOR THRUST LOSS DUE TO VENTILATION AND OUT OF THE WATER EFFECT

This chapter presents a prediction model for thrust loss due to ventilation and out of water effects. Since the flow physics are very complicated, first-principles based methods like potential flow panel methods or RANS-type CFD are very difficult to apply – see for instance Califano (2010), Kozłowska et.al. (2011) and Section 4.10.5 on the page 119. Therefore, there is a need for a practical method to provide a calculation tool that can be used to approximate the effect of propeller ventilation on the thrust and torque of propeller.

The calculation model presented in this chapter predicts the total thrust loss factor  $\beta_T = K_T/K_{Tn}$ , where  $K_T$  is the actual thrust coefficient and  $K_{Tn}$  is the time-averaged mean value of the thrust coefficient at the relevant advance number  $J$  obtained from the calm water, deeply submerged non-ventilated propeller. The calculation also predicts the ventilated blade area ratio  $A_V/A_0$  since it is required for the calculation of thrust loss in partial ventilation. Torque can then be estimated using the empirical relation between thrust loss factor  $\beta_T$  and torques loss factor  $\beta_Q$  presented in section 4.2.

A difficulty when creating the calculation model to study ventilation is covering all the ventilation regimes and submergences. The formulation of the model depends on the submergence, so in the following section, the calculation models valid for different submergences are explained in detail.

The calculation model presented in this chapter is compared and validated with experimental results from the *Kozl7* model tests.

### 5.1 DEEPLY SUBMERGED

When the propeller is deeply submerged it is considered not to experience any ventilation at any advance number. Therefore  $\frac{A_V}{A_0} = 0$  and the total thrust loss factor  $\beta_T = 1.0$ , meaning that there is no thrust reduction due to ventilation or out-of-water effects. In the calculation model, the limit for “deeply submerged” is set to  $h/R > 3.4$ .

## 5.2 SUBMERGED, VORTEX VENTILATION

In this regime of submergence, the propeller is prone to ventilation due to impact of a free surface vortex as explained in *Chapter 2*. Thrust loss for ventilating fully submerged propellers might be calculated using the idea presented by Kozłowska and Steen (2010), where the change in propeller blade lift coefficient due to ventilation is used to calculate the change of  $K_T$ .

Minsaas et.al. (1983) developed an expression for reduced thrust due to ventilation for fully ventilated propellers assuming that the suction side of the propeller blade is fully ventilated and the pressure on the pressure side of the propeller blade section is equal to static pressure. As explained in Section 2.1.6 on the page 22, that leads to the following expression for the thrust loss factor due to vortex ventilation.

$$\beta_{VC} = \frac{1.5EAR}{K_{Tn}} \cdot \left( \frac{\pi}{2} \alpha + \frac{2gh}{V_\infty^2} \right) \quad (5-1)$$

Where:  $g$  is acceleration of gravity,  $V_\infty$  is the relative velocity at the 70% radius propeller blade section,  $h$  is shaft submergence and  $\alpha$  is the angle of attack of the 70% radius propeller blade section.

Kozłowska and Steen (2010) conclude that this formula overestimate the thrust loss for deeply submerged propellers and underestimate the thrust loss for propellers working near the free surface. Kozłowska and Steen (2010) proposed a correction to equation (5-1) based on the assumptions that the thrust loss depends also on how much the blade area is covered by air. Thus, the lift coefficient for a partially ventilated propeller might be approximated from the formulas for lift coefficient of a non-ventilated flat plate and a fully ventilated flat plate, weighted by the ratios of ventilated and non-ventilated areas.

The resulting formula for the thrust loss due to ventilation is:

$$\beta_{VC} = \left( \frac{1.5EAR}{K_{Tn}} \cdot c_{LV} \cdot \frac{A_V}{A_0} \right) + \left( 1 - \frac{A_V}{A_0} \right) \quad (5-2)$$

where:  $A_V$  is ventilated propeller disc area,  $A_V=A_0$  means that the propeller is fully ventilated

$A_E/A_0$  is propeller blade area ratio,  $c_{LV}$  is the lift coefficient of the ventilated propeller, which can be calculated as:

$$c_{LV} = c_L(\sigma_V = 0) + \frac{2gh}{V_\infty^2} = \frac{\pi}{2}\alpha + \frac{2gh}{V_\infty^2} \quad (5-3)$$

The main problem with using equation (5-2) is to estimate the blade area that is covered by air  $A_V/A_0$ . For bollard condition ( $J < 0.1$ ) it is used the polynomial relation between the ventilated blade area ratio and submergences developed by Dalheim and presented by Steen et.al. (2016), see equation (2-21) on page 24.

By using the steady state vortex ventilation model based on the vortex model from Rott (1958) and the propeller momentum theory it is possible to estimate  $A_V/A_0$  due to vortex formation for advance numbers  $J \geq 0.1$ . The vortex model depends on two parameters: a source strength which is related to propeller loading and the ambient vorticity the sink is gathering to form the vortex. The ambient vorticity in the towing tank is partly generated by the propeller wake and therefore again related to the propeller load through the circulation. A tuning constant  $\eta_r$  is added to the calculation model in order to account for the effect that not all the propeller blade circulation is converted into ambient vorticity ( $0.6 \leq \eta_r \leq 0.8$ ). The vortex model from Rott (1958) is described in section 2.4.2 on the page 39.

### 5.2.1 Steady state vortex ventilation model

The proposed computational model for ventilating propellers uses a simplified approach to treat the complex problem of ventilation through a vortex terminating at the surface. The computational model is based on the idea by Luca Savio for predicting the vortex ventilation. The model implies many simplifications that are discussed here. The model assumes that the flow induced by the propeller can be approximated by the actuator disk model and that the vortex that draws air to the propeller is treated according to the model proposed by Rott (1958). The adoption of the actuator model enables simplifying largely the mathematical complexity of problem as it relates propeller operating parameters with fluid dynamic quantities in an elegant way. However, it bears also the limitations that are implicit to the method; among the limitations of the method, the following are the most critical for the presented model: it cannot tackle zero advance operating condition as that condition results in a singularity and it assumes that the chord wise distribution of load is constant. The vortex model proposed by Rott (1958) is based on an analytical solution of the Navier-Stokes equation for a particular flow condition. The particular flow condition assumes that there are two sinks that are at a distance  $2H$  from each other and that a vortex passes right through them. The two sinks generate a flow so that there exists a plane where



the velocities though the plane are equal to zero; this plane represents the water surface. This means that in the Rott model the water surface is undisturbed, which is in clear contradiction to the physical observation that the closeness of the propeller to the free surface generates waves. Further, the Rott model proposes a de-singularization of the commonly used Rankine vortex that assumes that there exists a viscous core of the vortex that is related to the viscosity of the fluid and the strength of the sinks. Finally, the vortex model does not include surface tension making it valid only for high Weber numbers.

The proposed calculation model combines the two models by computing the strength of the sinks through the actuator disk model. In case the tests are carried out in an enclosed space, like in the validation tests reported here, the actuator disk model is used also to compute the ambient vorticity as in this case the propeller is generating the vorticity that is gathered in the vortex. The first assumption is motivated by the fact that the propeller ventilation inception is related to both submergence and load. The second assumption is supported by the evidence that during tests in the towing tank the propeller tends to ventilate more easily after some time in operation.

The assumptions that are made here are many since the problem to be treated is complex and, since the goal of the method is to provide a calculation tool that could be used to approximate for simulations purposes the effect of propeller ventilation.

### **5.2.2 Actuator disk model**

The calculation model is based on the assumption that ventilation happens when the upstream suction radius  $R_A$ , computed by the momentum theory explained in *Section 2.3.1* is larger than the propeller submergence as shown in *Figure 5-1*. The continuous blue curves in *Figure 5-1* indicates the stream tube formed by the propeller.

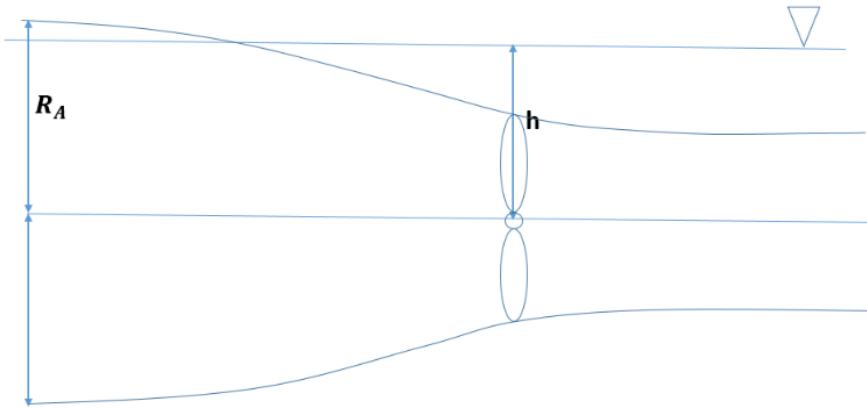


Figure 5-1 Sketch of propeller actuator disk stream tube, defining the upstream suction radius  $R_A$ .

Based on simple axial momentum theory one can express the ventilation suction radius as a function of propeller load factor  $c_{Tn}$  for non-ventilated deeply submerged propeller, see equation (2-12) on page 19. Ventilation suction radius is presented in equation (5-4) below.

$$R_A = (0.5 + 0.5 \cdot \sqrt{1 + c_{Tn}}) \cdot R \tag{5-4}$$

Figure 5-2 below, presents the definition of propeller emerged area  $A[m^2]$  and emerged area ratio  $AA_0[-]$ .

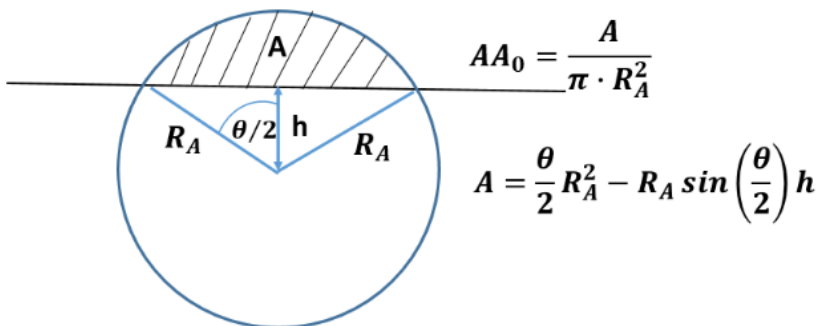


Figure 5-2 Propeller emerged area  $A[m^2]$  and emerged area ratio  $AA_0[-]$ .

$$AA_0 = \frac{A}{\pi \cdot R_A^2} \quad (5-5)$$

$$\frac{\theta}{2} = \arccos(h/R_A) = \frac{\theta}{2} R_A^2 - R_A \sin\left(\frac{\theta}{2}\right) h \quad (5-6)$$

### 5.2.3 Rott vortex model

For describing the flow on steady state, vortex ventilation model exact solution to the Navier Stokes is used see *Section 2.4.2*. The particular flow condition assumes that there are two sinks that are the distance  $2H$  from each other and that the vortex passes right through them. The two sinks generate the flow so that there exist a plane where the velocities through the plane are zero; this plane represent the water surface, for more detailed explanation see *Figure 2-13* on the *page 40*.

### 5.2.4 Sink strength from actuator disk

The flow model adopted is Rott vortex model. The sink strength is defined by  $q_3$  and it is related to propeller load. It is necessary to define an ambient vorticity the sink is gathering to form the vortex.

$$Q_P = V_0 \cdot \pi \cdot R_A^2 - \text{volumetric propeller flow rate} \quad (5-7)$$

$$q_3 = Q_P \cdot AA_0 \cdot \eta_\Gamma - \text{loss of propeller flow rate} \quad (5-8)$$

(The flow rate  $q_3$  is supposed to sustain the suction of the sink placed at the propeller center)

$$a = \frac{q_3}{2\pi h^3} - \text{flow gradient as defined in Rott (1958)} \quad (5-9)$$

The circulation of the propeller is derived by using approximate relation between propeller blade lift coefficient at 70% radius  $c_{L0.7}$ , thrust coefficient for non-ventilated, deeply submerged propeller  $K_{Tn}$  and blade area ratio  $EAR$ , which, according to Gutsche (1962) is valid for conventional propellers, see equation (2-17) on the page 23.

Using the Kutta Joukowski theorem, the lift coefficient can be linked to the circulation at the same blade section:

$$c_{L0.7} = \frac{\rho \cdot \Gamma \cdot V_c}{0.5 \cdot \rho \cdot V_c^2 \cdot c_{0.7}} \quad (5-10)$$

Where  $V_c$  is the local relative velocity at the blade section, which, when ignoring induced velocities can be calculated as  $V_c = \sqrt{V_A^2 + (0.7\pi nD)^2}$  where  $n$  is the propeller speed. By combining the two expressions for the lift coefficient, the expression for the circulation strength is obtained:

$$\Gamma = \frac{V_c \cdot c_{l0.7} \cdot K_T n}{3 \cdot E A R} \quad (5-11)$$

The deformation of the free surface is found according to:

$$\frac{\partial p}{\partial r} = \rho \frac{V_\theta^2}{r} \quad (5-12)$$

If it is considered the pressure drop to be counterbalanced by gravity it can be wrote as  $p = \rho g z$  which leads to:

$$\frac{dz}{dr} = \frac{1}{g} \frac{V_\theta^2}{r} \quad (5-13)$$

Which gives:

$$z(r) = h - \frac{1}{g} \cdot \int_\infty^r \frac{V_\theta^2}{r} dr \quad (5-14)$$

$$\left\{ \begin{array}{ll} \text{if } h + z(r) < 0 & A_{V0} = 1 - \text{fully ventilated} \\ \text{if } h + z(r) < R \text{ and } h + z(r) > 0 & A_{V0} = \frac{(R - (h + z(r)))^2}{R^2} - \text{part. ventilated} \\ \text{otherwise} & A_{V0} = 0 - \text{non ventilated} \end{array} \right. \quad (5-15)$$

## 5.2.5 Calculation diagram for thrust loss due to steady state vortex ventilation model

The procedure for calculating the thrust loss for fully, partially and non-ventilated regime, valid for  $J \geq 0.1$  and  $h/R \geq 1.2$  is shown in the calculation diagram, in *Figure 5-3*.

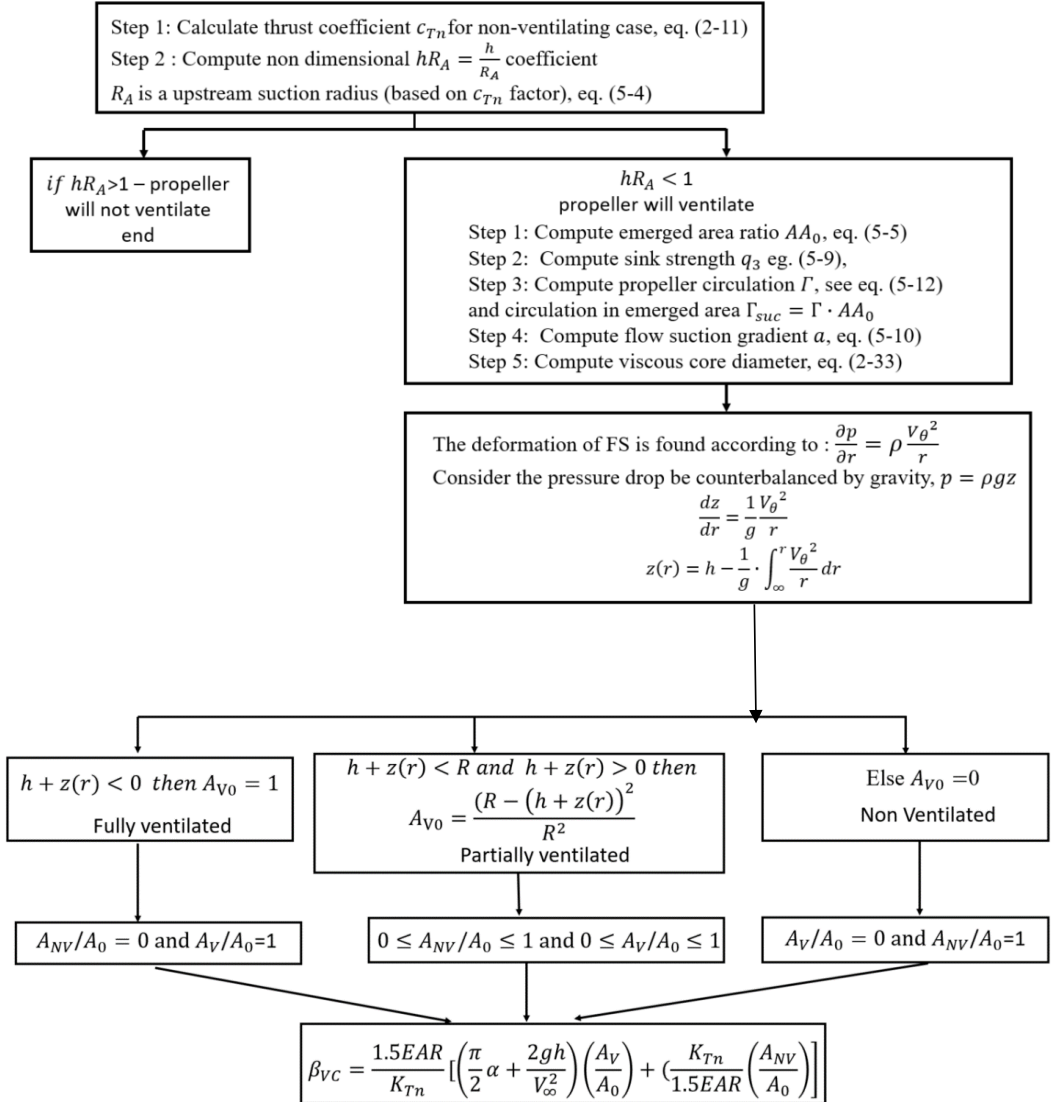


*Figure 5-3: Calculation diagram for thrust loss due to vortex ventilation for fully, partially and no ventilation regimes, valid for  $(J \geq 0.1$  and  $\frac{h}{R} \geq 1.2)$ .*

### 5.3 VENTILATION BY PIERCING THE FREE SURFACE

Free surface ventilation occurs for propeller submergences  $-1 < h/R < 1.2$ . The dominating thrust losses are not due to ventilation but due to loss of submerged propeller disk area. The thrust losses can be separated as follows: thrust loss due to loss of propeller disk area, thrust loss due to wave making, thrust loss due to ventilation and due to Wagner effect. For propeller submergence less than  $h/R < 1$  the thrust has to be corrected for loss of propeller disk area.

The total thrust losses can be divided in loss of propeller disk area ( $\beta_0$ ), Wagner effect ( $\beta_W$ ), steady wave motion ( $\beta_1$ ) and ventilation ( $\beta_{VC}$ ), see Section 2.1.7 on the page 24.

*Figure 5-4* presents the total thrust loss factor  $\beta_T = \beta_{VC} \cdot \beta_W \cdot \beta_0 \cdot \beta_1$  for high advance number  $J=1.0$ . As it is observed from the video recording, there is no ventilation for high advance numbers, thus  $\beta_{VC} = 1.0$ .

For the calculation an additional formula for thrust loss is introduced. It includes thrust loss due to loss of propeller disk area and thrust loss due to Wagner effect.

$$\beta_{W0} = \beta_0 \cdot \beta_W \quad (5-16)$$

Where  $\beta_0$  is calculated according to *equation (2-23)* and  $\beta_W$  according to *equation (2-24)*

The Minsaas formula in *equation (2-26)* claims to express total thrust loss, but it should be noted that the propeller loading is not a part of the expression. In *Figure 5-4* the thrust loss from experiments performed at a submergence of  $h/R=0$  (meaning that the propeller is submerged to the centre of the shaft) is shown. It is seen that the thrust loss is very sensitive to the advance number, representing variation of propeller loading. The Minsaas formula in *equation (2-26)* predicts a thrust loss factor of 0.325 which for this particular model corresponds to  $J=0.65$ . For  $J=1.0$ , corresponding to very lightly loaded propeller, the thrust loss factor is 0.4, see *Table 5-1*. From the photos in *Figure 5-4* it is seen that the propeller is free of ventilation for  $J=1.0$  for all submergences. The reason for larger thrust loss for lower  $J$  is believed to be mainly due to increasing amount of ventilation on the submerged part of the propeller. This hypothesis is based on observations of the model tests. Thus, it seems that the Minsaas formula is including some ventilation, corresponding to moderately loaded propeller.

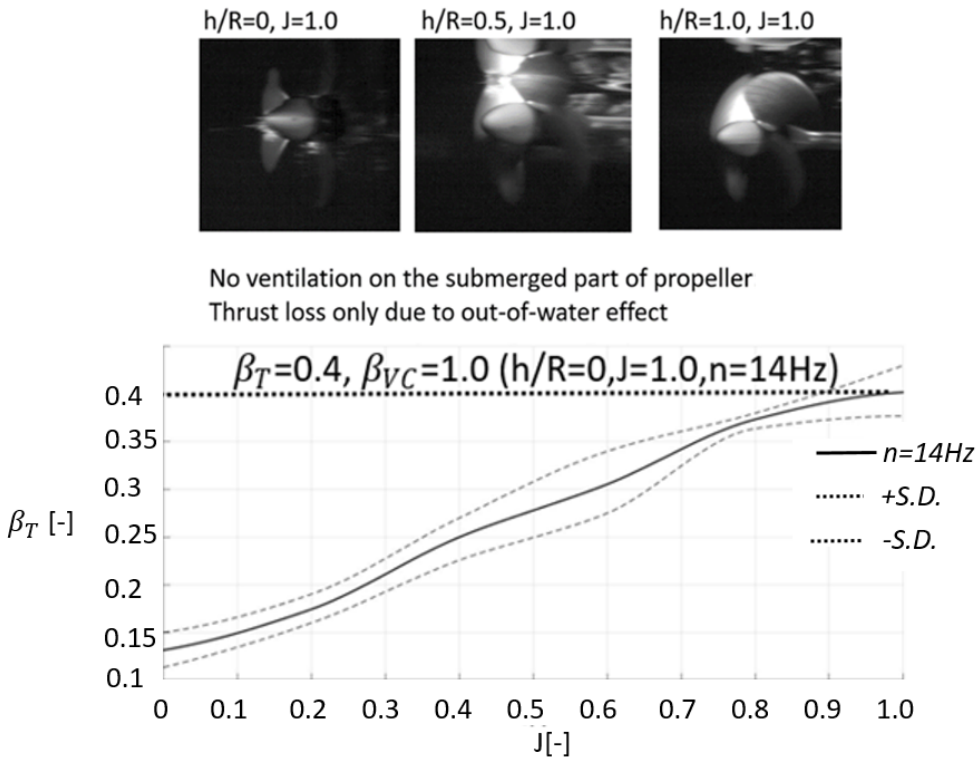


Figure 5-4: Total thrust loss factor  $\beta_T = \beta_{VC} \cdot \beta_W \cdot \beta_0 \cdot \beta_1$  for high advance number  $J=1.0, \beta_{VC} = 1.0$ .

Correction (red line) based on experiments	Experimental values presented in Figure 5-5
$h/R=1.0, J=1.0$	$\beta_T=0.95$ , see Figure 3-10
$h/R=0.5, J=1.0$	$\beta_T=0.65$ , see Figure 3-11
$h/R=0, J=1.0$	$\beta_T=0.4$ , see Figure 3-12

Table 5-1: Total thrust loss factor  $\beta_T = \beta_{VC} \cdot \beta_W \cdot \beta_0 \cdot \beta_1$  for high advance number  $J=1.0, \beta_{VC} = 1.0$

Figure 5-5 presents different thrust losses:

- Thrust losses calculated from Gutsche (1967) which include thrust loss due to loss of propeller disk area.

- Thrust losses calculated from Minsaas et.al. (1983) which include thrust loss due to loss of propeller disk area, wave making losses, Wagner effect as well as some ventilation, corresponding to moderately loaded propeller.
- Thrust losses due to loss of propeller disk area and Wagner effect.
- Experimental data, which include thrust loss due to loss of propeller disk area, Wagner effect and wave making losses. Since only high J-values are used to make this curve, the propeller is not ventilated.

By comparing the experimental values  $\beta_{exp} = \beta_W \cdot \beta_0 \cdot \beta_1$  and formula presented in equation (5-16) it can be noticed that the effect of thrust loss due to wave making by propeller  $\beta_1$  is negligible, thus the formula presented in equation (5-16) can be used to estimate the thrust loss due to out-of-the-water effect.

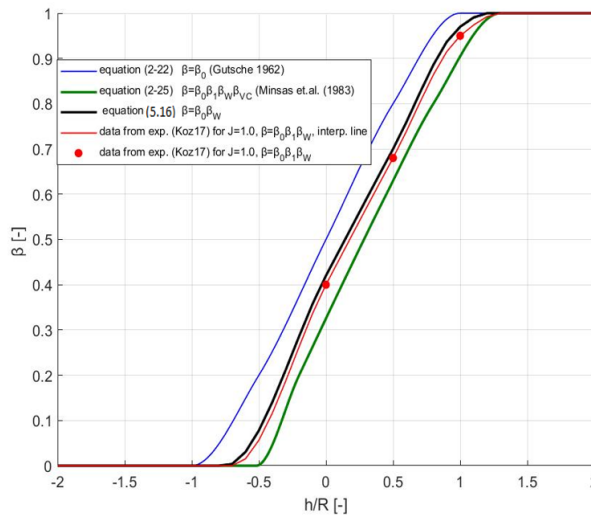


Figure 5-5: Thrust losses according to Gutsche (1967) - blue line, Minsaas et.al. (1983) - green line, thrust loss due to Wagner effect and loss of propeller disk area - black line, experimental values (Koz17) of total thrust loss factor  $\beta_T$  - red points and interpolation of experimental values (Koz17) - red line .

$\frac{A_V}{A_0}$  has been estimated based on visual observation from Koz17 experiments, see Table 5-2 and Figure 5-6 below



	$0 \leq J \leq 0.2$	$0.2 < J \leq 0.4$	$J > 0.5$
$h/R=1.0$	$\frac{A_V}{A_0} = 1$	$0.2 < \frac{A_V}{A_0} \leq 1$	$0.2 < \frac{A_V}{A_0} < 0$
$h/R=0.5$	$\frac{A_V}{A_0} = 1$	$\frac{A_V}{A_0} = 1$	$0.2 < \frac{A_V}{A_0} < 0$
	$J=0$	$0 < J \leq 1.0$	$J=1$
$h/R=0$	$\frac{A_V}{A_0} = 1$	$0 < \frac{A_V}{A_0} < 1$	$\frac{A_V}{A_0} = 0$
$h/R= -0.5$	$\frac{A_V}{A_0} = 1$	$0 < \frac{A_V}{A_0} < 1$	$\frac{A_V}{A_0} = 0$
$h/R= -1.0$	$\frac{A_V}{A_0} = 1$	$\frac{A_V}{A_0} = 1$	$\frac{A_V}{A_0} = 1$

Table 5-2: Ratio of ventilated propeller disk area to nominal disk area as a function of advance number for ( $h/R=1.0, 0.5, -0.5$  and  $-1.0$ ).

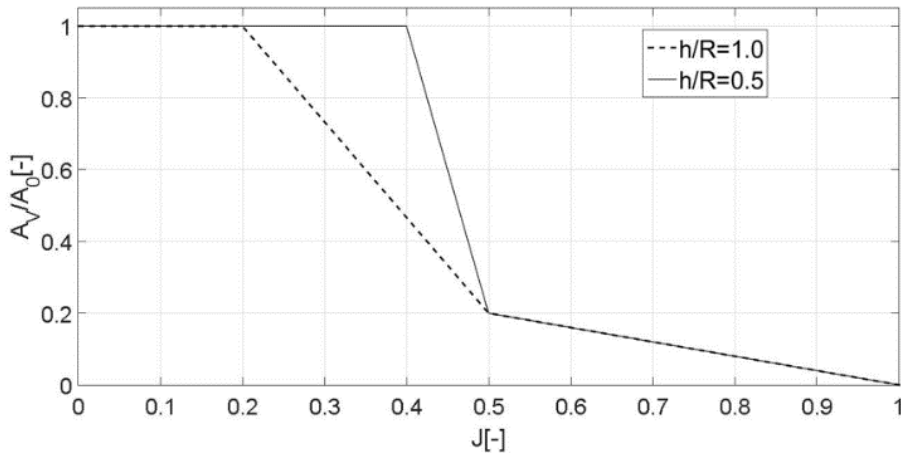


Figure 5-6: Ratio of ventilated propeller disk area to nominal disk area as a function of advance number for ( $h/R=1.0$ ) and ( $h/R=0.5$ ).

The total thrust losses are the summary of thrust loss due to ventilation and out-of-water effect, which include loss of propeller disk area, equation (2-23) and Wagner effect, equation (2-24). It was assumed that wave making by the propeller has negligible effect on thrust loss and can be omitted. Ventilating blade area ratio  $A_{V0}$  has been estimated for different advance numbers based on visual observation from *Koz17* experiments. Our data

shows that for propeller submergence  $h/R \leq 1.2$  the effect of different propeller revolutions is not so important for ventilation and thrust loss. Loss of propeller disk area was estimated by using purely geometrical considerations as in Gutsche (1967) and the Wagner effect accounts for dynamic lift effect and include the effect of the local relative velocity at the blade section. The empirical expression developed by Minsaas et.al. (1983), equation (2-26) for the combined effect of loss of disk area, wave making and Wagner effect has not been used in the calculation of the total thrust loss, instead equation (5-16) is used. The conclusion was that this formula is including effect of some ventilation, corresponding to a moderately loaded propeller.

#### 5.4 OVERVIEW OF COMPLETE CALCULATION MODEL

The complete calculation model to study ventilation and out-of-water effect covers the thrust loss prediction for the range of different propeller submergence  $h/R$ , propeller revolutions  $n$  and propeller advance number  $J$ . The calculation model predicts the total thrust loss factor  $\beta_T = K_T/K_{Tn}$  and the ventilated propeller disk area ratio  $A_{V0} = A_V/A_0$ . The procedure for calculating the thrust loss for fully, partially and non-ventilated regime is shown in the calculation diagram in *Figure 5-7*. When the propeller is deeply submerged  $h/R > 3.4$  it is considered not to experience any ventilation at any advance number. Therefore the total thrust loss factor  $\beta_T = 1.0$ . For  $1.2 \leq h/R < 3.4$  the propeller is prone to ventilation due to impact of a free surface vortex. Thrust loss for ventilating fully submerged propellers has been calculated using the idea presented by Kozłowska and Steen (2010). The main problem is to estimate the blade area, which is covered by air  $A_{V0}$ . For bollard condition it is used the polynomial relation between the ventilated blade area ratio and submergences developed by Dalheim and presented by Steen et.al. (2016). As a practical solution, the polynomial valid for bollard condition might be applied up to  $J < 0.1$ . For advance numbers  $J \geq 0.1$  the ventilated blade area ratio  $A_{V0}$  is calculated by using the steady state vortex ventilation model based on the vortex model from Rott (1958) and the propeller momentum theory. For propeller submergence  $-1 < h/R < 1.2$  the propeller experience free surface ventilation. The total thrust losses are the summary of thrust loss due to ventilation and out-of-the-water effect, which include loss of propeller disk area and Wagner effect. It was assumed that wave making by propeller has negligible effect on thrust loss and can be omitted. Ventilated blade area ratio  $A_{V0}$  has been estimated based on visual observation from experiments performed by *Kozl7*.

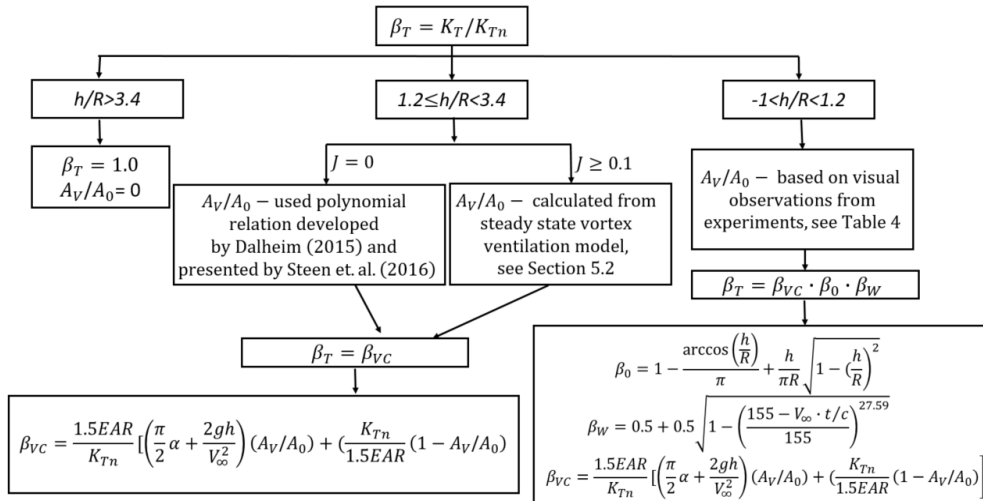


Figure 5-7: Calculation model to study ventilation and out-of-water-effect.

## 5.5 COMPARISON BETWEEN CALCULATION MODEL AND EXPERIMENTAL RESULTS (KOZ17)

In this section, the computational results for the propeller P1374 are compared with experimental results *Koz17*.

### 5.5.1 Comparison between calculations and experiments – amount of blade area ventilation

Figure 5-8 shows ventilated blade area ratio that is estimated by visual observations (high speed video) from experiments. Figure 5-9 shows the ventilated blade area ratio obtained by calculation using the steady state vortex ventilation model compared to the results of visual observations from experiments. The agreement between the calculation and experimental values is considered to be very good.

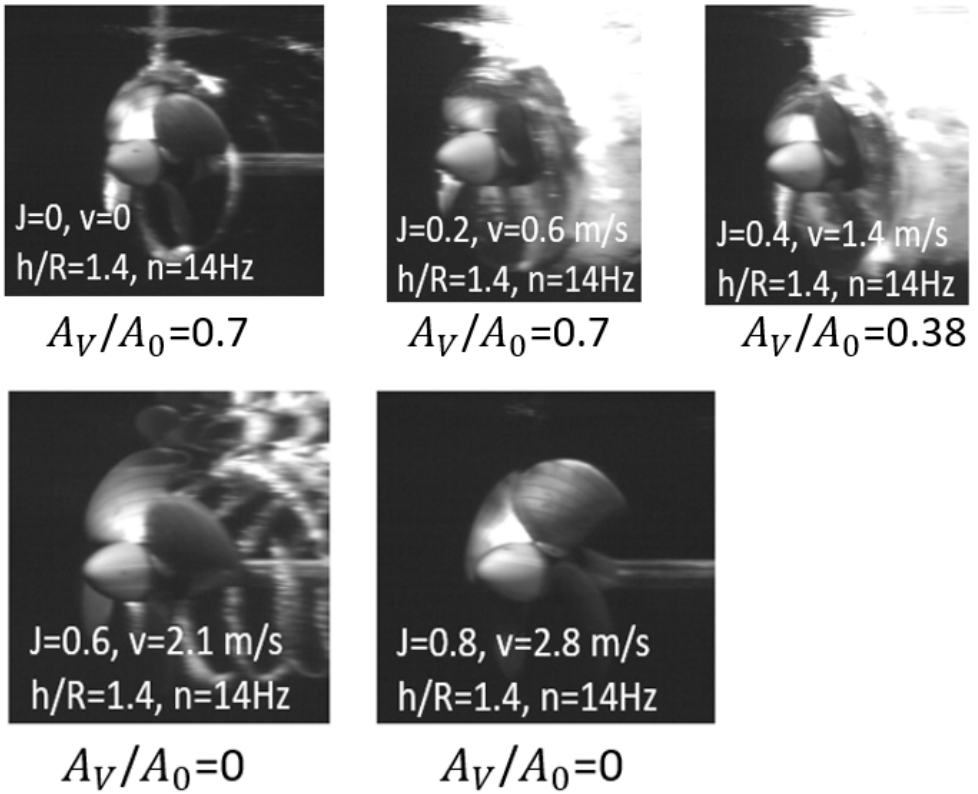


Figure 5-8: Ventiladed blade area ratio estimated by visual observation from experiments.

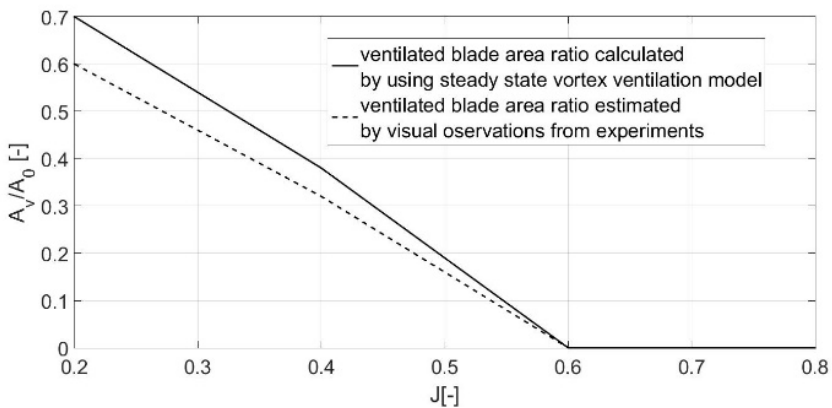


Figure 5-9: Ratio of ventilated propeller disk area  $A_v/A_0$  as a function of advance number for  $h/R=1.4$  based on calculations and visual observations from experiments.

Figure 5-10 shows the ratio of ventilated propeller disk area to nominal disk area as a function of advance number and submergence for  $n=16\text{Hz}$ , based on calculations  $h/R \geq 1.2$  and visual observations from experiments  $h/R < 1.2$ . The amount of ventilated propeller disk area is further used for thrust loss calculations, the results of which are shown in the next sub-chapter.

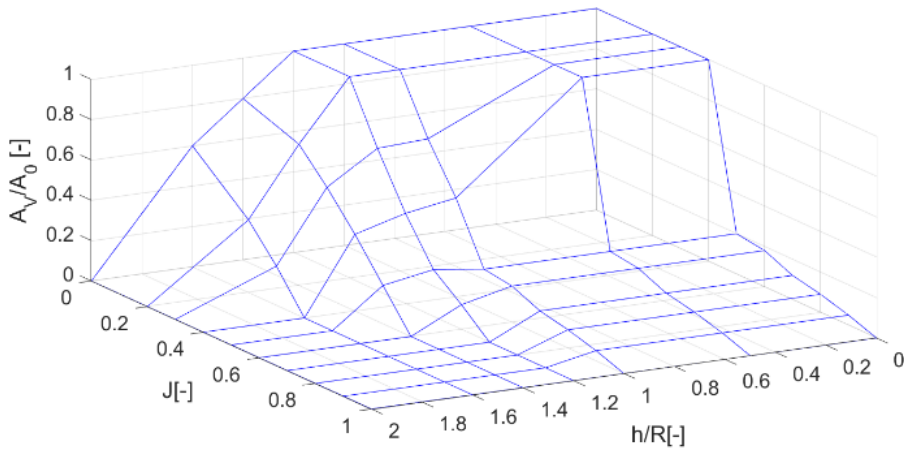


Figure 5-10: Ratio of ventilated propeller disk area to nominal disk area as a function of advance number for  $0 \leq h/R \leq 2.0$  and  $0 \leq J \leq 1.0$  for  $n=16\text{Hz}$ . For  $h/R \geq 1.2$  it is based on calculations and for  $h/R \leq 1.2$  it is based on visual observations from experiments.

### 5.5.2 Comparison between calculations and experiments – thrust loss

Figure 5-11, Figure 5-12 and Figure 5-13 show comparison between the calculations and the experiments for thrust loss as a function of advance number for the following propeller revolutions:  $n = 12, 14$  and  $16\text{Hz}$ . Figure 5-11, is for a submergence ratio of  $h/R=1.6$ , Figure 5-12 is for  $h/R=1.4$  and Figure 5-13 is for  $h/R=1.2$ . The agreement between calculations and experimental results is considered to be very good. As already mentioned, for  $n=12$ , effects of surface tension might influence the experimental results. For  $h/R \geq 1.2$  and  $J \geq 0.2$  the effect of propeller rotational speed and of inflow speed on ventilation it is taken into account in the vortex ventilation model. For  $h/R \geq 1.2$  and  $0 \leq J < 0.2$  propeller loading is not directly included as loading is “high” for practical cases, so this is not critical to include as a parameter. For  $-1 < h/R < 1.2$  the propeller

experience free surface ventilation and our data shows that propeller loading is not so important for ventilation inception and thrust loss due to ventilation.

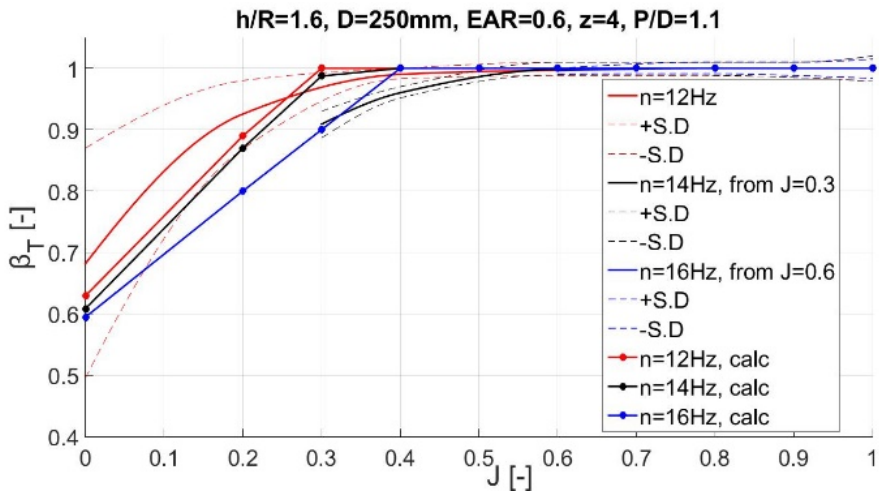


Figure 5-11: Thrust loss due to ventilation as a function of advance number for  $h/R=1.6$

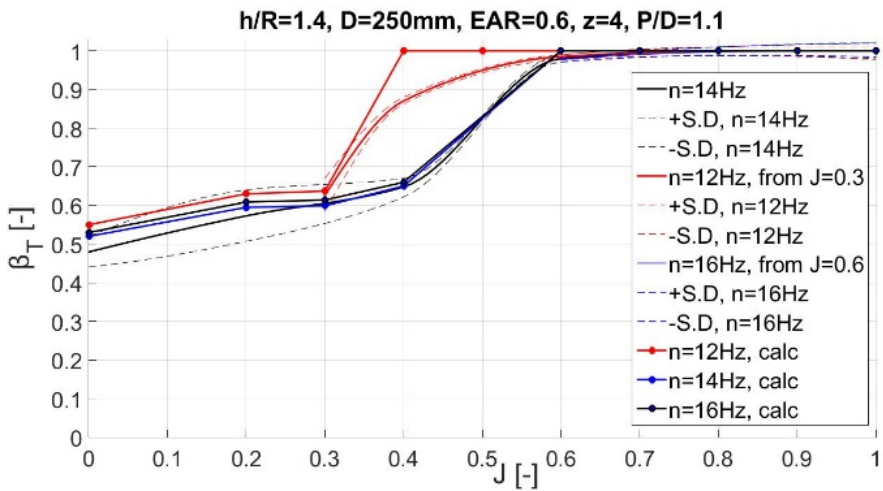


Figure 5-12: Total thrust loss as a function of advance number for  $h/R=1.4$ .

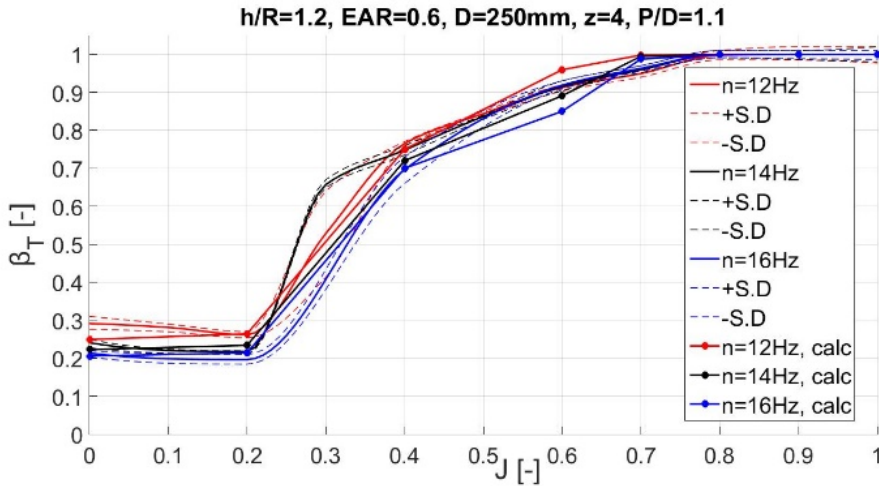


Figure 5-13: Total thrust loss as a function of advance number for  $h/R=1.2$ .

Figure 5-14 and Figure 5-15 show comparison between the calculations and the experiments for thrust loss due to free surface ventilation and out of the water effects as a function of advance number for the following propeller revolutions:  $n = 14$  and  $16\text{Hz}$ . Figure 5-14 is for a submergence ratio of  $h/R=1.0$ , while Figure 5-15 is for  $h/R=0.5$ .

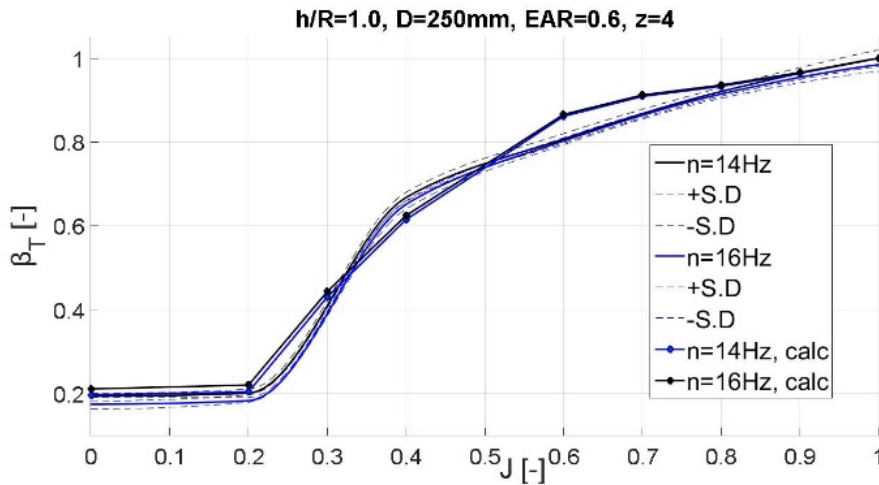


Figure 5-14: Comparison between calculation and experimental values of thrust loss due to free surface ventilation for  $n=14$  and  $16\text{Hz}$ ,  $h/R=1.0$ .

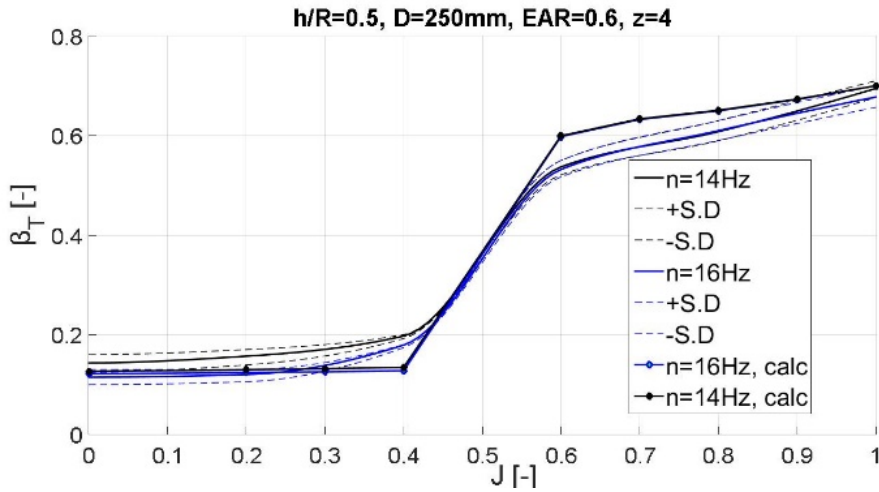


Figure 5-15: Comparison between calculation and experimental values of thrust loss due to free surface ventilation for  $n=14$  and  $16\text{Hz}$ ,  $h/R=0.5$ .

Figure 5-16 shows a 3D comparison between thrust loss due to vortex ventilation, free surface ventilation and out-of-water effects for calculated and experimental values, as a function of advance number  $0 \leq J \leq 1.0$  and propeller submergence  $0 \leq h/R \leq 2.0$ .

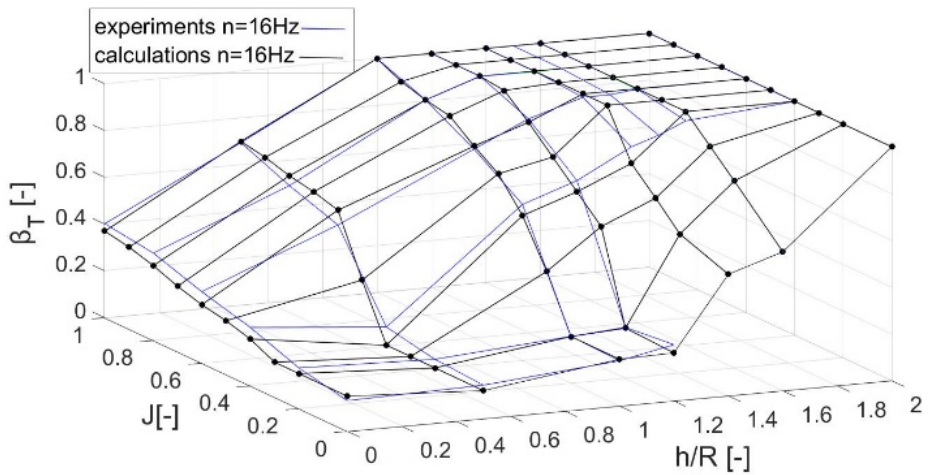


Figure 5-16 Comparison between calculation (black line,  $n=16\text{Hz}$ ) and experimental values of thrust loss due to ventilation and out of the water effects for  $0 \leq h/R \leq 2.0$  and  $0 \leq J \leq 1.0$ .





## 6 SIMULATION MODEL FOR THRUST LOSS DUE TO VENTILATION AND OUT OF THE WATER EFFECT

This chapter presents the time-domain simulation model PropSim (2018) for propeller forces due to vortex ventilation. The propeller simulation model is a further development of Dalheim's model, see Steen et.al. (2016), which was updated by including a physical model for estimating ventilated blade area based on propeller loading. The ventilated blade area ratio is computed using the steady-state vortex ventilation model based on the vortex model by Rott (1958) and the propeller momentum theory as it was described in section *Section 2.4.2* and *Chapter 2*. The simulation model PropSim (2018) is static in the sense that it is assuming that the response is quasi steady and based on the calculation model presented in *Chapter 2*.

It is also discussed in this chapter how the dynamic effects i.e. hysteresis effect and blade frequency dynamics can be included in the simulation model PropSim (2018).

### 6.1 TIME DOMAIN SIMULATION MODEL: PROPSIM 2018 AND PROPSIM 2016

The simulation model PropSim (2016) was developed by Dalheim (2015) and implemented into Simulink. The simulation model generates a time domain solution to the six degree of freedom propeller forces in varying operating conditions including: change of operating point, unsteady axial and tangential flow field, effect of oblique inflow in manoeuvring condition, Wagner effect, reduced propeller submergence and ventilation. The time domain simulation model in PropSim (2016) is quasi-static. For ventilation modelling PropSim (2016) used a formula based on an idea presented in Kozłowska and Steen (2010), where the change in lift coefficient due to ventilation is used to compute the change in  $K_T$ , resulting in the formula for the thrust loss calculations due to ventilation presented in equation (2-19). The main problem with equation (2-19) is to determine the amount of ventilation on the blades. For the PropSim (2016) simulation model, Dalheim used model tests from Kozłowska and Steen (2010) to construct a polynomial relation for the value of ventilated blade area ratio  $A_V/A_0$ . *Figure 6-1* contains two different curves, one for increasing and one for decreasing propeller submergence, which indicate the propeller hysteresis behaviour of the propeller ventilation.

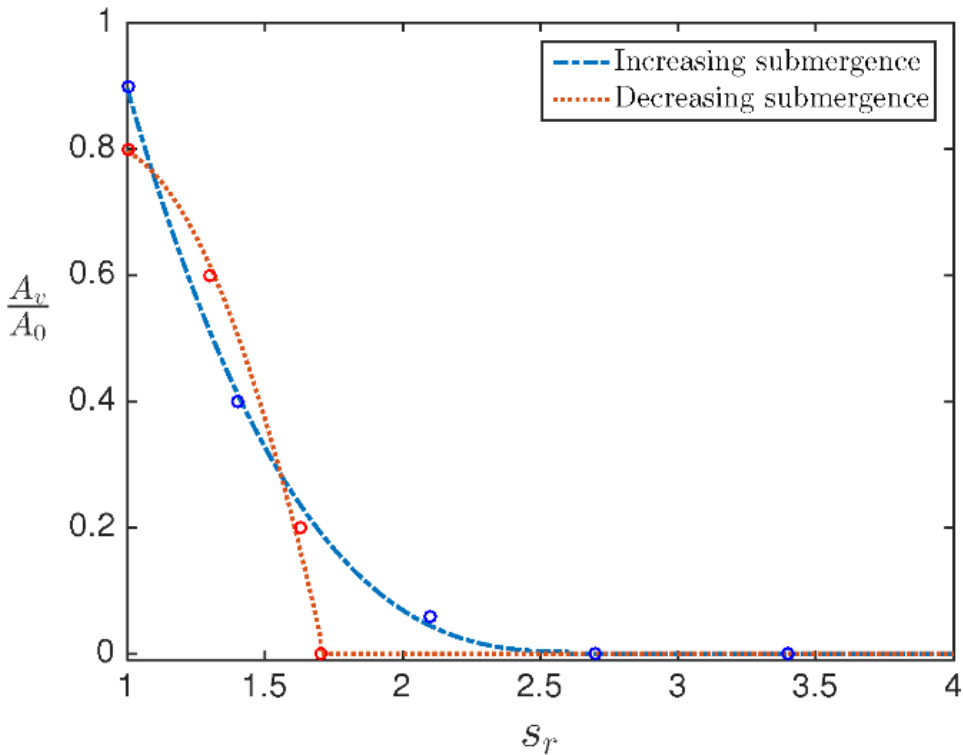


Figure 6-1 Ratio of ventilated propeller disk area to nominal disk area as function of propeller submergence ratios  $s_r$ , Dalheim (2015). Submergence ratio is denoted by the symbol  $s_r$ , for the other part of the thesis except Figure 6-2  $h/R$  relation to describe the same submergence factor is used.

The relation presented in Figure 6-1 can hardly be viewed as generally valid since other factors like forward speed and propeller loading must be expected to matter, Steen et. al. (2016). Therefore, the simulation model has been updated by adding the physical model for estimating the ventilated area of the propeller disc based on propeller loading and submergence, as outlined in Chapter 5. Like PropSim (2016), the simulation model PropSim (2018) is quasi static, since it is assuming that the response is quasi steady and based on the calculation model presented in Chapter 5.

## 6.2 SIMULATION MODEL VALIDATION

Validation of the simulation model denoted PropSim (2018) is carried out using model experiments performed by *Kou2006\_I* and *Koz17*. *Kou2006\_I* experiments were performed on an open pulling propeller exposed to forced sinusoidal heave motion, as explained in detail in Section 3.9. The carriage speed  $U$  and the propeller shaft frequency  $n$  were varied in order to obtain low advance numbers  $J$  (around 0.1). In order to obtain more data for validation purpose in higher advance numbers *Koz17* experiments were performed. These cases have been used for validation of the simulation model due to absence of data under dynamic heave motions for advance numbers higher than  $J=0.1$ . Also, it is believed that the hysteresis effect is connected with ventilating vortex so for high advance numbers, when the vortex ventilation does not appear, it has not a significant effect for thrust loss.

*Figure 6-2* shows the comparison between simulation performed by using PropSim (2016) and PropSim (2018) simulation models and experimental results, *Kou2006\_I*. PropSim (2016) model relate thrust loss to estimated ventilated blade area on an empirical relation that is based on the same model experiments as shown in the figure (*Kou2006\_I*). This is believed to be the reason why for this particular case the agreement between experimental results and calculation fitted better to 2016 version of the simulation model.

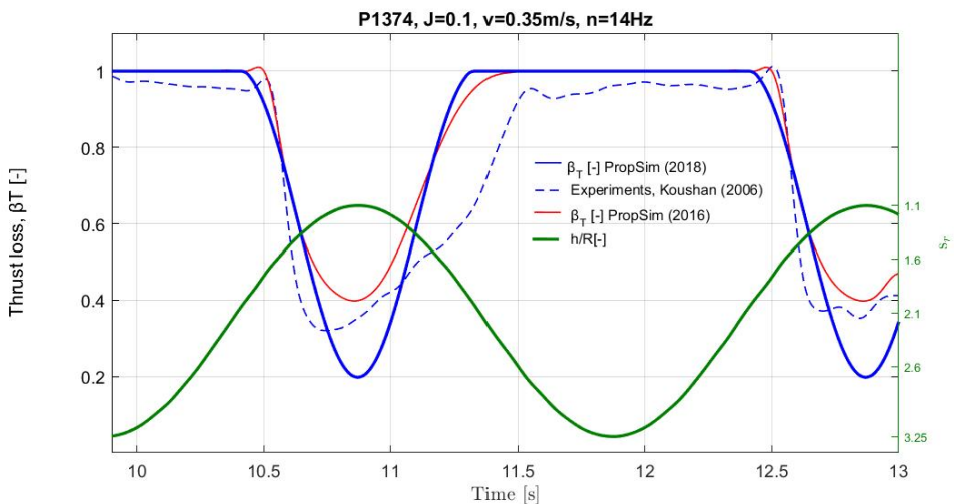


*Figure 6-2 Comparison of thrust loss between simulation performed by using PropSim(2016) simulation model, PropSim (2018) simulation model and experimental*

results Kou 2006\_I. Propeller submergence is denoted by the symbol  $s_r[-]$  only in this figure, for the other part of the thesis it is described as  $h/R [-]$ .

Figure 6-3 shows the comparison for thrust loss calculation between two different versions of the simulation model: PropSim (2016) and PropSim (2018). Propeller thrust loss is calculated for propeller working with constant propeller revolutions  $n=12\text{Hz}$  under dynamic heave motion conditions ( $1.2 \geq \frac{h}{R} \geq 2.2$ ) for high advance number  $J=0.4$ . There is no experimental conditions testing propeller ventilation during dynamic heave motion for high advance numbers, thus for validity purpose the simulation model results have to be compared with static conditions based on Koz17 experiments, implicitly assuming that the behaviour is quasi-static. It can be observed from Figure 6-3 that the thrust loss prediction agreed better with calculations performed by using the simulation model PropSim (2018). Simulation model PropSim (2016) overestimate thrust losses due to ventilation. For example for  $h/R=1.2$  the thrust loss due to ventilation is 0.84 based on propSim (2018) simulation model and is in the range of 0.45-0.5 for PropSim (2016) simulation model. The experimental measurements are equal to 0.78, which is closer to the updated simulation model PropSim (2018). The same behaviour were observed for other submergences,  $h/R=1.4, 1.6$  and  $2.0$ .

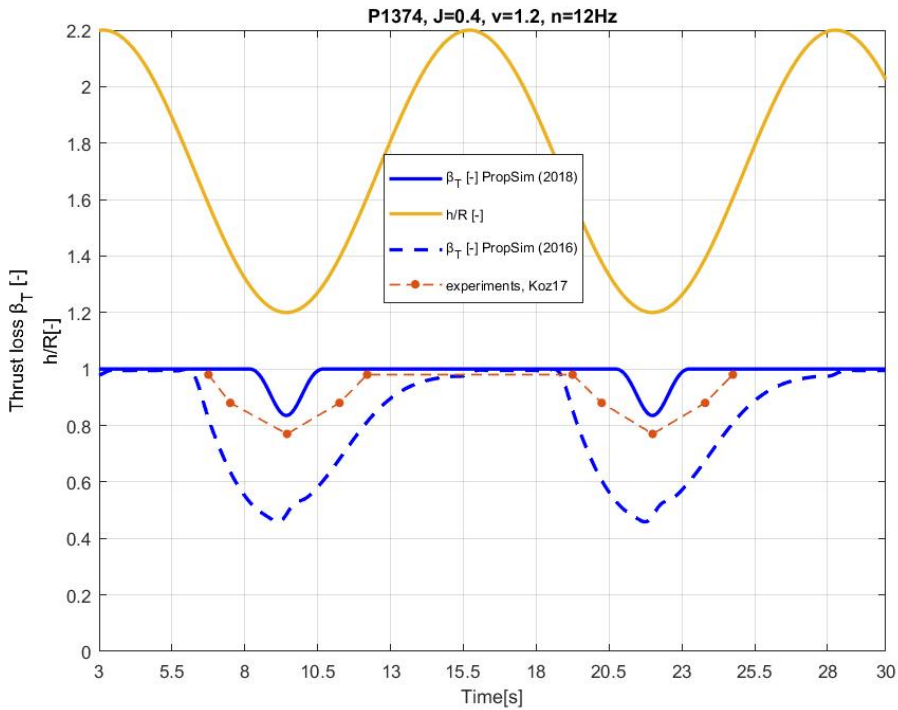


Figure 6-3 Comparison for thrust loss between simulation performed by Dalheim (PropSim(2016)) and Kozłowska (PropSim (2018)) and experimental results Koz17.

Figure 6-4 shows the comparison of thrust loss calculation using PropSim (2016) and PropSim (2018) simulation model. Propeller thrust loss is calculated for propeller working with constant propeller revolutions  $n=12\text{Hz}$  under dynamic heave motion conditions ( $1.2 \geq \frac{h}{R} \geq 2.2$ ) for high advance number  $J=0.6$ . There is no experimental conditions testing propeller ventilation during dynamic heave motion for high advance numbers, thus for validationary purpose the simulation model results have to be compared with static conditions based on the experiments Koz17. It can be observed from Figure 6-4 that the thrust loss prediction agreed better with calculation for simulation model PropSim (2018). Simulation model PropSim (2016) overestimate thrust losses due to ventilation. For example for  $h/R=1.2$  the thrust loss due to ventilation is 1.0 based on propSim (2018) simulation model and is in the range of 0.45-0.5 for PropSim(2016) simulation model. The experimental measurements are equal to 0.92, which is closer to the updated simulation model PropSim (2018). Also, experimental data based on experiments Koz17 shows no

thrust loss for  $J=0.6$  for submergence ratio  $1.4 \geq h/R \geq 2.2$ , the same as it was predicted by using PropSim (2018) simulation model.

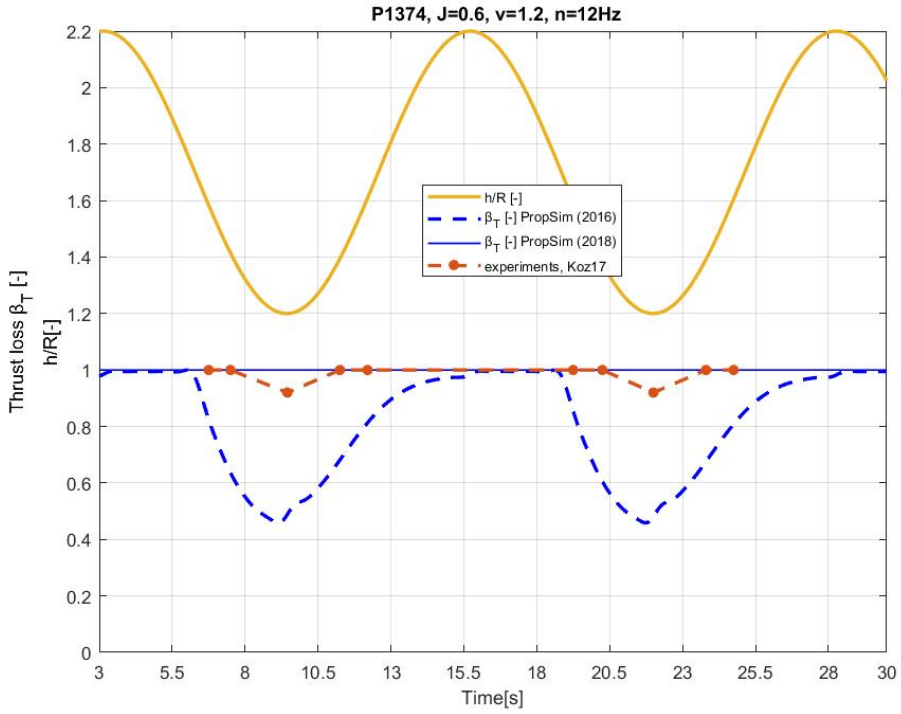


Figure 6-4 Comparison for thrust loss between simulation performed by Dalheim (PropSim(2016)) and Kozłowska (PropSim (2018)) and experimental results Koz17.

### 6.2.1 Dynamic effect causing hysteresis of the thrust loss during heave motion of the propeller: PropSim (2018\_hysteresis)

A significant dynamic effect of the propeller ventilation is connected with thrust and torque hysteresis effect, appearing mostly in connection with intermittent vortex ventilation. The hysteresis effect is caused by the fact that it takes a while for ventilation of a submerged propeller to be established, so in a situation with decreasing submergence or increasing propeller loading, there is less thrust loss than for the same condition in static operation, while when ventilation disappears, it takes time for thrust to build up, due to what is called Wagner effect, so then thrust loss is larger than the corresponding static operation.

In order to account for this effect the PropSim (2018) simulation model was updated. The dynamic effect was added by making propeller circulation, described in equation (5-11) as a time dependent function. The time dependent function was divided into two different cases. One, which corresponds with time, which is desired for ventilation to establish and the other, which correspond with time, which is desired for ventilation to disappear. Symbol  $n_s$ , which is used in *Figure 6-5* is the minimum number of propeller revolutions needed to establish ventilation, thus forming a ventilating vortex from the free surface and  $n_v$  symbol used in *Figure 6-5* is the minimum number of propeller revolutions needed for a vortex and thereby ventilation to disappear.  $n_s$  and  $n_v$  are functions of propeller submergence for low advance numbers  $0.08 < J < 0.15$ . It is believed that hysteresis effect is mainly connected with ventilation by vortex formation, so for high advance numbers (when the vortex ventilation is not present) it has not any significant effect on thrust loss. Propeller circulation as a function of time for establishing and disappearance of vortex ventilation is presented in *Figure 6-6*. Since the vortex ventilation is dependent on the surface tension, the proposed model is only valid for high Weber numbers. Polynomial approximations of  $n_s$  and  $n_v$  are presented in equations below.



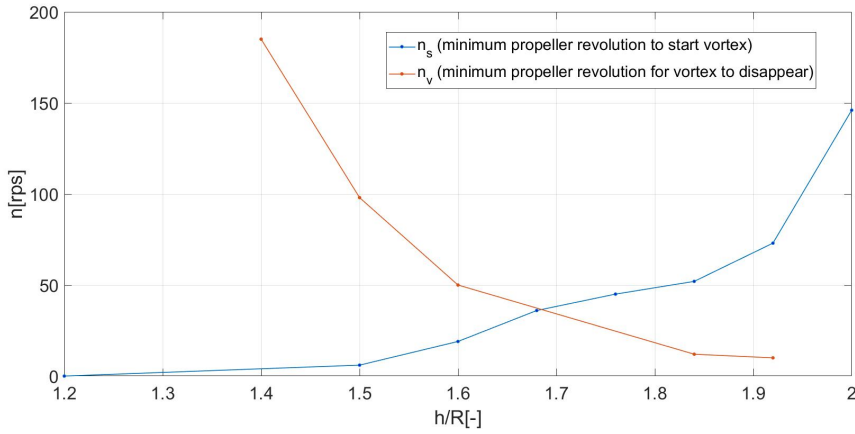


Figure 6-5 Minimum number of propeller revolution to establish a ventilating vortex ( $n_s$ ) and minimum number of propeller revolution for the vortex to disappear ( $n_v$ ) as a function of propeller submergence, valid only for high Weber number and low advance numbers  $0.08 < J < 0.15$ .

$$n_s = \begin{cases} 20 \left(\frac{h}{R}\right) - 24 & \text{for } 1.2 \leq h/R \leq 1.5 \\ 15664 \left(\frac{h}{R}\right)^4 - 106470 \left(\frac{h}{R}\right)^3 + 270657 \left(\frac{h}{R}\right)^2 - 304831 \left(\frac{h}{R}\right) + 128309 & \text{for } 1.5 \leq h/R \leq 2.0 \end{cases} \quad (6-1)$$

$$n_v = -1619.3 \left(\frac{h}{R}\right)^3 + 907.1 \left(\frac{h}{R}\right)^2 - 16843 \left(\frac{h}{R}\right) + 10496 \text{ for } 1.2 \leq h/R \leq 2.0 \quad (6-2)$$

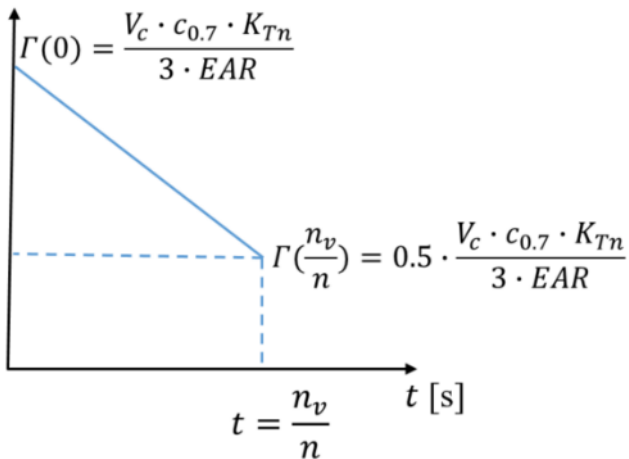
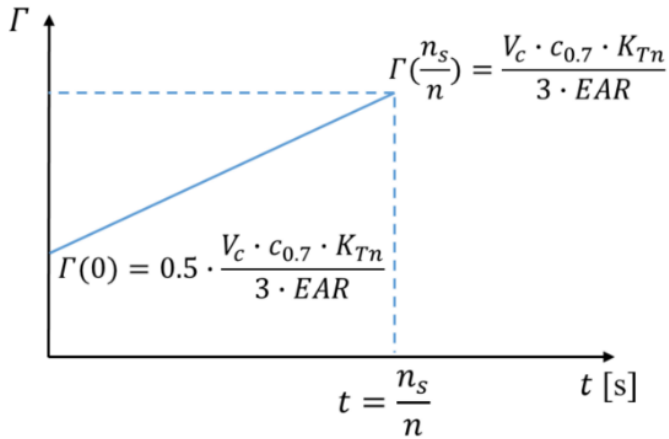


Figure 6-6 Propeller circulation as a function of time to establish the vortex ventilation (top side) and as a function of time for ventilation to disappear (bottom side),  $K_{Tn}$  is the thrust coefficient for non ventilating condition and  $K_T$  is the thrust coefficient for ventilating condition for given and constant propeller submergence  $h/R$ .

Table 6-1 shows five different experimental conditions, which were used for the comparison between calculations using PropSim (2018 hysteresis) simulation model and experimental results.

Case number	$h/R$ [-]		$A/R$ [-]	$A/T$ [m/s]	$T$ [s]	$J$ [-]	$n$ [rps]
<i>Dynamic condition (heave motion), Kou2006_I, low advance numbers</i>							
	min	max					
1	1.15	2.15	2.4	0.075	4	0.143	14
2	1.15	2.15	1.2	0.1	1.5	0.143	14
3	1.05	3.25	2.4	0.15	2	0.143	14
4	1.05	3.25	2.4	0.075	4	0.1	14
5	1.15	2.15	1.2	0.1	1.5	0.1	14

Table 6-1 Different experimental condition used for comparison between simulation model and experimental results.

Figure 6-7 and

Figure 6-8 show the comparison for thrust loss for experiments under dynamic heave motion for different heave amplitude and calculations by using simulation model PropSim (2018\_hysteresis), which include the hysteresis effect in the simulation. As it can be observed from the figures calculation performed by PropSim (2018\_hysteresis) simulation model agree quite well with experiments. This means that the simulation model account correctly for the hysteresis effect on ventilation due to propeller working with periodically varying submersions.

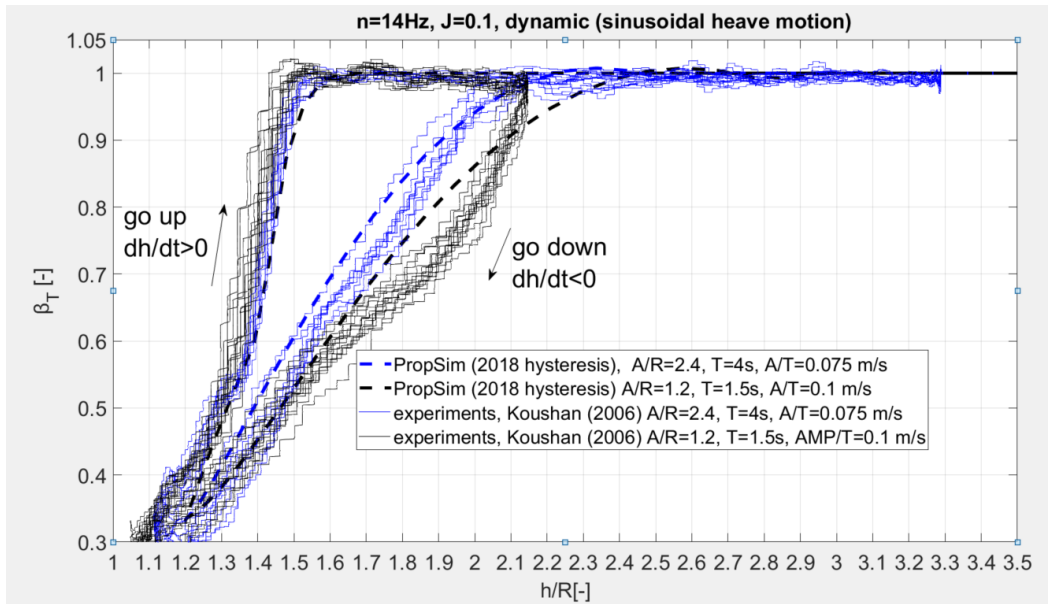


Figure 6-7 Comparison for thrust loss between experiments (dynamic) and simulation (PropSim2018\_hysteresis) for different amplitude of propeller (heave), see Case 4 & 5 presented in Table 6-1, simulation include hysteresis effect for two different motions of propeller (upwards and downwards), PropSim2018\_hysteresis.

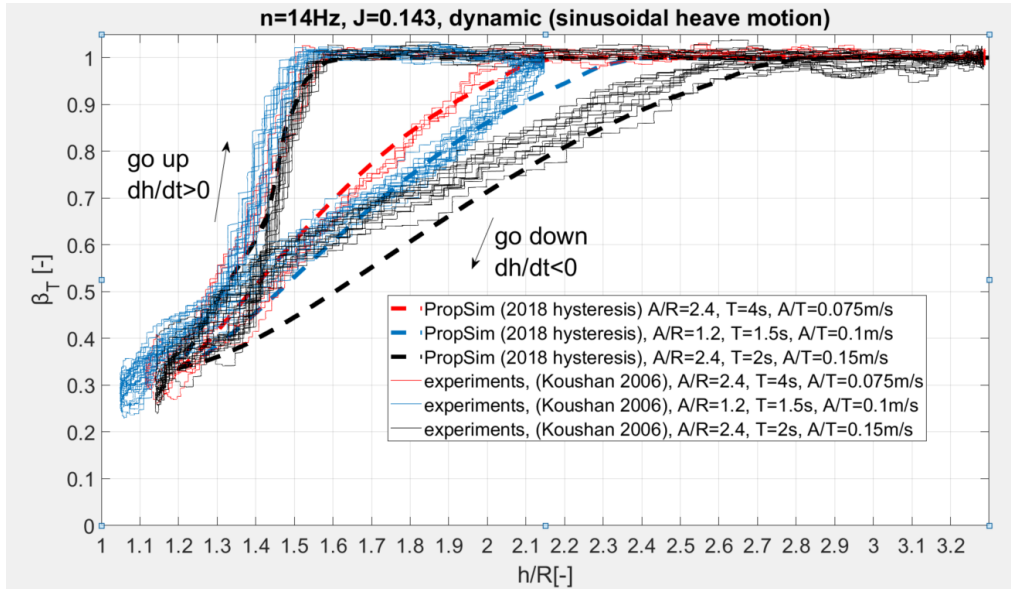


Figure 6-8 Comparison for thrust loss between experiments (dynamic) and simulation (PropSim2018\_hysteresis) for different amplitude of propeller (heave), see Case 1, 2 & 3 presented in Table 6-1, simulation include hysteresis effect for two different motions of propeller (upwards and downwards), PropSim2018\_hysteresis.

### **6.2.2 Dynamics thrust loss due to ventilation, out of water and Wagner effect as a function of blade position, PropSim (2018\_blade\_dynamics)**

From the experiments, it can be observed that the thrust varies with the position of the blade during one cycle of rotation when the propeller is ventilating and/or coming partly out of water. For deep and constant propeller submergence and low advance numbers (i.e.  $h/R=1.5$  and  $J=0.15$ , no out of water effect), the biggest thrust loss is when the blade is close to the free surface (between 315 and 90 deg). For the propeller blade position between 90 deg and 315 deg, the thrust is built up again and achieve values close to nominal thrust. The different thrust losses correspond to different ventilation extent. It is clear from the experiments that in this condition the propeller blade can be both fully, partially or non-ventilating depending on the blade position. When the propeller is coming out of the water (i.e.  $h/R=0$ ), the thrust loss also varies due to the blade position. The three reasons for this variation is ventilation, loss of propeller disk area and Wagner effect. The previous versions of the simulation model denoted PropSim (2016) and PropSim (2018) both include loss of propeller disk area and Wagner effect as a function of propeller position.

In this section, it is presented the thrust loss calculation due to ventilation, out of the water effect and Wagner effect as a function of blade position. The main modification is that for the calculation of the thrust loss due to ventilation, the propeller blade position is included as a parameter instead of including the constant propeller position (measured as a distance from the propeller shaft to the free surface).

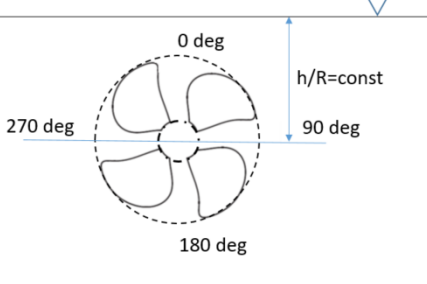
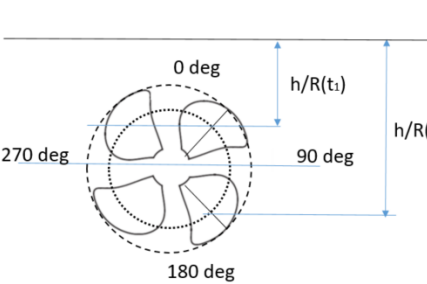
	
<p>Propeller thrust loss due to ventilation, constant for different blade position (PropSim(2018))</p>	<p>Blade thrust loss as a function of blade position, blade submergence varies during one cycle of revolution, PropSim (2018_blade_dynamics)</p>

Figure 6-9 Modification of the PropSim (2018) in order to account for the effect that blade thrust loss due to ventilation varies during one cycle of revolution PropSim (2018\_blade\_dynamics).

Figure 6-12 shows the comparison between calculations (CFD) and experiments Koz10 of the thrust loss due to ventilation as a function of blade position. It can be observed from the figure that prediction of thrust loss is more repeatable between revolutions for calculations (CFD) than experiments. Figure 6-13 shows the calculation of the thrust loss due to ventilation, which varies due to different blade position (PropSim(2018\_blade\_dynamics))

It can be observed from the comparison of Figure 6-10 and Figure 6-11 that the calculation made by using PropSim (2018\_blade\_dynamics) simulation model are more close to the CFD computational results than for experimental results. For both CFD and calculation results it is observed similar thrust loss for every propeller revolution. During measurements different thrust losses depending on the time in the experiments, see Figure 6-12

- $h/R=1.5$ ,  $n=18\text{Hz}$ ,  $J=0.15$  (low advance number)

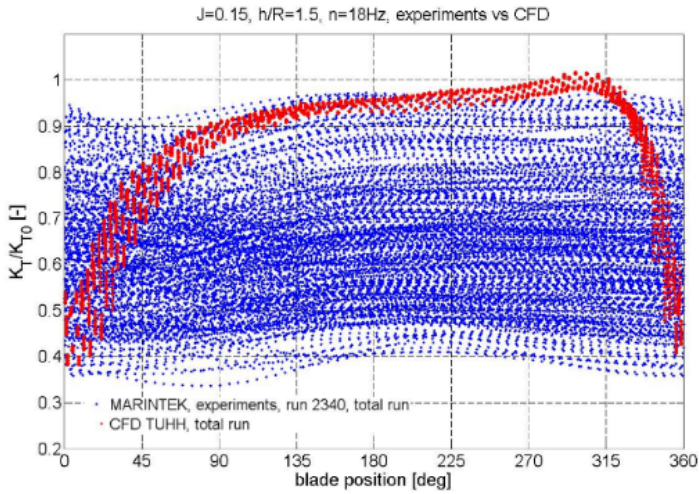


Figure 6-12 Thrust ratio during each revolution, red line correspond to CFD calculations and blue line correspond to experimental results (Koz10)

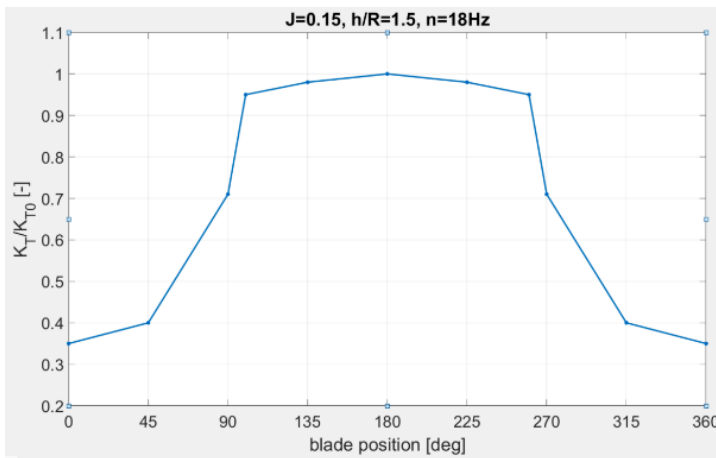


Figure 6-13 Calculation of thrust loss as a function of blade position

Figure 6-14 and Figure 6-15 show the thrust loss variations due to the different blade position.

Figure 6-14 shows the comparison between calculations (CFD) and experiments Koz10 of the thrust loss due to ventilation as a function of blade position. Figure 6-14 shows the



calculation of the thrust loss made by using PropSim (2018\_blade\_dynamics) simulation model.

- **$h/R=1.5$ ,  $n=18\text{Hz}$ ,  $J=0.6$  (high advance number)**

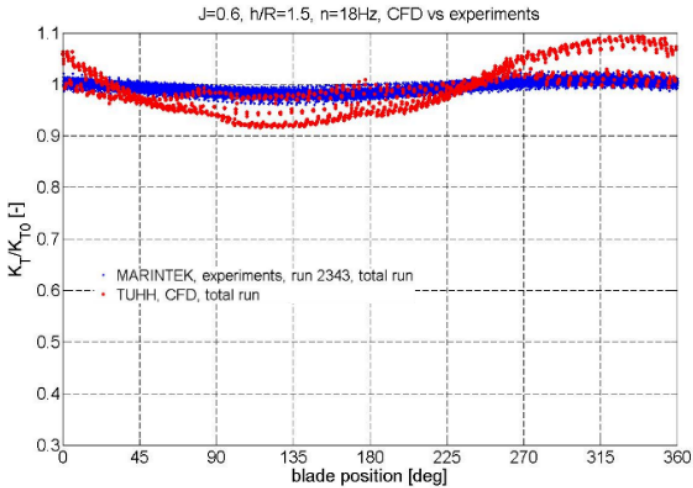


Figure 6-14 Thrust ratio during each revolution, red line correspond to CFD calculations and blue line correspond to experimental results (Koz10)

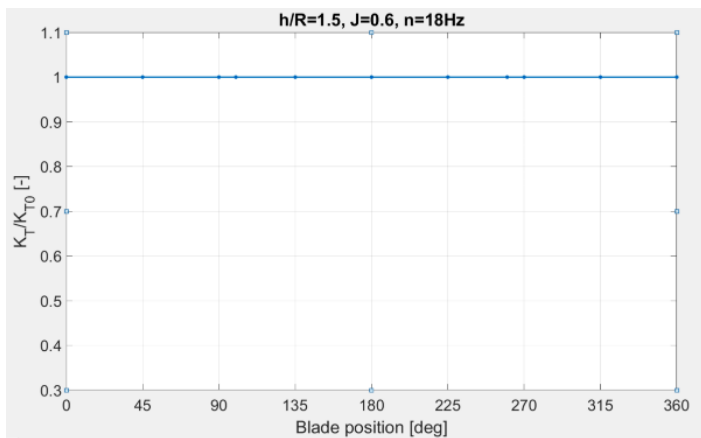
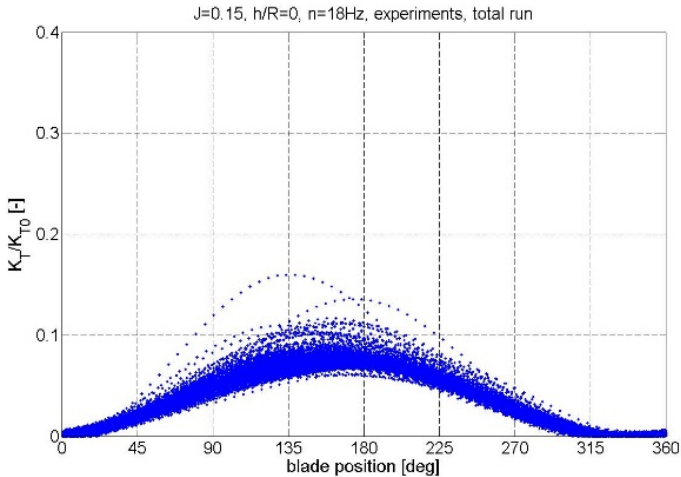


Figure 6-15 Calculation of thrust loss as a function of blade position

Figure 6-16 and Figure 6-17 show the thrust loss variations due to different blade position in one cycle of revolution for  $n=18\text{Hz}$  and low advance number. For this case

the propeller is half submerged so different thrust loss is a consequence of combination of out of water effect, Wagner effect and ventilation. *Figure 6-16* and *Figure 6-17* show good agreement between experimental results and calculations.

- **$h/R=0$  (half submerged),  $n=18\text{Hz}$ ,  $J=0.15$  (low advance number)**



*Figure 6-16* Thrust ratio during each revolution based on experimental results (Koz10)

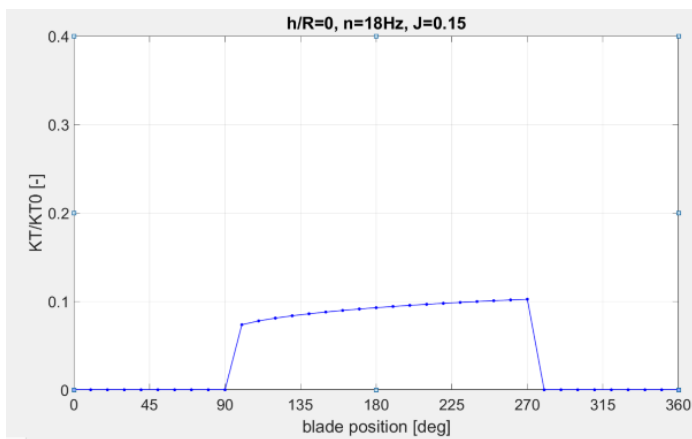


*Figure 6-17* Calculation of thrust loss as a function of blade position

*Figure 6-18* and *Figure 6-19* show the thrust loss variations due to different blade position in one cycle of revolution for  $n=18\text{Hz}$  and high advance number  $J=0.9$ . For these cases

the propeller is half submerged so different thrust loss is a consequence of combination of out of water effect, Wagner effect and ventilation. *Figure 6-18* and *Figure 6-19* show good agreement between experimental results and calculations.

- **6.2.2.5  $h/R=0$  (half submerged),  $n=18\text{Hz}$ ,  $J=0.9$  (high advance number)**

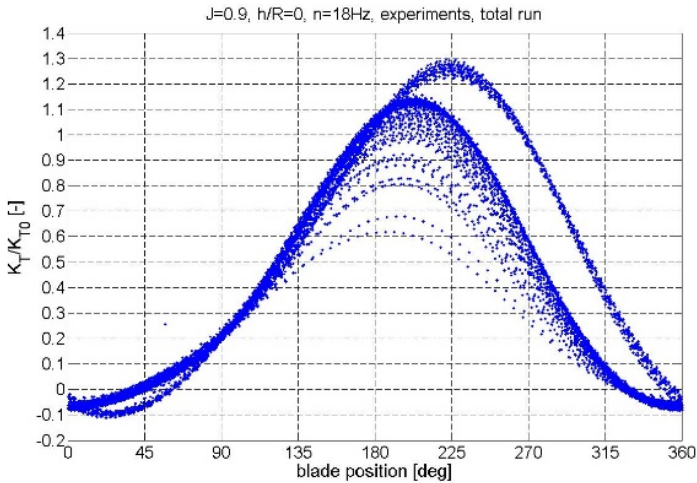


*Figure 6-18 Thrust ratio during each revolution, based on experimental results (Koz10)*

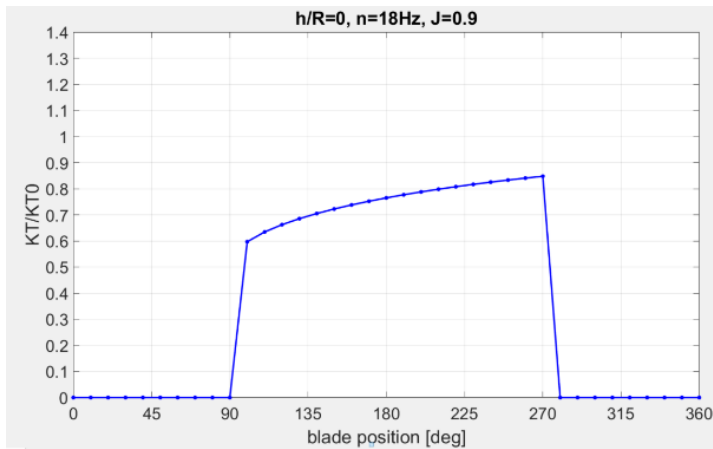


*Figure 6-19 Calculation of thrust loss as a function of blade position*

Figure 6-20 shows a time series of the computed thrust coefficient for a single blade and the propeller for  $J=0.15$ ,  $h/R=0$ ,  $n=18\text{Hz}$  made by using PropSim (2018\_blade\_dynamics) simulation model.

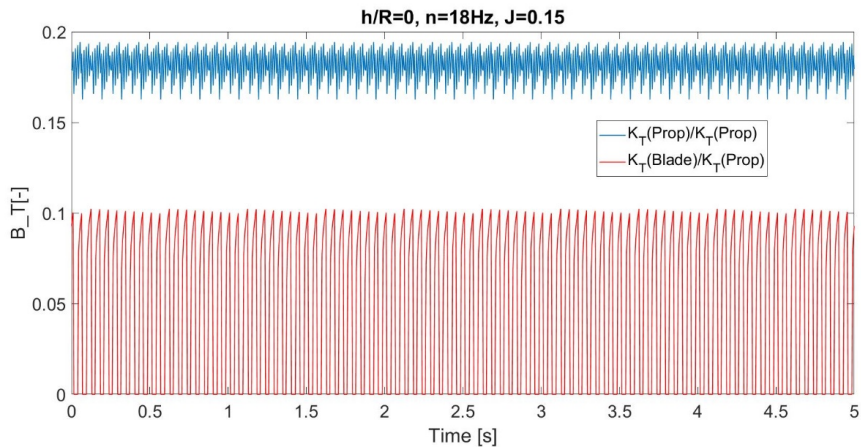
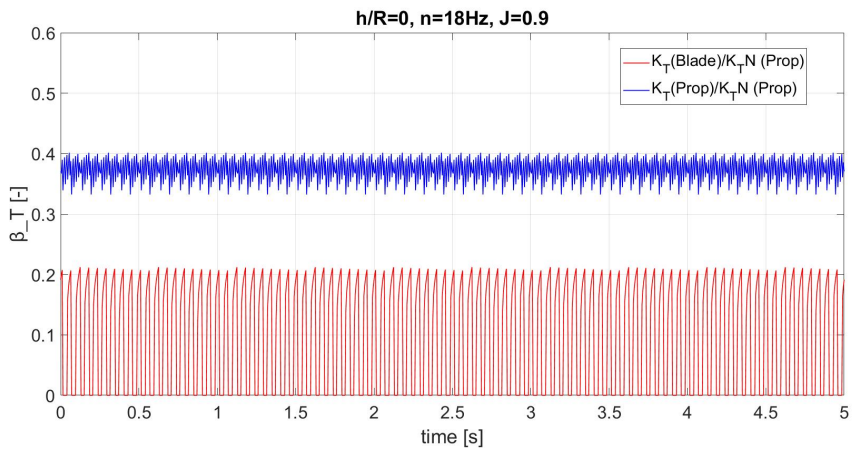


Figure 6-20 Time series of the computed thrust coefficient for a single blade and the propeller for  $J=0.9$ ,  $h/R=0$ ,  $n=18\text{Hz}$ .

Figure 6-21 shows a time series of the computed thrust coefficient for a single blade and the propeller for  $J=0.9$ ,  $h/R=0$ ,  $n=18\text{Hz}$  made by using PropSim (2018\_blade\_dynamics) simulation model.

Both Figure 6-20 and Figure 6-21 show how the amplitude of variation decrease and the dominating frequency of the variation is increasing for the entire propeller compared to a single blade.



*Figure 6-21 Time series of the computed thrust coefficient for a single blade and the propeller for  $J=0.9$ ,  $h/R=0$ ,  $n=18\text{Hz}$ .*

## 7 THE PROPELLER BLADE SLAMMING HYPOTHESIS

This chapter discusses the propeller blade slamming hypothesis, and presents the description of the set up and the results for four bladed propeller (P1374) obtained by *Koz08*, together with a review of the results of the experiments made by Mork (2007) of a one bladed propeller (P1362). Propeller model P1362 has a diameter of 250mm, design pitch ratio equal to 1.08 and blade area ratio equal to 0.685. Propeller model P1374 has a diameter of 250mm, blade area ratio equal to 0.6 design pitch ratio  $P/D=1.1$ , the propeller hub is 65mm. Geometry of the propeller (P1374) can be found in Appendix A.

### 7.1 INTRODUCTION

As it was described in the Section 1.1, it was believed that the TUFF damage needed at least one large overload (2-4 times the nominal load the gear was designed for) to be initiated. The mechanism of this critical load is not known, and it has at a later stage been doubted that such a large overload is required for TUFF to develop. It was believed that a possible mechanism leading to such large, critical loads could be that a propeller blade during partial out-of-water event would slam into a patch of free surface with a low relative angle between the blade and free surface, leading to propeller slamming. The main objective of the study reported here was to verify (or disprove) the slamming hypothesis and to get a good estimate of the slamming loads by means of model tests and calculations.

### 7.2 MSC THESIS BY MORK (2007)

The work presented in Mork (2007) Msc thesis had been done in co-operation with Rolls-Royce UTC to investigate the propeller blade slamming hypothesis. In order to find the forces resulting from an impact with a flat water surface, free surface disturbance and forward speed were neglected.

#### 7.2.1 Experiments

The aim of this model tests was to see how the slamming loads increase with the decreasing impact angle between the calm water surface and propeller blade. One model propeller blade from the conventional four-bladed propeller P1362 was tested for different impact angles to the free surface and rotational speeds. The design pitch ratio was  $P/D=1.08$  and the pitch angle 26.156 deg at  $r/R=0.7$ , which gives an impact angle equal to 63.8 deg.

Different conditions have been tested, i.e. different combination of the following parameters:

- Variations of propeller rotational velocity,  $n=9, 14, 15$  and  $16\text{Hz}$
- Variation of the impact angles between the blade and the calm water surface,  $-1.156\text{ deg}$ ,  $8.8\text{ deg}$ ,  $28.8\text{ deg}$ ,  $38.8\text{ deg}$ ,  $53.8\text{ deg}$  and  $63.8\text{ deg}$ .
- Variation of propeller shaft stiffness, see Mork (2007) for more detailed description of the test set up.

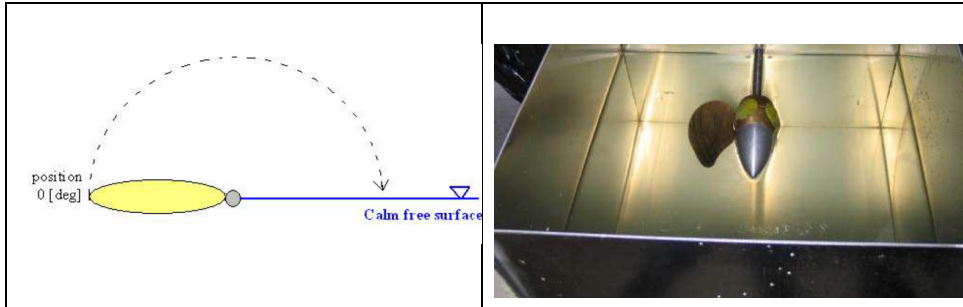


*Figure 7-1 Illustration of the blade start position (left) and photograph of propeller blade in basin (right), Mork (2007), P1362*

*Figure 7-2* below presents the photographs taken during measurements for the impact angles  $-1.156$  and  $38.8\text{ deg}$ . The rotational speed for both cases was  $n=9\text{rps}$ . It can be observed from the photographs that the slamming loads are very sensitive to the impact angle. As it can be seen from the *Figure 7-3*, the impact loads at  $-1.156\text{ deg}$  are very large compared to  $38.8\text{ deg}$ . The maximum torque for the two different impact angles  $-1.156\text{ deg}$  and  $38.8\text{ deg}$  is presented in *Figure 7-3* showing that for small impact angles ( $-1.156\text{ deg}$ ) it is observed impact loads, which can be categorized as a slamming loads. The initial large oscillations of torque seen in the time series in *Figure 7-3* comes from the very rapid acceleration of the blade rotation, and is therefore not related to hydrodynamic loading.

*Figure 7-4* shows the maximum torque due to the blade impact converted to full scale and made dimensionless with the nominal torque. Nominal torque means the torque equal to the rated full power of the thruster divided by  $2\pi$  times the propeller speed and divided by the number of blades. The figure shows that, under the idealized conditions of the test, a propeller blade impact can result in the large overloads believed necessary to initiate a TIFF damage.

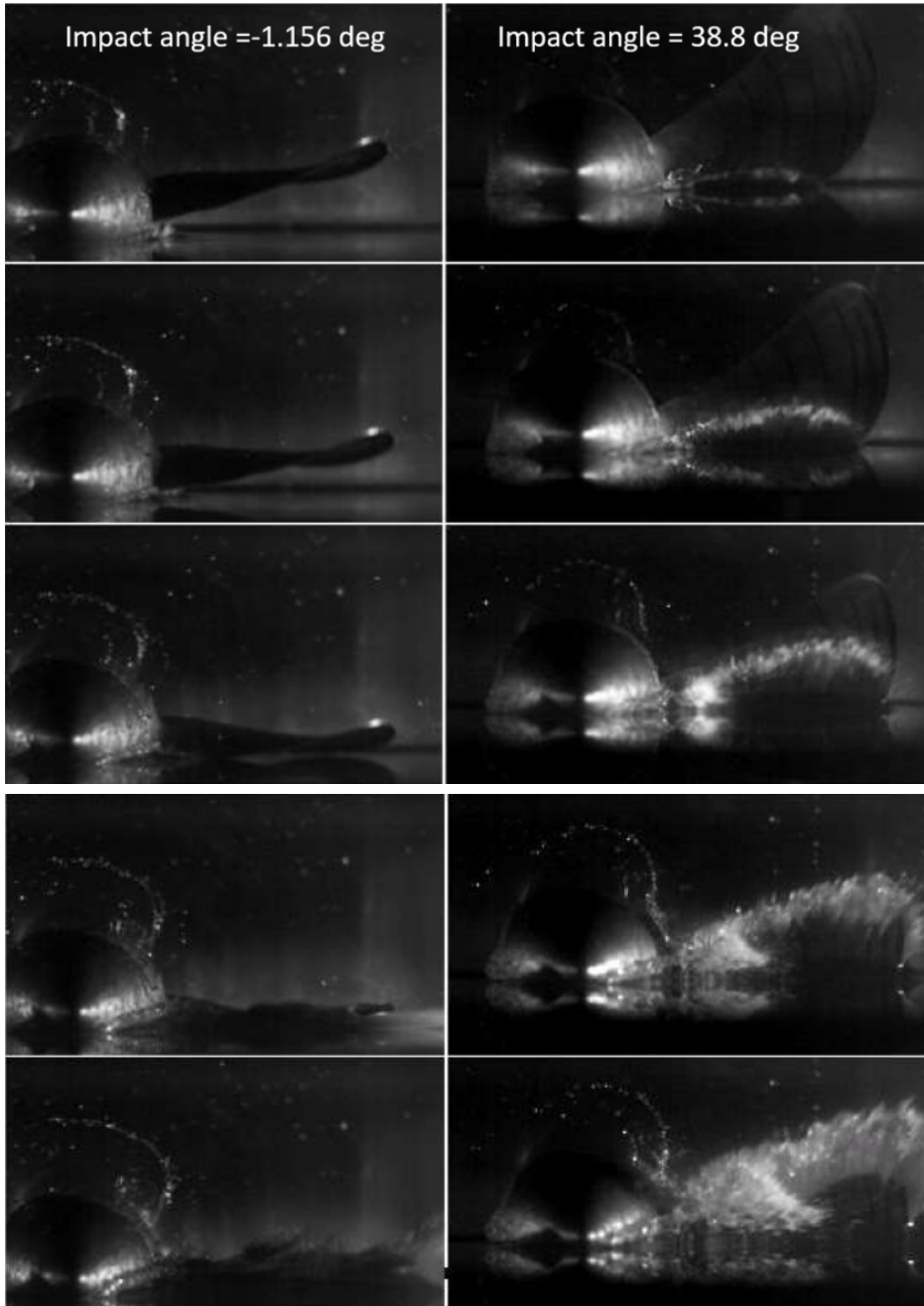


*Figure 7-2 Photograph of the slamming event,  $n=9rps$ , impact angle at  $r/R=0.7$  equal to -1.156 deg (left) and 38.8 (right), Mork (2007).*



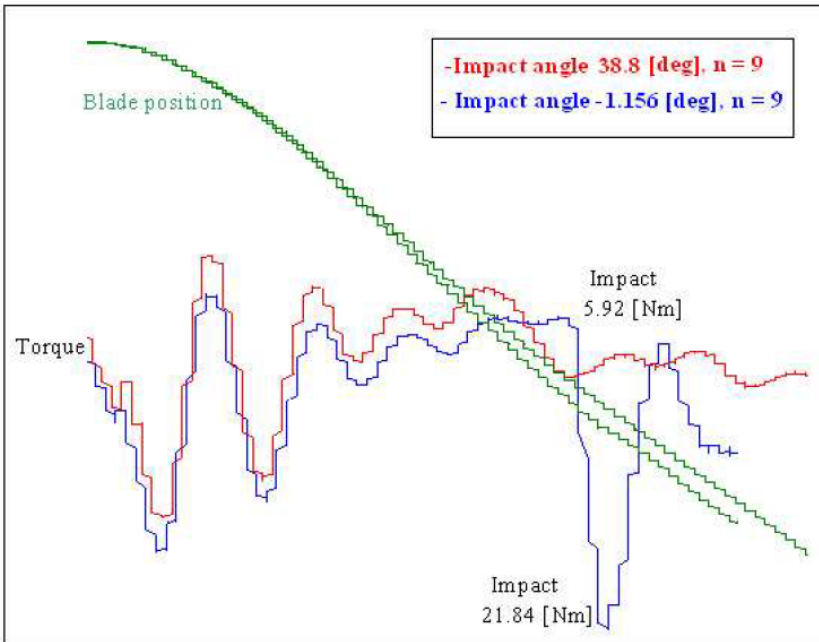


Figure 7-3 Impact loads for  $n=9\text{rps}$  and impact angle  $-1.156\text{ deg}$  and  $38.8\text{ deg}$ , Mork (2007)

The maximum torque in full scale presented as % of nominal loads, obtained from experiments is presented in Figure 7-4 and Table 7-1.

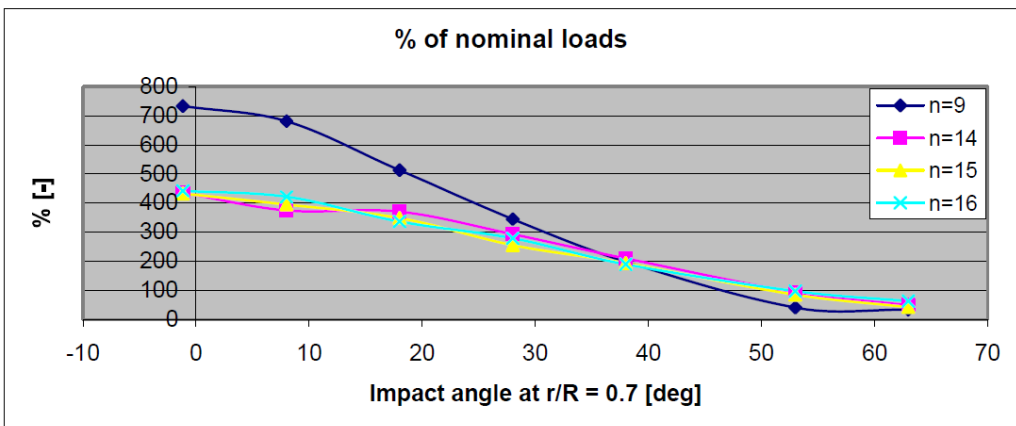


Figure 7-4 Maximum torque in full scale presented as % of nominal loads, obtained from experiments, impact angle  $-1.156$ , Mork (2007)

Table 7-1 shows that for  $n=9, 14, 15$  and  $16$  impact loads may be high enough to initiate TIFF damage according to the hypothesis when the impact angle is less than or equal to  $28$  deg.

	Impact angle: -1.156 [deg]	Impact angle: 8 [deg]	Impact angle: 18 [deg]	Impact angle: 28 [deg]	Impact angle: 38 [deg]
$n = 9$	733 %	681 %	513 %	345 %	199 %
$n = 14$	436 %	374 %	370 %	293 %	210 %
$n = 15$	433 %	395 %	349 %	255 %	194 %
$n = 16$	442 %	421 %	336 %	279 %	188 %

Table 7-1 Resulting impact torque in present of nominal torque for different propeller revolution speeds and impact angles (data from Mork 2007).

### 7.2.2 Calculations

Slam2D is a computer program based on the paper written by Zhao et.al. (1996). The program is based on potential flow theory and predicts forces, moments and the pressure distribution on a ship section due to slamming. The Slam2D program expects 2D ship sections and it was a challenge to implement propeller geometry in the program. Thus, the sections must have some kind of wedge shape.

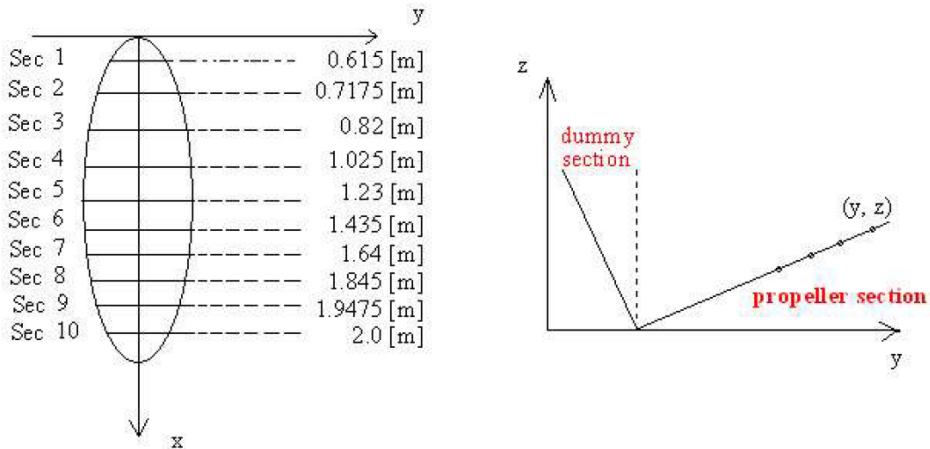
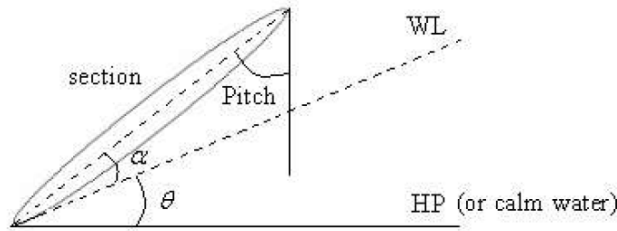


Figure 7-5 The orientation of a propeller blade in an x-y and y-z system of coordinate, Mork (2007).



$\alpha$  = angle between the free surface and a section of the propeller blade

$\theta$  = angle between the horizontal plane and the water line

WL = Water Line

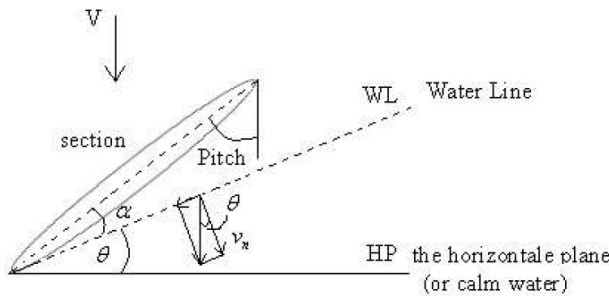
HP = the horizontal plane

Figure 7-6 A section of propeller blade an its angles to the free surface (WL) and calm water (HP), Mork (2007).

Figure 7-6 shows a section of propeller blade and its angles to the free surface (WL) and calm water (HP). The impact angle for each section is dependent of its pitch angle and is calculating by subtracting the pitch angle and the angle between the calm water (HP) from 90 [deg].

$$\alpha = 90 - \text{pitch angle} - \theta \tag{7-1}$$

Each case tested requires different velocity files. The free surface is denoted WL and calm water. The vertical velocity has to be decomposed to find the normal velocity.



$\alpha$  = angle between the free surface and a section of the propeller blade

$\theta$  = angle between the horizontal plane and the water line

Figure 7-7 A A section of a propeller blade and vertical impact velocity.

The calculation of a peak torque at different impact angles at  $r/R=0.7$  using Slam 2D is presented as % of nominal loads in *Figure 7-8*.

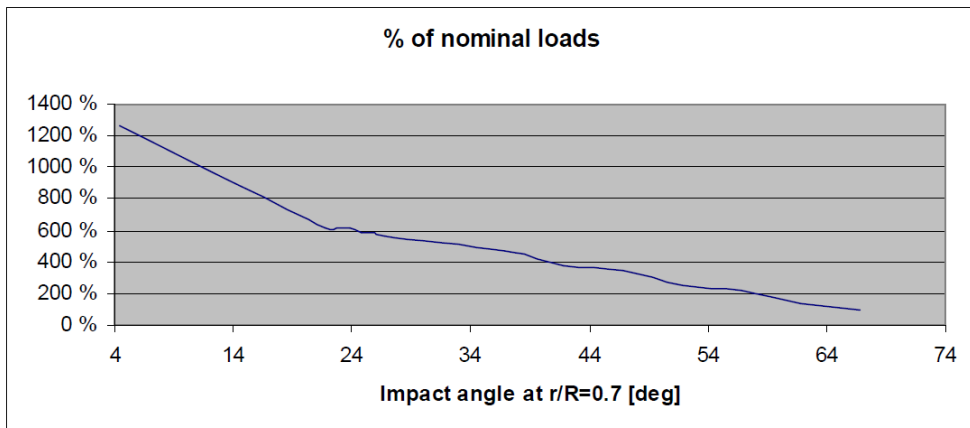


*Figure 7-8* Calculated, Slam 2D peak torque at different impact angles at  $r/R=0.7$ , presented as % of nominal loads, Mork (2007).

It was found that calculated loads were higher than measured one (approximately 35% deviation was found). Mork (2007) concluded that Slam 2D is not fit to calculate exact loads on propeller, but could be used as an estimation of slamming loads.

As a general conclusion one can say that experimental results shows that for small impact angles (equal and below 28 deg) the impact loads may be high enough to be categorized as a slamming loads and may be large enough to initiate TUFF damages, under the assumption that TUFF damages require a large overload (2-4 times nominal load) for initiation.

## 7.1 MODEL TESTS, (KOZ08)

The model tests and calculations by Mork (2007) confirmed that if a propeller blade slamming event actually occurs, large overloads – in the range 2-4 times the nominal torque, might be the result. As a continuation of the Mork (2007) work, it is of interests to go one step towards more realistic conditions by considering a four bladed propeller rotating continuously at forward speed. –Model tests were performed with the for four bladed propeller *P1374* in the large towing tank at the Marine Technology Centre. The main objective for the tests was to verify if slamming loads might occur for surface piercing propellers under such operational conditions. The tests were performed at

extremely high propeller pitch,  $P/D=15$  and  $P/D=7$ , which corresponds to angles equal to  $8$  and  $18$  deg between the blade and free surface. This was done to ensure sufficiently low relative angle between blade and the undisturbed water surface. Three different propeller positions were investigated in the experiment: propeller was half immersed (The shaft was at the free surface position) and propeller hub was up/down  $30\text{mm}$  from the free surface. For all submergences, the propeller revolution speed ( $n=5, 8, 9, 10, 11$  &  $15$ ) and forward speed (up to  $8\text{m/s}$ ) were varied in order to obtain different loading conditions. See section 3.8.1 for more detailed description of the model test set up.

Figure 7-9 presents the propeller torque measured during experiments for  $n=12\text{rps}$ ,  $P/D=15$  and  $h/R=0$  (Propeller was half immersed). Figure 7-9 and Figure 7-10 indicate that it is not observed slamming loads from the experiments, only the torque variations, which are caused by ventilation. Loads, which occur for surface piercing propeller (with very high pitch=small angle between blades and FS) in calm water can not be categorized as slamming loads. The conclusion was that the previous blade passing created enough air mixing and disturbance to reduce the loads to a level that is not sufficient to initiate TIFF damages according to the hypothesis of required 2-4 times overload.

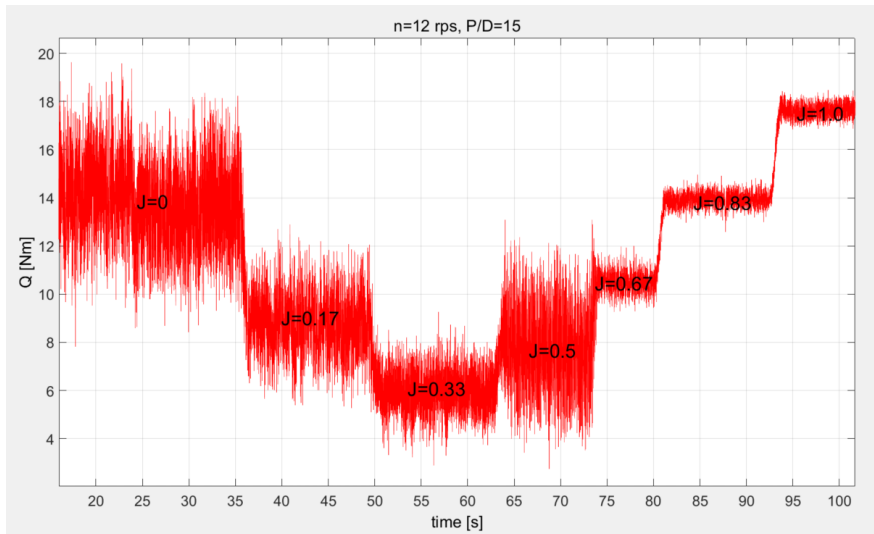


Figure 7-9 Propeller torque measured during experiments,  $n=12\text{rps}$ ,  $P/D=15$  (correspond to impact angle  $8$  [deg], propeller was half submerged).

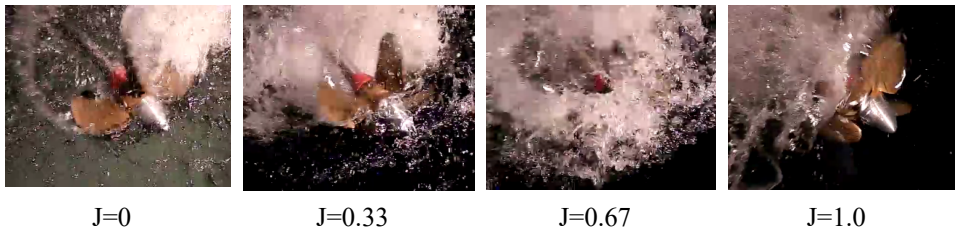


Figure 7-10 model tests,  $n=12$ ,  $P/D=15$ , propeller was half submerged.

Figure 7-11 , Figure 7-12 and Figure 7-13 shows histograms of total torque loss factor for propeller for both low ( $J=0$ ,  $J=0.333$ ) and high advance numbers ( $J=1.0$ ). The variations for low advance numbers are much higher than for high advance numbers. This is because for low advance numbers the propeller experienced ventilation of the propeller blades. For high advance number, the ventilation disappears due to high forward speed and low loading of the propeller.

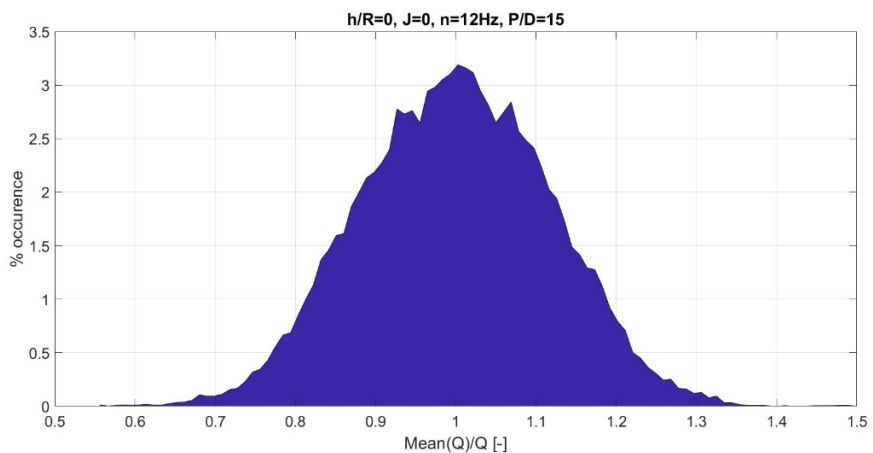


Figure 7-11 Histogram of total torque loss factor for  $J=0$ ,  $n=12\text{Hz}$ ,  $P/D=15$ , propeller was half submerged.

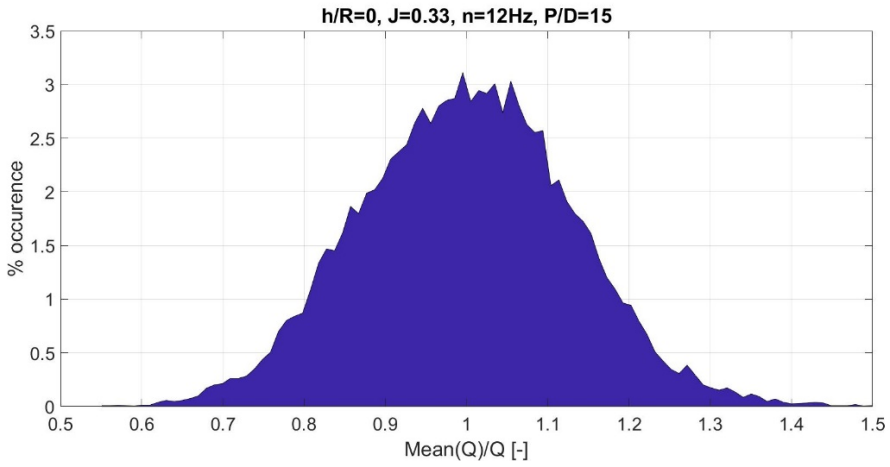


Figure 7-12 Histogram of total torque loss factor for  $J=0.33$ ,  $n=12\text{Hz}$ ,  $P/D=15$ , propeller was half submerged.

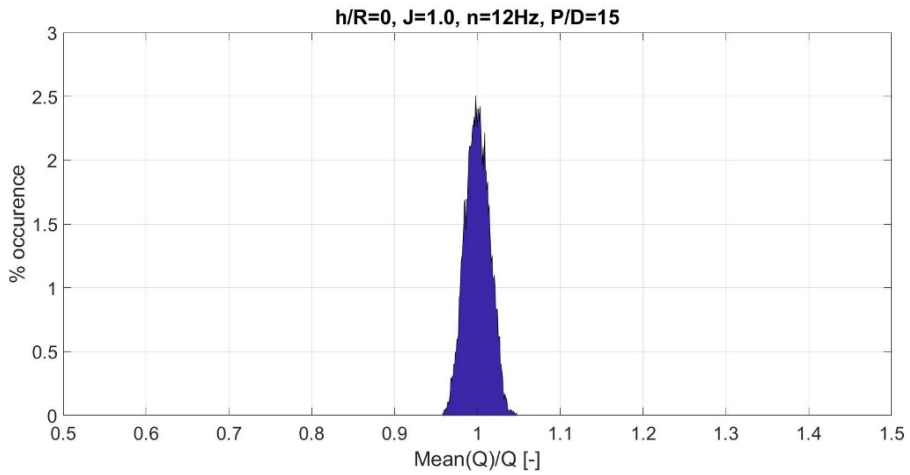


Figure 7-13 Histogram of total torque loss factor for  $J=1.0$ ,  $n=12\text{Hz}$ ,  $P/D=15$ , propeller was half submerged.

## 8 DISCUSSION, CONCLUSIONS AND RECOMMENDATIONS FOR FUTURE WORK

### 8.1 DISCUSSION

The work presented in this thesis is largely based on a number of model experiments. The experiments are done with only two propellers (see appendix A for details), both are four-bladed conventional propellers with moderate skew and blade area. Since the range of propeller parameters is so narrow one might wonder how much that limits the general validity of the results. Also, scale effects might impact the validity of the results. When it comes to the computational models, a number of simplifications and assumptions had to be made, and they might of course also impact the validity of the models.

This section outline the discussion about the expected generality of the presented results, when different conditions and propellers are considered. The amount of approximation used in the calculation and simulation model is commented and justified.

#### 8.1.1 Computational model

The complete calculation model covers the thrust loss prediction for the range of different propeller submergences, propeller revolutions and advance numbers. The procedure for calculating the thrust loss is divided into three different calculation models. When the propeller is deeply submerged  $h/R > 3.4$  it is considered not to experience any ventilation at any advance number. For  $1.2 \leq h/R \leq 3.4$  the propeller is subjected to propeller ventilation due to impact of the free surface vortex. Thrust loss for ventilating fully submerged propeller is calculated using the idea presented by Kozłowska and Steen (2010). The main problem is to estimate the blade area, which is covered by air. For advance numbers  $J \geq 0.1$  the ventilated blade area is calculated by using the steady state ventilation model, described in Chapter 5. This computational model use a simplified approach to treat the complex problem of ventilation through the vortex terminating in the free surface. The main simplifications included in the model are as follows: 1<sup>st</sup>: The model assumes that the flow induced by the propeller can be approximated by the actuator disk model and that the vortex that draws air to the propeller is treated according to the model proposed by Rott (1958). 2<sup>nd</sup>: The vortex model could not tackle zero advance operating condition, this conditions results in a singularity. Thus, for bollard condition the fraction of the blade area that is ventilated is computed using a fully empirical polynomial relation, which is function of the submergence ratio only. As a practical solution the polynomial



relation valid for bollard condition is applied up to  $J < 0.1$ . 3<sup>rd</sup>: The vortex model does not include surface tension, which makes it valid only for high Weber number.

For propeller submergence  $-1 < h/R \leq 1.2$  the propeller experience free surface ventilation. The total thrust loss is the summary of thrust loss due to ventilation and out of water effect, which include the loss of propeller disk area and Wagner effect. It was assumed that wave making by propeller has negligible effect and can be omitted. Ventilated blade area ratio was estimated based on visual observation from experiments performed by *Koz17*. The ventilated blade area might depend on the propeller geometry in such a way that the estimation is not generally valid for other propellers than P-1374.

The computational model presented in *Chapter 5* is static – assuming the response is quasi steady.

Two different dynamic effects of the ventilating vortex have been added as a development of the calculation model presented in *Chapter 5*. One effect is connected with the dynamic effect causing hysteresis and connected with propeller loading. The other dynamic effect is connected to the effect that the thrust loss varies with the position of the blade during one revolution.

The consequences of several assumptions and simplifications are listed below:

- **Actuator disk model**

It is assumed that the flow induced by the propeller can be approximated by the actuator disk model. It means that there is assumed infinite number of blades and there is no effect of the blade area ratio only the flow induced by the propeller. The calculation model is based on the assumption that ventilation happens when the upstream suction radius computed by the momentum theory is larger than propeller submergence. This approximation is not applicable for zero forward speed, since then the upstream suction radius becomes infinite. Therefore, a separate method is used for the lowest advance numbers ( $J < 0.1$ )

- **Weber Number**

It is assumed that the computational model is valid only for high Weber number, which is above a Weber number of *180*. This means that the surface tension effect would no longer influence the critical advance number.

- **Compressibility**

The air was assumed to be incompressible. When air cavities are closed, air compressibility matters and the air compressibility requires scaling of the atmospheric pressure to be correctly represented in a model test. In full scale, the air will expand and cover the larger portion of the blade, because of the higher-pressure difference. As a conclusion, one can say that the air drawn by the full scale propeller will be subject to an expansion leading to stronger ventilation, meaning that thrust loss due to ventilation might tend to be underestimated by model tests performed without scaled atmospheric pressure. However, the magnitude of this scale effects is very hard to quantify.

- **Advance coefficient**

As it was mentioned before the vortex model could not tackle zero advance operating condition, this condition results in a singularity. Thus, for bollard condition the fraction of the blade area that is ventilated is computed using a fully empirical polynomial relation, which is function of the submergence ratio only. Also this empirical relation is derived from model experiments presented in the thesis, meaning that it is based on a single propeller geometry. Thus, the empirical relation should be obtained and validated from other pitch settings and propeller geometries.

- **Simulation time**

Ventilation, especially by vortex formation is a time dependent phenomenon. The time effect on the ventilation has been added to the dynamic simulation model (PropSim2018\_hysteresis). The time dependent function was connected with propeller circulation and divided in two different cases. One, which corresponds with time, which is desired for ventilation to establish and the other, which correspond with time, which is desired for ventilation to disappear.

The time dependent function is only valid for low advance ratios and it is derived based on model experiments present in the thesis, which based on the similar propeller geometry and pitch characteristic. This leads to the conclusion that the relation concerning the time dependent function should be expanded and validated through different propeller geometries.

### **8.1.2 Scale effects**

Geometric similarity and satisfaction of scaling laws described in section 2.1.2 are needed to obtain similar hydrodynamic and hydro-elastic response between model and full scale

propellers. Satisfaction of Froude number similarity will lead to lower Reynolds number for the model than for the full scale propeller. For example for propeller model *P1440* used for experiments Koz10 and Kou10 the Reynolds number based on the chord length at  $r/R=0.7$  for the model propellers is  $0.5 \cdot 10^6$ , and the corresponding value for the full scale is  $2.8 \cdot 10^7$ . Thus, in both cases the flow is considered to be fully turbulent. According to Minsaas (1983) and Shiba (1953) they observed an impact for the Reynolds number only for small geometries and laminar flows. The influence of Reynolds number vanishes above the  $Re = 4.6 \cdot 10^5$ , see *Figure 2-1* and Helma (2015). Wockner-Kluwe (2013) performed a numerical calculation for ventilating propeller (P1440) for  $h/R=1.5$  and two different Reynolds number, one correspond for Reynolds number in model scale and was equal to  $0.5 \cdot 10^6$  and the other one correspond for Reynolds number for full scale and was equal to  $2.8 \cdot 10^7$ . The results follows the conclusion made by Minsaas (1983) that above the certain value of Reynolds number there is no marked difference for thrust loss calculations. Thus, it can be concluded that Reynolds scale effects are not very significant for the model tests used in this thesis.

Scale effects related to surface tension are governed by the Weber number. Most tests are performed at Weber number above 180, which is considered to be a practical threshold for when surface tension effects cease to be important.

Air compressibility effects might be of importance in cases where closed air cavities appear, and since the atmospheric pressure was not scaled, there might be a related scale effect. The magnitude of this is unknown. When air cavities are open, atmospheric pressure shall not give any scale effect, and this is mostly the case for the lower submergences.

### **8.1.3 Influence of propeller design parameters for ventilation**

In the following section it is discussed the influence of the propeller design parameters i.e. propeller diameter, number of propeller blades, expanded area ratio, skewback, pitch, rake, and blade thickness distribution for propeller ventilation and how these different parameters can be taken into account when using the calculation model presented in *Chapter 5 and Chapter 6*.

- **Influence of Expanded Blade Area Ratio**

The influence of the expanded area ratio upon ventilation was studied by Shiba (1953). He performed model tests with two propellers having the same submergence  $h/R=0.9$ . One

was the propeller No. 346 and the other was Propeller No. 365. Both have the same diameter 0.22m. The main differences between the propeller geometries are given in *Table 8-1* below.

Propeller No.		P346	P365
No. of blades	[-]	3	4
Blade area ratio	[-]	0.4	0.55
Diameter	[m]	0.22	0.22
Pitch ratio	[-]	1.0	1.0
Propeller revolutions	[rps]	15	15
Expanded area ratio	[-]	0.55	0.4
Chord length at 0.7R	m	0.0727	0.053
Blade thickness ratio at 0.7R	[-]	0.05	0.07
Camber ratio at 0.7R	[-]	0.025	0.035

*Table 8-1 Geometry of the propellers, P346 (3 bladed,  $A_E/A_0=0.4$ ) and P365 (4 bladed,  $A_E/A_0=0.55$ ), Shiba (1953)*

From experiments performed for propellers having the expanded area ratio 0.4 (P346, 4 bladed) and 0.55 (P365, 3 bladed) Shiba (1953) concluded that expanded area ratio has little effect upon critical advance number as long as the change is not so marked.

In the calculation model, the influence of the blade area ratio is directly included in the equation for calculating the circulation strength of the vortex, see equation (8-1).

$$\Gamma = \frac{V_c \cdot c_{0.7} \cdot K_{Tn}}{3 \cdot EAR} \quad (8-1)$$

The characteristic section lift coefficient is derived based on the blade area ratio.

$$c_{L0.7} = \frac{K_{Tn}}{k_{0.7} \cdot EAR} = \frac{K_{Tn}}{1.5 \cdot EAR} \quad (8-2)$$

- **Influence of Pitch Distribution**

Shiba (1953) performed model test for three propellers having three types of pitch distribution in radial direction: increasing, constant, decreasing. The influence of pitch distribution upon air drawing was investigated and it was concluded from experimental results and calculations that decreasing pitch is the best from the point of view of air drawing. The table below shows the calculation and measurements of critical advance number. It is seen that there is a clear, but rather small effect. One might think that the decreasing pitch reduces the tip vortex, and that is the main cause of the reduction of ventilation tendency.

Pitch ratio at 0.7R	Propeller No.	Critical advance number	
		Measured	Calculated
1.0 increasing type	P347	0.64-0.655	0.632
1.0 constant type	P346	0.625	0.625
1.0 decreasing type	P348	0.610-0.595	0.615

*Table 8-2 Calculation and experimental results of critical advance number for three different pitch distribution, Shiba (1953)*

- **Influence of Skew back**

Shiba (1953) investigated the influence of the skew back by testing four different propellers with skew back angle equal to 0 deg, 10 deg, 45 deg and 90 deg. Propeller submergence  $h/R=1.0$  and different propeller revolutions was tested. The general particulars of model propellers are given in *Table 8-3* and *Table 8-4*.

Propeller diameter	0.22m
Pitch ratio	1.0
Number of blades	3
Blade thickness ratio	0.050
Hub ratio	0.2

*Table 8-3 Details of propeller geometry which remains the same, Shiba (1953)*

Propeller No.	P901	P371	P902	P903
Rake/D	0	0.091	0	0
Skew Back	0	10°	45°	90°

*Table 8-4 Details of propeller geometry which are different for different propeller models*

By comparison of the test results it was noticed that the critical advance number increase with increasing skewback. By increasing the skewback from  $0^0$  to  $90^0$  one can increase the critical advance number from 0.54 to 0.67 (c.a. 24%), see *Table 8-5*.

Pitch ratio	Propeller No.	Critical advance number			
		$n=7Hz$	$n=9Hz$	$n=11Hz$	$n=13Hz$
		$h/R=1.0$	$h/R=1.0$	$h/R=1.0$	$h/R=1.0$
1.0	P901	0.46	0.54	0.56	0.60
1.0	P371	0.48	0.55	0.58	0.62
1.0	P902	0.52	0.58	0.63	0.66
1.0	P903	0.54	0.58	0.64	0.67

*Table 8-5 Experimental results of critical advance number for four different skewback, Shiba (1953)*

The influence of the skewback in the calculation model cannot be taken into account in the current model, since typically the skewback has marginal influence on the thrust and torque in subcavitating condition.

### **Summary**

The calculation model can only account for propeller design parameters like blade section geometry, rake and skewback through their influence on the propeller open water characteristics. Their effect on ventilation tendency, except for the thrust loading, cannot be accounted for. The experimental investigations of Shiba (1953) indicates that their influence on ventilation is moderate, as discussed above.

The effect of number of blades and blade area ratio was also investigated by Shiba (1953). He concluded that the effect of number of blades is small, and that the effect of blade area is moderate. In the calculation model, the effect of blade number and blade area ratio is included in the calculation of the vortex strength, used only in calculation of ventilation inception of fully submerged propellers. It was not possible to check the effect included in the calculation model against Shiba's results.

### **8.1.4 Uncertainty analysis**

A histogram of the total thrust loss factor for different advance numbers and propeller submergences are shown in *Figure 8-1*, *Figure 8-2*, *Figure 8-3* and *Figure 8-4*. Histograms summarize variations for the whole period of measurements. It is clear that the effect of ventilation is dynamic and is not necessarily repeatable from one revolution to the other. *Figure 8-3* shows a histogram of total thrust loss factor for a propeller operating in unstable ventilation regime. For  $h/R = 1.2$  it is observed two different levels of thrust loss for the

same experimental condition, indicating that the flow is “switching” between the two different states of ventilation.

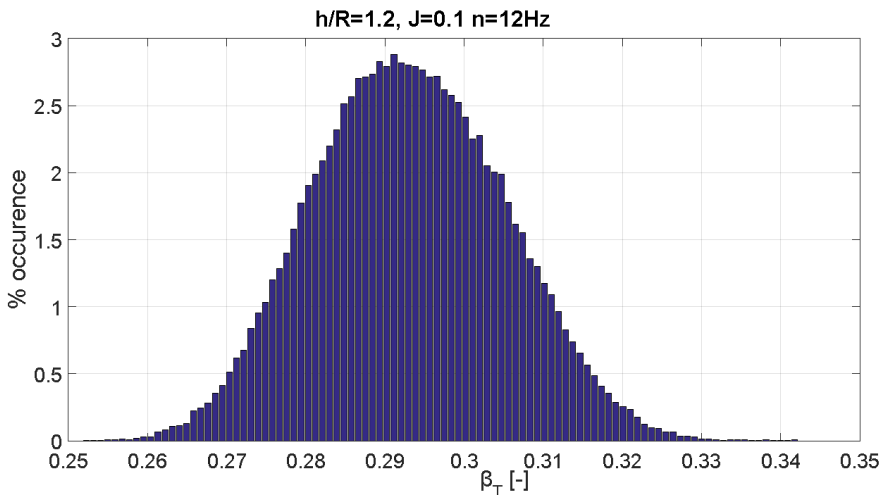


Figure 8-1 Histogram of total thrust loss factor for advance number  $J=0.1$ ,  $h/R=1.2$ , super-critical regime,  $\left(\frac{\beta_{T\text{mean}} - |S.D. |}{\beta_{T\text{mean}}}\right) \cdot 100\% = 4$ .

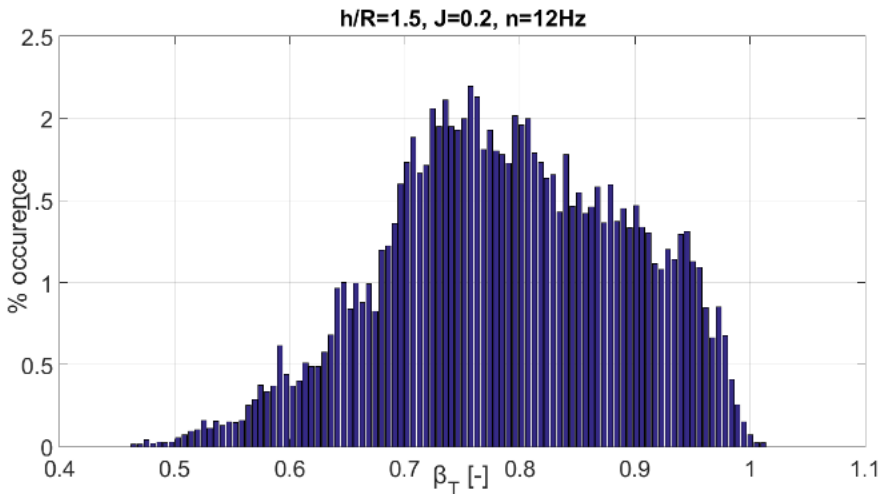


Figure 8-2 Histogram of total thrust loss factor for advance number  $J=0.2$ ,  $h/R=1.5$ , unstable regime,  $\left(\frac{\beta_{T\text{mean}} - |S.D. |}{\beta_{T\text{mean}}}\right) \cdot 100\% = 13\%$ .

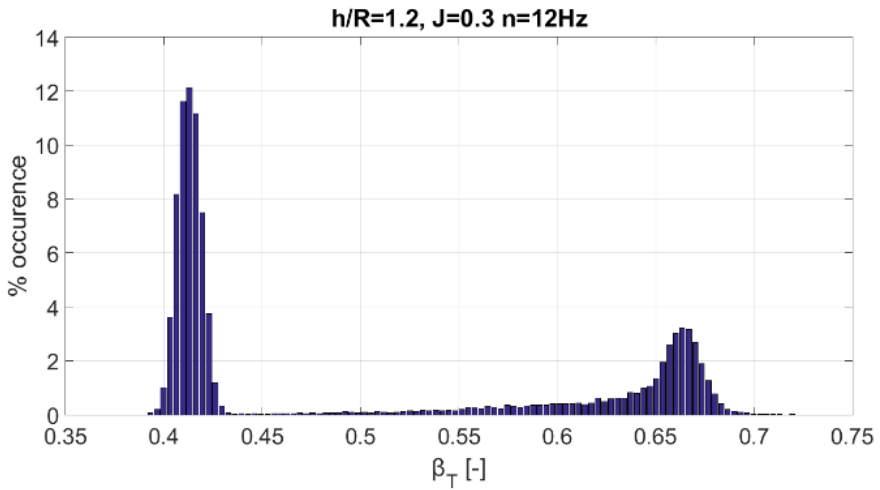


Figure 8-3 Histogram of total thrust loss factor for advance number  $J=0.3$ ,  $h/R=1.2$ , unstable regime,  $\left(\frac{\beta_{T_{mean}} - |S.D.|}{\beta_{T_{mean}}}\right) \cdot 100\% = 18\%$ .

It can be observed from the histogram that the thrust loss variations in time for the same experimental conditions are higher for unstable regime, see *Figure 8-2* and *Figure 8-3* than for super-critical regime presented in *Figure 8-1*. Also for the sub-critical regime presented in *Figure 8-4*, the propeller experienced very small ventilation and the thrust loss is low and show very little variation compared to the unstable regime.



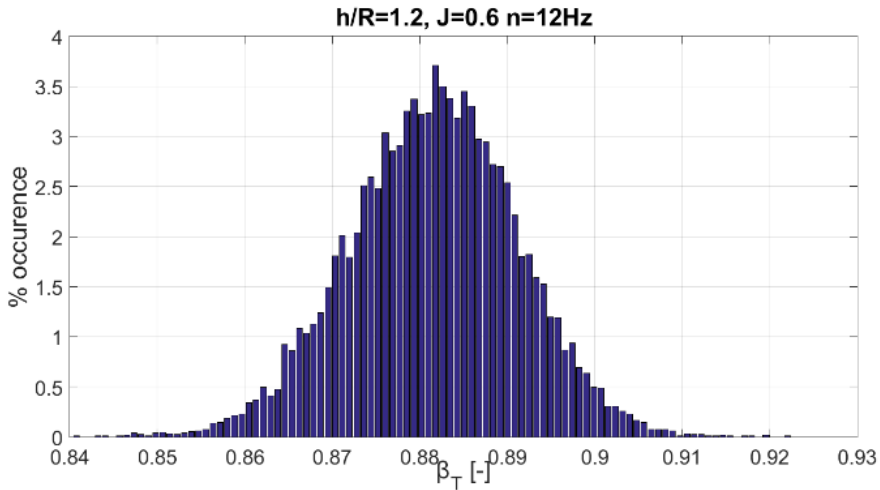


Figure 8-4 Histogram of total thrust loss factor for advance number  $J=0.6$ ,  $h/R=1.2$ , sub-critical regime,  $\left(\frac{\beta_{T_{mean}}^{-|S.D.|}}{\beta_{T_{mean}}}\right) \cdot 100\% = 1.05\%$ .

Table 8-6 below shows that the standard deviation calculated for series of experiments Koz17 varies from c.a. 30% of the mean value to only 1% depending on the test condition. The highest value of the standard deviation is observed for the unstable regime, which is characterized by deep submergence and low advance ratio. This is believed to be connected to the dynamic effect of the propeller loading, which was included in the dynamic simulation model presented in Chapter 6. When the propeller starts ventilating, the thrust drops, propeller load factor  $c_T$  drops, and then the amount of ventilation change. Thus, the ventilation can come and go during constant experimental conditions due to the dynamically changed propeller load factor.

h/R	J	n	$\beta_{T_{mean}}$	S.D.	$\frac{\beta_{T_{mean}} -  S.D. }{\beta_{T_{mean}}} \cdot 100\%$
[-]	[-]	[Hz]	[-]	[-]	[%]
1.6	0	12	0.68	0.19	<b>27.4</b>
1.6	0.2	12	0.92	0.06	<b>6.0</b>
1.6	0.4	12	0.99	0.01	1.1
1.6	0.6	12	1.00	0.01	1.1
1.6	0.8	12	1.00	0.01	1.1
1.5	0	12	0.56	0.08	<b>13.5</b>
1.5	0.2	12	0.79	0.10	<b>13.0</b>
1.5	0.4	12	0.92	0.01	0.8
1.5	0.6	12	0.98	0.01	0.7
1.5	0.8	12	1.00	0.01	1.2
1.4	0.2	12	0.57	0.07	<b>11.6</b>
1.4	0.4	12	0.65	0.02	3.7
1.4	0.6	12	0.98	0.01	1.0
1.4	0.8	12	1.00	0.01	1.1
1.2	0.1	12	0.29	0.01	3.9
1.2	0.3	12	0.64	0.11	<b>18.0</b>
1.2	0.6	12	0.92	0.009	1.05
1.0	0	12	0.28	0.009	3.0
1.0	0.2	12	0.26	0.004	1.6
1.0	0.4	12	0.76	0.003	0.4
1.0	0.6	12	0.91	0.003	0.3

Table 8-6 Variations in the S.D. for different testing conditions, based on experiments, Koz17.

Standard deviation as a function of blade position based on the series of experiments Koz09 is presented below. It can be observed from *Figure 8-5*, *Figure 8-6* and *Figure 8-7* that the highest standard deviation is observed for low advance speed and deep submergence. *Figure 8-5* presents the total thrust loss factor as a function of blade position for a sequence of propeller rotations (1620). During the measurements the thrust loss is quite constant during each revolution and depends on the duration of experiments. The maximum deviations  $\left(\frac{\beta_{T_{mean}} - |S.D.|}{\beta_{T_{mean}}}\right) \cdot 100\%$  is equal to 53% of the mean value of the thrust loss. Thrust

loss factor  $\beta_T$  is denoted as  $K_T/K_{T0}$  in the *Figure 8-5*, *Figure 8-6*, *Figure 8-7* and *Figure 8-8* below.

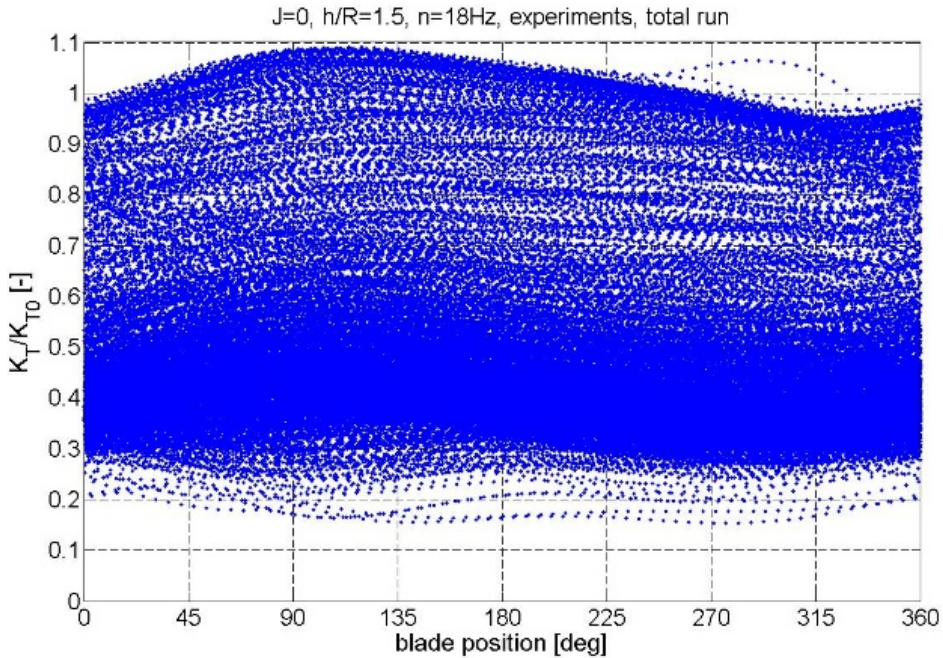


*Figure 8-5* Total thrust loss factor during each revolution, Koz10,  $h/R=1.5$ ,  $J=0$ ,  $n=18\text{Hz}$ .

*Figure 8-6* below show the variations of the S.D. as a function of blade position. For  $h/R=1$  and bollard condition S.D. varies due to the blade position. The maximum deviation of the thrust loss  $\left(\frac{\beta_{T_{mean}} - |S.D. |}{\beta_{T_{mean}}}\right) \cdot 100\%$  is the highest and equal 40% for corresponding blade position equal to 225deg, for blade position equal to 0 deg  $\left(\frac{\beta_{T_{mean}} - |S.D. |}{\beta_{T_{mean}}}\right) \cdot 100\%$  is 10%.

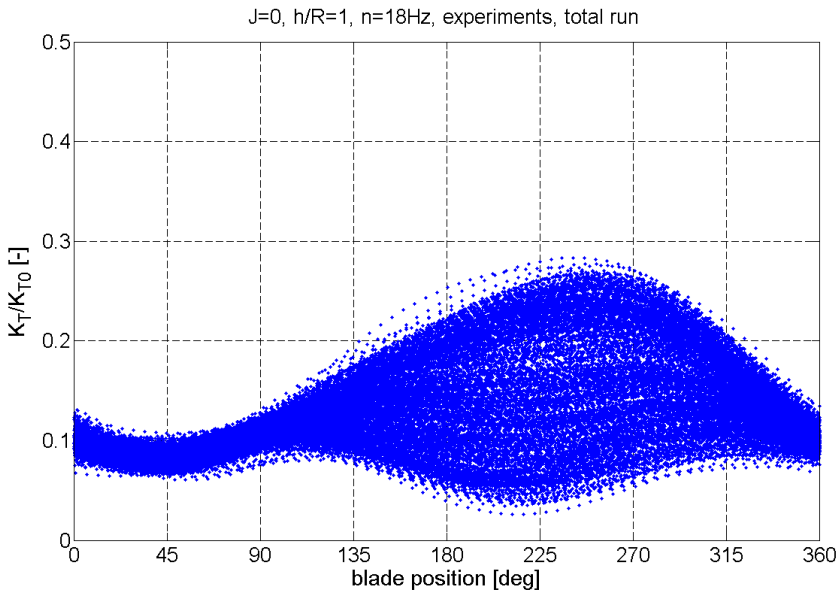
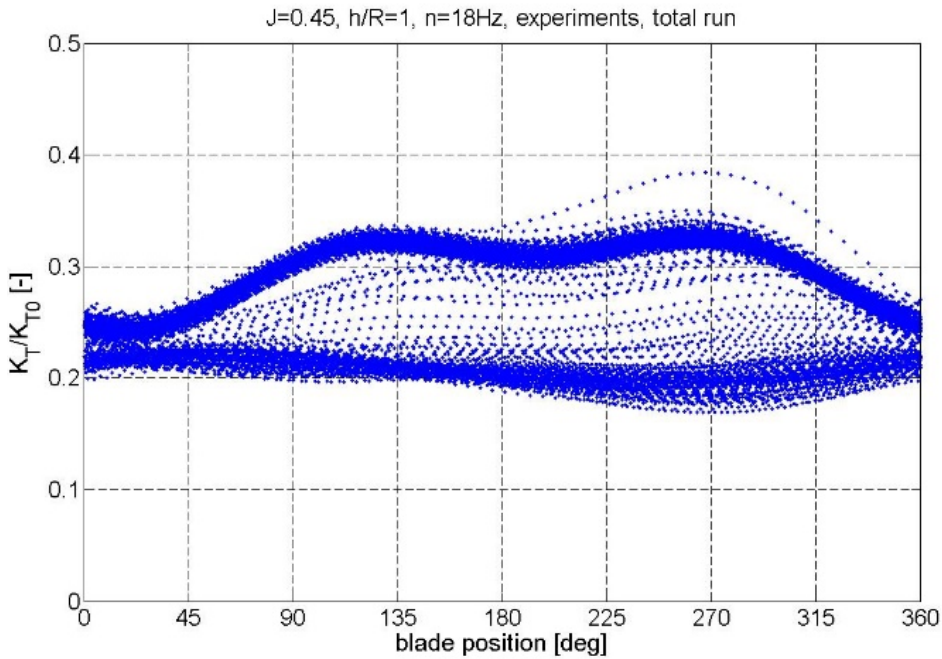


Figure 8-6 Total thrust loss factor during each revolution, Koz10,  $h/R=1.0$ ,  $J=0$ ,  $n=18Hz$ .

$$\left( \frac{\beta_{r_{mean}} - |S.D.1|}{\beta_{r_{mean}}} \right) \cdot 100\% = \begin{cases} 10\% & \text{for } 0 \text{ deg} \\ 40\% & \text{for } 225 \text{ deg} \end{cases}, \text{ see Figure 8-6}$$

Figure 8-7 below show two different thrust losses, which depends on the duration of the experiments.

As it was also presented in Figure 8-3 two different thrust losses for the same experimental conditions are observed, indicating that the flows is “switching” between the two different states of ventilation.



*Figure 8-7 Total thrust loss factor during each revolution, Koz10, h/R=1.0, J=0.45, n=18Hz.*

From comparison of the repeating tests for ventilating and non ventilating conditions one can say that the accuracy of the experiments are quite good. See for instance *Figure 3-21*, which presents the comparison for deep water thrust and torque coefficient of a single blade for open water tests and experimental results, Koz10. Also the comparison between different measurement campaigns and the same testing conditions shows a good agreement in relation to thrust loss, see *Figure 8-8* below. The main uncertainty is caused by the effect that the ventilation has a dynamic effect which is connected to the vortex formation. This effect has been included in the dynamic simulation model present in the *Chapter 6*.

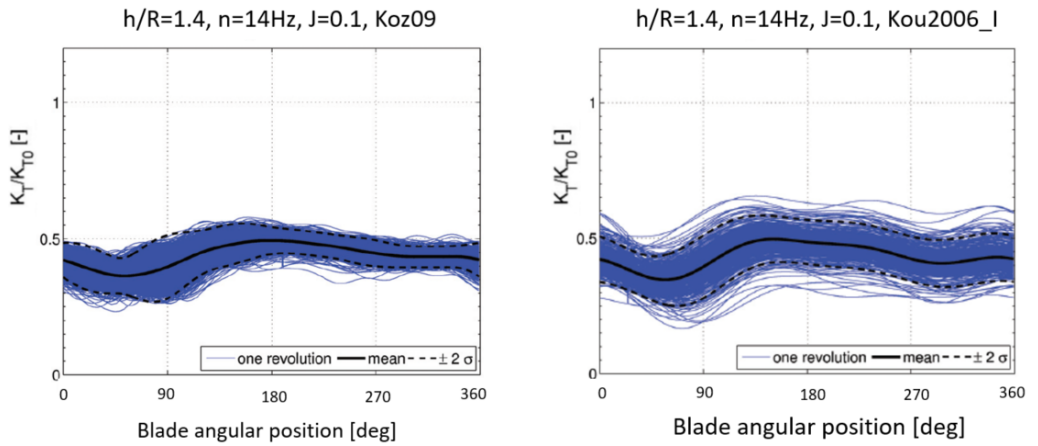


Figure 8-8 Total thrust loss factor due to ventilation as a function of blade position for two different experimental campaigns, Koz09 (right side) and Kou2006\_I (left side).

As a conclusion, one can say that the comparison between repeating test conditions for different measurement campaigns shows reasonably good agreement. The main uncertainty comes from the characteristic of the propeller ventilation, which is not repeatable from one revolution to the other. It is because ventilation shows the dynamic effect, which is connected to the dynamically changed load factor.

## 8.2 CONCLUSIONS

By means of model experiments, numerical simulations and comparison between calculation/simulation model and experimental data the present work aimed at understanding the physical mechanism related to propeller ventilation.

Propeller ventilation depends primarily on submergence, propeller loading and forward speed. The combination of above parameters determines the ventilation inception mechanisms. *Ventilation inception mechanism 1 (Impact of the free surface vortex ventilation)* occurs for highly loaded propellers at low advance number. Although ventilation is always connected to relatively high propeller loadings, *Ventilation mechanism 2 (surface-piercing ventilation)* typically occurs for higher advance number and/or lower loadings than *mechanism 1*. This means that for a given propeller pitch, the advance number is the most important factor, together with submergence.

Comparison of flow visualization recorded by high speed camera in a model test and CFD simulations shows that a fully submerged propeller ventilates more during experiments than predicted by CFD. Ventilation starts by forming a vortex, which forms a channel allowing air to be sucked down from the free surface and transporting it in the direction of propeller rotation. In the experiments, the vortex is connected much longer to the blade than in the calculations. This might be due to problems with resolving a thin ventilating vortex in CFD. Also, problems representing air bubbles in the CFD might be a reason for the large difference in visual appearance.

An analysis of the experimental data allows to define the boundaries between appearance or absence of ventilation by vortex formation for marine propellers working near the free surface. The factors determining the formation of vortex include propeller radius divided by the distance from the propeller to the free surface and the axial velocity at the propeller plane divided by the free stream velocity.

It has been shown that the vortex forming mechanism of Propeller Hull Vortex Cavitation (PHVC) is closely related to the mechanism of Propeller Free Surface Vortex Ventilation (PFSV) ventilation. The vorticity is formed by strong hydrodynamic interaction between the propeller and hull (or plate) (PHVC) and between propeller and free surface (PFSVV), which is further developed into a vortex. The occurrence of the PHVC and PFSVV depends on the propeller load coefficient  $c_T$ , tip clearance ratio  $c_t/D$  ( $h/R$  for PFSVV) and flow cavitation or ventilation number.

The relation between the cavitating/ventilating vortex and the pressure in the core of a given vortex was investigated in order to define the vortex ventilation inception. As the result a formula was obtained for the radius of cavitating/ventilating vortex, which

depends on the propeller circulation and the cavitation/ventilation number. Therefore, the relation between the ventilating minimum vortex core radius and the maximum advance number for ventilation to occur can be used to define ventilation inception.

A calculation model presented in the thesis is able to predict the thrust loss due to ventilation. The model can be applied to estimate the thrust loss for a wide range of propeller submergence ratios and at different advance numbers. The calculation model predicts the total thrust loss factor  $\beta_T = K_T/K_{Tn}$ , where  $K_T$  is the actual thrust coefficient and  $K_{Tn}$  is the time-averaged mean value of the thrust coefficient at the relevant advance number  $J$  obtained from the calm water, deeply submerged non-ventilated propeller. The calculation also predicts the ventilated blade area ratio  $A_V/A_0$  since it is required for the calculation of thrust loss in partial ventilation. For fully submerged propellers the ventilated blade area ratio  $A_V/A_0$  is computed using a steady state vortex ventilation model based on the vortex model by Rott (1958) and the propeller momentum theory. The vortex model depends on two parameters: a source strength which is related to propeller loading and the ambient vorticity the sink is gathering to form the vortex. The agreement between the experimental values (Kozl7) and calculations is very good both with respect to thrust loss calculation and amount of blade area ventilation calculated and observed from experiments. For free surface ventilation  $-1 < h/R < 1.2$  ventilated blade area ratio  $A_V/A_0$  is estimated based on visual observations from experiments Kozl7.

The thrust losses for partially submerged propellers are not only due to ventilation. One can separate the thrust losses as follows: thrust loss due to loss of propeller disc area, thrust loss due to wave making by propeller, thrust loss due to ventilation and due to Wagner effect. By comparing the experimental values  $\beta_{exp} = \beta_W \cdot \beta_0 \cdot \beta_1$  and additional formula for thrust losses  $\beta_{W0} = \beta_0 \cdot \beta_W$  it can be noticed that the effect of thrust loss due to wave making by propeller  $\beta_1$  is negligible.

A significant dynamic effect of the propeller ventilation is connected with thrust and torque hysteresis effect, appearing mostly in connection with intermittent vortex ventilation. The hysteresis effect is caused by the fact that it takes a while for ventilation of a submerged propeller to be established, so in a situation with decreasing submergence or increasing propeller loading, there is less thrust loss than for the same condition in static operation, while when ventilation disappears, it takes time for thrust to build up, due to what is called Wagner effect, so then thrust loss is larger than the corresponding static operation. In order to account for this effect the PropSim (2018) simulation model was updated. The dynamic effect was added by making propeller circulation, described in equation as a time dependent function. The comparison between the simulation model



PropSim (2018\_hysteresis) and model experiments shows good agreement, which means that the simulation model account correctly for the hysteresis effect on ventilation due to propeller working with periodically varying submersions.

The other dynamic effect, which is connected for the blade position during one cycle of rotation has been added to the simulation model denoted PropSim (2018\_blade\_dynamics). The comparison between the results obtained by simulation model, experiments and CFD calculations shows that the simulation model are more close to the CFD computational results than for experimental results. For both CFD and calculation results it is observed similar thrust loss for every propeller revolution. During measurements different thrust losses depending on the time in the experiments are observed.

The hypothesis that TIFF damages of the lower bevel gear of azimuth thrusters could be caused by a propeller blade hitting the free surface with a very low relative angle, and thereby resulting in a slamming-type load was investigated. It was found that if such a blade impact occurs, the loads might be in the order believed to be sufficient to initiate TIFF, but it was not confirmed that such an impact situation is actually likely to ever occur, since the previous blade passage creates excessive surface disturbance and air mixing.

### **8.3 RECOMMENDATIONS FOR FUTURE WORK**

The work related to the propeller simulation model PropSim (2018), PropSim (2018\_hysteresis) and PropSim (2018\_blade\_dynamics) are further developments of Dalheim's model PropSim (2016). PropSim (2016) simulation model has shown to be able to predict propeller forces (especially thrust and torque) with satisfactory results, however there was several improvements which were implemented. One of the improvements was to include a physical model for estimating ventilated blade area based on propeller loading (PropSim2018). The dynamic effects of ventilation have been added to further development of PropSim (2018) model and described below:

- PropSim (2018\_hysteresis) – hysteresis effect on ventilation due to heave motion of the propeller is added to the simulation model, see Section 6.2.1.
- PropSim (2018\_blade\_dynamics) – ventilation and thrust loss has been added as a function of blade position and it varies during one cycle of propeller rotation.

Other improvements that can be considered for the simulation model:

- Slamming model for partially working propeller can be added to calculate the impact loads between propeller changing from in - air and in - water and phase.
- Further validation of the complete simulation model with respect to full scale and model scale measurements.
- More experimental model tests are needed to validate the ventilation model for different propeller geometries

Propeller ventilation depends primarily on submergence, propeller loading and forward speed. In the currently reported method, it was chosen to combine propeller loading and forward speed into advance number, so that the two primary parameters are advance number and submergence. Only for ventilation of fully submerged propellers, the propeller loading is included as a variable. It is explained that for other submergences, excluding the propeller loading is an acceptable approximation. Since the relation between propeller loading and advance number is geometry (mainly pitch) dependent, using advance number instead of thrust loading and forward speed, means that the empirical parts of the method cannot be directly applied to other pitch settings or propeller geometries. This leads to the conclusion that test data for other pitch settings should be obtained and the method expanded and validated accordingly. The calculation and simulation model presented in the thesis was validated using just two different propellers, which have quite similar geometry and pitch characteristics. This also leads to the conclusion that the method should be expanded and validated through different propeller geometries

## REFERENCES

- Bertram, V. (2012). “Practical Ship Hydrodynamics”. 2<sup>nd</sup>ed. Butterworth – Heinemann, Oxford, UK.
- Breslin, J. P., Andersen, P. (1994). “Hydrodynamics of Ship Propellers“. Cambridge University Press, Cambridge.
- Califano, A. (2010). “Dynamics loads on marine propellers due to intermittent ventilation”. *PhD thesis*, Norwegian University of Science and Technology, Trondheim.
- Califano, A. and Steen, S. (2011\_a). “Identification of ventilation regimes of a marine propeller by means of dynamic-load analysis“. *Ocean Engineering* 38(2011), pages: 1600-1610.
- Califano, A. and Steen, S. (2011\_b). “Numerical Simulations of a fully submerged propeller subject to ventilation“. *Ocean Engineering* 38(2011) pages: 1582-1599.
- Hansen, M. O. L. (2008). “Aerodynamics of Wind Turbines“. *Second edition published by Earthscan in the UK and USA*, ISBN: 978-1-84407-438-9.
- Dalheim, Ø. Ø. (2015). “Development of a Simulation Model for Propeller Performance“. *M.Sc thesis*, Norwegian University of Science and Technology, Trondheim.
- Dang, J., Koning, J., Brouwer, J. and de Jong, J. (2013). “Dynamic Loads on Mechanical Azimuthing Thrusters“. *Proceedings of the PRADS2013*, 20-25 Oct. CECO, Changwon City, Korea.
- Denny, D. (1956). “Experimental study of air entering vortices in pump sumps“. *Institution of Mechanical Engineers- Proceedings*, 170(2):106-116.
- Dobrovolskaya, Z. N. (1969). “On some problem of similarity flow of fluid with a free surface“. *J. Fluid. Mech.*, Vol. 36 pp 805- 829.
- Faltinsen, O. M., Minsaas, K., Liapis, N. and Skjørdal, S. O. (1981) “Prediction of resistance and Propulsion of a ship in a seaway “. *In Proc. 13<sup>th</sup> Symp. on Naval Hydrodynamics. ed. T. Inui*. pp. 505-530. Tokyo, The Shipbuilding Research Association of Japan.

- Faltinsen, O. M. (1990). "Sea loads on ships and offshore structures". Cambridge University Press, Cambridge.
- Faltinsen, O. M. (2000). "Hydroelastic slamming". *Journal of Marine Science and Technology* (5), Page 49-65.
- Ferziger, J. H. and Peri'c, M. (2002). "Computational methods for fluid dynamics". Number 3rd, rev. ed. Springer, Berlin.
- Garabedian, P. R. (1953). "Oblique water entry of a wedge". *The mathematics of Nonlinear Systems*, SERC Meeting, Bath.
- Glauert, H. (1935). "Airplane propellers. Aerodynamic theory". Julius Springer, Berlin, Germany.
- Gutsche, F. (1962). "Der Einfluss der Kavitation auf die Profileigenschaften von Propellerblattschnitten". *Schiffbauforschung*, Heft 1.
- Gutsche, F. (1967). „Einfluss der Tauchung auf Schub und Wirkungs von Schiffspropellern“. Mitteilung der Schiffbau-Versuchsanstalt, Berlin.
- S. Helma (2015) "Reynolds Number Effect on Propeller Performance in Open Water" *Proceedings of Fourth International Symposium on Marine Propulsors. smp15*, Texas, USA.
- Howison, S. D., Ockendon, J. R. and Wilson, S. K. (1991). "Incompressible water entry problems at small deadrise angles", *J. Fluid Mech.*, 222. 215-230.
- Huse. (1971). "Propeller- Hull Vortex Cavitation". *Norwegian Ship Model Exp. Tank Publ.*
- Hutchison, S. and Steen, S. (2013). "Modelling of propeller hydrodynamics for implementation with multibody simulation". *Dresdner Maschinenelemente Kolloquium*, 2013 ISBN 978-3-944331-331. s. 365-384, MARINTEK NTNU.
- Jermey, M. and Ho, W. (2008). "Location of the vortex formation threshold at suction inlets near ground planes by computational fluid dynamic simulation". *Proceedings of the Institution of Mechanical Engineers*, Part G: Journal of Aerospace Engineering.
- Kempf (1934). "Immersion of Propellers". *Trans. North East Coast Institution*, Vol. 50. pp. 321 – 326, London. UK.

- Kerwin, J. E and Chang-Sup Lee (1978) "Prediction of steady and unsteady marine propeller performance by numerical lifting surface theory, SNAME Transactions, vol 86.
- Kinnas, S. A. and Hsin, C. Y. (1992) "A boundary element method for analysis of the unsteady flow around extreme propeller geometries". *AIAA Journal*, 30(3): 688-696.
- Koushan, K. (2004). "Environmental and interaction effects on propulsion systems used in dynamic positioning, an overview. In 9<sup>th</sup> Int. Symp. *Practical Design of Ships and Other Floating Structures (PRADS04)*, pages 1013-1020., Lubeck-Travemunde, Germany.
- Koushan, K. (2006a) "Dynamics of ventilated propeller blade loading on thrusters". *Proceedings of World Maritime Technology Conference (WMTC) 2006*, London, UK
- Koushan, K. (2006b) "Dynamics of Ventilated Propeller Blade Loading on Thrusters Due to Forced Sinusoidal Heave Motion". *26<sup>th</sup> Symp. On Naval Hydrodynamics*, Rome. Italy.
- Koushan, K. (2006c) "Dynamics of Propeller Blade and Duct Loadings on Ventilated Ducted Thrusters Operating at Zero Speed". *Proceedings of T-Podconference 2006*, International Conference on Technological Advances in Podded Propulsion, Brest, France
- Koushan, K., Spence S., Savio L. (2011). "Ventilated Propeller Blade Loadings and Spindle Moment of a Thruster in Calm Water and Waves". *Proceedings of Second International Symposium on Marine Propulsors. smp11*, Hamburg, Germany.
- Kozłowska, A., Steen, S. and Koushan, K. (2009). "Classification of different type of propeller ventilation and ventilation inception mechanisms". *First International Symposium on Marine Propulsors, smp09*, Trondheim, Norway.
- Kozłowska, A. and Steen, S. (2010). "Ducted and Open Propeller Subjected to Intermittent Ventilation". In *Eighteen International Conference on Hydrodynamics in Ship Design. Safety and Operation*, Gdansk.
- Kozłowska, A., Wockner, K., Rung, T. and Steen, S. (2011). "Numerical and Experimental study of propeller ventilation". *Proceedings of Second International Symposium on Marine Propulsors, smp11*, Hamburg, Germany.
- Kozłowska, A., Savio, L., Steen, S. (2017). "Predicting Thrust loss of ship propellers due to ventilation and out of water effect". *Journal of Ship research*. Vol. 61 (4).

- Kozłowska, A. and Steen, S. (2017). "Experimental analysis on the risk of vortex ventilation and the free surface ventilation of marine propellers". *Applied Ocean Research*. Vol 67.
- Kruppa (1972) "Testing of Partially Submerged Propellers", *Proc. 13th ITTC Report on Cavitation*. Berlin & Hamburg, Germany, 1972.
- Lerbs, H. W. (1952). "Moderately loaded propellers with a finite number of blades and an arbitrary distribution of circulation". *Transaction of SNAME* 60.
- MackAldener and Olsson (2000). "Interior fatigue fracture of gear teeth". *Fatigue & Fracture Engineering Materials & Structures*. 23(4): 283-292.
- MackAldener and Olsson (2002). "Analysis of crack propagation during tooth interior fatigue fracture". *Engineering Fracture Mechanics*. 69 (18): 2147-2162.
- Martio, J., Sipila, T., Sanchez-Caja, A., Saitso, I. and Siikonen, T. (2011). "Evaluation of propeller hull vortex cavitation using a RANS solver". *Proceedings of Second International Symposium on Marine Propulsors, smp11*, Hamburg, Germany.
- Minsaas, K., Wermter, R. and Hansen, A.G. (1975). "Scale Effects on Propulsion Factors". *14<sup>th</sup> International Towing Tank Conferences*, Proceedings Volume 3.
- Minsaas, K.J., Faltinsen, O. and Person, B. (1983). "On the importance of added resistance. propeller immersion and propeller ventilation for large ships in seaway". *Proceedings of International Symposium on Practical Design of Ships and other Floating Structures PRADS 1983*, Tokyo & Seoul.
- Minsaas, K. J., Thon, H. J., Kauczynski, W., and Karlsen, S. I. (1987). "Estimation of required capacity for operation of offshore vessels under severe weather conditions". In *Proceeding of International Symposium of Practical Design of Ships and Other Floating Structures – PRADS*
- Mork, L. (2007). "Slamming loads on thruster propellers". *M.Sc thesis*, Norwegian University of Science and Technology, Trondheim
- Nakayama, A. and Jones, J. R. (1996). "Vortex formation in inlet flow near the wall". In *34<sup>th</sup> Aerospace Science Meeting and Exhibit*. AIAA 96-0803.

- Nishiyama, S. (1986). "Experimental Research on propeller-hull vortex cavitation". In *Transactions of the West Japan Society of Naval Architects*.
- Olofsson, N. (1996). "Forces and Flow Characteristics of Partially Submerged Propellers". *PhD thesis*, Chalmers Tekniska Hogskola.
- Pien, P. C. (1961). "The calculation of marine propellers based on lifting surface theory". *Journal of Ship Research* 5.
- Rodert, L.A., Garret, F. B. (1955). "Ingestion of foreign objects into turbine engines by vortices". *NACATN* 3330.
- Rott, N. (1958). "On the viscous core of a line vortex". *Zeitschrift fur Angewandte Mathematik and Physik*. 9b (5-6):543-553.
- Rung, T. (2009). "Challenges and Perspectives for Maritime CFD Applications". *Jahrbuch der Schiffbautechnischen Gesellschaft*. 103. 2009.
- Philips, A. B., Turnock, S. R. and Furlong, M. (2009). "Evaluation of manoeuvring coefficients of a self-propelled ship using a blade element momentum model coupled to a Reynolds averaged Navier Stokes solver". *Ocean Engineering*, 365 (15-16): 1217:1225.
- Rankine, W. J. M. (1865). "On the mechanical principles of the action of propellers". *Transactions of the Institution of Naval Architects*.
- Rott, N. (1958). "On the viscous core of a line vortex". *Zeitschrift fur Angewandte Mathematik and Physik*, 9b(5-6):543-553.
- Ruth, E. (2008). "Propulsion control and thrust allocation on marine vessels". *PhD thesis*, Norwegian University of Science and Technology, Faculty of Engineering Service and Technology, Department of Marine Technology.
- Smogeli, (2006). "Control of Marine Propellers: From Normal to Extreme Conditions" *PhD Thesis*, Norwegian University of Science and Technology, Faculty of Engineering Service and Technology, Department of Marine Technology.
- Sato, et. al. (1986) "Observation of Flow on a Horizontal Flat Plate above a Working Propeller and Physics of Propeller- Hull Vortex Cavitation" *Proceed. International Symposium on Propeller and Cavitation*. Wuxi. China

- Savio, L. and Steen, S. (2012). "Identification and Analysis of full Scale Ventilation Events". *Hindawi Publishing Corporation, International Journal of Rotating Machinery*. Volume 2012. Article ID 951642, 19 pages.
- Shiba, H. (1953). "Air-drawing of marine propellers". *Technical report 9*, Transportation Technical Research Institute.
- Steen, S., Dalheim, Ø. Ø., Savio, L. and Koushan, K. (2016). "Time Domain modelling of propeller forces" *Proceedings of PRADS2016*, Copenhagen, Denmark.
- Tulin, M. P. and Burkart, M. P. (1956). "Supercavitating flow past foils and struts". In *National Physical Laboratory International Symposium on Cavitation in Hydrodynamics*, London. UK H.M.S.O.
- Von Karman, T. (1929). "The impact of seaplanes floats during landing". *N.A.C.A. TN321*, Washington.
- Wagner, H. (1932). "Über Stoß- und Gleitvorgänge an der Oberfläche von Flüssigkeiten". *Z.Angew.Math.Mech.12 (4)*, 192-235.
- Wockner-Kluwe, K. (2013). "Evaluation of the Unsteady Propeller Performance Behind Ships in Waves". *PhD thesis*, TUHH
- Zhao, R., Faltinsen, O. M. (1993). *J.Fluid.Mech.* vol 246pp593-612. Cambridge University Press.
- Zhao, R., Faltinsen, O. M. and Aarnes, J. (1996). "Water entry of arbitrary two dimensional sections with and without flow separation". In *Twenty-First Symposium on Naval Hydrodynamics*, MARINTEK, Norwegian University of Science and technology, Norway. pp. 408-423, National Research Council.



Appendix A  
Propellers geometry  
P1374  
P1440

**PROPELLER MODEL No.: P1374**

	Symbol	Unit	
Propeller diameter	D	[mm]	250
Pitch ratio at $r/R=0.7$	$P/D_{0.7}$	[-]	1.100
Blade area ratio	$A_E/A_0$	[-]	0.600
Number of blades	Z	[-]	4
Chord/Diameter ratio	$c/D_{0.7R}$		0.3876
Thickness/Chord ratio	$t/C_{0.7R}$	[-]	0.0410
Hub diameter ratio	$d/D$	[-]	0.240

## Test Conditions:

Propeller revolutions	n	[Hz]	11.22
Water temperature	T	[°C]	14.50
Average Reynolds no. at 0.75R	$R_n$	[-]	$1.45 \cdot 10^6$

No scaling is applied to the results

<b>J</b>	<b>K<sub>T</sub></b>	<b>K<sub>Q</sub></b>	<b>η<sub>0</sub></b>	<b>K<sub>T</sub>/J<sup>2</sup></b>
<b>[-]</b>	<b>[-]</b>	<b>[-]</b>	<b>[-]</b>	<b>[-]</b>
0.000	0.614	0.0900	0.000	
0.100	0.574	0.0851	0.107	57.396
0.200	0.528	0.0798	0.211	13.209
0.300	0.480	0.0743	0.309	5.333
0.400	0.431	0.0686	0.400	2.693
0.500	0.382	0.0629	0.483	1.529
0.600	0.335	0.0572	0.558	0.929
0.700	0.288	0.0513	0.624	0.587
0.800	0.241	0.0452	0.678	0.376
0.900	0.192	0.0385	0.715	0.237
1.000	0.140	0.0311	0.718	0.140
1.100	0.083	0.0228	0.640	0.069
1.200	0.019	0.0132	0.270	0.013
1.300	-0.056	0.0022	-5.257	-0.033

**PROPELLER MODEL No.: P1440**

	Symbol	Unit	
Propeller diameter	D	[mm]	200
Pitch ratio at $r/R=0.7$	$P/D_{0.7}$	[-]	1.200
Blade area ratio	$A_E/A_0$	[-]	0447
Number of blades	Z	[-]	4

Deep water thrust and torque coefficients of a single blade.

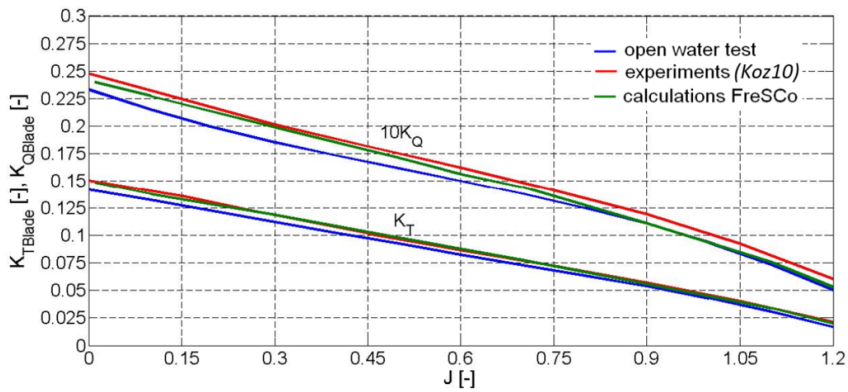


Figure 8-9 Deep water thrust and torque coefficients of a single blade.

Appendix B  
Experimental set-up and testing conditions  
*Kou2006\_I*

Purpose:

Investigator(s)	Year	Acronym	Place
Kourosh Koushan	2006	<i>Kou2006_I</i>	Marine Cybernetics Laboratory

## 1. Test Matrix

Propeller model: P1374, D=250mm

Draughts:  $h/R=2.4, 1.6, 1.2, 0.8, 0.4, 0$

Propeller speeds:  $5rps \leq n \leq 16$

Velocity of carriage:  $v=-0.35m/s, 0.35m/s, 0.5m/s, -0.5m/s$

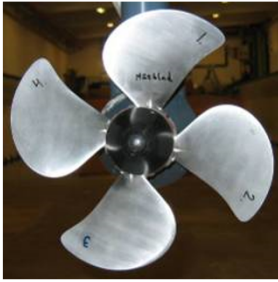
Azimuth angle:  $10deg, 20deg, 30deg$

Amplification:

	Period	Period	Period	
	[s]	[s]	[s]	
Amplification [mm]				
150	1	1.5	2	2.5
250	1.5	3	4	
300	2	4	8	

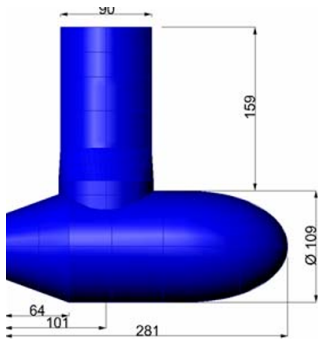
## 2. Experimental set-up

Test were performed at submergence ratios  $0 \leq h/R \leq 2.4$  in the Marine Cybernetics Laboratory at the Marine Technology Centre, having dimensions (length  $\times$  breadth  $\times$  depth) of 40m $\times$ 6.45m $\times$ 1.5m. The carriage speed  $U$  and the propeller shaft frequency  $n$  were varied in order to obtain low advance numbers  $J$  (around 0.1). The propeller (P1374) had a diameter of 250mm, blade area ratio equal to 0.6 design pitch ratio  $P/D=1.1$ , the propeller hub diameter was 65mm.



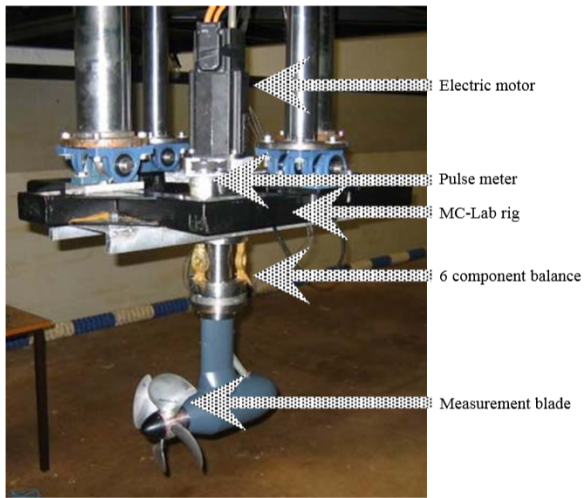
Suction side view of the open propeller

The open thruster body is 281 mm long and has a maximum diameter of 109 mm.



Open thruster body

Blade loadings of one of the four blades of the propeller of the open pulling thruster were measured using a blade dynamometer provided by Rolls-Royce Hydrodynamic Research Centre in Sweden that also provided thruster drive for these tests. This dynamometer measures blade axial and radial forces as well as moments about all three axes. The propellers were driven by electric motors on top of the thrusters. Blade loadings on one of the four propeller blades were measured. A six-component balance was positioned on top of the thruster unit, measuring loadings on the whole unit including the propeller. Data are collected at a high sampling rate. Two force transducers measured axial and transverse forces on the duct. A pulse meter indicated the angular position of the reference blade. Figure 3 shows a picture of the test set-up for open thruster. Underwater high-speed digital cameras were used to take pictures of interesting events. The cameras were mounted in streamlined underwater housings upstream of the propellers.



Test set up for open thruster



### 3. Matlab files

<i>Run</i>	<i>n</i>	<i>h/R</i>	<i>h</i>	<i>v</i>	<i>Amplitude</i>	<i>T</i>	<i>Alfa</i>
<i>[-]</i>	<i>[Hz]</i>	<i>[-]</i>	<i>[mm]</i>	<i>[-]</i>	<i>[mm]</i>	<i>[s]</i>	<i>[deg]</i>
1001	5	3,4	300	0	0	0	0
1002	5	3,4	300	0	0	0	0
1003	7	3,4	300	0	0	0	0
1004	8	3,4	300	0	0	0	0
1005	9	3,4	300	0	0	0	0
1006	10	3,4	300	0	0	0	0
1007	12	3,4	300	0	0	0	0
1008	14	3,4	300	0	0	0	0
1009	16	3,4	300	0	0	0	0
1010	up to 16	3,4	300	0	0	0	0
1011	12	3,4	300	0	0	0	0
1012	5 to 15	3,4	300	0	0	0	0
1101	12	3,4	300	0	0	0	0
1102	9	3,4	300	0	0	0	0
1103	14	3,4	300	0	0	0	0
1104	9	2,6	200	0	0	0	0
1105	11	2,6	200	0	0	0	0
1106	14	2,6	200	0	0	0	0
1107	14	2,6	200	0	0	0	0
1108	9	1,8	100	0	0	0	0
1109	11	1,8	100	0	0	0	0
1110	14	1,8	100	0	0	0	0
1111	6	1,8	100	0	0	0	0
1112	up to 6	1	0	0	0	0	0
1113	9	1	0	0	0	0	0
1114	11	1	0	0	0	0	0
1115	14	1	0	0	0	0	0
1116	6	1,4	50	0	0	0	0
1117	9	1,4	50	0	0	0	0
1118	11	1,4	50	0	0	0	0
1119	14	1,4	50	0	0	0	0
1120	Up to 14	1,4	50	0	0	0	0
1201	9	2,2	150	0	150	2,5	0
1202	11	2,2	150	0	150	2,5	0
1203	14	2,2	150	0	150	2,5	0
1204	14	2,2	150	0	150	2,5	0
1205	14	1,4	50	0	150	2,5	0
1206	11	1,4	50	0	150	2,5	0

1207	14	1,4	50	0	150	1	0
1208	11	1,4	50	0	150	1	0
1209	0 to 14	2,2	150	0	150	1	0
1210	14	2,2	150	0	150	1	0
1211	11	2,2	150	0	150	1,9	0
1212	0 to 9	1,4	50	0	250	4	0
1213	14	1,4	50	0	250	4	0
1214	11	1,4	50	0	250	4	0
1215	0 to 9	1,4	50	0	250	3	0
1216	14	1,4	50	0	250	3	0
1217	11	1,4	50	0	250	3	0
1218	0 to 9	1,4	50	0	250	1,5	0
1219	0 to 9	1	0	0	300	4	0
1220	14	1	0	0	300	4	0
1221	11	1	0	0	300	4	0
1222	14	1	0	0	300	2	0
1223	11	1	0	0	300	2	0
1224	0 to 9	1	0	0	300	2	0
1225	0 to 14	2,2	150	0	150	1,5	0
1226	14	2,2	150	0	150	1,5	0
1301	Up to 14	2,2	150	0,35	150	1,5	0
1302	14	1	0	0,35	150	1,5	0
1303	11	1	0	0,35	150	1,5	0
1304	14	1	0	0,35	300	4	0
1305	11	1	0	0,35	300	4	0
1306	14	1	0	0,5	300	4	0
1307	11	1	0	0,5	300	4	0
1308	14	1	0	0,5	150	1,5	0
1309	11	1	0	0,5	150	1,5	0
1310	9	1	0	0,5	150	1,5	0
1311	Up to 14	2,2	150	0,5	150	1,5	0
1312	Up to 14	2,2	150	0,5	150	1,5	0
1313	14	1	0	0,5	300	2	0
1314	11	1	0	0,5	300	2	0
1315	9	1	0	0,5	300	2	0
1316	6	1	0	0,5	300	2	0
1317	9	1	0	-0,5	300	4	0
1318	14	1	0	-0,35	300	4	0
1319	11	1	0	-0,35	300	4	0
1320	Up to 14	2,2	150	-0,35	150	1,5	0
1321	14	1	0	-0,35	150	1,5	0

1322	11	1	0	-0,35	150	1,5	0
1323	9	1	0	-0,35	150	1,5	0
1401	Up to 14	3,4	300	0,35	0	0	0
1402	14	1	0	0,35	0	0	0
1403	11	1	0	0,35	0	0	0
1404	9	1	0	0,35	0	0	0
1405	14	1,8	100	0,35	0	0	0
1406	11	1,8	100	0,35	0	0	0
1407	14	1,4	50	0,35	0	0	0
1408	11	1,4	50	0,35	0	0	0
1409	9	1,4	50	0,35	0	0	0
1410	9	1,4	50	0,35	0	0	0
1411	14	1,4	50	-0,35	0	0	0
1412	11	1,4	50	-0,35	0	0	0
1413	9	1,4	50	-0,35	0	0	0
1414	14	1	0	-0,35	0	0	0
1415	11	1	0	-0,35	0	0	0
1416	9	1	0	-0,35	0	0	0
1417	14	1,8	100	-0,35	0	0	0
1418	0 5 7 8	1,8	100	-0,35	0	0	0
1419	9	1,8	100	-0,35	0	0	0
1420	11	1,8	100	-0,35	0	0	0
1421	14	1,8	100	-0,35	0	0	0
1422	5 7 9	3,4	300	-0,35	0	0	0
1423	11 14	3,4	300	-0,35	0	0	0
1501	5 7	3,4	300	0,35	0	0	10
1502	0 9 11 14	3,4	300	0,35	0	0	10
1503	0 5 7	3,4	300	0,35	0	0	10
1504	11	3,4	300	-0,35	0	0	10
1505	11	3,4	300	-0,35	0	0	10
1506	14	3,4	300	-0,35	0	0	10
1601	7		84.5(-62.5)	0	0	0	0
1602	9		84.5(-62.5)	0	0	0	0
1603	11		84.5(-62.5)	0	0	0	0
1604	14		84.5(-62.5)	0	0	0	0
1605	5		22(-125)	0	0	0	0
1606	7		22(-125)	0	0	0	0
1607	9		22(-125)	0	0	0	0
1608	11		22(-125)	0	0	0	0
1609	14		22(-125)	0	0	0	0
1610	16		22(-125)	0	0	0	0

1611	5		-10.5(-157.5)	0	0	0	0
1612	7		-10.5(-157.5)	0	0	0	0
1613	9		-10.5(-157.5)	0	0	0	0
1614	11		-10.5(-157.5)	0	0	0	0
1615	14		-10.5(-157.5)	0	0	0	0
1616	16		-10.5(-157.5)	0	0	0	0
1630	7		84.5(-62.5)	-0,35	0	0	0
1631	9		84.5(-62.5)	-0,35	0	0	0
1632	11		84.5(-62.5)	-0,35	0	0	0
1633	14		84.5(-62.5)	-0,35	0	0	0
1634	9		22(-125)	-0,35	0	0	0
1635	11		22(-125)	-0,35	0	0	0
1636	14		22(-125)	-0,35	0	0	0
1637	9		-10.5(-157.5)	-0,35	0	0	0
1638	11		-10.5(-157.5)	-0,35	0	0	0
1639	11		-10.5(-157.5)	-0,35	0	0	0
1640	11		-10.5(-157.5)	-0,35	0	0	0
1641	16		-10.5(-157.5)	-0,35	0	0	0
1642	9		-10.5(-157.5)	0,35	0	0	0
1643	11		-10.5(-157.5)	0,35	0	0	0
1644	14		-10.5(-157.5)	0,35	0	0	0
1645	16		-10.5(-157.5)	0,35	0	0	0
1646	9		-10.5(-157.5)	0,35	0	0	0
1647	11		22(-125)	0,35	0	0	0
1648	14		22(-125)	0,35	0	0	0
1649	16		22(-125)	0,35	0	0	0
1650	9		84.5(-62.5)	0,35	0	0	0
1651	11		84.5(-62.5)	0,35	0	0	0
1652	14		84.5(-62.5)	0,35	0	0	0
1653	16		84.5(-62.5)	0,35	0	0	0
1701	7		-10.5(-157.5)	0,35	300	4	0
1702	9		-10.5(-157.5)	0,35	300	4	0
1703	11		-10.5(-157.5)	0,35	300	4	0
1704	14		-10.5(-157.5)	0,35	300	4	0
1705	9		-10.5(-157.5)	0,35	300	2	0
1706	11		-10.5(-157.5)	0,35	300	2	0
1707	14		-10.5(-157.5)	0,35	300	2	0
1708	9		-10.5(-157.5)	0,35	150	1,5	0
1709	11		-10.5(-157.5)	0,35	150	1,5	0
1710	14		-10.5(-157.5)	0,35	150	1,5	0
1711	9		-10.5(-157.5)	-0,35	150	1,5	0

1712	11		-10.5(-157.5)	-0,35	150	1,5	0
1713	14		-10.5(-157.5)	-0,35	150	1,5	0
1714	9		-10.5(-157.5)	-0,35	300	2	0
1715	11		-10.5(-157.5)	-0,35	300	2	0
1716	14		-10.5(-157.5)	-0,35	300	2	0
1717	9		-10.5(-157.5)	-0,35	300	4	0
1718	11		-10.5(-157.5)	-0,35	300	4	0
1719	14		-10.5(-157.5)	-0,35	300	4	0
1720	9		-10.5(-157.5)	0	300	4	0
1721	11		-10.5(-157.5)	0	300	4	0
1722	14		-10.5(-157.5)	0	300	4	0
1723	9		-10.5(-157.5)	0	300	2	0
1724	11		-10.5(-157.5)	0	300	2	0
1725	14		-10.5(-157.5)	0	300	2	0
1726	9		-10.5(-157.5)	0	150	1,5	0
1727	11		-10.5(-157.5)	0	150	1,5	0
1728	14		-10.5(-157.5)	0	150	1,5	0
1801	7		302(155)	-0,35	0	0	20
1802	9		302(155)	-0,35	0	0	20
1803	11		302(155)	-0,35	0	0	20
1804	14		302(155)	-0,35	0	0	20
1805	7&9		302(155)	0,35	0	0	20
1806	11&14		302(155)	0,35	0	0	20
1807	9		197(50)	0,35	0	0	20
1808	11		197(50)	0,35	0	0	20
1809	14		197(50)	0,35	0	0	20
1810	9		197(50)	0,35	0	0	30
1811	11		197(50)	0,35	0	0	30
1809	14		197(50)	0,35	0	0	20
1810	9		197(50)	0,35	0	0	30
1811	11		197(50)	0,35	0	0	30
1812	14		197(50)	0,35	0	0	30
1813	9		197(50)	-0,35	0	0	30
1814	14		197(50)	-0,35	0	0	30
1815	9		302(155)	0,35	0	0	30
1816	9		302(155)	-0,35	0	0	30
1817	14		302(155)	0,35	0	0	30
1818	14		302(155)	-0,35	0	0	30
1901	7		0(-270)	0,35	300	4	0
1902	11		0(-270)	0,35	300	4	0
1903	14		0(-270)	0,35	300	4	0

1904	7		0(-270)	0,35	300	2	0
1905	11		0(-270)	0,35	300	2	0
1906	14		0(-270)	0,35	300	2	0
1907	7		0(-270)	-0,35	300	4	0
1908	11		0(-270)	-0,35	300	4	0
1909	14		0(-270)	-0,35	300	4	0
1910	7		0(-270)	-0,35	300	2	0
1911	11		0(-270)	-0,35	300	2	0
1912	14		0(-270)	-0,35	300	2	0
2001	7		0(-270)	0	300	4	0
2002	11		0(-270)	0	300	4	0
2003	14		0(-270)	0	300	4	0
2004	7		0(-270)	0	300	2	0
2005	11		0(-270)	0	300	2	0
2006	14		0(-270)	0	300	2	0
2007	7		0(-270)	0	300	8	0
2008	11		0(-270)	0	300	8	0
2009	14		0(-270)	0	300	8	0
2010	5		0(-270)	0	300	8	0

Appendix C  
Experimental set-up and testing conditions  
*Kou2006\_II*

Purpose:

Investigator(s)	Year	Acronym	Place
Kourosh Koushan	2006	<i>Kou2006_II</i>	Marine Cybernetics Laboratory

#### 4. Test Matrix

Propeller model: P1374, D=250mm, ducted propeller

Duct type: 19A

Draughts:  $h/R=2.4, 1.6, 1.2, 1.0, 0.5, 0$

Propeller speeds:  $n=8rps, 9rps, 11rps, 14rps, 16rps$

Velocity of carriage:  $v=-0.35m/s, 0.35m/s, 0.5m/s, 0.75m/s, 1.0 m/s, 0m/s$

*Azimuth angle: 15deg, 45deg, 90deg, from (-10 to 10deg, speed 26deg/s)*

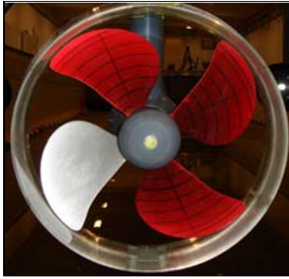
Amplification

	Period	Period
	[s]	[s]
Amplification [mm]		
150	2.5	
250	2	4

#### 5. Experimental set-up

Test were performed at submergence ratios  $0 \leq h/R \leq 2.4$  in the Marine Cybernetics Laboratory at the Marine Technology Centre, having dimensions (length  $\times$  breadth  $\times$  depth) of 40m $\times$ 6.45m $\times$ 1.5m. The carriage speed  $U$  and the propeller shaft frequency  $n$  were varied in order to obtain low advance numbers  $J$  (around 0.1). The propeller (P1374) had a diameter of 250mm, blade area ratio equal to 0.6 design pith ratio  $P/D=1.1$ , the propeller hub diameter was 65mm. The duct is a typical 19A design with a length–diameter ratio of 0.5. Tests were performed at different revolution rates and carriage speeds both at constant submersions and with periodically varying submersions, at constant azimuth angles and periodically varying azimuth angles.





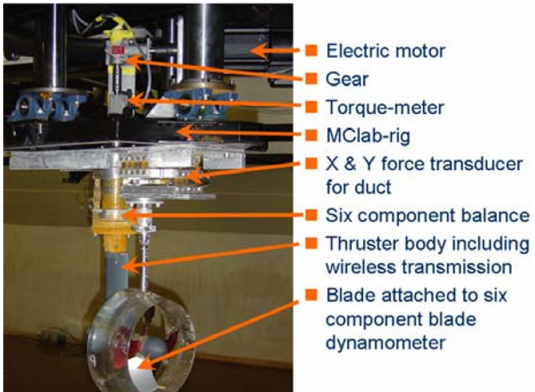
Pressure side view of the ducted propeller

The ducted thruster body is 181 mm long and has a maximum diameter of 92 mm.



Ducted thruster body

A novel blade dynamometer capable of measuring forces and moments in all six degrees of freedom was designed for the ducted pushing thruster tests in cooperation between MARINTEK and the Norwegian University of Science and Technology. The dynamometer is miniaturised and can be fitted into the propeller boss. A reliable wireless transmission system was developed to transfer the data from the blade dynamometer to the data acquisition system. This was also done in cooperation between MARINTEK and the University. The propellers were driven by electric motors on top of the thrusters. Blade loadings on one of the four propeller blades were measured. A six component balance was positioned on top of the thruster unit, measuring loadings on the whole unit including the propeller (but excluding the duct). Data are collected at a high sampling rate. Two force transducers measured axial and transverse forces on the duct. A pulse meter indicated the angular position of the reference blade. Figure 3 shows a picture of the test set-up for ducted thruster.



Test set up for ducted thruster

## 6. Matlab files

<i>Run</i>	<i>V</i>	<i>n</i>	<i>h/R</i>	<i>Angle</i>	<i>T</i>	<i>Amplitude</i>	<i>Ventilation</i>
<i>[-]</i>	<i>[m/s]</i>	<i>[Hz]</i>	<i>[-]</i>	<i>[-]</i>	<i>[s]</i>		<i>[-]</i>
6000	0	9	1,4	0	0	0	no vent'
6001	0	9	1,4	0	0	0	no vent
6002	0	14	1,4	0	0	0	no vent'
6003	0	11	1,4	0	0	0	no vent'
6004	0	14	1,4	0	0	0	vent'
6005	0	9	1,4	0	0	0	vent'
6006	0	11	1,4	0	0	0	vent'
6007	-0,35	14	1,4	0	0	0	vent'
6008	-0,35	9	1,4	0	0	0	littvent'
6009	-0,5	14	1,4	0	0	0	littvent'
6010	-0,5	9	2,4	0	0	0	littvent'
6011	0,35	14	2,4	0	0	0	littvent'
6012	0,35	9	2,4	0	0	0	novent'
6013	0,5	14	2,4	0	0	0	novent'
6014	0,75	14	2,4	0	0	0	novent'
6015	1	14	2,4	0	0	0	No vent
6016	0	14	1	0	0	0	vent'
6017	0	9	1	0	0	0	vent'
6018	-0,35	9	1	0	0	0	vent'
6019	-0,35	9	1	0	0	0	vent'
6020	0,5	14	1	0	0	0	vent'
6021	-0,5	14	1	0	0	0	vent'
6022	0,35	14	1	0	0	0	vent'
6023	0,35	9	1	0	0	0	vent'
6024	0,5	14	1	0	0	0	vent'
6025	0,5	9	1	0	0	0	vent'
6026	0,75	14	1	0	0	0	vent'
6027	0,75	9	1	0	0	0	vent'
6028	1	14	1	0	0	0	vent'
6029	1	9	1	0	0	0	vent'
6030	0,5	14	1	0	0	0	vent
6031	0,35	14	1	30	0	0	vent
6032	-0,35	9	1	30	0	0	vent
6033	0,35	14	1	30	0	0	vent
6034	0,35	14	1	30	0	0	vent
6035	0,35	9	1	30	0	0	vent
6036	0,5	14	1	30	0	0	vent
6037	0,5	9	1	30	0	0	vent

6038	0,75	14	1	30	0	0	vent
6039	0,75	9	1	30	0	0	vent
6040	0,75	9	1	30	0	0	vent
6041	0,75	14	1	15	0	0	vent
6042	0,75	9	1	15	0	0	vent
6043	0,5	14	1	15	0	0	vent
6044	0,5	14	1	15	0	0	vent
6045	0,5	9	1	15	0	0	vent
6046	0,35	14	1	15	0	0	vent
6047	0,35	9	1	15	0	0	vent
6048	0,35	14	1	30	0	0	vent
6049	0,35	9	1	30	0	0	vent
6050	0,35	14	1	15	0	0	vent
6051	0,35	9	1	15	0	0	vent
6052	0,35	14	1	45	0	0	vent
6053	0,35	9	1	45	0	0	vent
6054	0,35	14	1	45	0	0	vent
6055	0,35	9	1	90	0	0	vent
6056	0,35	14	1	90	0	0	vent
6057	0,35	9	1	90	0	0	vent
6058	0,35	14	1	90	0	0	vent
6059	0,35	9	1	90	0	0	vent
6060	0	14	0	azimuth(-10to10)	0	0	vent
6061	0	14	0	azimuth(-10to10)	0	0	vent
6062	0	14	0	0	0	0	vent
6063	0,5	14	0	0	0	0	vent
6064	0,5	9	0	0	0	0	vent
6065	0,35	14	1,7	0	0	0	vent
6066	0,35	9	1,7	0	0	0	vent
6067	0,35	14	1,7	0	0	0	vent
6068	0,35	9	1,7	0	0	0	vent
6069	0,5	14	1,7	0	0	0	vent
6070	0,5	9	1,7	0	0	0	vent
6071	0,75	14	1,7	0	0	0	vent
6072	0,75	9	1,7	0	0	0	novent
6073	0	14	1,7	0	0	0	vent
6074	0,35	14	1,7	15	0	0	vent
6075	0,35	9	1,7	15	0	0	vent
6076	-0,35	14	1,7	15	0	0	vent
6077	-0,35	9	1,7	15	0	0	vent
6078	0,35	14	1,7	30	0	0	vent

6079	0,35	9	1,7	30	0	0	vent
6080	0,35	14	1,7	30	0	0	vent
6081	0,35	9	1,7	30	0	0	vent
6082	0,35	14	1,7	45	0	0	vent
6083	0,35	9	1,7	45	0	0	vent
6084	0,35	14	1,7	45	0	0	vent
6085	0,35	9	1,7	45	0	0	vent
6086	0,35	14	1,7	90	0	0	vent
6087	0,35	9	1,7	90	0	0	vent
6088	0,35	14	1,7	90	0	0	vent
6089	0,35	9	1,7	90	0	0	vent
6090	0	14	1,7	azimuth(-10to10)	0	0	vent
6091	0	9	1,7	azimuth(-10to10)	0	0	vent
6092	-0,35	9	1,7	azimuth(-10to10)	0	0	vent
6093	-0,35	9	1,7	azimuth(-10to10)	0	0	vent
6094	0,35	14	1,7	azimuth(-10to10)	0	0	vent
6095	0,35	9	1,7	azimuth(-10to10)	0	0	vent
6096	0	9	1	azimuth(-10to10)	0	0	vent
6097	-0,35	14	1	azimuth(-10to10)	0	0	vent
6098	-0,35	9	1	azimuth(-10to10)	0	0	vent
6100	0,35	9	1	azimuth(-10to10)	0	0	
6101	0	14	1	0	2,5	150	
6102	0	9	1	0	2,5	150	
6103	0	14	1	0	1,5	150	
6104	0	9	1	0	1,5	150	
6105	-0,35	14	1	0	2,5	150	
6106	-0,35	9	1	0	2,5	150	
6107	0,35	14	1	0	2,5	150	
6108	0,35	9	1	0	2,5	150	
6109	0	14	2	0	0	0	
6110	0	14	2	0	0	0	
6111	0	9	2	0	0	0	
6112	-0,35	14	2	0	0	0	
6113	-0,35	9	2	0	0	0	
6114	0,35	14	2	0	0	0	
6115	0,5	14	2	0	0	0	
6116	1	14	2	0	0	0	
6117	-0,35	14	2	15	0	0	
6118	0,35	14	2	15	0	0	
6119	-0,35	14	2	30	0	0	
6120	0,35	14	2	30	0	0	

6121	-0,35	14	2	45	0	0	
6122	0,35	14	2	45	0	0	
6123	0,35	9	2	45	0	0	
6124	0,35	9	2	45	0	0	
6125	0,35	14	2	90	0	0	
6126	-0,35	9	2	90	0	0	
6127	0,35	14	2	90	0	0	
6128	0,35	9	2	90	0	0	
6129	0,35	14	2	(-10to10)'	0	0	
6130	0,35	9	2	(-10to10)'	0	0	
6131	-0,35	14	2	(-10to10)'	0	0	
6133	0,35	14	2	(-10to10)'	0	0	
6134	0,35	9	2	(-10to10)'	0	0	
6135	0	14	2,4	(-10to10)'	0	0	
6136	0	9	2,4	(-10to10)'	0	0	
6137	-0,35	14	2,4	(-10to10)'	0	0	
6138	-0,35	9	2,4	(-10to10)'	0	0	
6139	0,35	14	2,4	(-10to10)'	0	0	
6140	0,35	14	2,4	(-10to10)	0	0	
6141	0,35	9	2,4	(-10to10)'	0	0	
6142	-0,35	14	2,4	45	0	0	
6143	0,35	14	2,4	45	0	0	
6144	0	14	2,4	0	0	0	
6145	0	14	2,4	0	0	0	
6146	-0,35	14	2,4	90	0	0	
6147	0,35	14	2,4	90	0	0	
6148	-0,35	9	2,4	90	0	0	
6149	0,35	9	2,4	90	0	0	
6150	0	14	0	0	0	0	
6151	0	9	0	0	0	0	
6152	0	11	0	0	0	0	
6153	0	16	0	0	0	0	
6154	-0,35	14	0	0	0	0	
6155	0,35	9	0	0	0	0	
6156	0,35	14	0	0	0	0	
6157	0,35	9	0	0	0	0	
6159	0,5	14	0	0	0	0	
6160	0,5	9	0	0	0	0	
6161	0,75	14	0	0	0	0	
6162	0,75	9	0	0	0	0	
6163	1	14	0	0	0	0	

6164	1	9	0	0	0	0	
6165	-0,35	14	0	15	0	0	
6166	0,35	14	0	15	0	0	
6167	-0,35	9	0	15	0	0	
6168	0,35	9	0	15	0	0	
6169	-0,35	14	0	30	0	0	
6170	0,35	14	0	30	0	0	
6171	-0,35	9	0	30	0	0	
6172	0,35	9	0	30	0	0	
6173	-0,35	14	0	45	0	0	
6174	0,35	14	0	45	0	0	
6175	-0,35	9	0	45	0	0	
6176	0,35	9	0	45	0	0	
6177	-0,35	14	0	90	0	0	
6178	0,35	14	0	90	0	0	
6179	-0,35	9	0	90	0	0	
6180	0,35	9	0	90	0	0	
6181	0	14	0	(-10to10)	0	0	
6182	0	9	0	(-10to10)	0	0	
6183	-0,35	14	0	(-10to10)	0	0	
6184	0,35	14	0	(-10to10)	0	0	
6185	-0,35	9	0	(-10to10)	0	0	
6186	0,35	9	0	(-10to10)	0	0	
6187	0	14	0	0	2	250	
6188	0	9	0	0	2	250	
6189	0	14	0	0	4	250	
6190	0	9	0	0	4	250	
6191	-0,35	14	0	0	2	250	
6192	0,35	14	0	0	2	250	
6193	0	14	-1	0	2	250	
6194	0	9	-1	0	2	250	
6195	0	14	-1	0	4	250	
6196	0	9	-1	0	4	250	
6197	-0,35	14	-1	0	4	250	
6198	0,35	14	-1	0	4	250	
6199	0,35	9	-1	0	4	250	
6200	0,35	9	-1	0	4	250	
6201	-0,35	14	-1	0	2	250	
6202	-0,35	14	-1	0	2	250	
6203	-0,35	9	-1	0	2	250	
6204	0,35	9	-1	0	2	250	

6205	0	14	-1,4	0	1,5	250	
6206	0	16	-1,4	0	1,5	250	
6207	-0,35	14	-1,4	0	1,5	250	
6208	0,35	14	-1,4	0	1,5	250	
6209	-0,35	14	-1,4	0	2	250	
6210	0,35	14	-1,4	0	2	250	



Appendix D  
Experimental set-up and testing conditions  
*Koz09*

Purpose:

Investigator(s)	Year	Acronym	Place
Anna Kozłowska	2009	<i>Koz09</i>	Marine Cybernetics Laboratory

## 7. Test Matrix

Propeller model: P1374, D=250mm

Draughts: Test were conducted at submergence ratios  $h/R$  ranging from 2.97 (deep water case) and 1.0 (when the blade tip is touching the free surface). For all above water depths the carriage speed  $U$  and the propeller shaft frequency  $n$  were combined to obtain the advance number  $J$  around 0.1.

$h/R=2.97, 2.44, 2.24, 2.04, 1.96, 1.88, 1.80, 1.72, 1.64, 1.56, 1.48, 1.40, 1.32, 1.24, 1.00$			
$U[m/s]$	$n=12rps$	$n=14rps$	$n=16rps$
0.30	0.100	0.086	0.075
0.35	0.117	0.100	0.088
0.40	0.133	0.114	0.100

The different advance numbers were obtained at range of propeller speeds so that for the same advance numbers different thrust coefficient were tested.

## 8. Experimental set-up

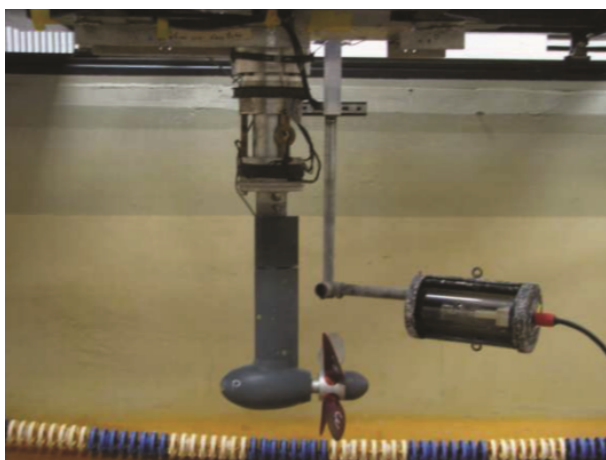
Test were performed at submergence ratios  $1.0 \leq h/R \leq 2.9$  in the Marine Cybernetics Laboratory at the Marine Technology Centre, having dimensions (length  $\times$  breadth  $\times$  depth) of 40m $\times$ 6.45m $\times$ 1.5m. The carriage speed  $U$  and the propeller shaft frequency  $n$  were varied in order to obtain advance numbers  $J$  around 0.1. The propeller (P1374) had a diameter of 250mm, blade area ratio equal to 0.6 design pitch ratio  $P/D=1.1$ , the propeller hub diameter was 65mm. During measurements images were acquired with a high speed camera at sampling frequencies in the range between 60 and 480 Hz, depending on the test conditions.



Front view of propeller



Front view of experimental set up



Lateral view of experimental set up

## 9. Test Procedure

Tests were performed for manual run

- start of data acquisition
- start of the carriage
- start of the propeller motor
- start of image acquisition after steady-state shaft frequency was reached, acquisition stops after available camera memory is full
- end of test
- stop data acquisition
- stop propeller motor
- stop carriage and start moving back to the initial position
- wait until water is calm

## 10. Matlab files

<i>h/R</i>	<i>MAT files</i>	<i>Test Log (video)</i>
2.97	001 : 009	001 : 009
2.44	010 : 012	010 : 012
2.24	013 : 015	013 : 015
2.04	016 : 023	016 : 023
1.96	024 : 030	024 : 030
1.88	031 : 040	031 : 040
1.80	041 : 049	041 : 049
1.72	050 : 083	050 : 083
1.64	084 : 093	084 : 093
1.56	068 : 076	068 : 076
1.48	094 : 0103	094 : 0103
1.40	0104 : 0112	0104 : 0112
1.32	0113 : 0121	0113 : 0121
1.24	0159 : 0168	0159 : 0168
1.00	0169 : 0177	0169 : 0177

<i>Run</i>	<i>J</i>	<i>V</i>	<i>h/R</i>	<i>n</i>
<i>[-]</i>	<i>[-]</i>	<i>[m/s]</i>	<i>[-]</i>	<i>[Hz]</i>
001	0.100	0.3	2.97	12
002	0.086	0.3	2.97	14
003	0.075	0.3	2.97	16
004	0.117	0.35	2.97	12
005	0.100	0.35	2.97	14
006	0.088	0.35	2.97	16
007	0.133	0.4	2.97	12
008	0.114	0.4	2.97	14
009	0.100	0.4	2.97	16
010	0.100	0.3	2.44	12
011	0.086	0.3	2.44	14
012	0.075	0.3	2.44	16
013	0.100	0.3	2.24	12
014	0.086	0.3	2.24	14
015	0.075	0.3	2.24	16
016	0.100	0.3	2.04	12
017	0.086	0.3	2.04	14
020	0.075	0.3	2.04	16
021	0.088	0.35	2.04	16
023	0.100	0.4	2.04	16
024	0.100	0.3	1.96	12
025	0.086	0.3	1.96	14
026	0.075	0.3	1.96	16
027	0.088	0.35	1.96	16
028	0.100	0.35	1.96	14
030	0.100	0.4	1.96	12
031	0.100	0.3	1.88	12
032	0.086	0.3	1.88	14
033	0.075	0.3	1.88	16
034	0.100	0.35	1.88	14
037	0.088	0.35	1.88	16
039	0.114	0.4	1.88	14
040	0.100	0.4	1.88	16
041	0.100	0.3	1.8	12
042	0.086	0.3	1.8	14
043	0.075	0.3	1.8	16
044	0.117	0.35	1.8	12
045	0.100	0.35	1.8	14

046	0.088	0.35	1.8	16
047	0.133	0.4	1.8	12
048	0.114	0.4	1.8	14
049	0.100	0.4	1.8	16
050	0.100	0.3	1.72	12
051	0.086	0.3	1.72	14
052	0.075	0.3	1.72	16
053	0.117	0.35	1.72	12
079	0.088	0.35	1.72	16
080	0.100	0.35	1.72	14
081	0.133	0.4	1.72	12
082	0.114	0.4	1.72	14
083	0.100	0.4	1.72	16
084	0.100	0.3	1.64	12
085	0.086	0.3	1.64	14
086	0.075	0.3	1.64	16
087	0.117	0.35	1.64	12
088	0.100	0.35	1.64	14
089	0.088	0.35	1.64	16
091	0.114	0.4	1.64	14
092	0.100	0.4	1.64	16
093	0.133	0.4	1.64	12
068	0.100	0.3	1.56	12
069	0.086	0.3	1.56	14
070	0.075	0.3	1.56	16
071	0.117	0.35	1.56	12
072	0.100	0.35	1.56	14
073	0.088	0.35	1.56	16
074	0.133	0.4	1.56	12
075	0.114	0.4	1.56	14
076	0.100	0.4	1.56	16
094	0.100	0.3	1.48	12
096	0.086	0.3	1.48	14
097	0.075	0.3	1.48	16
098	0.117	0.35	1.48	12
099	0.100	0.35	1.48	14
100	0.088	0.35	1.48	16
101	0.133	0.4	1.48	12
102	0.114	0.4	1.48	14
103	0.100	0.4	1.48	16
104	0.100	0.3	1.40	12

105	0.086	0.3	1.40	14
106	0.075	0.3	1.40	16
107	0.117	0.35	1.40	12
108	0.100	0.35	1.40	14
109	0.088	0.35	1.40	16
110	0.133	0.4	1.40	12
111	0.114	0.4	1.40	14
112	0.100	0.4	1.40	16
113	0.100	0.3	1.32	12
114	0.086	0.3	1.32	14
115	0.075	0.3	1.32	16
116	0.117	0.35	1.32	12
117	0.100	0.35	1.32	14
118	0.088	0.35	1.32	16
119	0.133	0.4	1.32	12
120	0.114	0.4	1.32	14
121	0.100	0.4	1.32	16
159	0.100	0.3	1.24	12
160	0.086	0.3	1.24	14
161	0.075	0.3	1.24	16
162	0.117	0.35	1.24	12
163	0.100	0.35	1.24	14
164	0.088	0.35	1.24	16
166	0.133	0.4	1.24	12
167	0.114	0.4	1.24	14
168	0.100	0.4	1.24	16
169	0.100	0.3	1.00	12
170	0.086	0.3	1.00	14
171	0.075	0.3	1.00	16
172	0.117	0.35	1.00	12
173	0.100	0.35	1.00	14
174	0.088	0.35	1.00	16
175	0.133	0.4	1.00	12
176	0.114	0.4	1.00	14
177	0.100	0.4	1.00	16

Appendix E  
Experimental set-up and testing conditions  
Experimental results  
Numerical calculations  
*Koz10*



Purpose: to obtain knowledge about the forces acting on propellers and thrusters in operation in heavy seas. This is performed thoroughly by experimental and numerical investigations followed by analysis and evaluation, which finally will result in recommendations and guidelines.

Investigator(s)	Year	Acronym	Place
Anna Kozłowska	2010	<i>Koz10</i>	Large Towing Tank at MARINTEK

## 11. Test Matrix

Propeller model: P1440, D=200mm

Draughts: 250mm, 150mm, 200mm, 0mm

Draughts (h/R): 2.5, 1.5, 1.0, 0

Propeller speeds:  $n=18rps$

Advance number:  $J=0.001, 0.15, 0.3, 0.45, 0.6, 0.75, 0.9, 1.05, 1.2$

## 12. Calculations (CFD)

Calculations were performed as a part of WP.2.1 task. The main focus of this work was to improve numerical methods. Two existing in-house codes, the potential flow method *ISThydro* and the RANS method *FreSCO<sup>+</sup>* were improved in order to obtain more accurate modeling of the flow around the propeller. The CFD calculations presented in this report based on in-house code *FreSCO<sup>+</sup>*. The CFD work has been done by Wockner-Kluwe (2013) in cooperation with the author. Two existing in-house codes, the potential flow method *ISThydro* and the RANS method *FreSCO<sup>+</sup>* were improved in order to obtain more accurate modeling of the flow around the propeller.

## 13. Experiments – work description

The experiments were conducted in Large Towing Tank at MARINTEK. The four bladed right handed propeller was mounted on the open water test ring. A novel blade dynamometer capable to measure 5 degrees of freedom (the centrifugal component was not measured) was used during these experiments. Use of high speed video cameras (one under and one above water) gives a visual understanding of ventilation phenomena. Post-processing the data includes the following four steps:

- Correction for the force measurement delay
- Data filtering
- Comparison with the calculations

#### 14. Correction for the force measurement delay

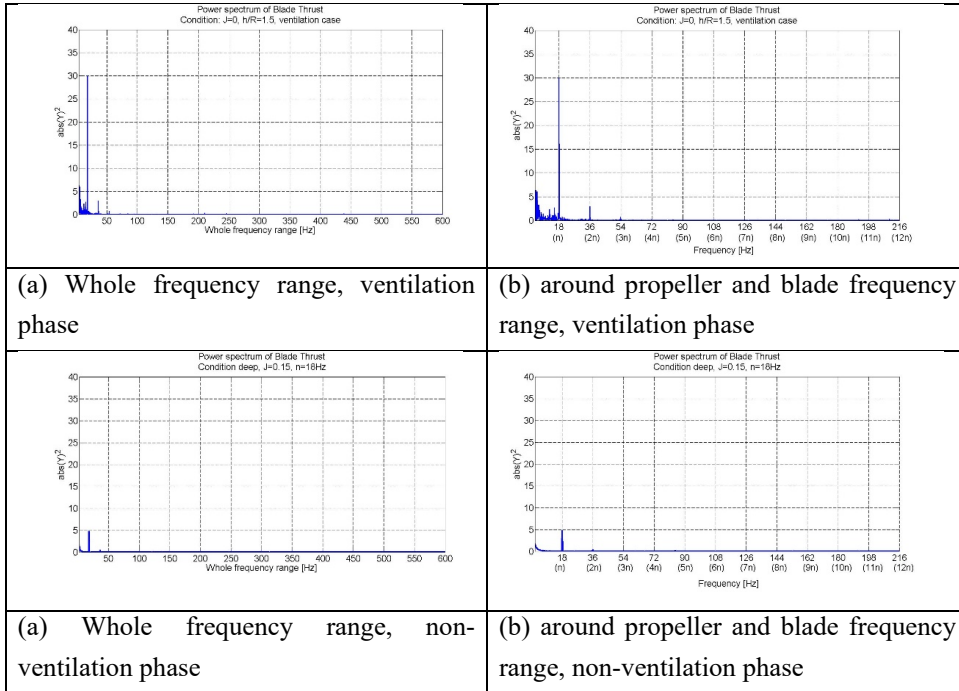
The latency of the wireless data transmission system was discovered during experiments. The latency is caused by the analogue to digital to analogue conversion that the signal paths takes prior to reaching the MGC data logging unit. To calculate the latency, an experiment was set up whereby a thruster was equipped with a 6 component shaft dynamometer and a 2 kg load was hung on a ball bearing attached to the dynamometer. The propeller rotated at 0.2, 6, 10, and 12 Hz and the data was recorded at 2400 Hz. Due to the mounting of the thruster on the model, which was inclined at 8 degrees in the longitudinal direction and 12 degrees in the lateral direction, the 2kg load provided forces in all three axial directions, but primarily on the Fz (vertical) channel.

The latency of the system appears to be constant and equal to 0.00569s. For more detailed description see Silas Spencer: Wireless Data Transmission Latency - Marintek report.

prop_rps	FY_Glob	FZ_Glob	Offset Angle	Time Offset
rps	N	N	deg	s
0.19	-0.32	17.87		
5.97	-4.08	17.18	12.15	0.00565
9.98	-6.53	16.27	20.33	0.00566
12.00	-7.75	15.54	24.57	0.00569

#### 15. Data filtering

In order to capture the dynamics a high samplings frequency of 1200 Hz was used during these experiments. The power spectrum of blade thrust for the raw data from experiments is plotted in Figure 1 below where the peaks due to propeller loads and due to noise can be noticed. A low-pass filter with a cutting frequency of 160Hz was applied during the comparison. Figure shows that the dominant frequency is propeller frequency both for non-ventilating and fully ventilating cases.



### Co-ordinate system

In order to have better comparison between calculations and experiments the same system of co-ordinates were used in this report.

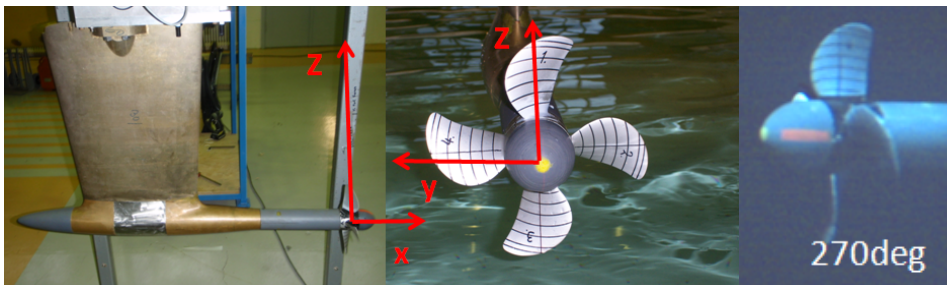


Figure 2. Co-ordinate system - used for comparison between calculations and experiments.

In this co-ordinate system  $x$  is the axis in propeller shaft direction. Thus  $F_{X\_B}$  is the blade thrust and  $M_{X\_B}$  is the blade torque. During the model tests a 5 axis blade dynamometer was used. The measurement blade was marked by the red line of the propeller shaft.

Force /Moment	Name	unit
FX_B	Blade Thrust	N
FY_B	Blade Side Force	N
MX_B	Blade Torque	Nm
MZ_B	Blade Spindle Moment	Nm
FX_B0	Nominal Blade Thrust	N
FY_B0	Nominal Blade Side Force	N
MX_B0	Nominal Blade Torque	Nm
MZ_B0	Nominal Blade Spindle Moment	Nm

Table 4. Co-ordinate system

## 16. Comparison matrix

Experimental test were conducted for four submergence ratios  $h/R=2.5, 1.5, 1$  (when the blade tip is touching the free surface (FS)) and 0 (when half of the propeller is out of water). For all four submergences the carriage speed was varied in order to obtain the following advance numbers ( $J=0, 0.15, 0.3, 0.45, 0.6, 0.75, 0.9, 1.05, 1.2$ ). Propeller revolution was constant and equal to 18 Hz. Calculations were performed for two propeller submergence  $h/R=2.5, 1.5$  and nine propeller advance numbers ( $J=0.001, 0.15, 0.3, 0.45, 0.6, 0.75, 0.9, 1.05, 1.2$ )

### Experiments

$h/R$ [-]	$J$ [-]	$n$ [Hz]
2.5	0, 0.15, 0.3, 0.45, 0.6, 0.75, 0.9, 1.05, 1.2	18Hz
1.5	0, 0.15, 0.3, 0.45, 0.6, 0.75, 0.9, 1.05, 1.2	18Hz
1	0, 0.15, 0.3, 0.45, 0.6, 0.75, 0.9, 1.05, 1.2	18Hz
0	0, 0.15, 0.3, 0.45, 0.6, 0.75, 0.9, 1.05, 1.2	18Hz

### Calculations (CFD)

$h/R$ [-]	$J$ [-]	$n$ [Hz]
2.5	0.001, 0.15, 0.3, 0.45, 0.6, 0.75, 0.9, 1.05, 1.2	18Hz
1.5	0.001, 0.15, 0.3, 0.45, 0.6, 0.75, 0.9, 1.05, 1.2	18Hz



$[-]$	$[mm]$	$[-]$	$[m/s]$	$[-]$	$[Hz]$	$[N]$	$[Nm]$
2031_1	0	0,75	2,70	0	18	169,59	3,58
2032_1	0	0,00	0,00	0	18	22,27	1,05
2033_1	0	0,15	0,53	0	18	17,75	0,96
2034_1	0	0,30	1,08	0	18	18,37	0,63
2035_1	0	0,45	1,62	0	18	23,96	0,63
2036_1	0	0,60	2,16	0	18	33,86	0,99
2037_1	0	0,75	2,70	0	18	56,90	1,25
2038_1	0	0,90	3,24	0	18	47,21	1,24
2039_1	0	1,05	3,78	0	18	33,13	0,91
2040_1	0	1,20	4,32	0	18	10,03	0,53
2022_1	100	0,00	0,00	1	18	63,34	1,19
2023_1	100	0,15	0,53	1	18	41,86	1,05
2024_1	100	0,30	1,08	1	18	50,92	1,28
2025_1	100	0,45	1,62	1	18	54,06	0,97
2026_1	100	0,60	2,16	1	18	177,80	4,13
2027_1	100	0,75	2,70	1	18	167,57	4,10
2028_1	100	0,90	3,24	1	18	135,70	2,10
2029_1	100	1,05	3,78	1	18	91,91	1,67
2030_1	100	1,20	4,32	1	18	56,81	1,02
2011_1	150	0,75	2,70	1,5	18	209,39	7,04
2012_1	150	0,00	0,00	1,5	18	212,76	6,99
2013_1	150	0,15	0,53	1,5	18	195,79	6,88
2014_1	150	0,30	1,08	1,5	18	190,64	5,79
2015_1	150	0,45	1,62	1,5	18	231,89	7,42
2016_1	150	0,60	2,16	1,5	18	202,69	6,46
2017_1	150	0,75	2,70	1,5	18	170,37	6,13
2018_1	150	0,90	3,24	1,5	18	132,56	5,61
2019_1	150	1,05	3,78	1,5	18	92,48	4,74
2020_1	150	1,20	4,32	1,5	18	49,69	2,80
2001_1	250	0,00	0,00	2,5	18	341,22	9,34
2002_1	250	0,15	0,53	2,5	18	305,28	8,36
2003_1	250	0,30	1,08	2,5	18	262,84	7,93
2004_1	250	0,45	1,62	2,5	18	233,88	7,53
2005_1	250	0,60	2,16	2,5	18	200,74	7,18
2006_1	250	0,75	2,70	2,5	18	169,10	6,64
2007_1	250	0,90	3,24	2,5	18	130,05	6,01
2008_1	250	1,05	3,78	2,5	18	97,84	5,84

### Deep water results $h/R=2.5$

Figure 3 shows the thrust and torque coefficients of the propeller blade in non-ventilating, deep water conditions ( $h/R=2.5$ ). Experimental data from the towing tank tests with blade

dynamometer are compared with corresponding open water test performed in the cavitation tunnel and calculations. The comparison is satisfactory although experiments and CFD calculations overpredicted the thrust and torque compared with the open water test in the cavitation tunnel. The agreement between CFD calculations and experiments are quite good.

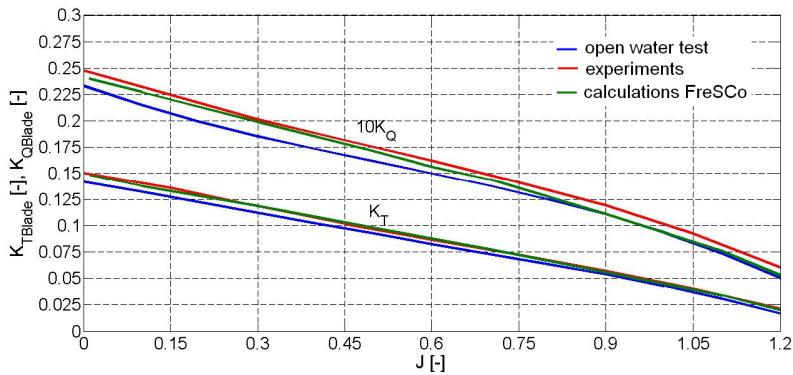
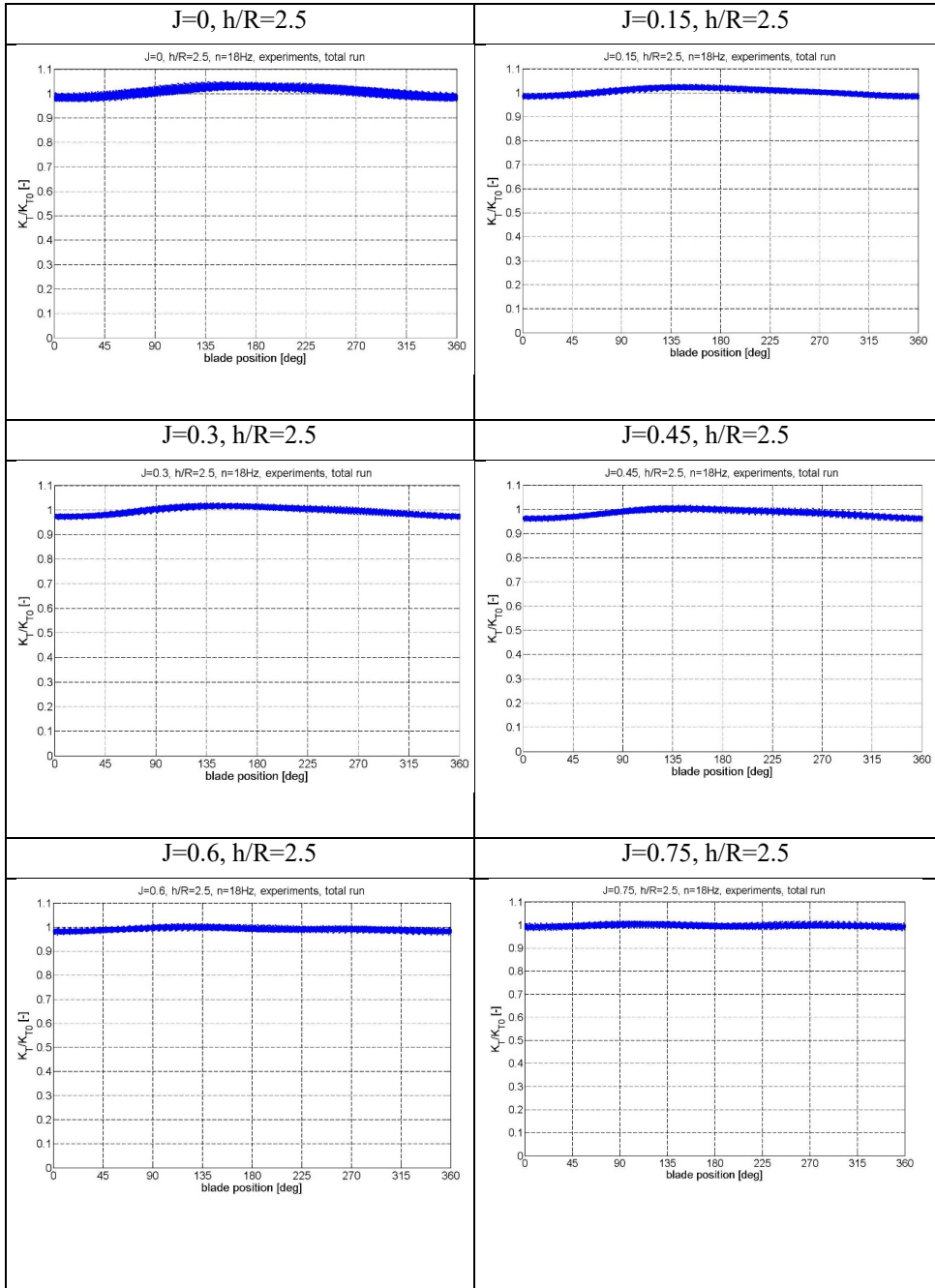
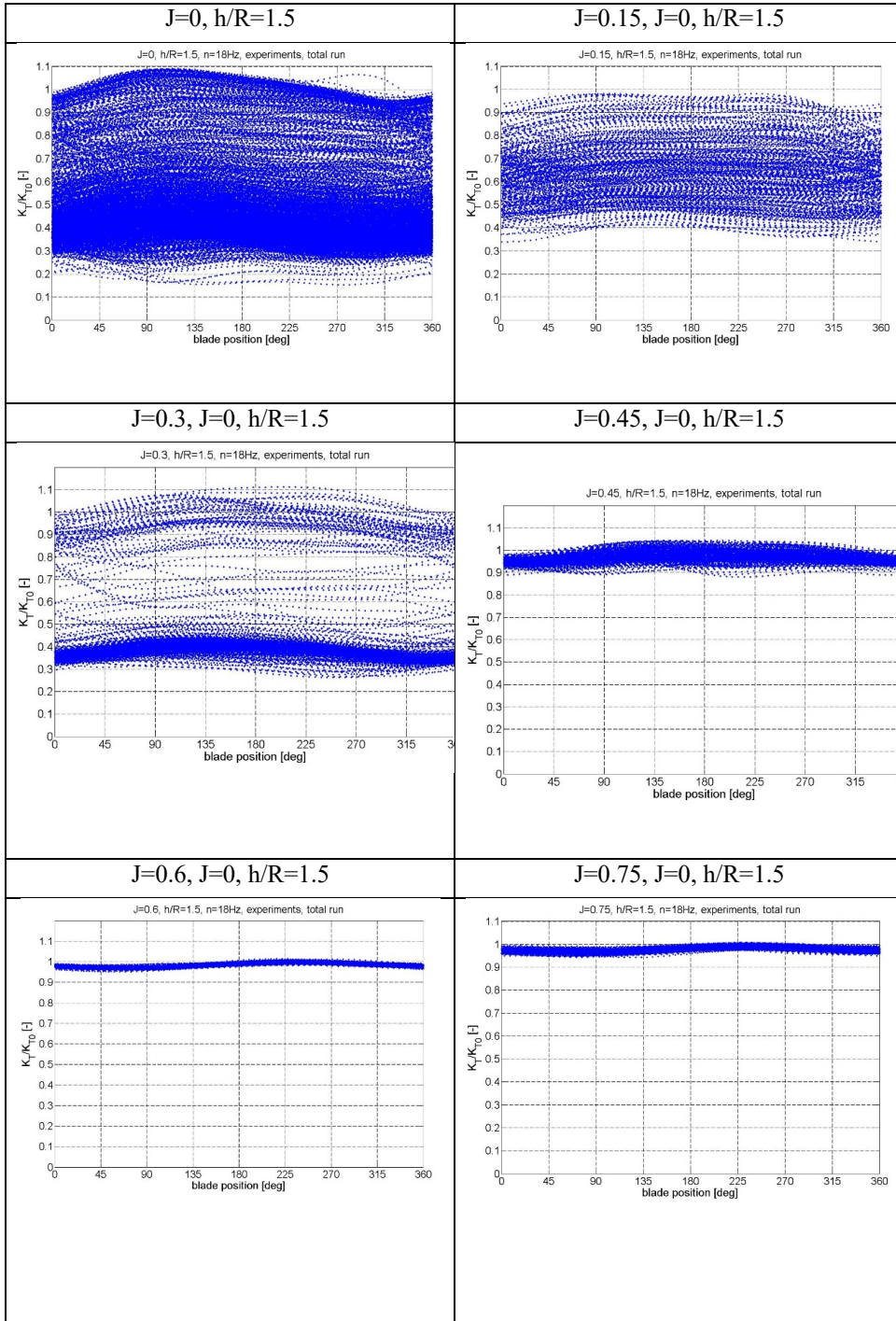


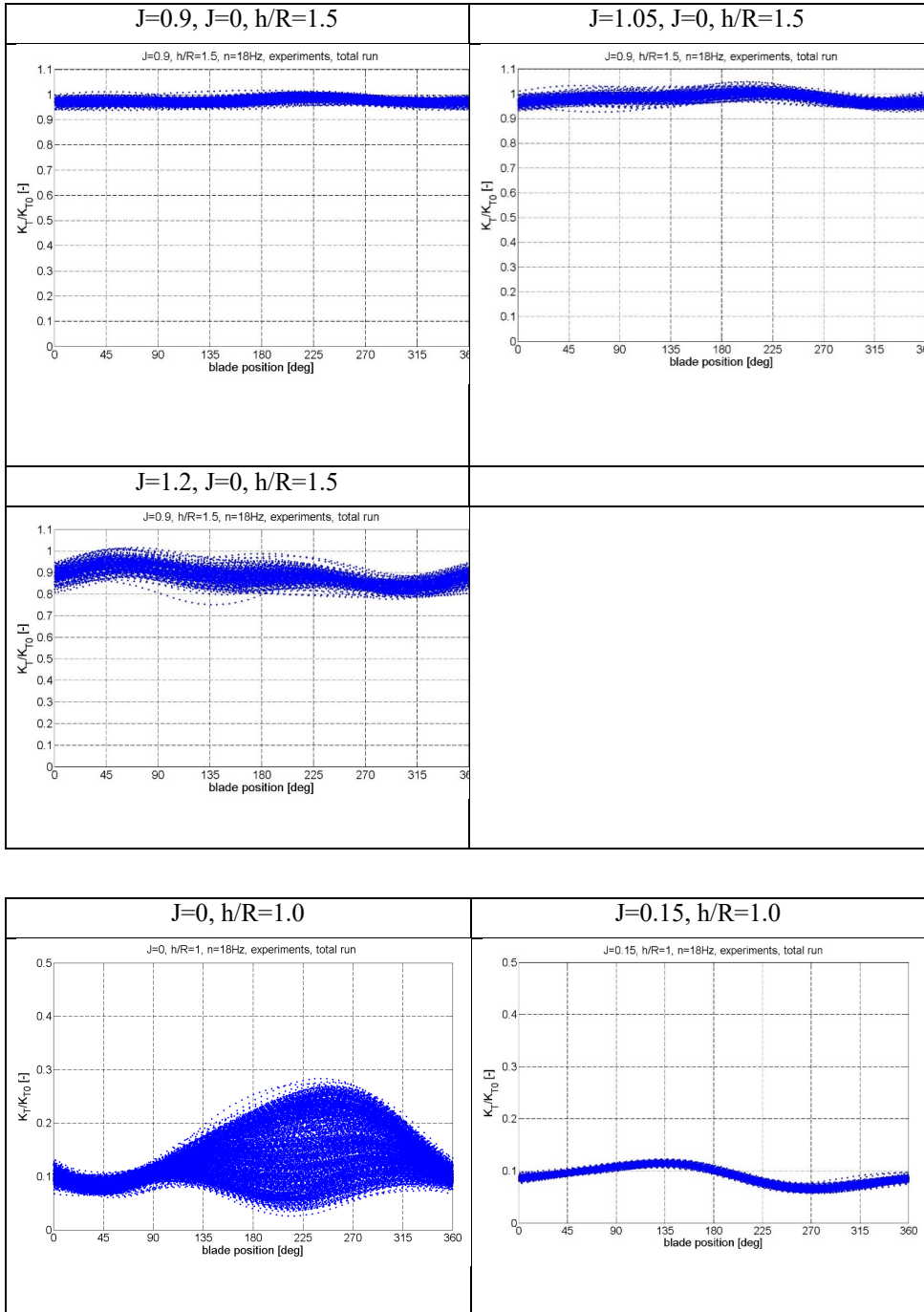
Figure 3. Blade thrust and torque coefficients for non-ventilating, deep water conditions for the present experiments (open water test) and CFD calculations

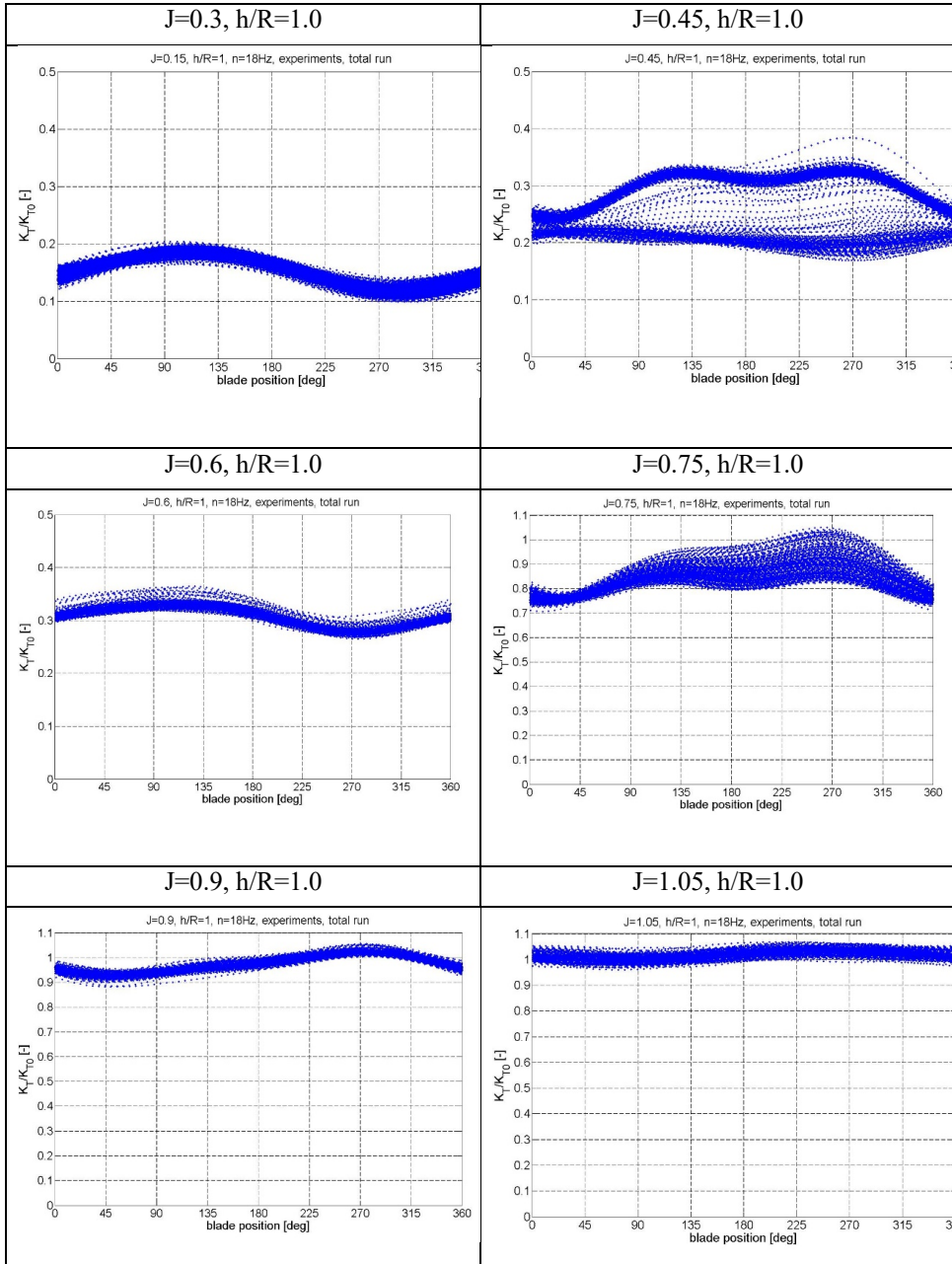
## 18. Complete experimental results

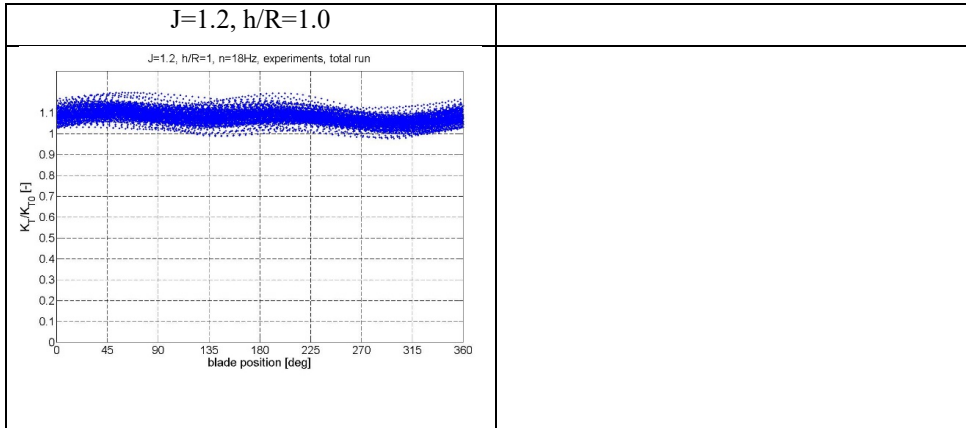


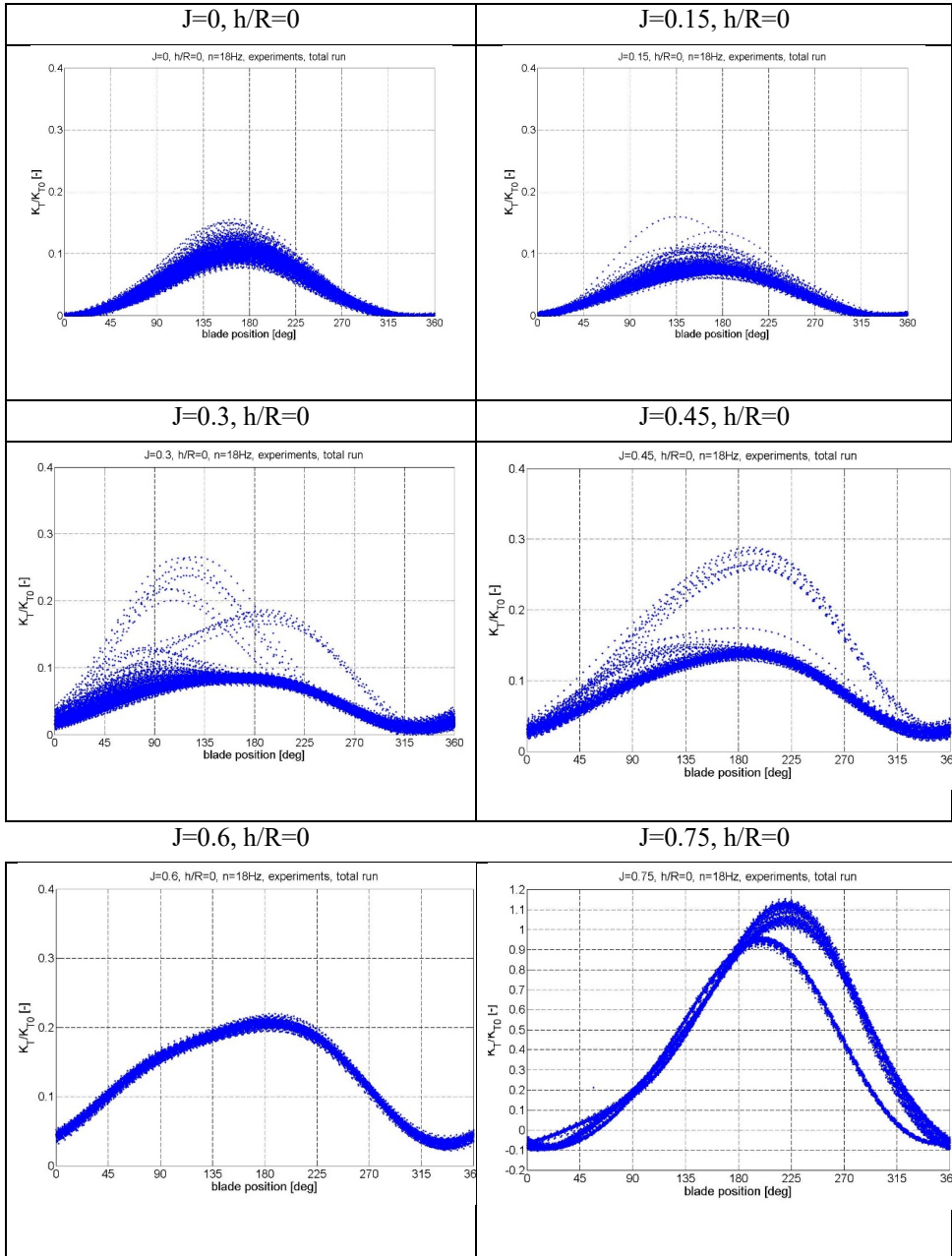


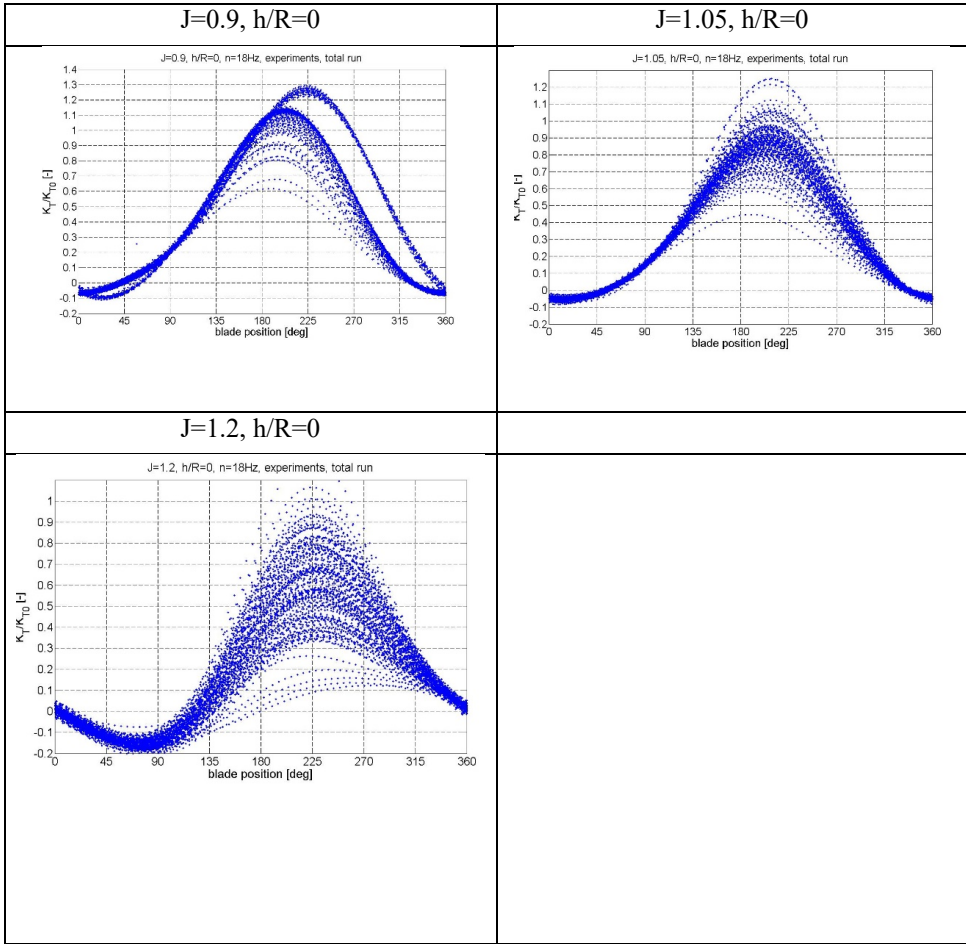




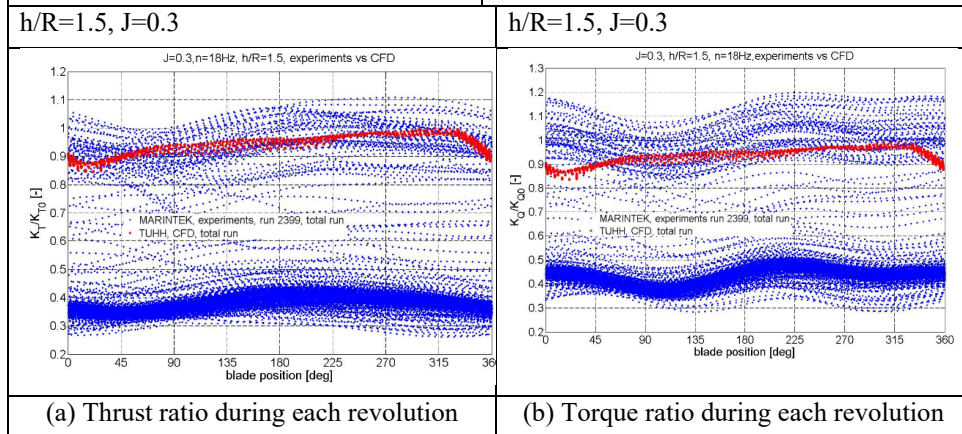
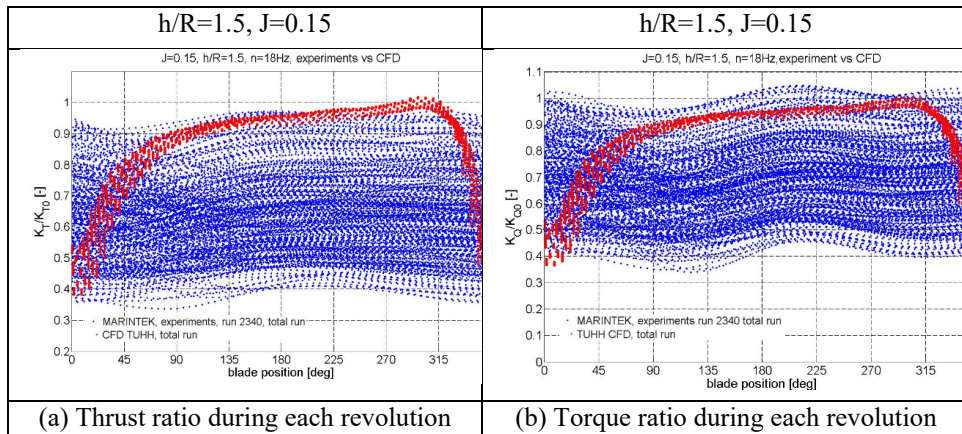
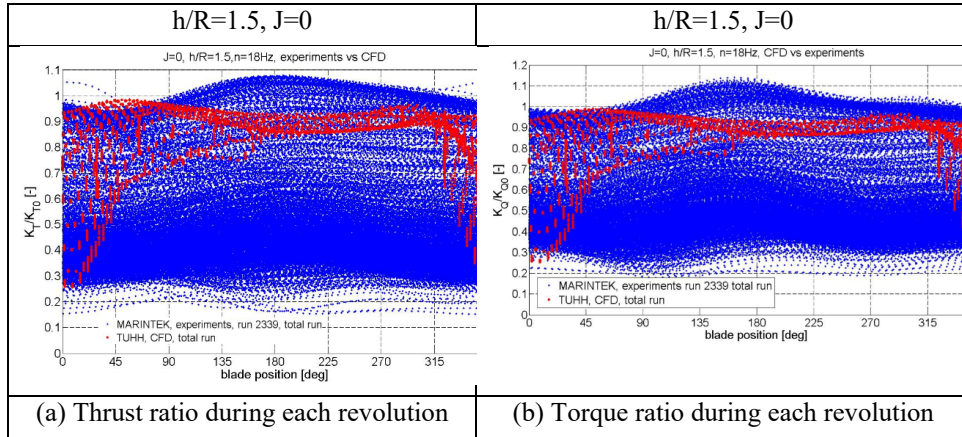


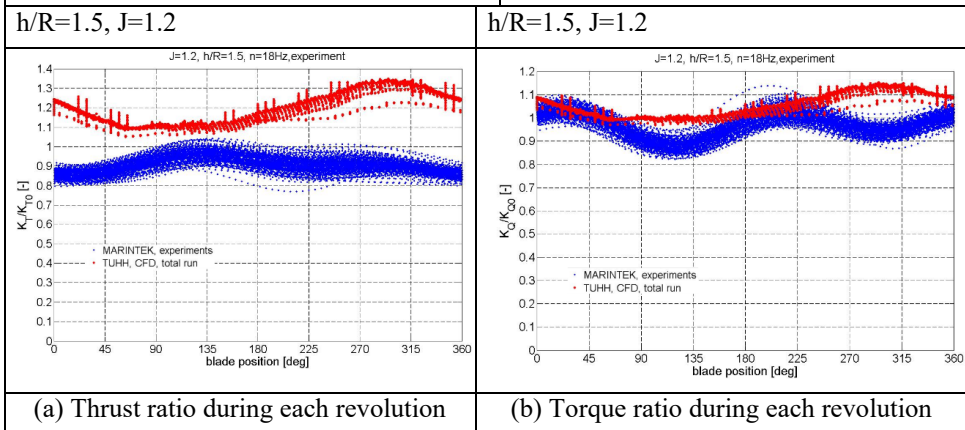
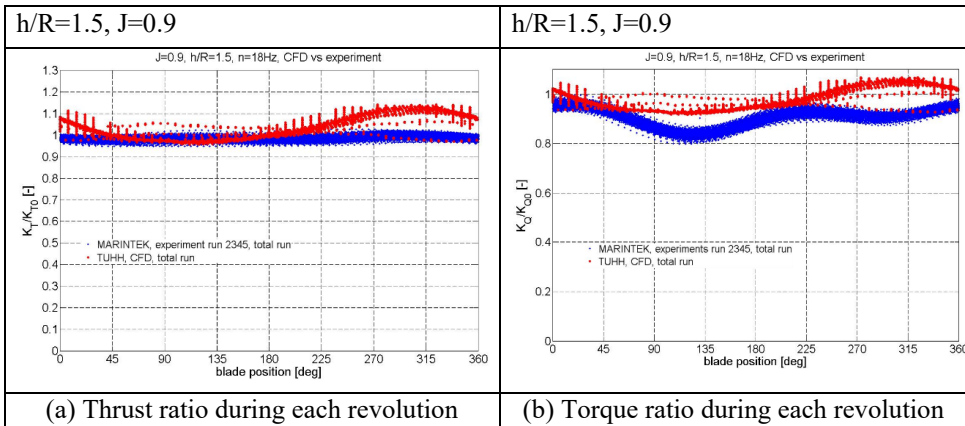
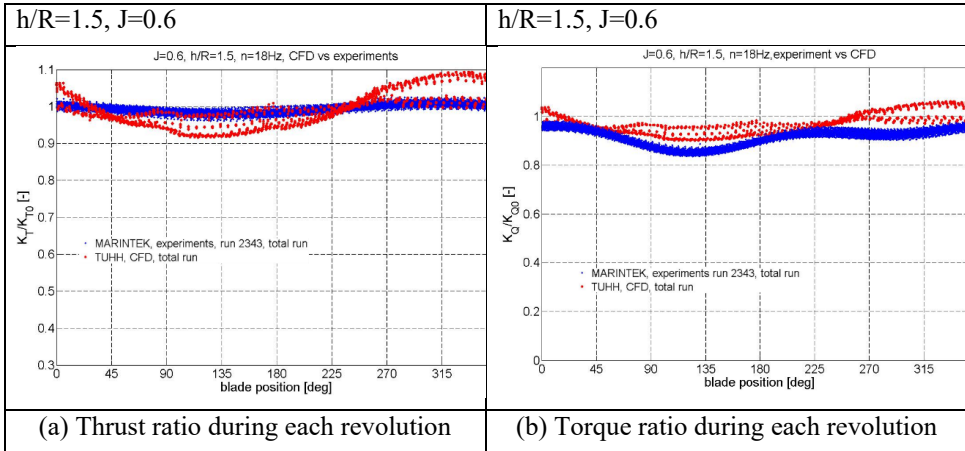






19. Comparison between calculations and experiments – data analysis







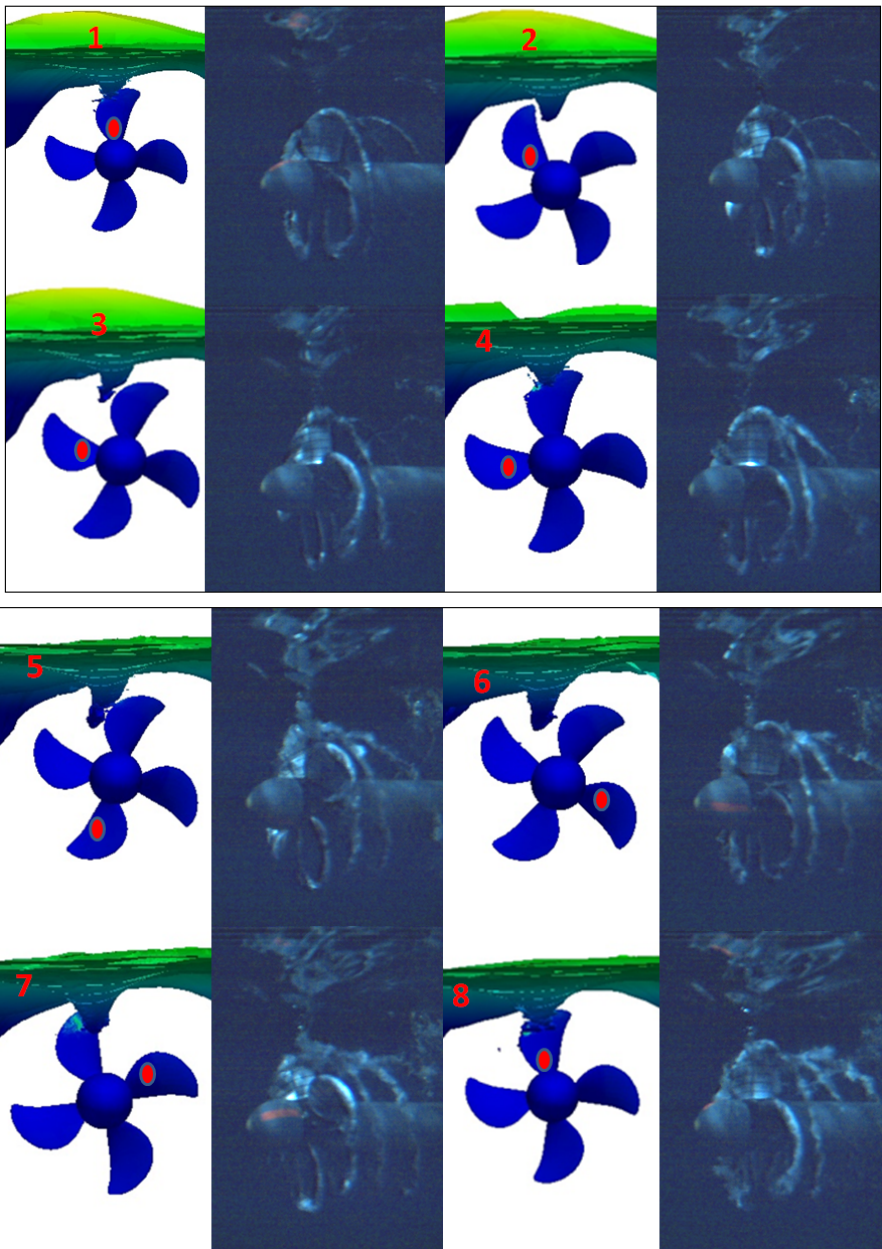
## 20. Comparison between calculations and experiments – flow visualization ( $h/R=1.5$ )

During experiments visualization of flow was performed by using two high speed cameras. The frame rate of the cameras was 500 Hz or 1000Hz, which means that during each propeller rotation 27 or 54 photos were recorded. Due to memory capacity it were able to record 555 photos, which correspond to 20.5 or 10.25 propeller rotations. Table below shows the comparison between the camera start time and CFD simulation.

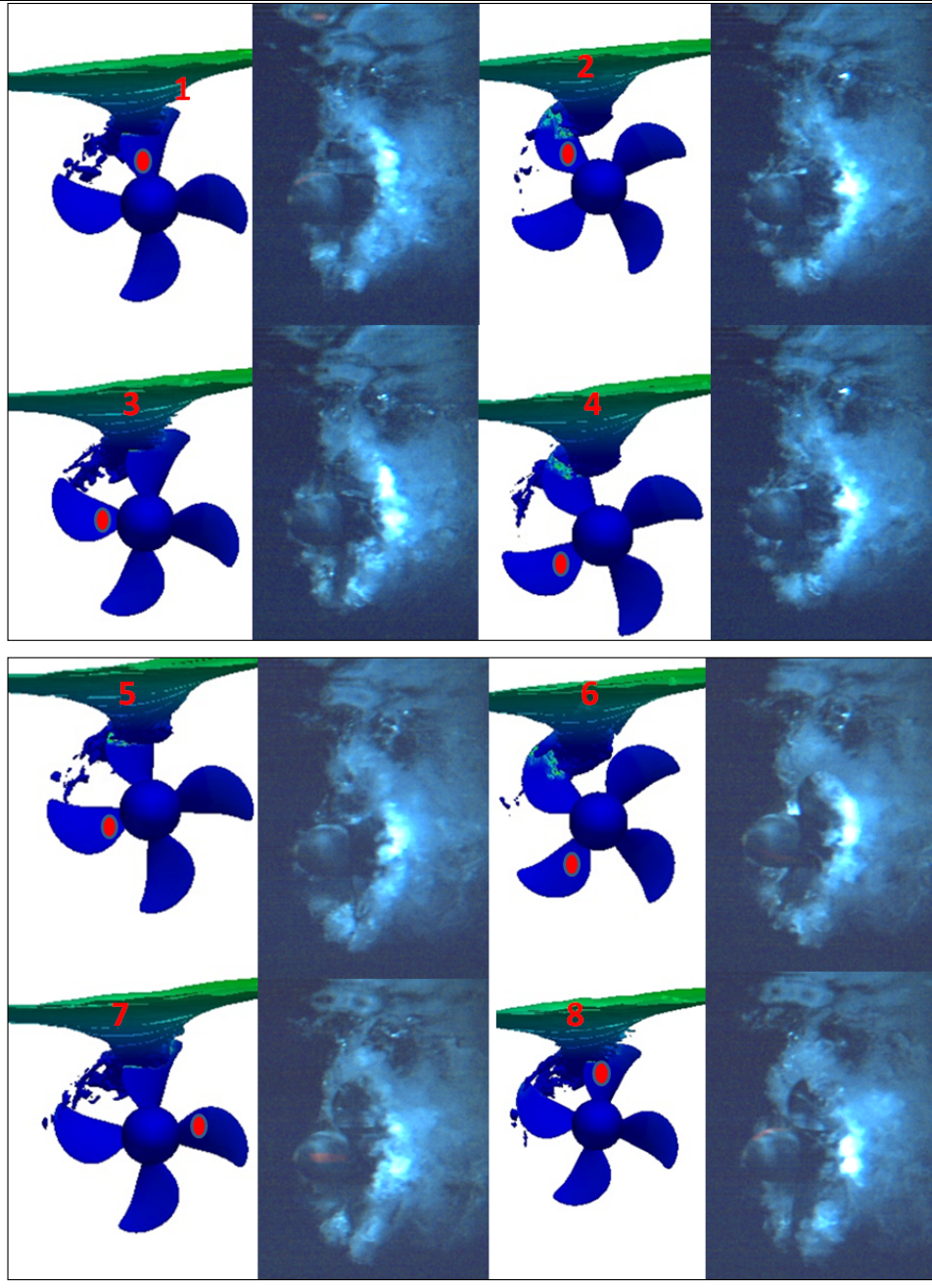
Run	Camera start (experiments)	Starting point(when the propeller and carriage achieve required speed)	CFD (simulation)
J=0	After 43.7 s from the starting point = 786 propeller rotations	11.9 s from the beginning of experiments	one rotation between 0.833s and 0.888s and one rotation between 1.0545s and 1.11s
J=0.15	After 7.85 s from the starting point = 141 propeller rotations	14.75 s from the beginning of experiments	one rotation between 0.3885s and 0.444s
J=0.3	After 19.51 s from the starting point = 351 propeller rotations	36.05 s from the beginning of experiments	one rotation between 0.3885s and 0.444s

Table 5 Time difference between camera start and CFD simulations.

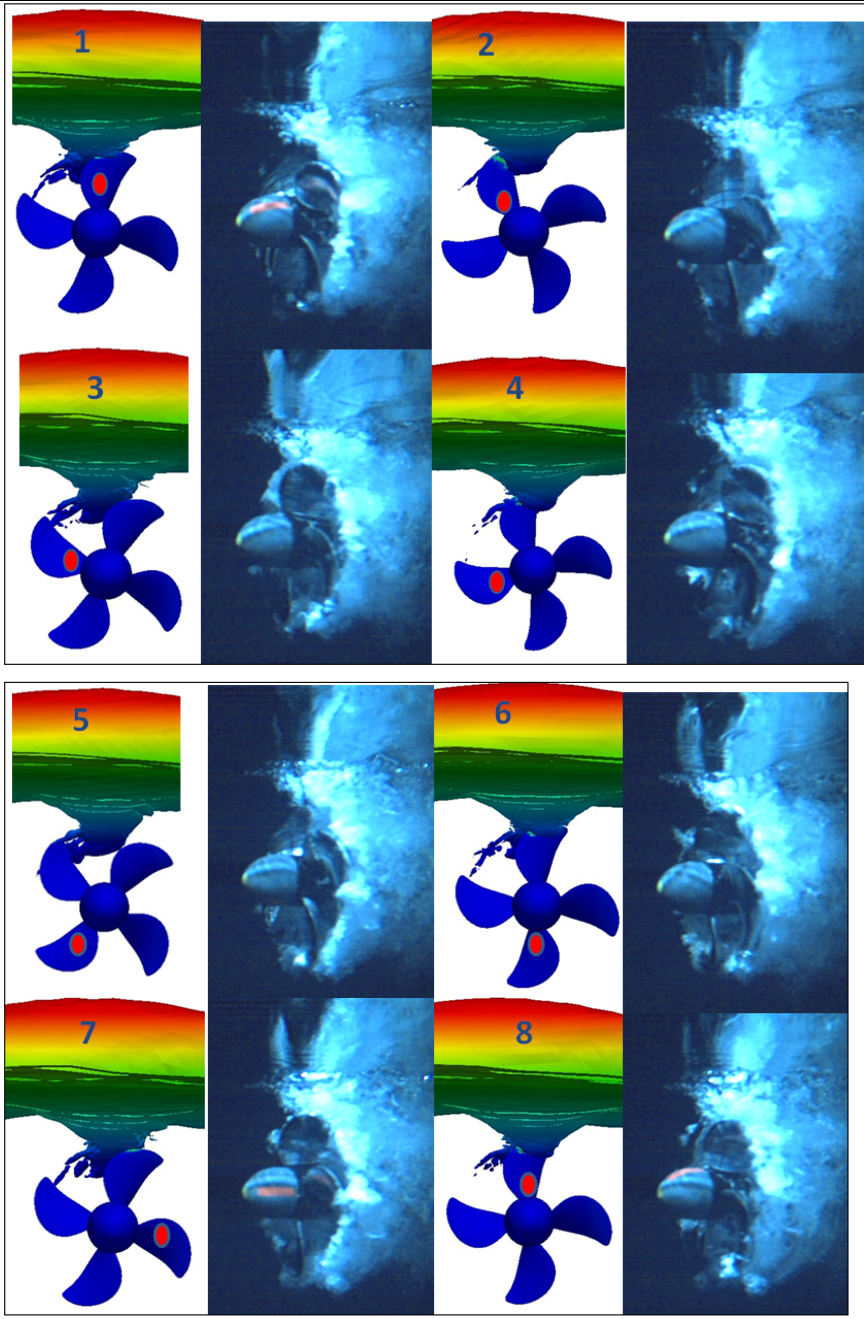
J=0, non ventilated and partially ventilated regime – one rotation (0.833s and 0.888s)



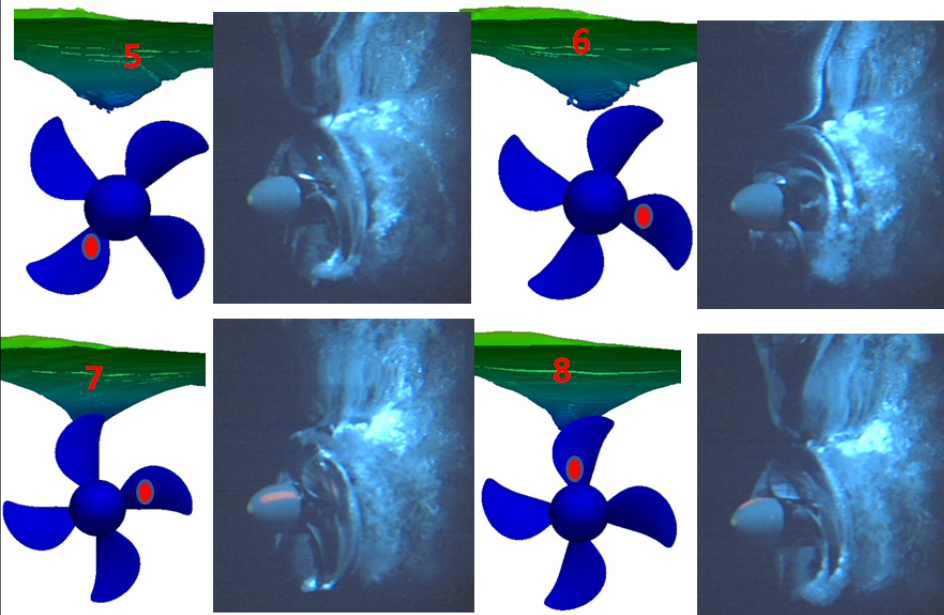
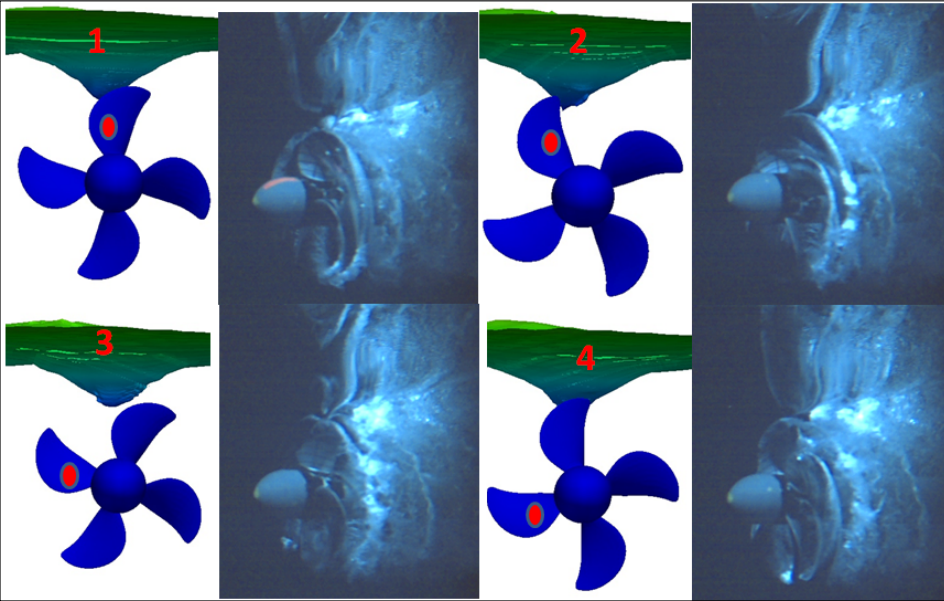
J=0, partially ventilated and fully ventilated regime- one rotation (1.0545s and 1.11s)



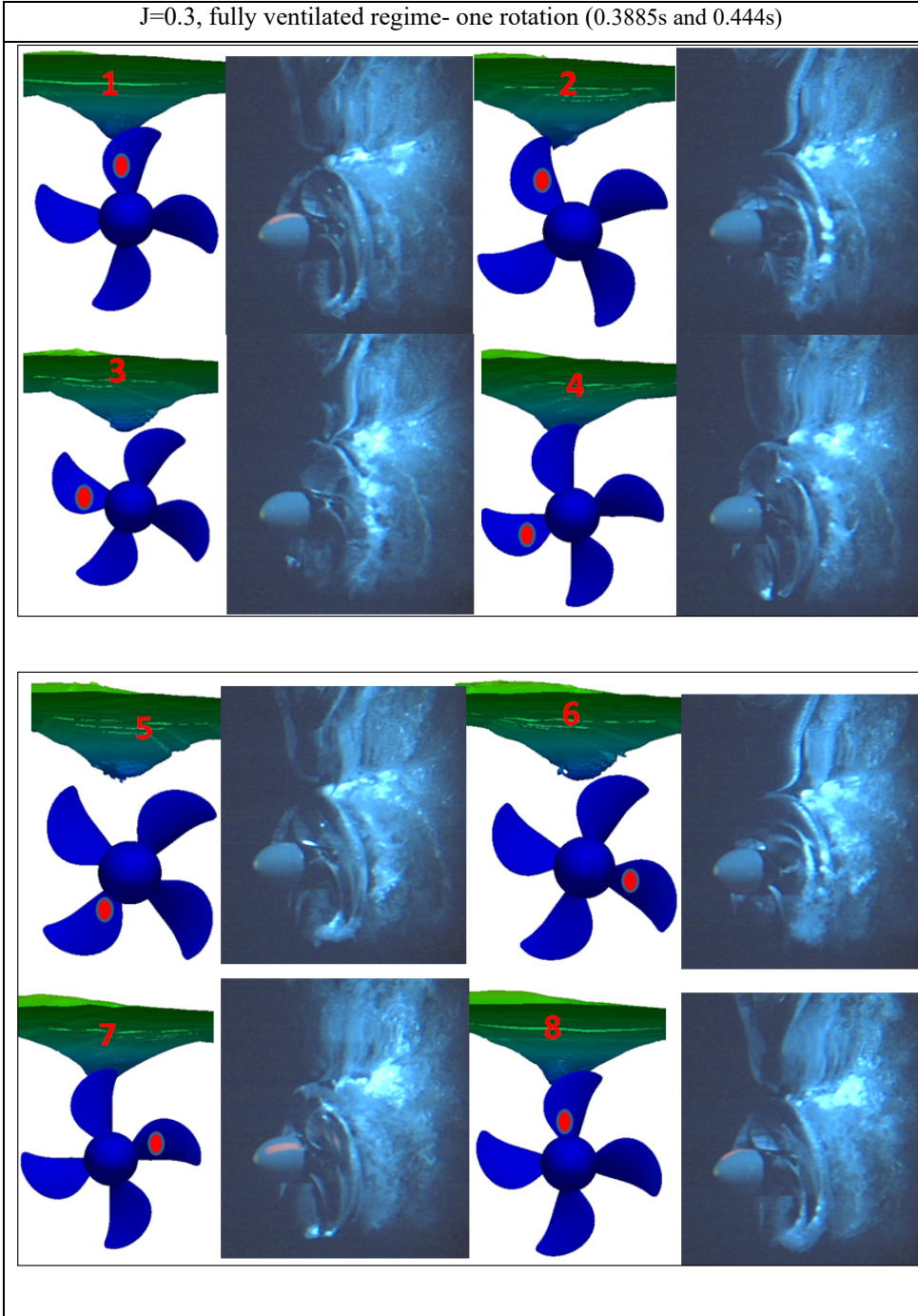
$J=0.15$ , partially ventilated and fully ventilated regime- one rotation (0.3885s and 0.444s)



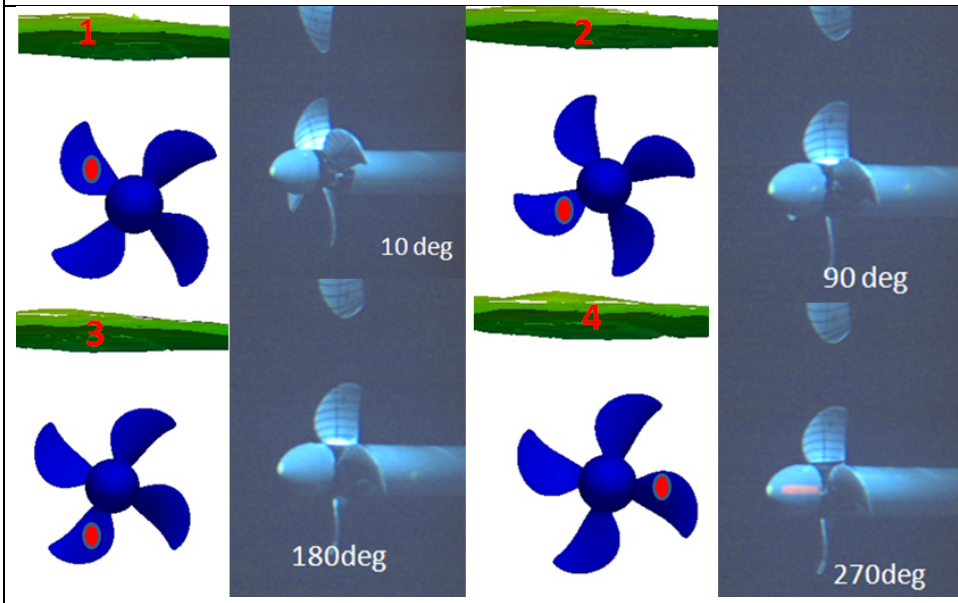
$J=0.15$ , partially ventilated and fully ventilated regime- one rotation (0.3885s and 0.444s)



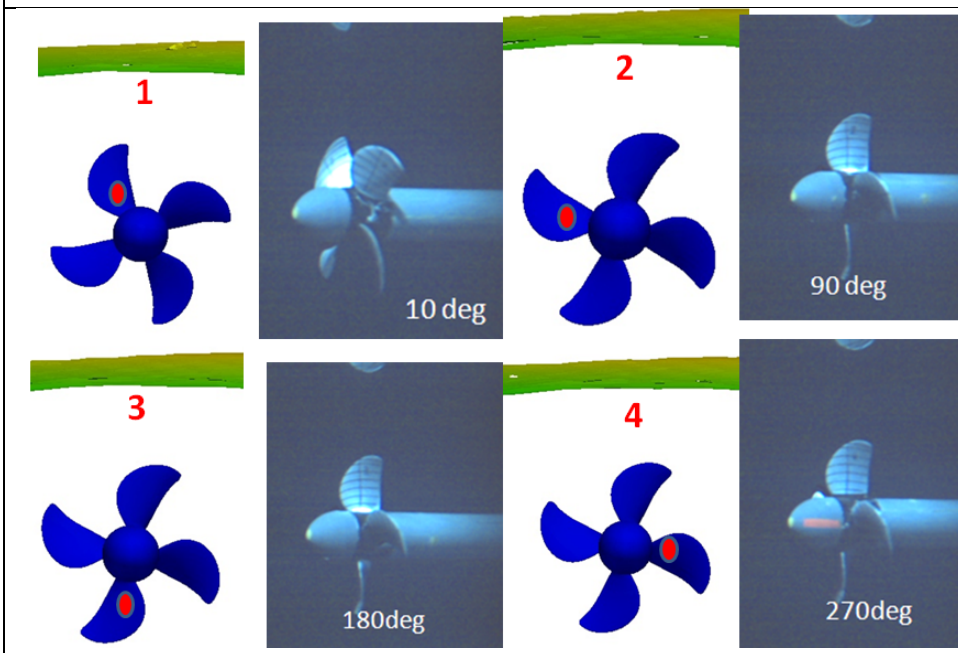
J=0.3, fully ventilated regime- one rotation (0.3885s and 0.444s)



J=0.6, non ventilated regime- one rotation (0.3885s and 0.444s)



J=0.9, non ventilated regime- one rotation (0.3885s and 0.444s)



Appendix F  
Experimental set-up and testing conditions  
Experimental Results  
*Koz17*



Purpose: To obtain data for validation purpose and to make empirical model for thrust loss and torque due to free surface proximity. We also want to get better data at higher advance numbers, and to vary both  $K_T$  and  $C_P$ .

Investigator(s)	Year	Acronym	Place
Anna Kozłowska	2016	<i>Koz16</i>	Large Towing Tank at MARINTEK

## 21. Test Matrix

Propeller model: P1374, D=250mm

Draughts:  $h/R=2.4, 2.0, 1.6, 1.5, 1.4, 1.2, 1.0, 0.5, 0, -0.5$

Propeller speeds:  $n=9rps, 12rps, 14rps, 16rps$

Advance number:  $0 \leq J \leq 1.0$

The different advance numbers were obtained at range of propeller speeds so that for the same advance numbers different thrust coefficient were tested.

## 22. Experimental set-up

Test were performed in large towing tank at MARINTEK having dimensions (length  $\times$  breadth  $\times$  depth) of 175m  $\times$  10.5m  $\times$  5.6 m. Four bladed, right handed propeller model (P1374) was used during the experiments. The propeller has a diameter of 250mm, blade area ratio equal to 0.6 design pitch ratio  $P/D=1.1$ , the propeller hub is 65mm.

Conventional two components propeller open water dynamometer was used to measured propeller thrust and torque. Due to the torque (15Nm) and force (400N) limit I had to limited the cases for higher propeller revolutions, see Table below.

$n$ [rps]	9 rps	12 rps	14 rps	16 rps
$J$ [-]	0 – 1.0	0 – 1.0	0.3 – 1.0 for $h/R > 1.4$ 0 – 1.0 for $h/R \leq 1.4$	0.6 – 1.0 for $h/R > 1.2$ 0 – 1.0 for $h/R \leq 1.2$
$V_A$ [-]	0 – 2.25	0 – 3.0	1.05 – 3.5 for $h/R > 1.4$ 0 – 3.5 for $h/R \leq 1.4$	2.4 – 4.0 for $h/R > 1.2$ 0 – 4.0 for $h/R \leq 1.2$
$h/R$ [-]	-0.5, 0, 0.5, 1.0, 1.2, 1.4, 1.5, 1.6, 1.8	-0.5, 0, 0.5, 1.0, 1.2, 1.4, 1.5, 1.6, 2.0	-0.5, 0, 0.5, 1.0, 1.2, 1.4, 1.5, 1.6, 2.0	-0.5, 0, 0.5, 1.0, 1.2, 1.4, 1.5, 1.6, 2.0

During measurements images are acquired with 2 high speed cameras (top and suction side view of the propeller) at sampling frequency 200 Hz. The camera is controlled by dedicated computer providing trigger pulses in order to extract time when the pictures were taken.

The wave making by the propeller were measured by using stationary wave probe in the tank to provide a longitudinal cut type wave pattern measurement.

The necessary light for the camera acquisition system is provide by two: one above and one underwater lamps. The configuration of the lights is sketched in Figure.

The signals were acquired at sampling frequency 200 Hz using a 20 Hz Butterworth filter.

### **Test Procedure**

Tests were performed for both manual and automatic run. The test procedure varies for this two different types of runs. For automatic runs was not possible to performed measurements for bollard conditions.

#### Manual run

- start of data acquisition
- start of the carriage
- start of the propeller motor
- start of image acquisition after steady-state shaft frequency was reached, acquisition stops after available camera memory is full
- end of test
- stop data acquisition
- stop propeller motor
- stop carriage and start moving back to the initial position
- wait until water is calm

#### Automatic run

- start of data acquisition
- start of the propeller motor
- start of the carriage
- start of image acquisition after decided time, acquisition stops after available camera memory is full
- end of test
- stop data acquisition
- stop propeller motor
- stop carriage and start moving back to the initial position
- wait (15 minutes) between runs until water is calm

**23. Matlab files**

h/R	MAT files	Test Log (video)
2.4	9001 : 9004	9001:9004
2.0	1005 : 1018	1001_5 : 1001_18
1.4	2001 : 2013	2001_1 : 2001_13
1.6	3001 : 3033	3001_1 : 3001_33
1.0	4001 : 4026	4001_1 : 4001_26
1.2	5001 : 5045	5001_1 : 5001_45
0	6001 : 6024	6001_1 : 6001_24
0.5	7001 : 7016	7001_1 : 7001_16
-0.5	8001 : 8010	8001_1 : 8001_10
1.5	101 : 120	0001_1 : 0001_20

## 24. Experimental Results

<i>Run</i>	<i>Sub</i>	<i>J</i>	<i>V</i>	<i>h/R</i>	<i>n</i>	<i>Mean Thrust</i>	<i>Mean Torque</i>	<i>Ventilation</i>
<i>[-]</i>	<i>[-]</i>	<i>[-]</i>	<i>[m/s]</i>	<i>[-]</i>		<i>[N]</i>	<i>[Nm]</i>	<i>[-]</i>
9000_1	1	0	0,00	2,40	9	195,4	7,4	no
	2	0,2	0,45	2,40	9	168,5	6,5	no
	3	0,4	0,90	2,40	9	138,0	5,6	no
	4	0,6	1,35	2,40	9	105,4	4,6	no
	5	0,8	1,80	2,40	9	72,6	3,6	no
	6	1	2,25	2,40	9	38,7	2,4	no
1001_5	1	0,2	0,45	2,00	9	169,3	6,5	no
1001_6	1	0,4	0,90	2,00	9	136,6	5,6	no
1001_7	1	0,6	1,35	2,00	9	103,8	4,6	no
1001_8	1	0,8	1,80	2,00	9	72,7	3,6	no
1001_9	1	1	2,25	2,00	9	39,6	2,5	no
1001_10	1	0,2	0,60	2,00	12	296,8	11,5	no
1001_11	1	0,4	1,20	2,00	12	238,4	9,7	no
1001_12	1	0,6	1,80	2,00	12	182,3	8,0	no
1001_13	1	0,8	2,40	2,00	12	128,0	6,3	no
1001_14	1	1	3,00	2,00	12	71,0	4,4	no
1001_15	1	0	0,00	2,00	9	192,3	7,3	yes, VV
1001_16	1	0	0,00	2,00	12	349,8	13,1	yes, VV
1001_17	1	0,3	1,05	2,00	14	363,5	14,4	no
1001_18	1	0,4	1,40	2,00	14	320,1	13,1	no
	2	0,6	2,10	2,00	14	245,9	10,8	no
	3	0,8	2,80	2,00	14	173,0	8,5	no
	4	1	3,50	2,00	14	97,7	5,9	no
1001_19	1	0,6	2,40	2,00	16	314,7	13,9	no
	2	0,8	3,20	2,00	16	221,2	10,9	no
	3	1	4,00	2,00	16	122,0	7,5	no
2001_1	1	0		1,40	9	116,8	4,8	yes, VV
2001_2	1	0,2		1,40	9	132,9	5,4	yes, VV
2001_3	1	0,4	0,00	1,40	9	126,0	5,1	yes, VV
2001_4	1	0,6	0,45	1,40	9	97,5	4,3	no
	2	0,8	0,90	1,40	9	68,8	3,4	no
	3	1	1,35	1,40	9	37,1	2,4	no
2001_5	1	0	1,80	1,40	12	167,1	7,0	yes, VV
2001_6	1	0,2	2,25	1,40	12	167,9	6,9	yes, VV
2001_7	1	0,4	0,00	1,40	12	153,8	6,3	yes, VV
2001_8	1	0,6	0,60	1,40	12	178,4	7,9	no

	2	0,8	1,20	1,40	12	126,8	6,3	no
	3	1	1,80	1,40	12	71,3	4,4	no
2001_9	1	0,3	2,40	1,40	14	226,4	8,8	yes
2001_10	1	0,4	3,00	1,40	14	281,9	11,4	yes
2001_11	1	0,6	1,05	1,40	14	244,2	10,8	yes
	2	0,8	1,40	1,40	14	173,4	8,5	no
	3	0,9	2,10	1,40	14	136,6	7,3	no
2001_12	1	0,6	2,80	1,40	16	316,7	13,9	yes, VV
2001_13	1	0,8	3,15	1,40	16	223,2	10,9	no
	2	1	2,40	1,40	16	124,0	7,6	no
9002	1	0	3,20	2,40	9	191,3	7,2	yes, VV
	2	0,2	4,00	2,40	9	164,3	6,4	no
	3	0,4	0,00	2,40	9	134,1	5,4	no
	4	0,6	0,45	2,40	9	102,1	4,5	no
	5	0,8	0,90	2,40	9	71,0	3,5	no
	6	0,9	1,35	2,40	9	54,7	3,0	no
	7	1,1	1,80	2,40	9	17,6	1,7	no
3001_1	1	0,2	2,03	1,60	9	167,2	6,5	yes, VV
3001_2	2	0,4	2,48	1,60	9	136,1	5,5	no
3001_3	3	0,6	0,45	1,60	9	102,8	4,5	no
3001_4	4	0,8	0,90	1,60	9	73,0	3,6	no
3001_5	5	0,9	1,35	1,60	9	57,2	3,1	no
3001_6	6	1,05	1,80	1,60	9	31,1	2,2	no
3001_7	7	0,2	2,03	1,60	12	271,6	10,6	Repeat
3001_8	8	0,4	2,36	1,60	12	235,7	9,6	Repeat
3001_9	9	0,6	0,60	1,60	12	181,5	8,0	no
3001_10	10	0,8	1,20	1,60	12	128,8	6,3	no
3001_11	11	0,9	1,80	1,60	12	101,4	5,4	no
3001_12	12	1,05	2,40	1,60	12	56,5	3,9	no
3001_13	13	0,3	2,70	1,60	14	328,9	12,9	repeat
3001_14	14	0,4	3,15	1,60	14	311,1	12,6	repeat
3001_15	15	0,6	1,05	1,60	14	247,6	10,9	no
3001_16	16	0,8	1,40	1,60	14	176,1	8,6	no
3001_17	17	0,9	2,10	1,60	14	139,2	7,4	no
3001_18	18	1,05	2,80	1,60	14	78,8	5,3	no
3001_19	19	0,6	3,15	1,60	16	322,8	14,2	repeat
3001_20	20	0,8	3,68	1,60	16	229,8	11,2	no
3001_21	21	0,9	2,40	1,60	16	181,5	9,6	no
3001_22	22	1,05	3,20	1,60	16	100,9	6,8	no
3001_23	1	0,2	3,60	1,60	12	268,8	10,5	yes, VV
3001_24	1	0	4,20	1,60	9	134,9	5,5	yes, VV

3001_25	1	0	0,60	1,60	12	237,6	9,7	yes, VV
3001_26	1	0,4	0,00	1,60	12	234,2	9,6	yes, VV
3001_27		0,6	0,00	1,60	12	179,9	7,9	no
3001_28		0,3	1,20	1,60	14	325,5	12,8	yes, VV, Repeat
3001_29		0,4	1,80	1,60	14	309,9	12,6	yes, VV
3001_30		0,6	1,05	1,60	16	321,1	14,1	no
3001_31		0,3	1,40	1,60	14	322,2	12,8	yes, VV
3001_32		0,4	2,40	1,60	14	308,2	12,6	yes, VV
3001_33		0,6	1,05	1,60	14	244,9	10,8	no
4001_1		0,2	1,40	1,00	9	76,0	3,0	yes, FSV
4001_2		0	2,10	1,00	9	75,0	3,1	yes, _FSV
4001_3		0,4	0,45	1,00	9	98,2	4,0	yes, FSV
4001_4		0,6	0,00	1,00	9	83,9	3,7	yes, FSV
4001_5		0,8	0,90	1,00	9	64,7	3,2	yes, FSV
4001_6		1	1,35	1,00	9	37,4	2,4	no vent
4001_7		0	1,80	1,00	12	78,8	3,5	yes, FSV
4001_8		0,1	2,25	1,00	12	73,1	3,2	yes, FSV
4001_9		0,2	0,00	1,00	12	73,3	3,2	yes,FSV
4001_10		0,3	0,30	1,00	12	153,7	6,0	yes,FSV
4001_11		0,4	0,60	1,00	12	165,6	6,7	yes, FSV
4001_12		0,6	0,90	1,00	12	149,9	6,6	not much
4001_13		0,8	1,20	1,00	12	117,8	5,8	no
4001_14		1	1,80	1,00	12	71,7	4,4	no
4001_15		0	2,40	1,00	14	91,6	4,1	yes, FSV
4001_16		0,2	3,00	1,00	14	79,6	3,6	yes, FSV
4001_17		0,4	0,00	1,00	14	215,8	8,6	yes, FSV
4001_18		0,6	0,70	1,00	14	199,5	8,8	yes, FSV
4001_19		0,8	1,40	1,00	14	157,2	7,7	no
4001_20		1	2,10	1,00	14	94,5	5,8	no
4001_21		0	2,80	1,00	16	107,8	4,9	yes, FSV
4001_22		0,2	3,50	1,00	16	94,6	4,2	yes, FSV
4001_23		0,4	0,00	1,00	16	275,0	11,0	yes, FSV
4001_24		0,6	0,80	1,00	16	259,2	11,4	yes, FSV
4001_25		0,8	1,60	1,00	16	204,1	10,0	not much
4001_26		1	2,40	1,00	16	120,9	7,4	not
9003	1	0	3,20	2,40	9	191,0	7,2	small vortex
	2	0,2	4,00	2,40	9	164,3	6,4	no
	3	0,4	0,00	2,40	9	134,0	5,4	no
	4	0,6	0,45	2,40	9	101,8	4,5	no
	5	0,8	0,90	2,40	9	71,0	3,5	no

	6	1	1,35	2,40	9	38,3	2,4	no
5001_1	1	0,1	1,80	1,20	9	82,3	3,3	yes
5001_2	1	0,2	2,25	1,20	9	77,2	3,1	yes
5001_3	1	0,3	0,23	1,20	9	81,4	3,3	yes
5001_4	1	0,4	0,45	1,20	9	105,0	4,3	yes
5001_5	1	0,5	0,68	1,20	9	103,9	4,4	yes
5001_6	1	0,6	0,90	1,20	9	94,9	4,2	yes
5001_7	1	0,7	1,13	1,20	9	83,4	3,9	yes
5001_8	1	0,8	1,35	1,20	9	71,4	3,5	yes
5001_9	1	0,9	1,58	1,20	9	56,4	3,0	yes
5001_10	1	1	1,80	1,20	9	40,4	2,5	yes
5001_11	1	0,1	2,03	1,20	12	90,0	3,9	yes
5001_13	1	0,2	2,25	1,20	12	76,4	3,3	yes
5001_17	1	0,3	0,30	1,20	12	140,1	5,5	yes
5001_19	1	0,4	0,60	1,20	12	181,7	7,3	yes
5001_20	1	0,5	0,90	1,20	12	177,0	7,4	yes
5001_21	1	0,6	1,20	1,20	12	166,0	7,3	yes
5001_22	1	0,7	1,50	1,20	12	146,0	6,7	yes
5001_23	1	0,8	1,80	1,20	12	125,4	6,2	no
5001_24	1	0,9	2,10	1,20	12	99,7	5,3	no
5001_25	1	1	2,40	1,20	12	71,6	4,4	no
5001_26	1	0,3	2,70	1,20	14	237,4	9,1	yes
5001_27	1	0,4	3,00	1,20	14	241,9	9,7	yes
5001_28	1	0,5	1,05	1,20	14	238,9	10,0	yes
5001_29	1	0,6	1,40	1,20	14	226,6	9,9	yes
5001_30	1	0,7	1,75	1,20	14	201,0	9,2	yes
5001_31	1	0,8	2,10	1,20	14	172,8	8,4	no
5001_32	1	0,9	2,45	1,20	14	137,8	7,3	no
5001_33	1	1	2,80	1,20	14	99,6	6,0	no
5001_34	1	0,6	3,15	1,20	16	297,3	13,0	yes
5001_35	1	0,7	3,50	1,20	16	263,7	12,1	yes
5001_36	1	0,8	2,40	1,20	16	226,1	11,0	no
5001_37	1	0,9	2,80	1,20	16	180,3	9,5	no
5001_38	1	1	3,20	1,20	16	129,3	7,8	no
5001_39	1	0,2	3,60	1,20	14	86,4	3,9	yes
5001_40	1	0	4,00	1,20	9	86,8	3,5	yes
5001_41	1	0	0,70	1,20	12	101,4	4,4	yes
5001_42	1	0	0,00	1,20	14	114,1	5,1	yes
5001_43	1	0	0,00	1,20	16	132,2	6,0	yes
5001_44	1	0,2	0,00	1,20	16	101,9	4,7	yes
5001_45	1	0,4	0,00	1,20	16	294,2	11,7	yes

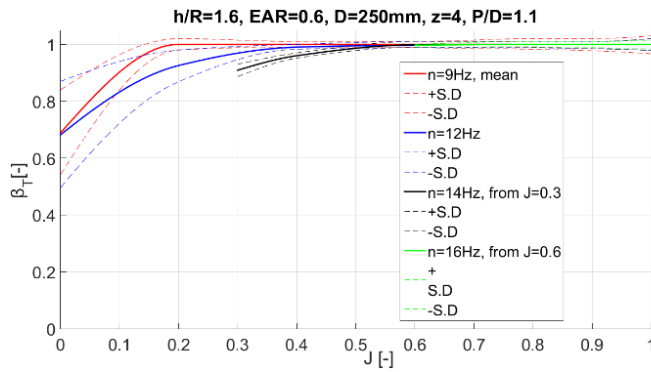


6001_1	1	0	0,80	0,00	9	38,0	1,4	out of water
6001_2	1	0	1,60	0,00	12	52,7	2,0	out of water
6001_3	1	0,2	0,00	0,00	9	38,1	1,4	out of water
6001_4	1	0,4	0,00	0,00	9	37,1	1,5	out of water
6001_5	1	0,6	0,45	0,00	9	34,1	1,5	out of water
6001_6	1	0,8	0,90	0,00	9	26,9	1,4	out of water
6001_7	1	1	1,35	0,00	9	15,0	1,0	out of water
6001_8	1	0,2	1,80	0,00	12	53,8	2,0	out of water
6001_9	1	0,4	2,25	0,00	12	60,7	2,4	out of water
6001_10	1	0,6	0,60	0,00	12	57,4	2,5	out of water
6001_11	1	0,8	1,20	0,00	12	45,2	2,3	out of water
6001_12	1	1	1,80	0,00	12	25,0	1,7	out of water
6001_13	1	0	2,40	0,00	14	62,1	2,3	out of water
6001_14	1	0,2	3,00	0,00	14	69,1	2,5	out of water
6001_15	1	0,4	0,00	0,00	14	79,7	3,1	out of water
6001_16	1	0,6	0,70	0,00	14	73,4	3,2	out of water
6001_17	1	0,8	1,40	0,00	14	60,4	3,1	out of water
6001_18	1	1	2,10	0,00	14	32,7	2,3	out of water
6001_19	1	0	2,80	0,00	16	64,8	2,5	out of water
6001_20	1	0,2	3,50	0,00	16	84,3	3,1	out of water
6001_21	1	0,4	0,00	0,00	16	97,4	3,8	out of water
6001_22	1	0,6	0,80	0,00	16	93,0	4,0	out of water
6001_23	1	0,8	1,60	0,00	16	78,3	4,0	out of water
6001_24	1	1	2,40	0,00	16	39,5	2,8	out of water
7001_1	1	0	3,20	0,50	9	53,0	2,2	out of water
7001_2	1	0,2	4,00	0,50	9	60,3	2,4	out of water
7001_3	1	0,4	0,00	0,50	9	65,0	2,7	out of water
	2	0,6	0,45	0,50	9	57,7	2,6	out of water
7001_4	1	0,8	0,90	0,50	9	44,1	2,3	out of water
	2	1	1,35	0,50	9	25,2	1,7	out of water
7001_5	1	0	1,80	0,50	12	64,0	2,8	out of water
7001_6	1	0,2	2,25	0,50	12	59,6	2,5	out of water
	2	0,4	0,00	0,50	12	52,8	2,4	out of water
7001_7	1	0,6	0,60	0,50	12	98,9	4,4	out of water
	2	0,8	1,20	0,50	12	75,6	3,9	out of water
7001_8	1	1	1,80	0,50	12	46,7	3,1	out of water
7001_9	1	0	2,40	0,50	14	67,8	3,0	out of water
7001_10	1	0,2	3,00	0,50	14	62,1	2,7	out of water
	2	0,4	0,00	0,50	14	62,5	2,9	out of water
7001_11	1	0,6	0,70	0,50	14	131,6	5,8	out of water
	2	0,8	1,40	0,50	14	101,9	5,2	out of water

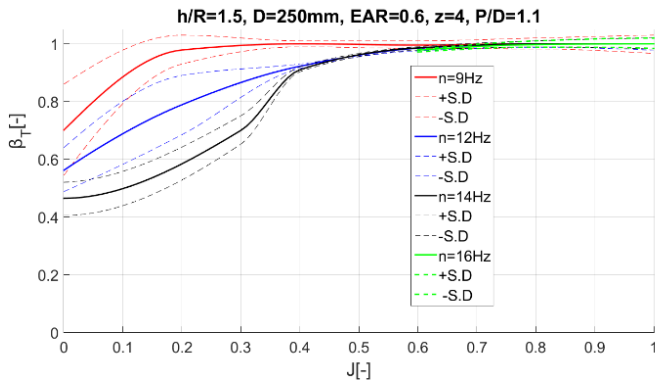
7001_12	1	1	2,10	0,50	14	62,7	4,1	out of water
7001_13	1	0	2,80	0,50	16	70,8	3,2	out of t water
7001_14	1	0,2	3,50	0,50	16	62,0	2,9	out of water
	2	0,4	0,00	0,50	16	74,1	3,5	out of water
7001_15	1	0,6	0,80	0,50	16	170,3	7,5	out of water
	2	0,8	1,60	0,50	16	133,7	6,8	out of water
7001_16	1	1	2,40	0,50	16	79,7	5,3	out of water
8001_1	1	0	3,20	-0,50	9	11,9	0,4	out of water
8001_2	1	0,25	4,00	-0,50	9	10,1	0,4	out of water
	2	0,5	0,00	-0,50	9	9,5	0,4	out of water
8001_3	1	0,75	0,56	-0,50	9	7,6	0,4	out of water
	2	1	1,13	-0,50	9	4,6	0,3	out of water
8001_4	1	0	1,69	-0,50	12	15,6	0,6	out of water
	2	0	2,25	-0,50	14	18,0	0,7	out of water
	3	0	0,00	-0,50	16	19,9	0,8	out of water
8001_5	1	0,25	0,00	-0,50	12	15,1	0,6	out of water
	2	0,5	0,00	-0,50	12	16,4	0,7	out of water
8001_6	1	0,75	0,75	-0,50	12	11,8	0,6	out of water
	2	1	1,50	-0,50	12	7,1	0,5	out of water
8001_7	1	0,25	2,25	-0,50	14	19,4	0,8	out of water
	2	0,5	3,00	-0,50	14	22,1	0,9	out of water
8001_8	1	0,75	0,88	-0,50	14	16,3	0,8	out of water
	2	1	1,75	-0,50	14	8,9	0,6	out of water
8001_9	1	0,25	2,63	-0,50	16	24,6	1,0	out of water
	2	0,5	3,50	-0,50	16	29,0	1,2	out of water
8001_10	1	0,75	1,00	-0,50	16	20,9	1,0	out of water
	2	1	2,00	-0,50	16	10,3	0,8	out of water
0001_1	1	0	3,00	1,50	9	137,3	5,6	no
9004	1	0	4,00	2,40	9	193,8	7,3	no
	2	0,2	0,00	2,40	9	166,4	6,4	no
	3	0,4	0,00	2,40	9	135,8	5,5	no
	4	0,6	0,45	2,40	9	104,2	4,6	no
	5	0,8	0,90	2,40	9	72,3	3,6	no
	6	1	1,35	2,40	9	39,5	2,5	no
0001_2	1	0	1,80	1,50	12	195,6	8,1	yes
	2	0	2,25	1,50	14	220,2	9,3	yes
	3	0	0,00	1,50	16	255,3	10,9	yes
0001_3	1	0,2	0,00	1,50	9	161,4	6,3	yes
0001_4	1	0,4	0,00	1,50	9	134,2	5,5	yes
0001_5	1	0,6	0,45	1,50	9	101,8	4,5	no
0001_6	1	0,8	0,90	1,50	9	72,4	3,6	no

0001_7	1	1	1,35	1,50	9	40,4	2,5	yes
0001_8	1	0,2	1,80	1,50	12	231,3	9,5	yes
0001_9	1	0,4	2,25	1,50	12	219,3	8,9	yes
0001_10	1	0,6	0,60	1,50	12	179,2	7,9	no
0001_11	1	0,8	1,20	1,50	12	128,5	6,3	no
0001_12	1	1	1,80	1,50	12	71,9	4,4	no
0001_13	1	0,3	2,40	1,50	14	252,9	9,8	yes
0001_14	1	0,4	3,00	1,50	14	294,6	11,9	yes
0001_15	1	0,6	1,05	1,50	14	244,4	10,8	no
0001_16	1	0,8	1,40	1,50	14	173,4	8,5	no
0001_17	1	1	2,10	1,50	14	97,8	6,0	no
0001_18	1	0,6	2,80	1,50	16	319,4	14,1	no
0001_19	1	0,8	3,50	1,50	16	227,1	11,1	no
0001_20	1	1	2,40	1,50	16	128,0	7,8	no

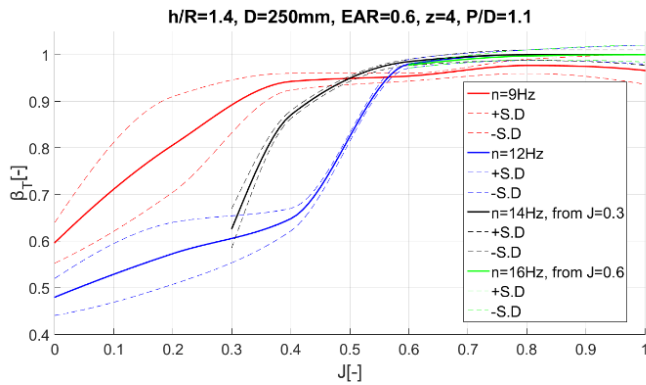
**h/R=1.6**



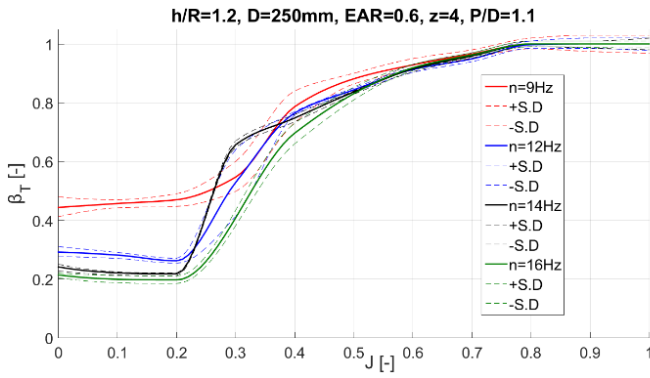
**h/R=1.5**



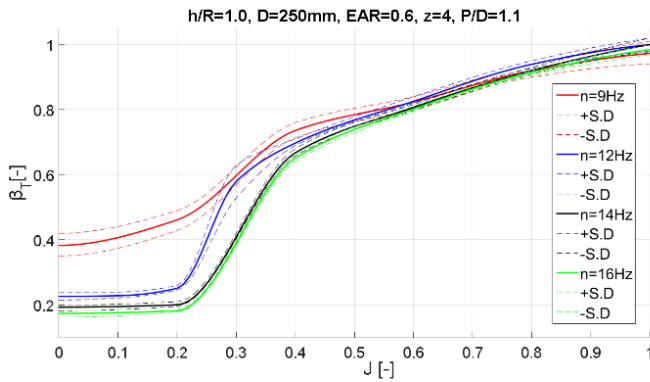
**h/R=1.4**



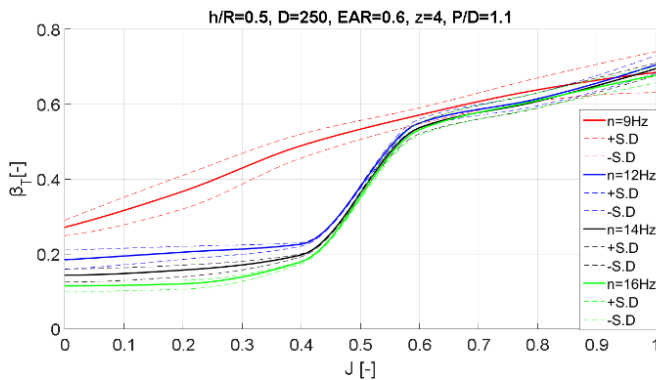
**h/R=1.2**

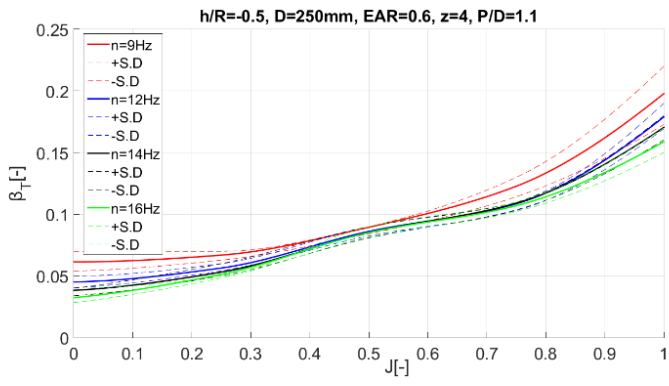


**h/R=1.0**



**h/R=0.5**



**$h/R=-0.5$** 

Appendix G  
Experimental set-up and testing conditions  
*Slamming Experiments*  
*Koz08*

Date	Time	Test nr.	Comment
26.06.08	1240	1000	5 rps, 0.25 – 2 m/s,
	1317	1001	5 rps. 0 – 4.5 m/s, kamera
	1327	1002	5 rps. 5 – 6 m/s, kamera
		1003	5 rps. – 7 m/s, kamera
		1004	5 rps. 7.5 – 8 m/s, kamera
		1005	8 rps. 0 – 3.5m/s, kamera
	1432	1006	8 rps 4 – 5.5m/s, kamera
		1007	8 rps 6 – 7.0 m/s, kamera
		1008	9 rps 0 – 4.5 m/s, kamera
		1009	9 rps 5 – 6.5 m/s, kamera
		1010	10 rps 0 – 4.5 m/s,
		1011	11 rps 0- 4 m/s
		1012	12 rps 0-4m/s
		1013	13 rps 0-4 m/s
		1014	13 rps 0-4 m/s
		1015	14 rps 0-4 m/s
		1016	15 rps 0- 4 m/s
27.06.08		P/D=7	
		1017	9 rps 0-4.5 m/s
		1018	30 mm change propeller hub immersion 9 rps 0-4.5 m/s
		1019	Continous acceleration 0-9 m/s, a=1/ms <sup>2</sup> 9 rps
		1020	Change prop immersion under water 9 rps 0-4.0 m/s
		1021	Fully submerged , 5 rps (due to torque limits) 0-4 m/s
		1022	Angeled forward, water level at centre hub 9 rps 0-4.5 m/s



Appendix H  
Calculation model  
Ventilation

## Input file

```

1 -   clc
2 -   clear
3 -   close all
4
5 -   J = [0.2 0.3 0.4 0.5 0.6 0.7 0.8 0.9 1 1.1 1.2];
6 -   KT = [0.528 0.48 0.431 0.382 0.335 0.288 0.241 0.192 0.14 0.083 0.019];
7 -   n=16; %propeller RPS
8 -   D = .25; %proller diameter
9 -   h = .15 %propeller submergence (from shaft to free surface)
10 -  nu = 1e-6; %water kinemaltic viscosity
11 -  eta = 0.8;
12 -  c=0.053; %chord length
13 -  EAR=0.6; %blade area ratio
14 -  T=KT*1000*n^2*D^4; %propeller thrust for non ventilating condition
15 -  VA = J*n*D; % propeller advance speed
16 -  Vc=(VA.^2+(0.7*pi()*n*D).^2).^0.5;%local relative velocity at the blade section
17 -  V0v=Vc./VA;
18
19
20 -  Vp = VA + .5*(-VA+sqrt(VA.^2 + 2*T/(1000*pi/4*D^2)))%velocity through the propeller disk
21 -  gammaAMB=KT.*Vc*c/(3*EAR)%circulation strenght
22
23 -  for i =1: length(J)
24
25 -      [AA0(i)] = vent_vort_2(J(i),KT(i),n,D,h,nu,gammaAMB(i),eta);
26
27 -  end
28
29 -  figure(4)
30
31 -  hold on
32 -  plot(J, AA0)

```

## Calculation model

```

1
2  function [AA01] = vent_vort_2(J,KT,n,D,h,nu,gammaAMB,eta)
3
4  % J = prop advance coefficient
5  % KT = Propeller thrust coefficient
6  % n = prop revs [rps]
7  % D = prop diameter [m]
8  % h = prop submergence [m]
9  % nu = kinematik viscosity
10 % eta = suction efficiency (0 to 1)
11
12 %AA0 = 1 - ventilated area over disc area
13
14 CT = 8/pi.*KT./(J.^2) %Propeller load coefficient [-]
15 Ra = (.5 +.5*sqrt(1+CT))*D/2 % section A radius (suction radius)
16                                     %of momentum theory suction radius
17                                     %where section A is upstream the propeller
18                                     %[m]
19 hRa = h./Ra % Submergence to suction radius ratio
20
21 %if hRa>1 the propeller will not interfere with the free surface
22 % (according to momentum theory), so we don't bother
23
24 ids = hRa < 1
25 ids = ~ids
26 hRa(ids) = 1
27
28 teta2 = acos(hRa) % half of submergence angle [rad]
29
30 A = (Ra.^2).*teta2 - Ra.*sin(teta2)*h %emerged area [m2]
31 AA0 = A./(pi.*Ra.^2) % emerged area to suction area ratio [-]
32 VA = J*n*D; %propeller advance speed [m/s]
33
34 T = KT*1000*n^2*D^4; %propeller thrust [N]
35 %Q = KQ*1000*n^2*D^5; %propeller torque [Nm]
36 Tsuct = T.*AA0; % lost propeller thrust [N]
37
38 QP = VA.*pi.*Ra.^2
39 q3 = QP .*AA0*eta % lost propeller flow rate [m3/s]
40
41 Gsuc = gammaAMB.*AA0 % circulation in the emerged area [m2/s]
42 a = q3./(2*pi*h^3) % flow suction gradient [1/s]
43 rstar = sqrt(2*nu./a)%Viscous core diameter [m]
44
45
46 r0 = linspace(1e-7,rstar,10);
47 r1 = [linspace(2*r0(end)-r0(end-1),10*rstar,20) linspace(11*rstar,D/2,20)];
48 % linspace(rstar(i),D,100) ;

```

```

49 % Rott vortex
50 - r = [r0 r1];
51
52 - v1 = Gsuc./(4*pi*r1).*(1-exp(-a*r1/(2*nu)));%.*fact +vlower - vupper ;
53 %%circulation outside the core
54 - v0 = v1(1).*(r0./rstar); %%circulation inside the core
55 - v = [v0 v1];
56
57 - figure(1)
58 - plot(r, v, '*-k');
59
60 - dzdr = 1/9.81*(v.^2)./r;
61
62 - zr = cumtrapz(r(end:-1:1),dzdr(end:-1:1))
63
64 - figure(2)
65 - hold on
66 - plot(r(end:-1:1), h+zr, '*-k');
67 - hold off
68 - figure(3)
69 - hold on
70 - plot(r(end:-1:1), h+zr, '*-k');
71 - ylim([0 h])
72 - xlim([0 max(r)]);
73 - hold off
74 - if min(h+zr)<0
75
76 -     AA01 = 1;
77
78 - elseif min(h+zr) < D/2 && min(h+zr)>0
79
80 -     AA01 = (D/2 - min(h+zr))^2/(D/2)^2;
81
82 - else
83
84 -     AA01=0;
85
86 - end

```

**Previous PhD theses published at the Department of Marine Technology  
(earlier: Faculty of Marine Technology)  
NORWEGIAN UNIVERSITY OF SCIENCE AND TECHNOLOGY**

<b>Report No.</b>	<b>Author</b>	<b>Title</b>
	Kavlie, Dag	Optimization of Plane Elastic Grillages, 1967
	Hansen, Hans R.	Man-Machine Communication and Data-Storage Methods in Ship Structural Design, 1971
	Gisvold, Kaare M.	A Method for non-linear mixed -integer programming and its Application to Design Problems, 1971
	Lund, Sverre	Tanker Frame Optimalization by means of SUMT-Transformation and Behaviour Models, 1971
	Vinje, Tor	On Vibration of Spherical Shells Interacting with Fluid, 1972
	Lorentz, Jan D.	Tank Arrangement for Crude Oil Carriers in Accordance with the new Anti-Pollution Regulations, 1975
	Carlsen, Carl A.	Computer-Aided Design of Tanker Structures, 1975
	Larsen, Carl M.	Static and Dynamic Analysis of Offshore Pipelines during Installation, 1976
UR-79-01	Brigt Hatlestad, MK	The finite element method used in a fatigue evaluation of fixed offshore platforms. (Dr.Ing. Thesis)
UR-79-02	Erik Pettersen, MK	Analysis and design of cellular structures. (Dr.Ing. Thesis)
UR-79-03	Sverre Valsgård, MK	Finite difference and finite element methods applied to nonlinear analysis of plated structures. (Dr.Ing. Thesis)
UR-79-04	Nils T. Nordsve, MK	Finite element collapse analysis of structural members considering imperfections and stresses due to fabrication. (Dr.Ing. Thesis)
UR-79-05	Ivar J. Fylling, MK	Analysis of towline forces in ocean towing systems. (Dr.Ing. Thesis)
UR-80-06	Nils Sandsmark, MM	Analysis of Stationary and Transient Heat Conduction by the Use of the Finite Element Method. (Dr.Ing. Thesis)
UR-80-09	Sverre Haver, MK	Analysis of uncertainties related to the stochastic modeling of ocean waves. (Dr.Ing. Thesis)
UR-81-15	Odland, Jonas	On the Strength of welded Ring stiffened cylindrical Shells primarily subjected to axial Compression

UR-82-17	Engesvik, Knut	Analysis of Uncertainties in the fatigue Capacity of Welded Joints
UR-82-18	Rye, Henrik	Ocean wave groups
UR-83-30	Eide, Oddvar Inge	On Cumulative Fatigue Damage in Steel Welded Joints
UR-83-33	Mo, Olav	Stochastic Time Domain Analysis of Slender Offshore Structures
UR-83-34	Amdahl, Jørgen	Energy absorption in Ship-platform impacts
UR-84-37	Mørch, Morten	Motions and mooring forces of semi submersibles as determined by full-scale measurements and theoretical analysis
UR-84-38	Soares, C. Guedes	Probabilistic models for load effects in ship structures
UR-84-39	Aarsnes, Jan V.	Current forces on ships
UR-84-40	Czujko, Jerzy	Collapse Analysis of Plates subjected to Biaxial Compression and Lateral Load
UR-85-46	Alf G. Engseth, MK	Finite element collapse analysis of tubular steel offshore structures. (Dr.Ing. Thesis)
UR-86-47	Dengody Sheshappa, MP	A Computer Design Model for Optimizing Fishing Vessel Designs Based on Techno-Economic Analysis. (Dr.Ing. Thesis)
UR-86-48	Vidar Aanesland, MH	A Theoretical and Numerical Study of Ship Wave Resistance. (Dr.Ing. Thesis)
UR-86-49	Heinz-Joachim Wessel, MK	Fracture Mechanics Analysis of Crack Growth in Plate Girders. (Dr.Ing. Thesis)
UR-86-50	Jon Taby, MK	Ultimate and Post-ultimate Strength of Dented Tubular Members. (Dr.Ing. Thesis)
UR-86-51	Walter Lian, MH	A Numerical Study of Two-Dimensional Separated Flow Past Bluff Bodies at Moderate KC-Numbers. (Dr.Ing. Thesis)
UR-86-52	Bjørn Sortland, MH	Force Measurements in Oscillating Flow on Ship Sections and Circular Cylinders in a U-Tube Water Tank. (Dr.Ing. Thesis)
UR-86-53	Kurt Strand, MM	A System Dynamic Approach to One-dimensional Fluid Flow. (Dr.Ing. Thesis)
UR-86-54	Arne Edvin Løken, MH	Three Dimensional Second Order Hydrodynamic Effects on Ocean Structures in Waves. (Dr.Ing. Thesis)
UR-86-55	Sigurd Falch, MH	A Numerical Study of Slamming of Two-Dimensional Bodies. (Dr.Ing. Thesis)
UR-87-56	Arne Braathen, MH	Application of a Vortex Tracking Method to the Prediction of Roll Damping of a Two-Dimension Floating Body. (Dr.Ing. Thesis)

UR-87-57	Bernt Leira, MK	Gaussian Vector Processes for Reliability Analysis involving Wave-Induced Load Effects. (Dr.Ing. Thesis)
UR-87-58	Magnus Småvik, MM	Thermal Load and Process Characteristics in a Two-Stroke Diesel Engine with Thermal Barriers (in Norwegian). (Dr.Ing. Thesis)
MTA-88-59	Bernt Arild Bremdal, MP	An Investigation of Marine Installation Processes – A Knowledge - Based Planning Approach. (Dr.Ing. Thesis)
MTA-88-60	Xu Jun, MK	Non-linear Dynamic Analysis of Space-framed Offshore Structures. (Dr.Ing. Thesis)
MTA-89-61	Gang Miao, MH	Hydrodynamic Forces and Dynamic Responses of Circular Cylinders in Wave Zones. (Dr.Ing. Thesis)
MTA-89-62	Martin Greenhow, MH	Linear and Non-Linear Studies of Waves and Floating Bodies. Part I and Part II. (Dr.Techn. Thesis)
MTA-89-63	Chang Li, MH	Force Coefficients of Spheres and Cubes in Oscillatory Flow with and without Current. (Dr.Ing. Thesis)
MTA-89-64	Hu Ying, MP	A Study of Marketing and Design in Development of Marine Transport Systems. (Dr.Ing. Thesis)
MTA-89-65	Arild Jæger, MH	Seakeeping, Dynamic Stability and Performance of a Wedge Shaped Planing Hull. (Dr.Ing. Thesis)
MTA-89-66	Chan Siu Hung, MM	The dynamic characteristics of tilting-pad bearings
MTA-89-67	Kim Wikstrøm, MP	Analysis av projekteringen for ett offshore projekt. (Licenciat-avhandling)
MTA-89-68	Jiao Guoyang, MK	Reliability Analysis of Crack Growth under Random Loading, considering Model Updating. (Dr.Ing. Thesis)
MTA-89-69	Arnt Olufsen, MK	Uncertainty and Reliability Analysis of Fixed Offshore Structures. (Dr.Ing. Thesis)
MTA-89-70	Wu Yu-Lin, MR	System Reliability Analyses of Offshore Structures using improved Truss and Beam Models. (Dr.Ing. Thesis)
MTA-90-71	Jan Roger Hoff, MH	Three-dimensional Green function of a vessel with forward speed in waves. (Dr.Ing. Thesis)
MTA-90-72	Rong Zhao, MH	Slow-Drift Motions of a Moored Two-Dimensional Body in Irregular Waves. (Dr.Ing. Thesis)
MTA-90-73	Atle Minsaas, MP	Economical Risk Analysis. (Dr.Ing. Thesis)
MTA-90-74	Knut-Aril Farnes, MK	Long-term Statistics of Response in Non-linear Marine Structures. (Dr.Ing. Thesis)
MTA-90-75	Torbjørn Sotberg, MK	Application of Reliability Methods for Safety Assessment of Submarine Pipelines. (Dr.Ing. Thesis)

MTA-90-76	Zeuthen, Steffen, MP	SEAMAID. A computational model of the design process in a constraint-based logic programming environment. An example from the offshore domain. (Dr.Ing. Thesis)
MTA-91-77	Haagensen, Sven, MM	Fuel Dependant Cyclic Variability in a Spark Ignition Engine - An Optical Approach. (Dr.Ing. Thesis)
MTA-91-78	Løland, Geir, MH	Current forces on and flow through fish farms. (Dr.Ing. Thesis)
MTA-91-79	Hoen, Christopher, MK	System Identification of Structures Excited by Stochastic Load Processes. (Dr.Ing. Thesis)
MTA-91-80	Haugen, Stein, MK	Probabilistic Evaluation of Frequency of Collision between Ships and Offshore Platforms. (Dr.Ing. Thesis)
MTA-91-81	Sødahl, Nils, MK	Methods for Design and Analysis of Flexible Risers. (Dr.Ing. Thesis)
MTA-91-82	Ormberg, Harald, MK	Non-linear Response Analysis of Floating Fish Farm Systems. (Dr.Ing. Thesis)
MTA-91-83	Marley, Mark J., MK	Time Variant Reliability under Fatigue Degradation. (Dr.Ing. Thesis)
MTA-91-84	Krokstad, Jørgen R., MH	Second-order Loads in Multidirectional Seas. (Dr.Ing. Thesis)
MTA-91-85	Molteberg, Gunnar A., MM	The Application of System Identification Techniques to Performance Monitoring of Four Stroke Turbocharged Diesel Engines. (Dr.Ing. Thesis)
MTA-92-86	Mørch, Hans Jørgen Bjelke, MH	Aspects of Hydrofoil Design: with Emphasis on Hydrofoil Interaction in Calm Water. (Dr.Ing. Thesis)
MTA-92-87	Chan Siu Hung, MM	Nonlinear Analysis of Rotordynamic Instabilities in Highspeed Turbomachinery. (Dr.Ing. Thesis)
MTA-92-88	Bessason, Bjarni, MK	Assessment of Earthquake Loading and Response of Seismically Isolated Bridges. (Dr.Ing. Thesis)
MTA-92-89	Langli, Geir, MP	Improving Operational Safety through exploitation of Design Knowledge - an investigation of offshore platform safety. (Dr.Ing. Thesis)
MTA-92-90	Sævik, Svein, MK	On Stresses and Fatigue in Flexible Pipes. (Dr.Ing. Thesis)
MTA-92-91	Ask, Tor Ø., MM	Ignition and Flame Growth in Lean Gas-Air Mixtures. An Experimental Study with a Schlieren System. (Dr.Ing. Thesis)
MTA-86-92	Hessen, Gunnar, MK	Fracture Mechanics Analysis of Stiffened Tubular Members. (Dr.Ing. Thesis)
MTA-93-93	Steinebach, Christian, MM	Knowledge Based Systems for Diagnosis of Rotating Machinery. (Dr.Ing. Thesis)
MTA-93-94	Dalane, Jan Inge, MK	System Reliability in Design and Maintenance of Fixed Offshore Structures. (Dr.Ing. Thesis)



MTA-93-95	Steen, Sverre, MH	Cobblestone Effect on SES. (Dr.Ing. Thesis)
MTA-93-96	Karunakaran, Daniel, MK	Nonlinear Dynamic Response and Reliability Analysis of Drag-dominated Offshore Platforms. (Dr.Ing. Thesis)
MTA-93-97	Hagen, Arnulf, MP	The Framework of a Design Process Language. (Dr.Ing. Thesis)
MTA-93-98	Nordrik, Rune, MM	Investigation of Spark Ignition and Autoignition in Methane and Air Using Computational Fluid Dynamics and Chemical Reaction Kinetics. A Numerical Study of Ignition Processes in Internal Combustion Engines. (Dr.Ing. Thesis)
MTA-94-99	Passano, Elizabeth, MK	Efficient Analysis of Nonlinear Slender Marine Structures. (Dr.Ing. Thesis)
MTA-94-100	Kvålsvold, Jan, MH	Hydroelastic Modelling of Wetdeck Slamming on Multihull Vessels. (Dr.Ing. Thesis)
MTA-94-102	Bech, Sidsel M., MK	Experimental and Numerical Determination of Stiffness and Strength of GRP/PVC Sandwich Structures. (Dr.Ing. Thesis)
MTA-95-103	Paulsen, Hallvard, MM	A Study of Transient Jet and Spray using a Schlieren Method and Digital Image Processing. (Dr.Ing. Thesis)
MTA-95-104	Hovde, Geir Olav, MK	Fatigue and Overload Reliability of Offshore Structural Systems, Considering the Effect of Inspection and Repair. (Dr.Ing. Thesis)
MTA-95-105	Wang, Xiaozhi, MK	Reliability Analysis of Production Ships with Emphasis on Load Combination and Ultimate Strength. (Dr.Ing. Thesis)
MTA-95-106	Ulstein, Tore, MH	Nonlinear Effects of a Flexible Stern Seal Bag on Cobblestone Oscillations of an SES. (Dr.Ing. Thesis)
MTA-95-107	Solaas, Frøydis, MH	Analytical and Numerical Studies of Sloshing in Tanks. (Dr.Ing. Thesis)
MTA-95-108	Hellan, Øyvind, MK	Nonlinear Pushover and Cyclic Analyses in Ultimate Limit State Design and Reassessment of Tubular Steel Offshore Structures. (Dr.Ing. Thesis)
MTA-95-109	Hermundstad, Ole A., MK	Theoretical and Experimental Hydroelastic Analysis of High Speed Vessels. (Dr.Ing. Thesis)
MTA-96-110	Bratland, Anne K., MH	Wave-Current Interaction Effects on Large-Volume Bodies in Water of Finite Depth. (Dr.Ing. Thesis)
MTA-96-111	Herfjord, Kjell, MH	A Study of Two-dimensional Separated Flow by a Combination of the Finite Element Method and Navier-Stokes Equations. (Dr.Ing. Thesis)
MTA-96-112	Æsøy, Vilmar, MM	Hot Surface Assisted Compression Ignition in a Direct Injection Natural Gas Engine. (Dr.Ing. Thesis)
MTA-96-113	Eknes, Monika L., MK	Escalation Scenarios Initiated by Gas Explosions on Offshore Installations. (Dr.Ing. Thesis)

MTA-96-114	Erikstad, Stein O., MP	A Decision Support Model for Preliminary Ship Design. (Dr.Ing. Thesis)
MTA-96-115	Pedersen, Egil, MH	A Nautical Study of Towed Marine Seismic Streamer Cable Configurations. (Dr.Ing. Thesis)
MTA-97-116	Moksnes, Paul O., MM	Modelling Two-Phase Thermo-Fluid Systems Using Bond Graphs. (Dr.Ing. Thesis)
MTA-97-117	Halse, Karl H., MK	On Vortex Shedding and Prediction of Vortex-Induced Vibrations of Circular Cylinders. (Dr.Ing. Thesis)
MTA-97-118	Igland, Ragnar T., MK	Reliability Analysis of Pipelines during Laying, considering Ultimate Strength under Combined Loads. (Dr.Ing. Thesis)
MTA-97-119	Pedersen, Hans-P., MP	Levendefiskteknologi for fiskerfartøy. (Dr.Ing. Thesis)
MTA-98-120	Vikestad, Kyrre, MK	Multi-Frequency Response of a Cylinder Subjected to Vortex Shedding and Support Motions. (Dr.Ing. Thesis)
MTA-98-121	Azadi, Mohammad R. E., MK	Analysis of Static and Dynamic Pile-Soil-Jacket Behaviour. (Dr.Ing. Thesis)
MTA-98-122	Ulltang, Terje, MP	A Communication Model for Product Information. (Dr.Ing. Thesis)
MTA-98-123	Torbergsen, Erik, MM	Impeller/Diffuser Interaction Forces in Centrifugal Pumps. (Dr.Ing. Thesis)
MTA-98-124	Hansen, Edmond, MH	A Discrete Element Model to Study Marginal Ice Zone Dynamics and the Behaviour of Vessels Moored in Broken Ice. (Dr.Ing. Thesis)
MTA-98-125	Videiro, Paulo M., MK	Reliability Based Design of Marine Structures. (Dr.Ing. Thesis)
MTA-99-126	Mainçon, Philippe, MK	Fatigue Reliability of Long Welds Application to Titanium Risers. (Dr.Ing. Thesis)
MTA-99-127	Haugen, Elin M., MH	Hydroelastic Analysis of Slamming on Stiffened Plates with Application to Catamaran Wetdecks. (Dr.Ing. Thesis)
MTA-99-128	Langhelle, Nina K., MK	Experimental Validation and Calibration of Nonlinear Finite Element Models for Use in Design of Aluminium Structures Exposed to Fire. (Dr.Ing. Thesis)
MTA-99-129	Berstad, Are J., MK	Calculation of Fatigue Damage in Ship Structures. (Dr.Ing. Thesis)
MTA-99-130	Andersen, Trond M., MM	Short Term Maintenance Planning. (Dr.Ing. Thesis)
MTA-99-131	Tveiten, Bård Wathne, MK	Fatigue Assessment of Welded Aluminium Ship Details. (Dr.Ing. Thesis)
MTA-99-132	Søreide, Fredrik, MP	Applications of underwater technology in deep water archaeology. Principles and practice. (Dr.Ing. Thesis)

MTA-99-133	Tønnessen, Rune, MH	A Finite Element Method Applied to Unsteady Viscous Flow Around 2D Blunt Bodies With Sharp Corners. (Dr.Ing. Thesis)
MTA-99-134	Elvekrok, Dag R., MP	Engineering Integration in Field Development Projects in the Norwegian Oil and Gas Industry. The Supplier Management of Norne. (Dr.Ing. Thesis)
MTA-99-135	Fagerholt, Kjetil, MP	Optimeringsbaserte Metoder for Ruteplanlegging innen skipsfart. (Dr.Ing. Thesis)
MTA-99-136	Bysveen, Marie, MM	Visualization in Two Directions on a Dynamic Combustion Rig for Studies of Fuel Quality. (Dr.Ing. Thesis)
MTA-2000-137	Storteig, Eskild, MM	Dynamic characteristics and leakage performance of liquid annular seals in centrifugal pumps. (Dr.Ing. Thesis)
MTA-2000-138	Sagli, Gro, MK	Model uncertainty and simplified estimates of long term extremes of hull girder loads in ships. (Dr.Ing. Thesis)
MTA-2000-139	Tronstad, Harald, MK	Nonlinear analysis and design of cable net structures like fishing gear based on the finite element method. (Dr.Ing. Thesis)
MTA-2000-140	Kroneberg, André, MP	Innovation in shipping by using scenarios. (Dr.Ing. Thesis)
MTA-2000-141	Haslum, Herbjørn Alf, MH	Simplified methods applied to nonlinear motion of spar platforms. (Dr.Ing. Thesis)
MTA-2001-142	Samdal, Ole Johan, MM	Modelling of Degradation Mechanisms and Stressor Interaction on Static Mechanical Equipment Residual Lifetime. (Dr.Ing. Thesis)
MTA-2001-143	Baarholm, Rolf Jarle, MH	Theoretical and experimental studies of wave impact underneath decks of offshore platforms. (Dr.Ing. Thesis)
MTA-2001-144	Wang, Lihua, MK	Probabilistic Analysis of Nonlinear Wave-induced Loads on Ships. (Dr.Ing. Thesis)
MTA-2001-145	Kristensen, Odd H. Holt, MK	Ultimate Capacity of Aluminium Plates under Multiple Loads, Considering HAZ Properties. (Dr.Ing. Thesis)
MTA-2001-146	Greco, Marilena, MH	A Two-Dimensional Study of Green-Water Loading. (Dr.Ing. Thesis)
MTA-2001-147	Heggelund, Svein E., MK	Calculation of Global Design Loads and Load Effects in Large High Speed Catamarans. (Dr.Ing. Thesis)
MTA-2001-148	Babalola, Olusegun T., MK	Fatigue Strength of Titanium Risers – Defect Sensitivity. (Dr.Ing. Thesis)
MTA-2001-149	Mohammed, Abuu K., MK	Nonlinear Shell Finite Elements for Ultimate Strength and Collapse Analysis of Ship Structures. (Dr.Ing. Thesis)
MTA-2002-150	Holmedal, Lars E., MH	Wave-current interactions in the vicinity of the sea bed. (Dr.Ing. Thesis)

MTA-2002-151	Rognebakke, Olav F., MH	Sloshing in rectangular tanks and interaction with ship motions. (Dr.Ing. Thesis)
MTA-2002-152	Lader, Pål Furset, MH	Geometry and Kinematics of Breaking Waves. (Dr.Ing. Thesis)
MTA-2002-153	Yang, Qinzheng, MH	Wash and wave resistance of ships in finite water depth. (Dr.Ing. Thesis)
MTA-2002-154	Melhus, Øyvinn, MM	Utilization of VOC in Diesel Engines. Ignition and combustion of VOC released by crude oil tankers. (Dr.Ing. Thesis)
MTA-2002-155	Ronæss, Marit, MH	Wave Induced Motions of Two Ships Advancing on Parallel Course. (Dr.Ing. Thesis)
MTA-2002-156	Økland, Ole D., MK	Numerical and experimental investigation of whipping in twin hull vessels exposed to severe wet deck slamming. (Dr.Ing. Thesis)
MTA-2002-157	Ge, Chunhua, MK	Global Hydroelastic Response of Catamarans due to Wet Deck Slamming. (Dr.Ing. Thesis)
MTA-2002-158	Byklum, Eirik, MK	Nonlinear Shell Finite Elements for Ultimate Strength and Collapse Analysis of Ship Structures. (Dr.Ing. Thesis)
IMT-2003-1	Chen, Haibo, MK	Probabilistic Evaluation of FPSO-Tanker Collision in Tandem Offloading Operation. (Dr.Ing. Thesis)
IMT-2003-2	Skaugset, Kjetil Bjørn, MK	On the Suppression of Vortex Induced Vibrations of Circular Cylinders by Radial Water Jets. (Dr.Ing. Thesis)
IMT-2003-3	Chezian, Muthu	Three-Dimensional Analysis of Slamming. (Dr.Ing. Thesis)
IMT-2003-4	Buhaug, Øyvind	Deposit Formation on Cylinder Liner Surfaces in Medium Speed Engines. (Dr.Ing. Thesis)
IMT-2003-5	Tregde, Vidar	Aspects of Ship Design: Optimization of Aft Hull with Inverse Geometry Design. (Dr.Ing. Thesis)
IMT-2003-6	Wist, Hanne Therese	Statistical Properties of Successive Ocean Wave Parameters. (Dr.Ing. Thesis)
IMT-2004-7	Ransau, Samuel	Numerical Methods for Flows with Evolving Interfaces. (Dr.Ing. Thesis)
IMT-2004-8	Soma, Torkel	Blue-Chip or Sub-Standard. A data interrogation approach of identity safety characteristics of shipping organization. (Dr.Ing. Thesis)
IMT-2004-9	Ersdal, Svein	An experimental study of hydrodynamic forces on cylinders and cables in near axial flow. (Dr.Ing. Thesis)
IMT-2005-10	Brodtkorb, Per Andreas	The Probability of Occurrence of Dangerous Wave Situations at Sea. (Dr.Ing. Thesis)

IMT-2005-11	Yttervik, Rune	Ocean current variability in relation to offshore engineering. (Dr.Ing. Thesis)
IMT-2005-12	Fredheim, Arne	Current Forces on Net-Structures. (Dr.Ing. Thesis)
IMT-2005-13	Heggernes, Kjetil	Flow around marine structures. (Dr.Ing. Thesis)
IMT-2005-14	Fouques, Sebastien	Lagrangian Modelling of Ocean Surface Waves and Synthetic Aperture Radar Wave Measurements. (Dr.Ing. Thesis)
IMT-2006-15	Holm, Håvard	Numerical calculation of viscous free surface flow around marine structures. (Dr.Ing. Thesis)
IMT-2006-16	Bjørheim, Lars G.	Failure Assessment of Long Through Thickness Fatigue Cracks in Ship Hulls. (Dr.Ing. Thesis)
IMT-2006-17	Hansson, Lisbeth	Safety Management for Prevention of Occupational Accidents. (Dr.Ing. Thesis)
IMT-2006-18	Zhu, Xinying	Application of the CIP Method to Strongly Nonlinear Wave-Body Interaction Problems. (Dr.Ing. Thesis)
IMT-2006-19	Reite, Karl Johan	Modelling and Control of Trawl Systems. (Dr.Ing. Thesis)
IMT-2006-20	Smogeli, Øyvind Notland	Control of Marine Propellers. From Normal to Extreme Conditions. (Dr.Ing. Thesis)
IMT-2007-21	Storhaug, Gaute	Experimental Investigation of Wave Induced Vibrations and Their Effect on the Fatigue Loading of Ships. (Dr.Ing. Thesis)
IMT-2007-22	Sun, Hui	A Boundary Element Method Applied to Strongly Nonlinear Wave-Body Interaction Problems. (PhD Thesis, CeSOS)
IMT-2007-23	Rustad, Anne Marthine	Modelling and Control of Top Tensioned Risers. (PhD Thesis, CeSOS)
IMT-2007-24	Johansen, Vegar	Modelling flexible slender system for real-time simulations and control applications
IMT-2007-25	Wroldsen, Anders Sunde	Modelling and control of tensegrity structures. (PhD Thesis, CeSOS)
IMT-2007-26	Aronsen, Kristoffer Høye	An experimental investigation of in-line and combined inline and cross flow vortex induced vibrations. (Dr. avhandling, IMT)
IMT-2007-27	Gao, Zhen	Stochastic Response Analysis of Mooring Systems with Emphasis on Frequency-domain Analysis of Fatigue due to Wide-band Response Processes (PhD Thesis, CeSOS)
IMT-2007-28	Thorstensen, Tom Anders	Lifetime Profit Modelling of Ageing Systems Utilizing Information about Technical Condition. (Dr.ing. thesis, IMT)
IMT-2008-29	Refsnes, Jon Erling Gorset	Nonlinear Model-Based Control of Slender Body AUVs (PhD Thesis, IMT)

IMT-2008-30	Berntsen, Per Ivar B.	Structural Reliability Based Position Mooring. (PhD-Thesis, IMT)
IMT-2008-31	Ye, Naiquan	Fatigue Assessment of Aluminium Welded Box-stiffener Joints in Ships (Dr.ing. thesis, IMT)
IMT-2008-32	Radan, Damir	Integrated Control of Marine Electrical Power Systems. (PhD-Thesis, IMT)
IMT-2008-33	Thomassen, Paul	Methods for Dynamic Response Analysis and Fatigue Life Estimation of Floating Fish Cages. (Dr.ing. thesis, IMT)
IMT-2008-34	Pákozdi, Csaba	A Smoothed Particle Hydrodynamics Study of Two-dimensional Nonlinear Sloshing in Rectangular Tanks. (Dr.ing.thesis, IMT/ CeSOS)
IMT-2007-35	Grytøy, Guttorm	A Higher-Order Boundary Element Method and Applications to Marine Hydrodynamics. (Dr.ing.thesis, IMT)
IMT-2008-36	Drummen, Ingo	Experimental and Numerical Investigation of Nonlinear Wave-Induced Load Effects in Containerships considering Hydroelasticity. (PhD thesis, CeSOS)
IMT-2008-37	Skejic, Renato	Maneuvering and Seakeeping of a Singel Ship and of Two Ships in Interaction. (PhD-Thesis, CeSOS)
IMT-2008-38	Harlem, Alf	An Age-Based Replacement Model for Repairable Systems with Attention to High-Speed Marine Diesel Engines. (PhD-Thesis, IMT)
IMT-2008-39	Alsos, Hagbart S.	Ship Grounding. Analysis of Ductile Fracture, Bottom Damage and Hull Girder Response. (PhD-thesis, IMT)
IMT-2008-40	Graczyk, Mateusz	Experimental Investigation of Sloshing Loading and Load Effects in Membrane LNG Tanks Subjected to Random Excitation. (PhD-thesis, CeSOS)
IMT-2008-41	Taghipour, Reza	Efficient Prediction of Dynamic Response for Flexible amd Multi-body Marine Structures. (PhD-thesis, CeSOS)
IMT-2008-42	Ruth, Eivind	Propulsion control and thrust allocation on marine vessels. (PhD thesis, CeSOS)
IMT-2008-43	Nystad, Bent Helge	Technical Condition Indexes and Remaining Useful Life of Aggregated Systems. PhD thesis, IMT
IMT-2008-44	Soni, Prashant Kumar	Hydrodynamic Coefficients for Vortex Induced Vibrations of Flexible Beams, PhD thesis, CeSOS
IMT-2009-45	Amlashi, Hadi K.K.	Ultimate Strength and Reliability-based Design of Ship Hulls with Emphasis on Combined Global and Local Loads. PhD Thesis, IMT
IMT-2009-46	Pedersen, Tom Arne	Bond Graph Modelling of Marine Power Systems. PhD Thesis, IMT

IMT-2009-47	Kristiansen, Trygve	Two-Dimensional Numerical and Experimental Studies of Piston-Mode Resonance. PhD-Thesis, CeSOS
IMT-2009-48	Ong, Muk Chen	Applications of a Standard High Reynolds Number Model and a Stochastic Scour Prediction Model for Marine Structures. PhD-thesis, IMT
IMT-2009-49	Hong, Lin	Simplified Analysis and Design of Ships subjected to Collision and Grounding. PhD-thesis, IMT
IMT-2009-50	Koushan, Kamran	Vortex Induced Vibrations of Free Span Pipelines, PhD thesis, IMT
IMT-2009-51	Korsvik, Jarl Eirik	Heuristic Methods for Ship Routing and Scheduling. PhD-thesis, IMT
IMT-2009-52	Lee, Jihoon	Experimental Investigation and Numerical in Analyzing the Ocean Current Displacement of Longlines. Ph.d.-Thesis, IMT.
IMT-2009-53	Vestbøstad, Tone Gran	A Numerical Study of Wave-in-Deck Impact using a Two-Dimensional Constrained Interpolation Profile Method, Ph.d.thesis, CeSOS.
IMT-2009-54	Bruun, Kristine	Bond Graph Modelling of Fuel Cells for Marine Power Plants. Ph.d.-thesis, IMT
IMT-2009-55	Holstad, Anders	Numerical Investigation of Turbulence in a Skewed Three-Dimensional Channel Flow, Ph.d.-thesis, IMT.
IMT-2009-56	Ayala-Uraga, Efrén	Reliability-Based Assessment of Deteriorating Ship-shaped Offshore Structures, Ph.d.-thesis, IMT
IMT-2009-57	Kong, Xiangjun	A Numerical Study of a Damaged Ship in Beam Sea Waves. Ph.d.-thesis, IMT/CeSOS.
IMT-2010-58	Kristiansen, David	Wave Induced Effects on Floaters of Aquaculture Plants, Ph.d.-thesis, CeSOS.
IMT-2010-59	Ludvigsen, Martin	An ROV-Toolbox for Optical and Acoustic Scientific Seabed Investigation. Ph.d.-thesis IMT.
IMT-2010-60	Hals, Jørgen	Modelling and Phase Control of Wave-Energy Converters. Ph.d.thesis, CeSOS.
IMT-2010-61	Shu, Zhi	Uncertainty Assessment of Wave Loads and Ultimate Strength of Tankers and Bulk Carriers in a Reliability Framework. Ph.d. Thesis, IMT/ CeSOS
IMT-2010-62	Shao, Yanlin	Numerical Potential-Flow Studies on Weakly-Nonlinear Wave-Body Interactions with/without Small Forward Speed, Ph.d.thesis,CeSOS.
IMT-2010-63	Califano, Andrea	Dynamic Loads on Marine Propellers due to Intermittent Ventilation. Ph.d.thesis, IMT.

IMT 2010-64	El Khoury, George	Numerical Simulations of Massively Separated Turbulent Flows, Ph.d.-thesis, IMT
IMT 2010-65	Seim, Knut Sponheim	Mixing Process in Dense Overflows with Emphasis on the Faroe Bank Channel Overflow. Ph.d.thesis, IMT
IMT 2010-66	Jia, Huirong	Structural Analysis of Intact and Damaged Ships in a Collision Risk Analysis Perspective. Ph.d.thesis CeSoS.
IMT 2010-67	Jiao, Linlin	Wave-Induced Effects on a Pontoon-type Very Large Floating Structures (VLFS). Ph.D.-thesis, CeSOS.
IMT 2010-68	Abrahamsen, Bjørn Christian	Sloshing Induced Tank Roof with Entrapped Air Pocket. Ph.d.thesis, CeSOS.
IMT 2011-69	Karimirad, Madjid	Stochastic Dynamic Response Analysis of Spar-Type Wind Turbines with Catenary or Taut Mooring Systems. Ph.d.-thesis, CeSOS.
IMT - 2011-70	Erlend Meland	Condition Monitoring of Safety Critical Valves. Ph.d.-thesis, IMT.
IMT – 2011-71	Yang, Limin	Stochastic Dynamic System Analysis of Wave Energy Converter with Hydraulic Power Take-Off, with Particular Reference to Wear Damage Analysis, Ph.d. Thesis, CeSOS.
IMT – 2011-72	Visscher, Jan	Application of Particle Image Velocimetry on Turbulent Marine Flows, Ph.d.Thesis, IMT.
IMT – 2011-73	Su, Biao	Numerical Predictions of Global and Local Ice Loads on Ships. Ph.d.Thesis, CeSOS.
IMT – 2011-74	Liu, Zhenhui	Analytical and Numerical Analysis of Iceberg Collision with Ship Structures. Ph.d.Thesis, IMT.
IMT – 2011-75	Aarsæther, Karl Gunnar	Modeling and Analysis of Ship Traffic by Observation and Numerical Simulation. Ph.d.Thesis, IMT.
Imt – 2011-76	Wu, Jie	Hydrodynamic Force Identification from Stochastic Vortex Induced Vibration Experiments with Slender Beams. Ph.d.Thesis, IMT.
Imt – 2011-77	Amini, Hamid	Azimuth Propulsors in Off-design Conditions. Ph.d.Thesis, IMT.
IMT – 2011-78	Nguyen, Tan-Hoi	Toward a System of Real-Time Prediction and Monitoring of Bottom Damage Conditions During Ship Grounding. Ph.d.thesis, IMT.



IMT-2011-79	Tavakoli, Mohammad T.	Assessment of Oil Spill in Ship Collision and Grounding, Ph.d.thesis, IMT.
IMT-2011-80	Guo, Bingjie	Numerical and Experimental Investigation of Added Resistance in Waves. Ph.d.Thesis, IMT.
IMT-2011-81	Chen, Qiaofeng	Ultimate Strength of Aluminium Panels, considering HAZ Effects, IMT
IMT-2012-82	Kota, Ravikiran S.	Wave Loads on Decks of Offshore Structures in Random Seas, CeSOS.
IMT-2012-83	Sten, Ronny	Dynamic Simulation of Deep Water Drilling Risers with Heave Compensating System, IMT.
IMT-2012-84	Berle, Øyvind	Risk and resilience in global maritime supply chains, IMT.
IMT-2012-85	Fang, Shaoji	Fault Tolerant Position Mooring Control Based on Structural Reliability, CeSOS.
IMT-2012-86	You, Jikun	Numerical studies on wave forces and moored ship motions in intermediate and shallow water, CeSOS.
IMT-2012-87	Xiang ,Xu	Maneuvering of two interacting ships in waves, CeSOS
IMT-2012-88	Dong, Wenbin	Time-domain fatigue response and reliability analysis of offshore wind turbines with emphasis on welded tubular joints and gear components, CeSOS
IMT-2012-89	Zhu, Suji	Investigation of Wave-Induced Nonlinear Load Effects in Open Ships considering Hull Girder Vibrations in Bending and Torsion, CeSOS
IMT-2012-90	Zhou, Li	Numerical and Experimental Investigation of Station-keeping in Level Ice, CeSOS
IMT-2012-91	Ushakov, Sergey	Particulate matter emission characteristics from diesel engines operating on conventional and alternative marine fuels, IMT
IMT-2013-1	Yin, Decao	Experimental and Numerical Analysis of Combined In-line and Cross-flow Vortex Induced Vibrations, CeSOS
IMT-2013-2	Kurniawan, Adi	Modelling and geometry optimisation of wave energy converters, CeSOS
IMT-2013-3	Al Ryati, Nabil	Technical condition indexes of auxiliary marine diesel engines, IMT
IMT-2013-4	Firoozkoobi, Reza	Experimental, numerical and analytical investigation of the effect of screens on sloshing, CeSOS
IMT-2013-5	Ommani, Babak	Potential-Flow Predictions of a Semi-Displacement Vessel Including Applications to Calm Water Broaching, CeSOS

IMT-2013-6	Xing, Yihan	Modelling and analysis of the gearbox in a floating spar-type wind turbine, CeSOS
IMT-7-2013	Balland, Océane	Optimization models for reducing air emissions from ships, IMT
IMT-8-2013	Yang, Dan	Transitional wake flow behind an inclined flat plate---- Computation and analysis, IMT
IMT-9-2013	Abdillah, Suyuthi	Prediction of Extreme Loads and Fatigue Damage for a Ship Hull due to Ice Action, IMT
IMT-10-2013	Ramirez, Pedro Agustin Pérez	Ageing management and life extension of technical systems- Concepts and methods applied to oil and gas facilities, IMT
IMT-11-2013	Chuang, Zhenju	Experimental and Numerical Investigation of Speed Loss due to Seakeeping and Maneuvering. IMT
IMT-12-2013	Etemaddar, Mahmoud	Load and Response Analysis of Wind Turbines under Atmospheric Icing and Controller System Faults with Emphasis on Spar Type Floating Wind Turbines, IMT
IMT-13-2013	Lindstad, Haakon	Strategies and measures for reducing maritime CO2 emissions, IMT
IMT-14-2013	Haris, Sabril	Damage interaction analysis of ship collisions, IMT
IMT-15-2013	Shainee, Mohamed	Conceptual Design, Numerical and Experimental Investigation of a SPM Cage Concept for Offshore Mariculture, IMT
IMT-16-2013	Gansel, Lars	Flow past porous cylinders and effects of biofouling and fish behavior on the flow in and around Atlantic salmon net cages, IMT
IMT-17-2013	Gaspar, Henrique	Handling Aspects of Complexity in Conceptual Ship Design, IMT
IMT-18-2013	Thys, Maxime	Theoretical and Experimental Investigation of a Free Running Fishing Vessel at Small Frequency of Encounter, CeSOS
IMT-19-2013	Aglen, Ida	VIV in Free Spanning Pipelines, CeSOS
IMT-1-2014	Song, An	Theoretical and experimental studies of wave diffraction and radiation loads on a horizontally submerged perforated plate, CeSOS
IMT-2-2014	Rogne, Øyvind Ygre	Numerical and Experimental Investigation of a Hinged 5-body Wave Energy Converter, CeSOS
IMT-3-2014	Dai, Lijuan	Safe and efficient operation and maintenance of offshore wind farms ,IMT
IMT-4-2014	Bachynski, Erin Elizabeth	Design and Dynamic Analysis of Tension Leg Platform Wind Turbines, CeSOS

IMT-5-2014	Wang, Jingbo	Water Entry of Freefall Wedged – Wedge motions and Cavity Dynamics, CeSOS
IMT-6-2014	Kim, Ekaterina	Experimental and numerical studies related to the coupled behavior of ice mass and steel structures during accidental collisions, IMT
IMT-7-2014	Tan, Xiang	Numerical investigation of ship's continuous- mode icebreaking in level ice, CeSOS
IMT-8-2014	Muliawan, Made Jaya	Design and Analysis of Combined Floating Wave and Wind Power Facilities, with Emphasis on Extreme Load Effects of the Mooring System, CeSOS
IMT-9-2014	Jiang, Zhiyu	Long-term response analysis of wind turbines with an emphasis on fault and shutdown conditions, IMT
IMT-10-2014	Dukan, Fredrik	ROV Motion Control Systems, IMT
IMT-11-2014	Grimsmo, Nils I.	Dynamic simulations of hydraulic cylinder for heave compensation of deep water drilling risers, IMT
IMT-12-2014	Kvittem, Marit I.	Modelling and response analysis for fatigue design of a semisubmersible wind turbine, CeSOS
IMT-13-2014	Akhtar, Juned	The Effects of Human Fatigue on Risk at Sea, IMT
IMT-14-2014	Syahroni, Nur	Fatigue Assessment of Welded Joints Taking into Account Effects of Residual Stress, IMT
IMT-1-2015	Böckmann, Eirik	Wave Propulsion of ships, IMT
IMT-2-2015	Wang, Kai	Modelling and dynamic analysis of a semi-submersible floating vertical axis wind turbine, CeSOS
IMT-3-2015	Fredriksen, Arnt Gunvald	A numerical and experimental study of a two-dimensional body with moonpool in waves and current, CeSOS
IMT-4-2015	Jose Patricio Gallardo Canabes	Numerical studies of viscous flow around bluff bodies, IMT
IMT-5-2015	Vegard Longva	Formulation and application of finite element techniques for slender marine structures subjected to contact interactions, IMT
IMT-6-2015	Jacobus De Vaal	Aerodynamic modelling of floating wind turbines, CeSOS
IMT-7-2015	Fachri Nasution	Fatigue Performance of Copper Power Conductors, IMT
IMT-8-2015	Oleh I Karpa	Development of bivariate extreme value distributions for applications in marine technology, CeSOS

IMT-9-2015	Daniel de Almeida Fernandes	An output feedback motion control system for ROVs, AMOS
IMT-10-2015	Bo Zhao	Particle Filter for Fault Diagnosis: Application to Dynamic Positioning Vessel and Underwater Robotics, CeSOS
IMT-11-2015	Wenting Zhu	Impact of emission allocation in maritime transportation, IMT
IMT-12-2015	Amir Rasekhi Nejad	Dynamic Analysis and Design of Gearboxes in Offshore Wind Turbines in a Structural Reliability Perspective, CeSOS
IMT-13-2015	Arturo Jesús Ortega Malca	Dynamic Response of Flexibles Risers due to Unsteady Slug Flow, CeSOS
IMT-14-2015	Dagfinn Husjord	Guidance and decision-support system for safe navigation of ships operating in close proximity, IMT
IMT-15-2015	Anirban Bhattacharyya	Ducted Propellers: Behaviour in Waves and Scale Effects, IMT
IMT-16-2015	Qin Zhang	Image Processing for Ice Parameter Identification in Ice Management, IMT
IMT-1-2016	Vincentius Rumawas	Human Factors in Ship Design and Operation: An Experiential Learning, IMT
IMT-2-2016	Martin Storheim	Structural response in ship-platform and ship-ice collisions, IMT
IMT-3-2016	Mia Abrahamsen Prsic	Numerical Simulations of the Flow around single and Tandem Circular Cylinders Close to a Plane Wall, IMT
IMT-4-2016	Tufan Arslan	Large-eddy simulations of cross-flow around ship sections, IMT
IMT-5-2016	Pierre Yves-Henry	Parametrisation of aquatic vegetation in hydraulic and coastal research,IMT
IMT-6-2016	Lin Li	Dynamic Analysis of the Instalation of Monopiles for Offshore Wind Turbines, CeSOS
IMT-7-2016	Øivind Kåre Kjerstad	Dynamic Positioning of Marine Vessels in Ice, IMT
IMT-8-2016	Xiaopeng Wu	Numerical Analysis of Anchor Handling and Fish Trawling Operations in a Safety Perspective, CeSOS
IMT-9-2016	Zhengshun Cheng	Integrated Dynamic Analysis of Floating Vertical Axis Wind Turbines, CeSOS
IMT-10-2016	Ling Wan	Experimental and Numerical Study of a Combined Offshore Wind and Wave Energy Converter Concept

IMT-11-2016	Wei Chai	Stochastic dynamic analysis and reliability evaluation of the roll motion for ships in random seas, CeSOS
IMT-12-2016	Øyvind Selnes Patricksson	Decision support for conceptual ship design with focus on a changing life cycle and future uncertainty, IMT
IMT-13-2016	Mats Jørgen Thorsen	Time domain analysis of vortex-induced vibrations, IMT
IMT-14-2016	Edgar McGuinness	Safety in the Norwegian Fishing Fleet – Analysis and measures for improvement, IMT
IMT-15-2016	Sepideh Jafarzadeh	Energy efficiency and emission abatement in the fishing fleet, IMT
IMT-16-2016	Wilson Ivan Guachamin Acero	Assessment of marine operations for offshore wind turbine installation with emphasis on response-based operational limits, IMT
IMT-17-2016	Mauro Candeloro	Tools and Methods for Autonomous Operations on Seabed and Water Column using Underwater Vehicles, IMT
IMT-18-2016	Valentin Chabaud	Real-Time Hybrid Model Testing of Floating Wind Turbines, IMT
IMT-1-2017	Mohammad Saud Afzal	Three-dimensional streaming in a sea bed boundary layer
IMT-2-2017	Peng Li	A Theoretical and Experimental Study of Wave-induced Hydroelastic Response of a Circular Floating Collar
IMT-3-2017	Martin Bergström	A simulation-based design method for arctic maritime transport systems
IMT-4-2017	Bhushan Taskar	The effect of waves on marine propellers and propulsion
IMT-5-2017	Mohsen Bardestani	A two-dimensional numerical and experimental study of a floater with net and sinker tube in waves and current
IMT-6-2017	Fatemeh Hoseini Dadmarzi	Direct Numerical Simulation of turbulent wakes behind different plate configurations
IMT-7-2017	Michel R. Miyazaki	Modeling and control of hybrid marine power plants
IMT-8-2017	Giri Rajasekhar Gunnu	Safety and efficiency enhancement of anchor handling operations with particular emphasis on the stability of anchor handling vessels
IMT-9-2017	Kevin Koosup Yum	Transient Performance and Emissions of a Turbocharged Diesel Engine for Marine Power Plants
IMT-10-2017	Zhaolong Yu	Hydrodynamic and structural aspects of ship collisions

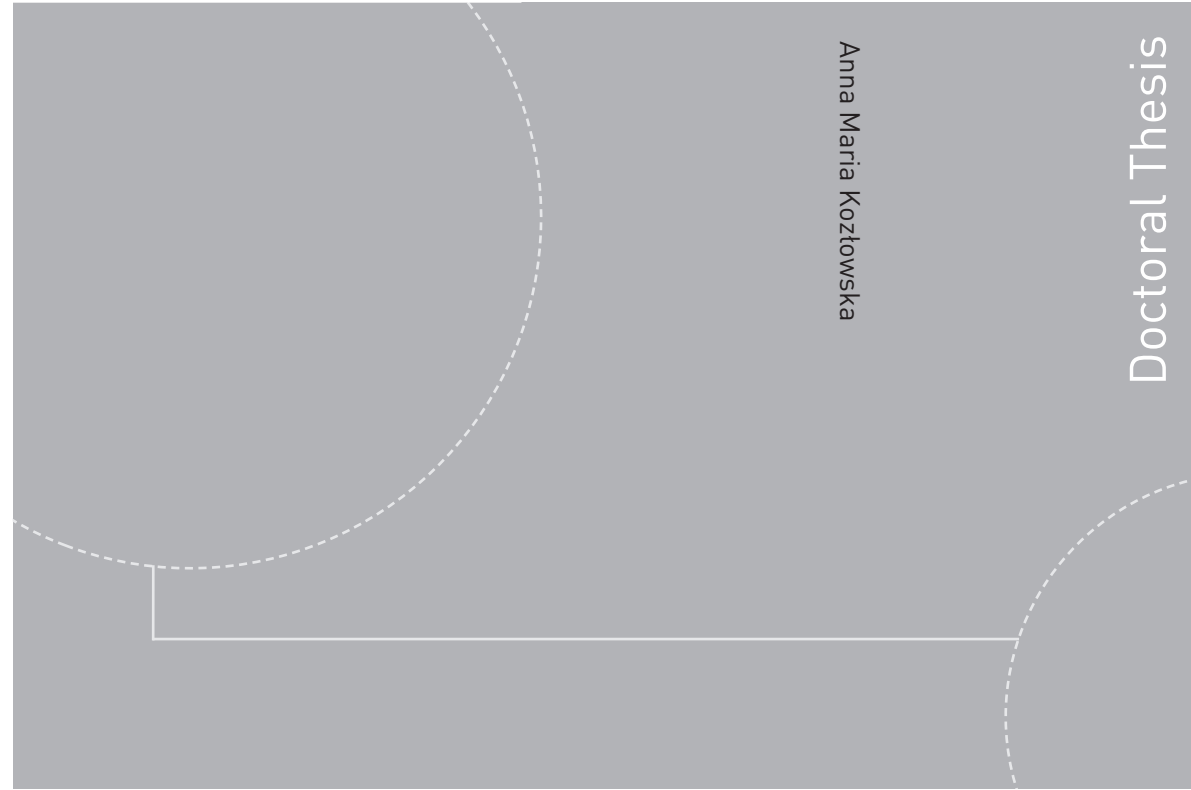
IMT-11-2017	Martin Hassel	Risk Analysis and Modelling of Allisions between Passing Vessels and Offshore Installations
IMT-12-2017	Astrid H. Brodtkorb	Hybrid Control of Marine Vessels – Dynamic Positioning in Varying Conditions
IMT-13-2017	Kjersti Bruserud	Simultaneous stochastic model of waves and current for prediction of structural design loads
IMT-14-2017	Finn-Idar Grøtta Giske	Long-Term Extreme Response Analysis of Marine Structures Using Inverse Reliability Methods
IMT-15-2017	Stian Skjong	Modeling and Simulation of Maritime Systems and Operations for Virtual Prototyping using co-Simulations
IMT-1-2018	Yingguang Chu	Virtual Prototyping for Marine Crane Design and Operations
IMT-2-2018	Sergey Gavrilin	Validation of ship manoeuvring simulation models
IMT-3-2018	Jeevith Hegde	Tools and methods to manage risk in autonomous subsea inspection, maintenance and repair operations
IMT-4-2018	Ida M. Strand	Sea Loads on Closed Flexible Fish Cages
IMT-5-2018	Erlend Kvinge Jørgensen	Navigation and Control of Underwater Robotic Vehicles
IMT-6-2018	Bård Stovner	Aided Inertial Navigation of Underwater Vehicles
IMT-7-2018	Erlend Liavåg Grotle	Thermodynamic Response Enhanced by Sloshing in Marine LNG Fuel Tanks
IMT-8-2018	Børge Rokseth	Safety and Verification of Advanced Maritime Vessels
IMT-9-2018	Jan Vidar Ulveseter	Advances in Semi-Empirical Time Domain Modelling of Vortex-Induced Vibrations
IMT-10-2018	Chenyu Luan	Design and analysis for a steel braceless semi-submersible hull for supporting a 5-MW horizontal axis wind turbine
IMT-11-2018	Carl Fredrik Rehn	Ship Design under Uncertainty
IMT-12-2018	Øyvind Ødegård	Towards Autonomous Operations and Systems in Marine Archaeology
IMT-13-2018	Stein Melvær Nornes	Guidance and Control of Marine Robotics for Ocean Mapping and Monitoring
IMT-14-2018	Petter Norgren	Autonomous Underwater Vehicles in Arctic Marine Operations: Arctic marine research and ice monitoring

IMT-15-2018	Minjoo Choi	Modular Adaptable Ship Design for Handling Uncertainty in the Future Operating Context
MT-16-2018	Ole Alexander Eidsvik	Dynamics of Remotely Operated Underwater Vehicle Systems
IMT-17-2018	Mahdi Ghane	Fault Diagnosis of Floating Wind Turbine Drivetrain-Methodologies and Applications
IMT-18-2018	Christoph Alexander Thieme	Risk Analysis and Modelling of Autonomous Marine Systems
IMT-19-2018	Yugao Shen	Operational limits for floating-collar fish farms in waves and current, without and with well-boat presence
IMT-20-2018	Tianjiao Dai	Investigations of Shear Interaction and Stresses in Flexible Pipes and Umbilicals
IMT-21-2018	Sigurd Solheim Pettersen	Resilience by Latent Capabilities in Marine Systems
IMT-22-2018	Thomas Sauder	Fidelity of Cyber-physical Empirical Methods. Application to the Active Truncation of Slender Marine Structures
IMT-23-2018	Jan-Tore Horn	Statistical and Modelling Uncertainties in the Design of Offshore Wind Turbines
IMT-24-2018	Anna Swider	Data Mining Methods for the Analysis of Power Systems of Vessels
IMT-1-2019	Zhao He	Hydrodynamic study of a moored fish farming cage with fish influence
IMT-2-2019	Isar Ghamari	Numerical and Experimental Study on the Ship Parametric Roll Resonance and the Effect of Anti-Roll Tank
IMT-3-2019	Håkon Strandenes	Turbulent Flow Simulations at Higher Reynolds Numbers
IMT-4-2019	Siri Mariane Holen	Safety in Norwegian Fish Farming – Concepts and Methods for Improvement
IMT-5-2019	Ping Fu	Reliability Analysis of Wake-Induced Riser Collision
IMT-6-2019	Vladimir Krivopolianskii	Experimental Investigation of Injection and Combustion Processes in Marine Gas Engines using Constant Volume Rig

IMT-7- 2019	Hans-Martin Heyn	Motion Sensing on Vessels Operating in Sea Ice: A Local Ice Monitoring System for Transit and Stationkeeping Operations under the Influence of Sea Ice
IMT-8- 2019	Anna Maria Kozłowska	Hydrodynamic Loads on Marine Propellers Subject to Ventilation and out of Water Condition.



ISBN 978-82-326-3774-4 (printed version)  
ISBN 978-82-326-3775-1 (electronic version)  
ISSN 1503-8181



Anna Maria Kozłowska

Doctoral Thesis

Doctoral theses at NTNU, 2019:86

Anna Maria Kozłowska

**Hydrodynamic Loads on Marine  
Propellers Subject to  
Ventilation and Out of Water Condition**

Doctoral theses at NTNU, 2019:86

**NTNU**  
Norwegian University of  
Science and Technology  
Faculty of Engineering  
Department of Marine Technology

 **NTNU**  
Norwegian University of  
Science and Technology

 **NTNU**

 **NTNU**  
Norwegian University of  
Science and Technology